

University of Nottingham

UK | CHINA | MALAYSIA

Electrical conductivity enhancement of alkaline earth titanates for high-temperature thermoelectric applications.

Thesis

Alexandre Manon

Supervisors : Dr Ming Li, Professor David Grant

Faculty of Engineering

Advanced Materials Research Group (AMRG)

Abstract

With the global energy crisis, new methods and devices to decrease primary energy consumption are needed. In many sectors with unexploited exhausted heat where standard thermodynamic cycle such as the Rankine cycle cannot be used, the use of a thermoelectric generator can produce electricity from waste exhaust heat to increase the efficiency. The state-of-the-art n-type oxide thermoelectric materials are based on rare-earth doped strontium titanate ($SrTiO_3$). Alkaline earth titanates have a similar electronic structure. It is then expected that doped barium titanate ($BaTiO_3$) and calcium titanate ($CaTiO_3$) are potential candidates for n-type oxide thermoelectric materials. These materials were the subject of numerous studies, however, studies to make them performant thermoelectric materials are rare. Electrical conductivity is one key parameter to achieve high thermoelectric performances. Reports of conductive barium titanate are scarce, and none of them reported sufficient electrical conductivity for thermoelectric applications. Reports of high electrical conductivity of rare-earth-doped calcium titanate are even fewer.

Creating oxygen loss and donor doping (e.g., replacing one Sr^{3+} on the A-site with one La^{3+} in $SrTiO_3$) are two common strategies to create electrons and achieve high electrical conductivity in metal oxides. These reactions are often energetically unfavourable. A high sintering temperature with a low oxygen partial pressure is typically needed to facilitate both oxygen loss and donor doping. Often sintering is conducted in a reducing atmosphere using a tube furnace with a limited maximum temperature (typically <1,600°C for conventional tube furnaces). In this project, a combination of arc melting and spark plasma sintering was specifically chosen to obtain high electrical conductivity of lanthanum-doped barium titanate and lanthanum-doped calcium titanate. These two techniques offer extremely high temperatures, high heating/cooling rates and low oxygen partial pressure. The electronic compensation mechanism via donor doping, in which the alkaline earth element is substituted by a lanthanum that increases the number of charge carriers by one electron, becomes favoured over the ionic compensation mechanism under such conditions, giving rise to high charge carrier concentration. Additional oxygen vacancies can be created, further increasing the electron concentrations by two electrons for each oxygen vacancy. Three families of compositions based on lanthanum-doped barium titanate and lanthanum-doped calcium titanate were synthesised and characterised. Two families of the

compositions are designed according to the electronic compensation mechanism via lanthanum donor doping (general formula $La_xBa_{1-x}TiO_3$ and $La_xCa_{1-x}TiO_3$). In the third family of the compositions, the lanthanum doping in calcium titanate is charge-compensated by creation of calcium vacancies (general formula: $La_xCa_{1-(3/2x)}TiO_3$).

X-ray diffraction revealed a complete solid solubility for both $La_xBa_{1-x}TiO_3$ and $La_xCa_{1-x}TiO_3$. Perovskite structures were observed for $0 \leq x \leq 1$ with changes of lattice parameters following Vegard's law. Compositional analysis using electron probe microanalysis (EPMA), scanning electron microscopy (SEM) and energy dispersive X-ray spectroscopy (EDS) showed the atomic ratios of the total A-site cations to the B-site cations (Ti) are close to the nominal ratio of 1:1 in both $La_xBa_{1-x}TiO_3$ and $La_xCa_{1-x}TiO_3$ systems. Inhomogeneous distribution of the two A-site cations (La and Ba in $La_xBa_{1-x}TiO_3$, La and Ca in $La_xCa_{1-x}TiO_3$) were observed in some compositions. For lanthanum-doped calcium titanate with A-site deficient doping mechanism ($La_xCa_{1-1.5x}TiO_3$), titanium-rich secondary phases were observed, suggesting this doping mechanism is not favoured under the used synthesis conditions. Exceptionally high electrical conductivity was achieved in all the three families of compositions. The three systems showed metallic behaviours from in all lanthanum-doped compositions. Electrical conductivity increased with the doping level (x) until the drop of the sinterability. For lanthanum-doped barium titanate, the composition of x=0.3 ($La_{0.3}Ba_{0.7}TiO_3$) exhibited an electrical conductivity of 3,700 $S.cm^{-1}$ at room temperature, which is the highest electrical conductivity achieved to date for this family of compositions. A high power factor of 0.6 $mW.m^{-1}.K^{-2}$ was obtained at 365 °C in the composition x=0.2 ($La_{0.2}Ba_{0.8}TiO_3$). For lanthanum-doped calcium titanate with the electronic compensation mechanism, the composition x=0.5 ($La_{0.5}Ca_{0.5}TiO_3$) showed a high electrical conductivity of 3,200 $S.cm^{-1}$ at room temperature. The highest power factor of 0.97 $mW.m^{-1}.K^{-2}$ was obtained at 270°C in the sample x=0.2 ($La_{0.2}Ca_{0.8}TiO_3$) sintered at 1500°C, which is comparable to the highest power factor values reported in the literature that were obtained at much higher temperatures (∼740 °C).

This project demonstrates the significant capability of arc melting and spark plasma sintering for boosting oxygen loss and donor doping to generate electrons and achieve exceptionally high electrical conductivity in metal oxides. This manufacture approach can be applied to fabricate a wide range of highly conductive n-type metal oxides.

Acknowledgements

Firstly, I would like to express my sincere gratitude to my supervisors Dr Ming Li and Professor David Grant for the continuous support of my Ph.D study and related research, for their patience, motivation, and immense knowledge. Their guidance helped me in all the time of research and writing of this thesis. My gratitude also goes toward my internal examiner Dr Xianghui Hou.

I thank the University of Nottingham for the Vice-Chancellors Scholarship for Research Excellence (European Union) as well as the Faculty of Engineering for the funding.

Besides I want to thank the researchers, Tianhui Liu, Lei Lei, Yu Yu, Zanpeng Xu, Yiming Lyu, Qinxuan Wang, Marcus Adam, Jacob Porter, and Sweta Munshi for their advice and training. My sincere thanks also go to all the staff and technicians who worked in the Wolfson building and the Research Acceleration and Demonstration Building. Special thanks to Rory Screaton, William Boardman, and John Kirk for the help to fix numerous broken equipment. To Hannah Constantin and Nigel Neate for training and advice for XRD experiments. I also want to thank the staff of the Nanoscale and Microscale Research Centre, special thank to Grace Belshaw, Elisabeth Steer, and Martin Roe for their advice, training, and help. I am grateful to Natasha Parhar for helping improve my writing skills.

Contents

Glossary **1**

1 Introduction, the thermoelectric effects **3**

2 Literature review **10**

2.1 Properties and performances of the stats of arts thermoelectric meterials 10

2.1.1 Metal thermoelectric materials 10

2.1.2 Oxide thermoelectric materials 14

2.2 Properties and defect chemistry of ABX_3 alkaline earth titanates 19

2.3 Aims and objectives 38

3 Methodology **40**

3.1 Raw Materials 40

3.2 Material preparation 41

3.3 Microstructural characterisation 45

3.4 Testing and evaluation of performance 49

4 Synthesis, structural, and thermoelectric properties of $La_xBa_{1-x}TiO_3$ **53**

4.1 Introduction 53

4.2 Influence of the synthesis route. 54

4.3 Structure, microstructure, and oxidation properties 57

4.4 Evaluation of the thermoelectric performances. 95

4.5 Summary 105

5 Synthesis, structural, and thermoelectric properties of $La_xCa_{1-x}TiO_3$ **106**

5.1 Introduction 106

5.2 Structure, microstructure, and oxidation properties 106

5.3 Evaluation of the thermoelectric performances 133

5.4 Summary 140

6 Synthesis, structural, and thermoelectric properties of $La_xCa_{1-(3/2x)}TiO_3$ **142**

6.1 Introduction 142

6.2 Investigation of the doping mechanism by structural and microstructural analysis. . 142

6.3 Evaluation of the electrical performances 149

6.4 Summary 151

7 Conclusion **152**

8 Future work **153**

9 References **155**

10 Appendice **179**

List of Figures **190**

List of Tables **202**

Glossary

α : Thermal diffusivity

β : Full width at half maximum

C_p : Heat capacity at constant pressure

D : Density

η : Efficiency

EDX / EDS : Energy-dispersive X-ray spectroscopy

EPMA : Electron probe micro-anayser

I_{ab} : Electric current from a to b

K : Shape factor

κ : Thermal conductivity $\kappa = \alpha\rho C_p$

L : Crystallite size

LFA : Laser flash analysis

λ : Wavelenght

N_A : Avogadro constant : $6.02214076 \cdot 10^{23} mol^{-1}$

Π_{ab} : Peltier coefficient of the junction at materials a and b

PF : Power factor PF = $S^2\sigma$

Q_{ab} : Heat transfered from a to b

R_A : Ionic radius of the cation A

R_B : Ionic radius of the cation B

R_X : Ionic radius of the anion X

S : Absolute Seebeck coefficient

S_{ab} : Relative Ceebeck coeffcient of the junction of material a and b

σ : Electrical conductivity

SEM : Scanning electron microscopy

SPS : Spark plasma sintering

t : Goldshmidt's tolerance factor

τ : Relaxation time

T_{av} : Average temperature of the thermoelectric device

T_{hot} : Temperature at the hot side

T_{cold} : Temperature at the cold side

TGA : Thermogravimetric analysis

XPS : X-Ray photoelectron spectrometry

XRD : X-ray diffraction

WDX : Wavelenght-dispersice X-ray spectroscopy

ZT : Figure of merit $ZT = \frac{PFT}{\kappa} = \frac{S^2 \sigma T}{\kappa}$

1 Introduction, the thermoelectric effects

With the ever-growing concern about the climate crisis, the dependency on fossil fuels is diminishing. It is highly important to develop novel green technologies during such a shift. A significant fraction of societal energy usage is in either heating or cooling. In 2012 the total global rejected energy was 340.512 PJ for a total energy consumption of 474.171 PJ. For the industrial sector only, the rejected energy totalled 54.233 PJ, among the loss 30% was exhaust heat. Depending on the sector the "quality" of the heat is different, as examples in the residential and electricity sector, 100% of the exhaust heat is under 300°C, while in the transport sector 54% is higher than 300°C, and in the industrial sector 38% is higher than 300°C [1]. In Germany it was estimated that among the exhaust heat 8.88 PJ had T $\geq$ 400°C, 5.543 PJ had T $\geq$ 600°C, and 2.99 PJ had T $\geq$ 800°C [2]. One way to decrease the global energy consumption is to produce electricity with the heat waste, because the temperatures of the waste are different, different classes of materials should be developed. Thermoelectric generators are an asset to achieve this aim, while they are less efficient than e.g. a Rankin cycle, they are less voluminous and could be included in processes where other thermodynamic cycles could not.

Thermoelectrics can be in two different configurations, as a generator, where a difference of temperature is applied and an electric current is collected, or as a cooler, where an electric current in applied and a heat flow is produced from the cooler surface to the hotter surface. In both cases, the number of potential applications is as large as the number of existing heat sources and needs for cooling. Among others, the heat can be harvested from chipsets, human bodies, car exhaust gas, radioisotope heaters, power stations exhaust gas, or in cooler configuration it can be use as portable refrigerators. In 2014, the efficiency of commercially available thermoelectric modules was less than 10% [3], even if research groups obtained higher efficiency, as example 13.3% at T_h = 801.3 K and T_c = 385.8 K with silver antimony lead telluride based modules [4]. Because of their still limited performances and high costs, the use of thermoelectric generators is limited to a few applications such as electricity generation from radioisotopes for space exploration [5–7].

There are three thermoelectric effects: the Seebeck Effect, the Peltier Effect and the Thomson

Effect. The Seebeck effect, as illustrated in Figure 1.1 is described as follows : when a gradient of temperature is applied on a junction of a material "a" with a non-zero Seebeck coefficient and a material "b", the carrier diffusivity would generally be higher at the hotter location compared to the colder location, leading to a gradient of carrier concentration at the equilibrium, resulting in a difference of electric potential between the hot and the cold side. In the Seebeck effect the thermal energy at the hot end results in greater kinetic energy of the valence electrons and these valence electrons migrate more rapidly towards the other (colder) end as compared to the colder part's electrons migrating towards the warmer part. At the hot side there is a higher concentration of electrons above the Fermi energy but on the cold side there are fewer electrons above the Fermi energy. Electrons go to where the energy is lower so therefore it will move from the warmer end to the colder end, which leads to the transporting energy and eventually equilibrating the temperature.

-The absolute Seebeck coefficient is defined by [8] :

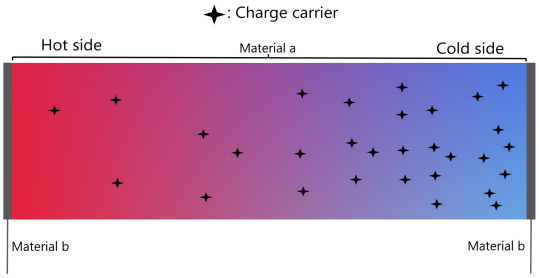


Figure 1.1: Illustration of the Seebeck effect induced by a gradient of temperature at the junction of a material "a" and "b". The charge carriers (e.g. electrons or holes) move from the colder to the hotter side and are collected by the material "b" which closes the circuit.

$$S = \frac{-\Delta V}{\Delta T} \tag{1}$$

Where ΔV is the difference of electric potential and ΔT the difference of temperature. The Seebeck coefficient or the thermoelectric power represents the ability of a material to produce a difference of electric potential induced by Seebeck effect in response to a gradient of temperature. The sign of

the coefficient is determined by the electric charge of the dominant charge carrier, so the coefficient will be negative for negatively charge carrier like electron and the coefficient will be positive for positively charge carrier like holes. In practice it is the relative Seebeck coefficient that is measured, the relative Seebeck coefficient is the Seebeck coefficient of the material and the probes used to measure ΔV and ΔT. To obtain the absolute Seebeck coefficient, the relative Seebeck coefficient is subtracted by the absolute Seebeck coefficient of the probes.

The Peltier effect is the opposite of the Seebeck effect, when an electric current is applied on a junction of a material "a" with a non-zero Seebeck coefficient and a material "b", electrons will transport entropy and heat would be transported. The Peltier coefficient is defined by the heat transported from material "a" to "b" divided by the current intensity [9]:

$$\Pi_{ab} = \frac{Q_{ab}}{I_{ab}} \tag{2}$$

With Q_{ab} the heat flow transported from the material "a" to material "b" and I_{ab} the intensity of the electric current through the materials "a" and "b". The Seebeck effect and Peltier effect are connected together by the Kelvin relationship [9]:

$$\Pi_{ab} = S_{ab}T \tag{3}$$

With S_{ab} the relative Seebeck coefficient of the junction ab. The third thermoelectric effect is the Thomson effect. When the Seebeck coefficient of a material is temperature dependent ($\frac{dS}{dT} \neq 0$), a local gradient of temperature would generate a difference of Seebeck coefficient within the material, if an electric current pass through the material a heat flow would be created through the material (similar to a Peltier effect when two materials are connected). The Thomson effect is illustrated in Figure 1.2 and it follows the equation below [10]:

$$\vec{Q} = \Delta S \vec{J} \tag{4}$$

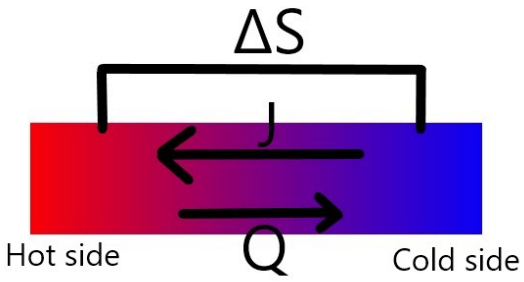


Figure 1.2: Illustration of the Thomson effect, a gradient of temperature at a material with a temperature-dependent Seebeck coefficient induces a difference of Seebeck coefficient ΔS, then if an electric current J is imposed by a generator and pass through the material, it would result in a heat flow Q.

The thermoelectric generators are based on the Seebeck effect and the thermoelectric coolers are based on the Peltier effect. Both types of devices are composed of one or several pairs in series of n-type and p-type thermoelectric materials. When an n-type semiconductor and a p-type semiconductor are connected in the presence of a gradient of temperature, an electric current is generated by Seebeck effect, as illustrated in Figure 1.3. If an electric current is applied through the n-type and p-type materials, then a heat flow is produced by Peltier effect and a temperature difference is created, as illustrated in Figure 1.4.

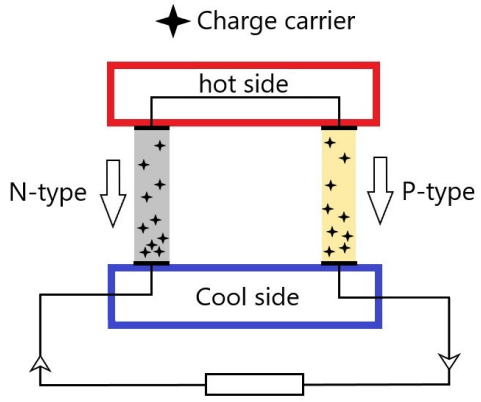


Figure 1.3: Thermoelectric generator circuit. Electricity is created from the movement of charge carriers of an n-type (electrons) and a p-type (holes) materials induced by a difference of temperature.

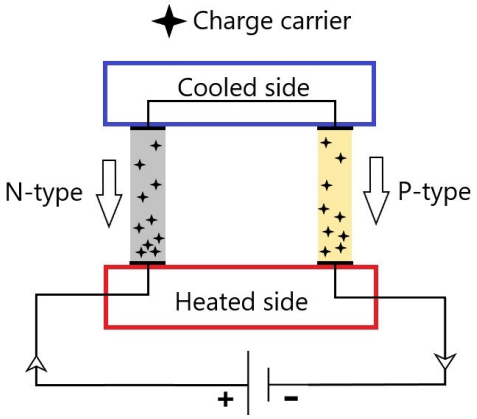


Figure 1.4: Thermoelectric cooler circuit. Heat flow is created from the electrical current passing through an n-type and a p-type materials with a temperature difference.

A thermoelectric material is characterised, depending on the temperature, by :

- The electrical conductivity σ, which is the product of the mobility of carrier and the density of carrier.
- The thermal conductivity κ which is the sum of the contribution of the phonons and the electrons.
- The absolute Seebeck coefficient.

In order to easily compare the performance of a thermoelectric material, two others variables have been introduced : the power factor PF and the figure of merit ZT. The power factor is simply the multiplication of the electrical conductivity and the squared Seebeck coefficient [11]:

$$PF = S^2\sigma \tag{5}$$

-ZT, the figure of merit is the power factor multiplied by the temperature and divided by the

thermal conductivity [11]:

$$ZT = \frac{PFT}{\kappa} = \frac{S^2\sigma T}{\kappa} \tag{6}$$

It is the final application that determines, which of these two variables should be maximised. If the source of heat can be considered as unlimited, or if the thermoelectric needs to participate to the dissipation of the heat, the power factor should be maximised. It is highly evident that σ, S, and κ are not independent, and an improvement of one variable could result in the deterioration of another. For example, a diminution of the thermal conductivity could be the result of an increase of the electron-phonon scattering that would also decrease the electrical conductivity. The result is that it is challenging to tune one of these properties without changing the others. Therefore, in order to develop a high performing thermoelectric, it is important to not focus on one variable but to maximise all the parameters.

The efficiency η of a thermoelectric generator for heat harvesting is proportional to the ZT [11]:

$$\eta = \frac{T_{hot} - T_{cold}}{T_{hot}} \frac{\sqrt{1 + ZT_{av}} - 1}{\sqrt{1 + ZT_{av}} + \frac{T_{cold}}{T_{hot}}} \tag{7}$$

Figure 1.5 shows the efficiency for different ZT according to T_h for $T_c = 300$ K.

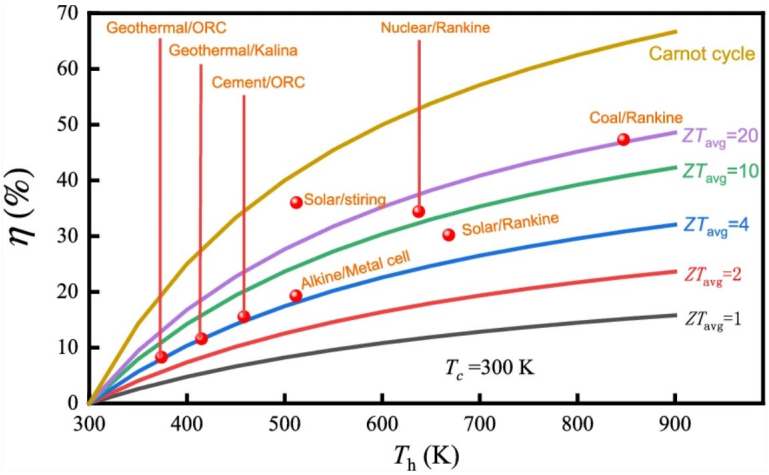


Figure 1.5: η against T_h for different ZT, reproduced with permission from ref [12].

The thesis structure succeeding the introduction about the three thermoelectric effects is as follows, section two is a literature review covering the current best-performing metals and oxides thermoelectric in order for the reader to have an overview of common approaches, physic mechanisms used in the thermoelectric materials field, and the actual performances of the best thermoelectric materials. Then a review of the alkaline earth titanates $SrTiO_3$, $BaTiO_3$, and $CaTiO_3$ focusing on the thermoelectric properties and the doping chemistry mechanisms. The review will end with a summary and a proposed analysis of the current knowledge and the research gap about the n-type oxide thermoelectric materials; then the approach developed and aims of this project. Next is section three with the methodology, followed by three main chapters four, five, and six, each containing results and discussion; one about the La-doped $BaTiO_3$, one about the La-doped $CaTiO_3$, and one about La-doped $CaTiO_3$ with A-site deficiency. The thesis is ended with the conclusion and the future work.

2 Literature review

2.1 Properties and performances of the stats of arts thermoelectric meterials

2.1.1 Metal thermoelectric materials

Telluride Historically, the state-of-the-art metal-based materials were telluride-based such as PbTe or BiTe. The maxiumum ZT for a selection of thermoelectric materials is plotted in Figure 2.1. The material has a layered structure where there is periodic weak Van der waals bond in the c direction (Figure 2.2). One main effect of these layered structures is a strong anisotropy that affects the thermal and the electrical conductivity as well as the mechanical properties. Due to the weak Van Der Waal forces, phonon scattering in the c direction is extremely high and so the thermal conductivity extremely low, for example around 1.82 $W.m^{-1}.K^{-1}$ for Tl doped PbTe at RT [13].

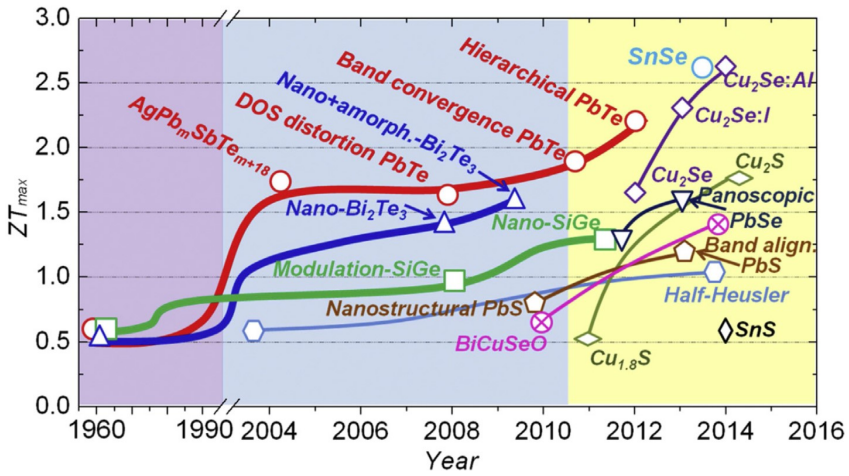


Figure 2.1: Plot of the maximum ZT of the state of art thermoelectric materials from 1960 to 2016, reproduced with permission from ref [14].

For these telluride-based systems, a ZT of 1.5 or more have been achieved in several works. For p-type for example, 1.5 at 773K has been achieved for Tl doped PbTe [13], 1.6 at 721K for Sn doped GeTe [16], ZT of 1.8 at 850K with Se doped PbTe [17], in 2012 Biswas et al demonstrated a ZT

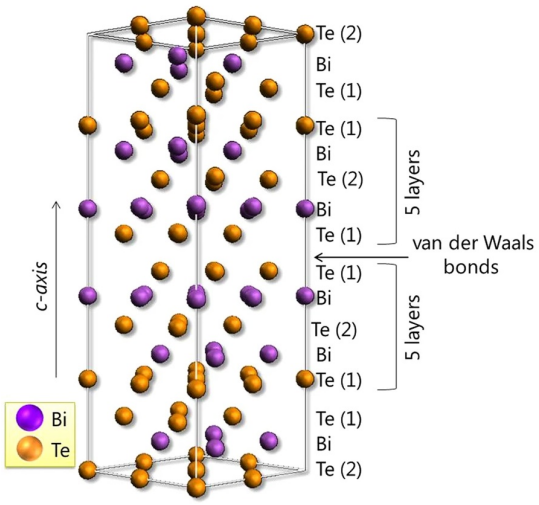


Figure 2.2: Structure of Bi_2Te_3 from ref [15], reproduced with permission.

of 2.2 at 900K for 4% mol SrTe doped PbTe synthesised by a melting followed by a spark plasma sintering (SPS) sintering [18]. N-type examples include: 1.8 at 773K for I doped PbTe [19]. Hsu et al obtained a high ZT of 2.2 at 800K with an alloy of $AgPn_mSbTe_{2+m}$ for m = 10 and m = 18 [20].

Selenide The performances of the telluride systems were surpassed in 2014 when Zhao et al observed in the b axis of a p-type single crystal of SnSe a ZT of 2.6 at 923K [21]. This discovery has been followed by numerous approaches to produce p-type or n-type SnSe based thermoelectrics. SnSe is a chalcogenides and so possesses a layered structure (Figure 2.3). While a significant amount of research has investigated p-type SnSe, the work on n-type SnSe are rarer, possibly because it is not easy to substitute elements into SnSe, to make an n-type conductor. Duong et al obtained a ZT of 2.2 at 733K for a Bi doped SnSe single crystal [22] and later Chang et al obtained a ZT of 2.8 at 773K for a Br doped SnSe single crystal [23]. The high cost of single crystal synthesis and practical application requirements means that polycrystalline materials are needed. The challenge is to maintain the strong anisotropy of this structure with the material in polycrystalline form because of the difficulties to keep the crystals in the same orientation. To try to keep the aniosotropy of the structure, a post treatment sintering with a uniaxial pressure is often applied (Figure 2.4),

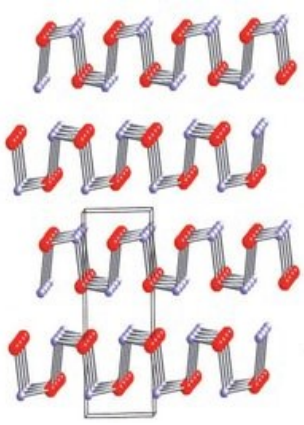


Figure 2.3: Chalcogenide structure of SnSe, Sn in grey and Se in red. From ref [24], reproduced with permission.

such as hot pressing or SPS [25]. Most of researchs on polycrystalline based SnSe do not achieve a figure of merit much higher than 1.5. Of those that do, Shi et al obtained a figure of merit of 1.7 at 823K with a p-type Cd doped SnSe produced by solvathermal synthesis followed by a SPS post treatment [25] and Lin et al 1.67 at 823K for Ag doped $(SnSe)_{1-x}(SnS)_x$ by melting and hot pressing sintering [27]. For n-type polycrystalline materials, Chang et al obtained a ZT of 1.2 at 773 with a Pb and Br doped SnSe by melting followed by SPS sintering [28].

Another high-performing p-type is the copper-based chalcogenide CuSe. Two structures exist depending on the temperature, a low-temperature α phase, and a high-temperature β phase (Figure 2.5). When in the beta phase the material is a mixed electronic-ionic conductor and the Cu ion conduction leads to multiscale disorders that produces liquid like thermal conductivity that is even lower than a glass thermal conduction. Liu et al obtained a ZT of 1.5 at 1000K for such a polycrystalline sample. Olvera et al introduced Indium additions that produced a localisation of Cu^+ that increased the electrical conductivity and decreased the already low thermal conductivity, and reached a figure of merit of 2.6 at 850K [30]. Zhong et al increased the performances by Al doping in order to increase the orientation of the lamellar grain that results in ZT = 2.62 at 756°C for $Cu_{1.94}Al_{0.02}Se$ [31]. A peak performance of ZT = 2.3 was achieved during the phase transition around 380K, in which the temperature of transition can be tuned by substituting Se by Iodine [32].

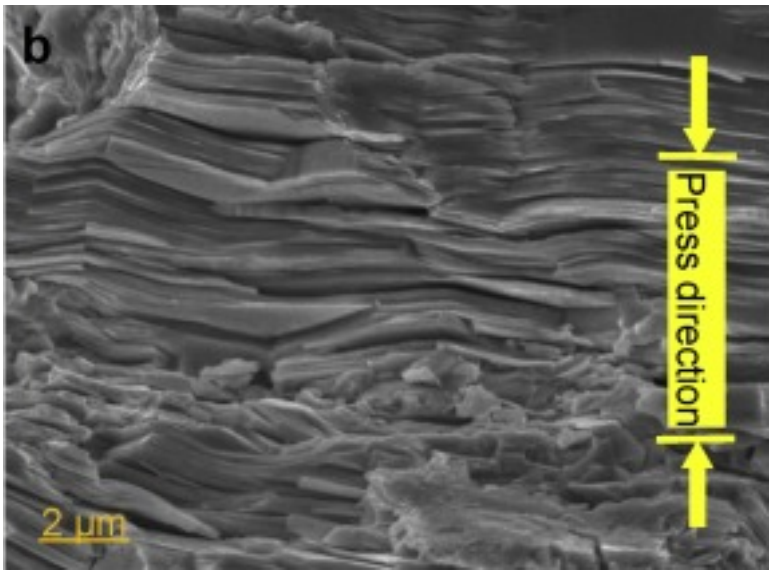


Figure 2.4: Cross section of hot pressed SnSe polycrystal, reproduced from ref [26] with permission.

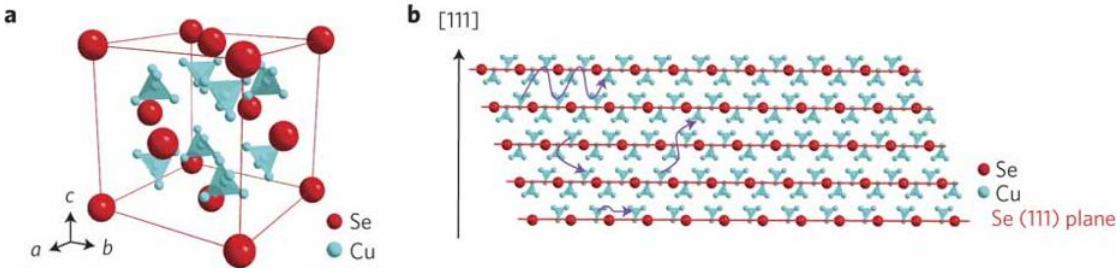


Figure 2.5: a, Unit cell where only the 8c and 32f interstitial positions are shown with Cu atoms. b, Projected plane representation of the crystal structure along the cubic direction. The arrows indicate that the Cu ions can freely travel among the interstitial sites. There are two Cu layers between the neighbouring Se (111) planes. The structure changes to a monoclinic -phase by stacking the ordered Cu ions along the cubic [111] direction when cooled to room temperature. From ref [29], reproduced with permission.

One problem of this material is the structural and chemical instability at high temperature, mainly because of Se evaporation and Cu leakage [30].

2.1.2 Oxide thermoelectric materials

The above metal materials are composed of elements that are rare (Te [33]), toxic (Pb [34], Te [35]), or with low melting points (Bi [36], Pb [37], Se [38], Sn [39], Te [40]). For an application at high temperature (e.g. 800°C) these materials are not ideal because they can melt, decomposed or be oxidised. Oxides, because of their nature suffer less of these problems.

Layered cobalt oxide Until the discovery of oxyselenide, which will be discussed in the Oxyselenide BiCuSeO part, layered cobalt oxide was probably considered the most promising p-type oxide system for thermoelectric applications. Among these, two types are the most distinct : calcium cobaltate and sodium cobaltate. Calcium cobaltate such as $Ca_3Co_4O_9$ has a layered structure composed of a succession of rock salt $Ca_2CoO_3^+$ separated by a layer of CoO_2^- (Figure 2.6). Likewise Na_xCoO_2 is similar, except that the rock salt layer is replaced by one or several layers of monovalent sodium (Figure 2.7). In regards to the performance and behaviour towards doping, similarities and differences are both present. Similar to the chalcogenide systems they possess a strong anisotropy, the Van Der Waals liaison is not favourable for the phonon propagation and this decreases the thermal conductivity in the c-axis, making $Ca_3Co_4O_9$ and Na_xCoO_2 well adapted for epithaxial thin film. In these materials the dominant charge carrier are holes, and because of the anisotropy the holes are predominately transported along the CoO_2^- layers. [41]. The maximum figure of merit for bulk pristine calcium cobaltate with conventional synthesis methods and in the absence of any post treatment is around 0.2 [44]. To improve this, substitution of several elements have been tried of which silver is the most interesting. Silver can be used either as a dopant, as a second phase, or both and each strategy can increase the performances [44]. The best results were obtained for a composite $Ca_{2.7}Ag_{0.3}Co_4O_9$ with 10 wt% of Ag, that gave a maximum ZT of 0.5 at 1000K [45].
As it is an anisotropic material, texturation to decrease the thermal conductivity is a good strategy, and Kwoon et al achieved a ZT of 0.4 utilising this approach with an undoped composition with

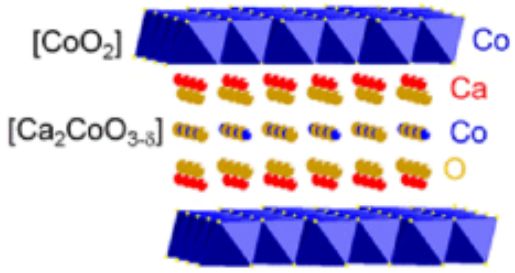


Figure 2.6: $Ca_3Co_4O_9$ structure, reproduced from ref [42] with permission.

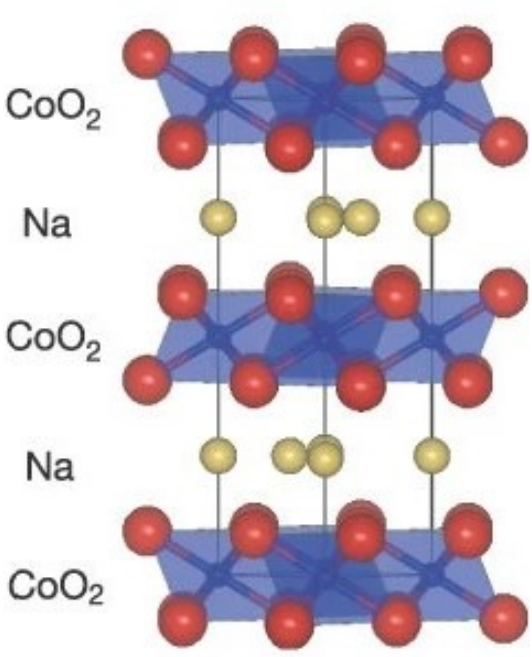


Figure 2.7: $NaCoO_2$ structure, reproduced from ref [43] with permission.

a multisheet cofiring technique [46]. For sodium cobalate, the number of layers of monovalent ion greatly modify the final results, the maximum ZT is only 0.05 for a ratio of $\frac{Na}{Co} = 0.5$ [47], but 0.78 for $\frac{Na}{Co} = 0.85$ [48]. In contrast to calcium cobalate, even if the doping improved some of the thermoelectric properties, the benefits did not overcome the diminishing of the other parameters and so did not increases the figure of merit [44]. Like calcium cobalate the fabrication of a composite with silver as a second phase increase the maximum ZT; a ZT higher than 0.9 at 950K was measured with a composite containing 10 wt% of Ag [49].

Oxyselenide BiCuSeO The oxyselenide BiCuSeO system is a p-type oxide thermoelectric material that overpassed a figure of merit of 1, and has the advantage of being composed of non-toxic and abundant elements. Studies surrounding this system have their origins in the discovery of the superconductivity in the F-doped LaFeAsO system [50]. This discovery drove a lot of attention in similar systems like BiCuSeO and even if no superconductivity was observed, a large Seebeck

coefficient has been reported for these ironoxypnictides [51, 52], generating a keen interest for the oxyselenide oxides. The crystal structure of this system is a ZrCuSiAs type structure that can be described as a 2D layered structure of an alternation of fluorite like Bi_2O_2 and Cu_2Se_2 along the C-axis (Figure 2.8) [53]. The microstructure, like the crystal structure forms lamellar grain that followed the directional lattices (Figure 2.9). The microstructure therefore produce anisotropic transport properties [54]. The level of anisotropy is probably the source of the differences in thermoelectric data, being dependent on the method of densification.

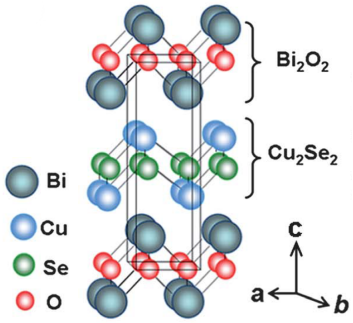


Figure 2.8: Crystal structure of the BiCuSeO from ref [55], reproduced with permission.

The power factor of this system is relatively low, $Bi_{0.925}Ca_{0.075}CuSeO$ achieved 4.74 $mW.cm^{-1}.K^{-2}$ at 923K , therefore the good performances of the material is due to the very low thermal conductivity for an oxide (0.9 $W.m^{-1}.K^{-1}$ at 300K, 0.45 $W.m^{-1}.K^{-1}$ at 900 K) such that a figure of merit of 0.5 at 923K was observed [54]. To further enhance the performances of the oxide, several strategies were explored, and because of the low power factor and the already low thermal conductivity, a lot of research was focused on optimising the carrier concentration, a simple ionic model can be used to develop and understand doping strategies [57]. A route to increase the performance is by the introduction of copper vacancies to create more holes according to the following mechanism [58] :

$$2\,BiCu_{1-x}SeO=(Bi_2O_2)^{2+} + (Cu_{2(1-x)}Se_2)^{2(1+x)-} + 2\,xV_{Cu}^{-} + 2\,xh^{+} \quad (1)$$

In this model, the holes are generated in the $(Cu_2Se_2)^{2-}$ conductive layer and a ZT of 0.81 at 923K

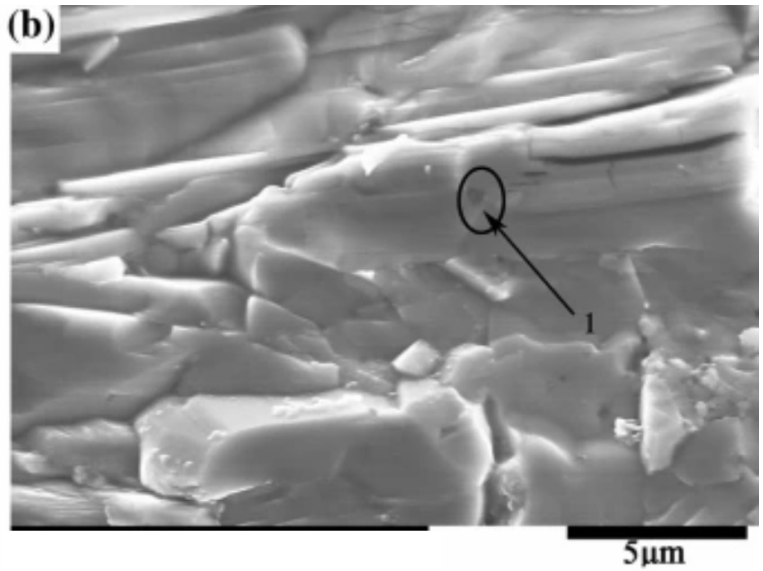


Figure 2.9: Microstructure of BiCuSeO from ref [56], reproduced with permission.

was achieved for $BiCu_{0.975}SeO$ [58].

Another approach is by doping with acceptor elements, but because the valence configuration of Cu is +1, there is no possible doping strategies to increase the holes concentration by substituting Cu, additionaly only few elements with an negative valence are candidates to substitute Se or O. Therefore the easiest strategy, and the mostly commonly applied, is the substitution of Bi by an element with a positive lower valence with the mechanism below :

$$2\,(Bi_{1-x}M_xCuSeO) = (Bi_{2(1-x)}M_{2x}O_2)^{2(1-x)+} + (Cu_2Se_2)^{2-} + 2\,xh^+ \tag{2}$$

Where M is an element with a valence of +2. In this case, the holes are generated in the Bi_2O_2 layer and then transferred to the top of the valence band, in the Cu-Se states [57, 59]. Using this approach, the maximum figure of merit was increased to 0.67, 0.9, 0.76, and 1.1 for a doping with Mg, Ca, Sr, and Ba element respectively [54, 59–61]. Among the chosen elements with a valence of +2, Pb is of particuliar interest because nanodots were observed. Even if the chemical compositions of these nanodots are not known [62], these nanodots are sources of phonon scattering, plus it was

observed that the density of states of the Pb doped BiCuSeO was changed. These effects led to a maximum ZT of 1.14 at 823K for $Bi_{0.94}Pb_{0.06}CuSeO$.

As a results of the anisotropy of the crystal structure, the orientation of the grain of a polycrystalline sample has a significant effect on the final performance of the bulk materials. The orientation of the grains may be influenced by extrinsic forces. In order to take advantage of the phenomena, methods were developed to control the grains coherence orientation. For example, Sui et al used several hot forging steps after a two steps solid states reaction route with $Bi_{0.875}Ba_{0.125}CuSeO$. In the perpendicular direction of the deformation, the figure of merit was improved from 1.1 to 1.4 at 923K [63]. This hot forging approach is shown in Figure 2.10.

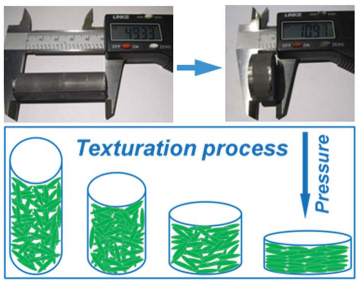


Figure 2.10: Pictures and draw of the texturation process by hot forging, from ref [64], reproduced with permission.

ZnO ZnO is also a well-studied material largely due to its band gap in the UV region around 3.3 eV [65], proving particularly useful for opto-electric and sensor devices, ZnO and $SrTiO_3$ are the two state of art n-type thermoelectric materials. This interest in sensor developments is what helped direct research towards its potential thermoelectric properties. ZnO also has the advantage of having good chemical and thermal stability in air, up to 750°C at least [66]. It is also relatively cheap, non-toxic, and the methods to produce it as a stable thin film are well established. N-type ZnO semiconductors have been easily produced by Al doping [67–71] but the best ZT obtained were below 0.2, with 0.17 at 600K for $Zn_{0.97}Al_{0.03}O$ [71]. Ni doping reduced the grain size and increased both the electrical conductivity and the Seebeck coefficient, reaching a PF of $1.76 \cdot 10^{-3} W.m^{-1}.K^{-2}$ at 800°C compared to $0.62 \cdot 10^{-4} W.m^{-1}.K^{-2}$ for undoped ZnO [72]. Sb doping also decreased the

grain size, not full dissolution and the formation of a secondary phase was also observed, the PF was increased but was lower than Ni doping with $3.88 \cdot 10^{-4} W.m^{-1}.K^{-2}$ at 1073K [73]. Performances by using Sn as a co-dopant with Sb were superior with $1.15 \cdot 10^{-3} W.m^{-1}.K^{-2}$ at 800°C [74]. Ti / Al two dopants approach also increased the PF compared to Al only, $3.8 \cdot 10^{-4} W.m^{-1}.K^{-2}$ compared to around $2.05 \cdot 10^{-4} W.m^{-1}.K^{-2}$ at 800°C [75].

The best couple of co-dopants was Al and Ga, Ohtaki et al obtained a ZT of 0.47 at 1000 K and 0.65 at 1247 K with the composition $Zn_{0.96}Al_{0.02}Ga_{0.02}O$ in 2009 [76]. This was the highest ZT reported for an n-type oxide thermoelectric, only equaled in 2017 [77], and surpassed in 2021 by $SrTiO_3$ based oxide [78], discussed in the next subsection. Ou et al induced bandgap narrowing in several oxide semiconductors by arc melting processing, with ZnO among the studied oxides [79]. They suggest that the arc melting process can immobilize metastable phase and highly concentrated defects, they observed an increase of defects by high-resolution TEM without change of the crystal structure and a reduction of the bandgap from 3.32 eV to 2.5 eV. They also observed similar behaviour for Cu_2O, Y_2O_3, ZrO_2, Nb_2O_5, In_2O_3, SnO_2, CeO_2, and WO_3.

2.2 Properties and defect chemistry of ABX_3 alkaline earth titanates

Donor doped $SrTiO_3$ Donor doped $SrTiO_3$ is an n-type oxide thermoelectric with a cubic perovskite structure (Figure 2.11) at room temperature that has accumulated a lot of interest. All of the elements are abundantly present and non-toxic, plus it possesses a high melting point around 2000°C, which allows it to be used at very high temperatures. Perovskite is a crystal structures with the chemical formula ABX_3, where A is the biggest cation, B the smallest cation and X the anion such as $CaTiO_3$, $SrZrO_3$, or $BiScO_3$. To predict which crystal system would be adopted, the Godlshmidt's tolerance factor has been introduced [80] :

$$t = \frac{R_A + R_X}{(R_B + R_X) \cdot \sqrt{2}} \tag{8}$$

where R_A, R_B and R_X are the ionic radius of the A cation, the B cation and the anion X respectively. It has been empirically determined which crystal structure is favoured according to the value of t

in Table 2.1 [81].

Table 2.1: Theoretical crystal structures from the Godlshmidt's tolerance factor.

>1	Hexagonal or Tetragonal
0.9-1	Cubic
0.71-0.9	Orthorhombic/Rhombohedral
<0.71	Different structures

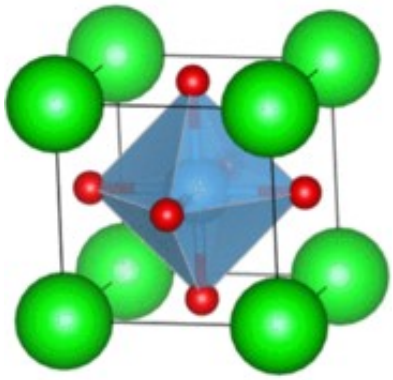


Figure 2.11: Example of a perovskite structure : $SrTiO_3$ at high temperature, Sr in green, Ti in blue, and O in red. From ref [82], reproduced with permission.

Like many metal oxides the oxygen content is a key factor, especially for the electrical conductivity and the effective mass. The conduction band of the $SrTiO_3$ came from the degenerated Ti $3d - t_{2g}$ orbital and the large Seebeck coefficient is attribuated to this degenerancy [83, 84]. The electronic structure is similar to the other alkaline earth titanates and explains their similar transport properties [85, 86]. When the proportion of oxygen vacancies is increased an enhancement of the electrical conductivity is observed. Studies attribute these enhancements to the increase of the number of free electrons and the modifications of the density of state of the materials. [87, 88]. An ionic model is described below:

$$O_O^{\times} \rightleftharpoons 2\,e' + \frac{1}{2}\,O_2 + V_O^{\bullet\bullet} \tag{3}$$

$$2\,\mathrm{Ti}_{\mathrm{Ti}}^{\times} + 2\,\mathrm{e}' \rightleftharpoons 2\,\mathrm{Ti}_{\mathrm{Ti}}' \tag{4}$$

The creation of an oxygen vacancy is accompanied by the reduction of two Ti cations and two electrons fill the conductive band. This mechanism has been highlighted several times by XPS and X-ray absorption fine structure, where the ratio Ti^{3+} /Ti^{4+} is up to seven times higher for samples sintered or annealed in inert or reducing atmosphere compared to the air [88, 89]. To take advantage of this mechanism, the sintering or an extra annealing step in inert or in reducing atmosphere is often used to produce doped $SrTiO_3$ for thermoelectric applications. In order to decrease the oxygen partial pressure, carbon burial sintering can be used (Figure 2.12) in which the pressed pellets are covered by graphite. Carbon burial sintering in argon flow can produce doped $SrTiO_3$ with over a tenfold increase of the conductivity compared to when produced when sintered in argon flow alone [88]. If undoped, the materials remains an insulator and can be easily tuned into a n-type semiconductor or metal by substituting a cation. When doping the A-site, the chosen dopant is generally a rare earth that act as an electron donor. The use of rare earths is consistent with the classical n doping strategy to increase the number of carrier by substituting Sr^{2+} by R^{3+} as described below :

$$\mathrm{La_2O_3} + 2\,\mathrm{TiO_2} \longrightarrow 2\,\mathrm{La}_{\mathrm{Sr}}^{\bullet} + 6\,\mathrm{O}_{\mathrm{O}}^{\times} + \frac{1}{2}\,\mathrm{O_2} + 2\,\mathrm{Ti}_{\mathrm{Ti}}^{\times} + 2\,\mathrm{e}' \tag{5}$$

Different rare earths and other dopants have been explored [90–93]. As expected, the choice of the rare earth plays a key role in the final properties and seems to be directed by the ionic size [94, 95]. Low thermal conductivity is achieved with small ions, like Gd, Dy, or Y. This is easily explained by the smaller the ion size, the more the difference with Sr, then this difference increases the lattice distortion that increases the phonon scattering. Similarly, a high power factor is achieved with larger rare earth like La or Nd. To combine these two effects Liu et al tried two elements doping in the A-site and achieved a figure of merit of 0.31 at 973K for $Sr_{0.8}La_{0.18}Yb_{0.02}TiO_3$; with single doping, La and Nd doping provided the highest figure of merits (around 0.25 at 1000K for a replacement of 20% of the Sr). Therefore the two elements doping for the A-site approach has

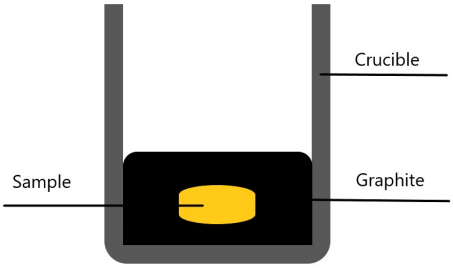


Figure 2.12: Schematic representing the carbon burial sintering, sample covered by graphite and placed in the crucible.

driven most of the studies for doped $SrTiO_3$ thermoelectrics.

The effect of an A-site deficiency has also been studied [89,96–99]. The evidence of the formation of the A-site vacancies have been confirmed by atomic resolution with aberration correction TEM using a high-angle annular dark field where A-site vacancies have been observed without ordering [89,100]. This mechanism is relatively simple when the sample is prepared in air. However, the chemistry produced in a reducing atmosphere is more complex due to the interaction between the oxygen vacancies and Ti^{3+}, facilitating the direct compensation of La^{3+} [100], and in a reducing atmosphere an exsolution of TiO_2 was observed at 1000K, this suggests that in a reducing atmosphere, a lower content of A-site vacancies are formed compared to when in air [101, 102].

Besides A-site doping, Ti substitutions have been widely studied too, especially with niobium doping that also acts as electron donor [103–109]. Nb doping achieved high figure of merit such as 0.38 at 1000K by Srivastava et al for $Sr_{0.8}La_{0.06}Nb_{0.2}Ti_{0.8}O_3$ with the addition of iron nitrate solution to the synthesized powder to produce metal inclusions in the final bulk material. Ohta et al compared La and Nb doping, they found that La achieved both higher power factor ($23 \cdot 10^{-4} W.m^{-1}.K^{-2}$ for La and $20 \cdot 10^{-4} W.m^{-1}.K^{-2}$ for Nb) and higher figure of merit (0.08 for La, 0.06 for Nb) at RT compared to Nb doping [109]. They focussed on the carrier concentration when investigating Nb doping, they observed that the carrier concentration to be proportional to the Nb concentration,

the highest ZT was 0.37 at 1000K for $SrTi_{0.8}Nb_{0.2}O_3$ [107].

Lu and et al obtained the highest performance for single doped material without making a composite material for the system $Sr_{1-1.5x}La_xTiO_3$ for x = 0.15, that correspond approximately to $Sr_{0.775}La_{0.15}Ti^{4+}_{0.86}Ti^{3+}_{0.14}O_{2.93}$, with a maximum figure of merit of 0.41 at 973 K by combining A-site vacancy and a reduction in $N_2(95\%)/H_2(5\%)$ atmosphere [100]. This improvement came from both a high electrical conductivity around 2400 $S.cm^{-1}$ at 473K and a relatively small thermal conductivity, around 5.85 $W.m^{-1}.K^{-1}$ at 473K. An even smaller thermal conductivity has been observed by Popuri et al with $Sr_{1-x}La_{0.67x}\oslash_{0.33x}TiO_3$ were $\oslash$ is the symbol for vacancies, in which a glass-like behaviour was observed at x = 0.8 that represent A-site vacancies of 27% [96]. This led to a decrease in 80 % of the thermal conductivity at 323K and 60% at 823K. Unfortunately, these A-site vacancies also decrease the power factor and the maximum figure of merit remained at 0.3 which is comparable to several other studies without A-site vacancies. It is worth mentioning that if the power factor would not have changed, the figure of merit would have reached 0.6 [96]. The highest figure of merit for doped $SrTiO_3$ without the addition of a foreign material has been achieved by Wang et al with Nb and La co-doping nano powder produced by hydrothermal synthesis followed by cold isostatic pressing and carbon burial sintering (Figure 2.12), in this approach the pressed oxide powder is covered by graphite in the crucible before sintering to increase the reduction during the sintering. They achieved the best performance with $La_{0.1}Sr_{0.9}Nb_{0.1}Ti_{0.9}O_3$ with a ZT = 0.65 at 1100K, the high performance is attributed to the grain structure. The main phase having a grain size between 1-5 μm and a second phase consisting of TiO_2 grains containing $SrTiO_3$ nano inclusion forming a TiO_2−$SrTiO_3$ heterostructure. It is postulated the second phase may have a contribution to the phonon scattering and low energy electron filtering that promote relatively low thermal conductivity and high absolute Seebeck coefficient without lowering the electrical conductivity too much. In addition, the relatively high doping content induced a high carrier concentration and lattice distortion that promoted the thermoelectric performance.

The highest figure of merit for a $SrTiO_3$ based material was reported by Acharya et al in 2021 [78] with a composite of $SrTi_{0.85}Nb_{0.15}O_3$ + 0.5 weight% of graphite powder. The addition of graphite significantly increased the electrical conductivity by increasing in the electron mobility. The carrier

concentration remain unchanged and the Seebeck coefficient was almost unaffected resulting in a significant increase in the power factor. Whereas the electronic contribution of the thermal conductivity increased with the graphite content, the graphite inclusion significantly decreased the phonon mean free path and the lattice contribution of the thermal conductivity, resulting in a figure of merit 15 times higher than $SrTi_{0.85}Nb_{0.15}O_3$ without a graphite addition, they observed a ZT of 1.42 at 1050K, this value is a huge gap with all of the other ZT reported in the literature and yet no other group reported similar results. In 2022, similar work was done with $La_{0.07}Sr_{0.93}Ti_{0.93}Nb_{0.07}O_3$, the highest figure of merit was observed with 1 wt% of graphite with a ZT of 0.68 at 980K [110]. Besides the effect of the chemical composition or the gas atmosphere, work has been done to find a superior method to the conventional solid-state and sol-gel method to produce polycrystalline bulk materials. Due to the SPS capability to have a low, or even no grain growth during sintering, SPS post-treatment is a widely utilised method to produce high-quality thermoelectrics. Much research has been done with solution combustion processing to produce nanocrystalline powder and a SPS step to produce highly dense bulk thermoelectric oxide materials [111–118]. With this approach, Kikuchi et al and Park et al obtained a maximum ZT of 0.37 with $La_{0.08}Sr_{0.92}TiO_3$ at 1045K, and $La_{0.09}Sr_{0.91}TiO_3$ at 973K respectively [119, 120].

Numerous applications such as on-chip cooling require the thermoelectric materials to not be a bulk but a thin film [121]. Efforts have been made to produce thermoelectric doped $SrTiO_3$ thin films, and observed the effect of the doping on the oxygen vacancies [107, 111, 122–125]. Kozuka et al observed an enhancement in the electron mobility with $SrTiO_3$ thin film when the doped layer thickness is decreased where an enhancement of the electron mobility is observed [126]. A large Seebeck coefficient was observed by Ohta et al in a two-dimensional electron gas in $SrTiO_3$ through producing an electron confinement by making a $SrTiO_3/TiO_2$ heterointerface via thin film deposition. The maximum Seebeck coefficient reached a value of 1050 $\mu V.K^{-1}$ and the best calculated figure of merit was 2.4 at 300K, but this value was only at the heterointerface and the figure of merit of all the material, including the barrier layer, was 0.24 at 300K.

Table 2.2: Summary of the thermoelectric properties of some doped $SrTiO_3$ from the literature. Data partially taken from ref [127], data taken graphically from the publications if not written in the text by the authors, when not included in the publications the power factor $\sigma S^2 T$ where calculated with the values obtained graphically. *Text claims at 1000K but figures show at 1100K.

Composition	Mechanism	σ $(S.cm^{-1})$ at low T	σ $(S.cm^{-1})$ at max ZT	S $(\mu V.K^{-1})$ at max ZT	PF $(mW\ m^{-1}K^{-1})$ at max ZT	K $(W.m^{-1}.K^{-1})$ at max ZT	ZT max	refs
$Sr_{0.775}La_{0.15}TiO_3$	Defective perovskite lattices containing conditions of A and O site vacancies	2335 (200°C)	404	-168	1.140	2.65	0.41 at 973 K	[100]
$La_{0.08}Sr_{0.92}TiO_3$	SPS at 1573 K for different holding times. Sample sintered for 5 min shows highest zT	3025 (RT)	166	-238	0.9403	3.03	0.37 at 1045 K	[119]
$La_{0.09}Sr_{0.91}TiO_3$	Nanostructured bulk prepared from the nanoparticles of La-doped $SrTiO_3$ by SPS	371 (50°)	281	-204	1.1694	3.02	0.37 at 973 K	[120]
$La_{0.1}Sr_{0.9}TiO_3$	With 20 wt % nanosized Ag	105 (65°C)	101	-241	0.5866	1.67	0.30 at 883 K	[128]
La-doped $SrTiO_3$	With a Brij-S10 surfactant molar ratio of 0.1 in the $SrTiO_3$ film with mesoporous structure	3.36 (50°C)	2.72	+947	$5.2008.10^{-4}$	4.66	0.03 at 473 K	[129]
$SrTi_{0.8}Nb_{0.2}O_3$	Mesoporous $SrTiO_3$ films with Brij-S10 surfactant	N/A	24	-156	1.10^{-4}	6.10^{-3}	0.04 at 300 K	[130]
$La_{0.08}Sr_{0.92}TiO_3$	Carbon-burial sintering for bulk sample preparation	142 (45°C)	85	-272	0.6299	3.37	0.2 at 1100 K*	[131]
YSZ-$SrNb_{0.15}Ti_{0.85}O_3$	Nanoinclusion of yttria-stabilized zirconia (YSZ)	1898 (RT)	350	-135	0.6267	2.67	0.21 at 900 K	[132]
$SrNb_{0.1}Ti_{0.9}O_3$	Sr site vacancies, prepared by high-energy ball milling, followed by carbon burial sintering	1179 (50°C)	169	-192	0.6	3.1	0.21 at 1100 K	[133]
$SrNb_{0.15}Ti_{0.85}O_3 + TiO_2$	Nanosized titania on the strontium titanate grains using liquid-phase deposition approach	1575 (RT)	493	-160	1.2856	3.5	0.33 at 900 K	[134]
$La_{0.1}Sr_{0.9}Nb_{0.1}Ti_{0.9}O_3$	Nanoscale modulation doping and microstructure controlling approach	413 (RT)	200	-286	1.6473	2.78	0.65 at 1100 K	[77]

Composition	Mechanism	σ $(S.cm^{-1})$ at RT	σ $(S.cm^{-1})$ at max ZT	S $(\mu V.K^{-1})$ at max ZT	PF $(mW\ m^{-1}K^{-2})$ at max ZT	K $(W.m^{-1}\ .K^{-1})$ at max ZT	ZT Max	ref
$Sr_{0.8}La_{0.18}Y_{0.02}TiO_3$	Doped with large ions of La and simultaneously, slightly codoped with small ions of Y	790 (50°C)	290	-174	0.8778	2.96	0.31 at 1023 K	[95]
$Sr_{0.8}La_{0.06}Nb_{0.2}Ti_{0.8}O_3$	Inclusion of Cu	1000 (RT)	584	-144	1.21	3.19	0.36 at 900 K	[135]
$Sr_{0.8}La_{0.06}Nb_{0.2}Ti_{0.8}O_3$	Inclusion of Fe	763 (RT)	391	-167	1.09	2.98	0.38 at 1000 K	[135]
$La_{0.1}Dy_{0.1}Sr_{0.75}TiO_3$	Sr-deficient $SrTiO_3$ ceramics	233 (50°C)	87.6	-291	0.74	1.92	0.29 at 723 K	[99]
$La_{0.1}Dy_{0.1}Sr_{0.75}TiO_3$	Sr and O vacancies in $SrTiO_3$ ceramics	283 (100°C)	130	-239	0.8022	3.01	0.19 at 723 K	[136]
$SrTiO_3 + La_{0.1}Sr_{0.9}Nb_{0.2}Ti_{0.8}O_3$	Composite of pure and doped $SrTiO_3$ with a molar ratio of 1:1	309 (50°C)	150	-246	0.878	2.57	0.35 at 1000 K	[137]
$La_{0.05}Sr_{0.95}Nb_{0.05}Ti_{0.95}O_3$	Synthesized under various reducing atmospheres	205 (RT)	185	-113	2.37	4.98	0.22 at 473 K	[88]
$La_{0.05}Dy_{0.05}Sr_{0.9}Ti_{0.95}Nb_{0.05}O_3$	Sythesized by mechanical alloying and carbon burial sintering	2088 (RT)	274	-166	0.7555	2.97	0.28 at 1100 K	[138]
$SrTi_{0.85}Nb_{0.15}O_3$	Formation of a nanocomposite by graphite powder addition	1100 (RT)	1210	-186	5.4	3.11	1.42 at 1050 K	[78]

Donor doped $BaTiO_3$ $BaTiO_3$ is a similar system to $SrTiO_3$, and is a well-studied material. Most studies are focused on dielectric [139] and ferroelectric properties [140,141] as there are many possible functional applications, for example piezoelectric [142] and capacitors [143]. However, unlike $SrTiO_3$, very few papers were published in the field of thermoelectric for doped $BaTiO_3$. Like $SrTiO_3$, $BaTiO_3$ has the advantage to be constituted from non-harmful, relatively cheap and abundant elements.

The mechanism responsible for the change of the conductive properties (from isolating to semi conductor) has been controversial. Several studies proposed that equilibrium mechanism for donor doped $BaTiO_3$ is the formation of Ti vacancies and so requiring a Ti-rich phase [144] according the following mechanism :

$$5\,BaO + 2\,Nb_2O_5 \longrightarrow 5\,Ba_{Ba} + 4\,Nb^{\bullet}_{Ti} + V^{''''}_{Ti} + 15\,O^{\times}_{O} \tag{6}$$

However, Morrison et al showed experimentally that the mechanism responsible for the switching from insulating to semiconductor, when the sample is sintered in a low PO_2 atmosphere, originates from a change in the oxygen content of the materials [145, 146]. In this case, the mechanism is the same than described in equations 3, 4, and 5 (page 20) for $SrTiO_3$. Donor doping is then also possible :

$$La_2O_3 + 2\,TiO_2 \longrightarrow 2\,La^{\bullet}_{Ba} + 6\,O^{\times}_{O} + \frac{1}{2}\,O_2 + 2\,Ti^{\times}_{Ti} + 2\,e' \tag{7}$$

High absolute Seebeck coefficients, from -300 $\mu V.K^{-1}$ to -650 $\mu V.K^{-1}$, of reduced $BaTiO_3$ has been reported for a long time, but with a very low or insulating electrical conductivity, as example Lee et al obtained with a quenched $BaTiO_3$ -650 $\mu V.K^{-1}$ and 7 $S.cm^{-1}$ at room temperature [147–149]. Khan et al studied the thermoelectric properties of up to 5% Nb doped and reduced $BaTiO_3$ [150]. They obtained an insulating to moderate resistivity value of 0.18 Ω at 400K but the absolute Seebeck coefficient was very high from -50 $\mu V.K^{-1}$ to -650 $\mu V.K^{-1}$ at room temperature. No clear trend of the influence of the doping content on the electrical conductivity and the Seebeck coefficient

was present.

Xiao et al studied the thermoelectric properties of the $Ba_{1-x}Eu_xTiO_3$ solid solution from x=0.2 to x=0.9 synthesized by Pechini process followed by sintering in 5% H_2/95%Ar [151]. All of the compositions were single-phase perovskite, and the conductivity of the samples was increased compared to $BaTiO_3$ but they were semiconductors, unconducive at RT and below 15 $S.cm^{-1}$ at 600K. The carrier concentration and mobility were proportional to the Eu content, Eu had 2+ oxidation state and the increase of conductivity was attributed to the Eu 4f electrons, thus Eu doping does not increase the number of charge carrier of the Ti-3d conduction band. This mechanism could not be applied wit La, because even if possible to synthesize [152], La does not have a very stable 2+ oxidation state [153]. All samples were found to be poorly conducting at room temperature and inferior to 100 $S.cm^{-1}$ at high temperatures but the electrical conductivity increased with increasing Eu content. The opposite trend was observed for the absolute Seebeck coefficient and all of the samples exhibited high absolute Seebeck coefficient from -300 $\mu V.K^{-1}$ for x=0.9 to -375 $\mu V.K^{-1}$ for x=0.2. Likewise for the electrical conductivity the power factor increased with the Eu content from 0.132 $mW.m.K^{-2}$ to 0.55 $mW.m.K^{-2}$ at 1125K. All samples showed relatively low thermal conductivity and an increase with the Eu content from 2.1 to 2.69 $W.m^{-1}.K^{-1}$ at 1123K. The figure of merit also increased with the Eu content from 0.1 to 0.24 at 1123K.

Rubi et al studied from 2K to 400K co-doped A and B sites system $Ba_{0.7}Eu_{0.3}Ti_{1-x}Nb_xO_3$ from x=0 to x=0.1 sintered in 5% H_2/95%Ar. Several compositions were conductive at room temperature with a maximum of 320 $S.cm^{-1}$ for x=0.1 at 400K with varying x [154]. The absolute Seebeck coefficient decreased but remained relatively high between 613 $\mu V.K^{-1}$ to 63 $\mu V.K^{-1}$ for $0.001 \leq x \leq 0.10$, giving a power factor higher than 1 $\mu W.cm^{-1}.K^{-2}$ for x=0.01, x=0.03, x=0.05, and x= 0.1. All samples exhibited low thermal conductivity at 400K, all within the range 0.7-1 $W.m^{-1}.K^{-1}$. The combination of the high power factor and low thermal conductivity results in a figure of merit of 0.12 at 400K for x=0.01. Unfortunately, there is an absence of data at temperatures higher than 400K.

The use of an arc melter in the production of ceramic is rarely reported in the literature. As mentioned previously in the ZnO part (page 19), Ou et al studied the Bandgap narrowing of sev-

eral oxide semiconductors by arc melting [79]. Four reports (by Johnston et al [155], Sunstrom et al [156], Fritsh et al [157], and Eylem et al [158]) explored doped $BaTiO_3$ produced with an arc melter in Ar atmosphere by using different raw materials for the synthesis, the following is a summary of the differences and main results of these reports. It is not clear if the differences in results were due to the different intrinsic properties of the raw materials or if they were due to the differences in the quality of the raw materials. For example, when $LaTiO_3$ is used as a raw material, if during $LaTiO_3$ synthesis a batch becomes contaminated or slightly oxidized, the final properties of doped $BaTiO_3$ may differ. The use of Ti metal granules gives a consistent raw material quality but it also increases the risk of off-stoichiometry as it is difficult to grind it homogeneously with the rest of the oxide powders.

Johnston et al made the La doped $BaTiO_3$ by melting La_2O_3, $BaTiO_3$, and Ti_2O_3 [155]. Eylem et al studied $R_xBa_{1-x}TiO_3$ where R is a rare-earth La, Nd, Gd, Er, and Y by mixing $BaTiO_3$, the rare earth oxides, Ti metal, and TiO_2 [158]. Sunstrom et al as well as Fritsh et al used $BaTiO_3$ and $LaTiO_3$ [156, 157]. The authors did not agree about the space group at room temperature of $La_xBa_{1-x}TiO_3$. Eylem et al are in qualitative agreement with the previous work of Johnston et al since they identified undoped $BaTiO_3$ as tetragonal P4mm and the main phase of La-doped (the lowest La content was $La_{0.15}Ba_{0.85}TiO_3$) to be cubic Pm3m until $La_{0.8}Ba_{0.2}TiO_3$, from $La_{0.8}Ba_{0.2}TiO_3$ they described the structure as orthorhombic Pbnm. For the region $0.6 \leq x \leq 0.8$, Eylem et al described it as biphasic as they observed the presence of a cubic or orthorhombic secondary phase. They used TEM for this as the XRD-data was not sufficiently sensitive to illustrate the presence of these biphasic phases. Additionally, for La, they observed a BaO impurity in the range $0.5 \leq x \leq 0.8$ that was not reported by Johnston et al. Eylem et al also prepared samples with a Ba deficiency that was successful in not forming BaO impurities. They did not observe an Ibmm structure for any composition and described $LaTiO_3$ as orthorhombic Pbnm. They observed that the range of the solid solution decreased with the size of the rare-earth, Nd, and La formed a solid solution from zero to the full substitution, whereas for Er, a solid solution is formed only until x=0.3. Sunstrom et al studied the system from $0.5 \leq x \leq 1$. They agreed that an orthorhombic Pbnm phase is formed from $LaTiO_3$ to $La_{0.8}Ba_{0.2}TiO_3$ but proposed Ibmm (also named Imma) for

the rest of the composition to explain the broadness of the peaks. They did not observe the presence of biphasic compounds but did not characterise the samples by TEM or neutron diffraction and they also observed La_2O_3 phases by the use of an EPMA (electron microprobe analyzer) and EDX (energy-dispersive X-ray spectroscopy). The Ibmm space group is orthorhombic with symmetry between the orthorhombic Pbnm and the cubic Pm3m. They also made the same conclusion when comparing $La_xSr_{1-x}TiO_3$ prepared by arc melting and analysed with neutron diffraction [159].
Johnston et al focused their work on the structural properties and the absolute Seebeck coefficient, the absolute value of the Seebeck coefficient decreased with the La content, all of their samples had a conductivity between 1 and 100 $S.cm^{-1}$ at room temperature. Sunstrom et al focused their measurements in the cryogenic temperatures range about the PTCR effect (positive temperature coefficient of resistance) and magnetic properties. They provided little data about the electrical conductivity and no data about the Seebeck coefficient. Eylem et al gave informations about the magnetic and the electrical properties at room temperature shown in Table 2.3, the samples with less than 40 % of La even if not nonconductive remained under 100 $S.cm^{-1}$ at room temperature and they did not measure the Seebeck coefficient. Fritsh et al found the samples $La_{0.1}Ba_{0.9}TiO_3$ and $La_{0.2}Ba_{0.8}TiO_3$ to be isolating with $La_{0.1}Ba_{0.9}TiO_3$ to have a resistivity about a quarter of undoped arc melted $BaTiO_3$ and the transition from insulator to metal to occur around $La_{0.35}Ba_{0.65}TiO_3$. The lack of quantitative data about the electrical properties may be because of the use of the arc melter. An arc melter applies in a gas-controlled chamber a high difference of electric potential between the cathode and the anode crucible plate to create an electric arc that melts the sample (Figure 2.13). The Cu plate is water cooled, it results with a high difference of temperature between the top and the bottom of the sample during the cooling, that may results in fractures. Making crack free $BaTiO_3$ samples with arc melter may be difficult if not impossible. This issue could be addressed by sintering the powder from the arc melted samples in order to produce dense crack-free samples.

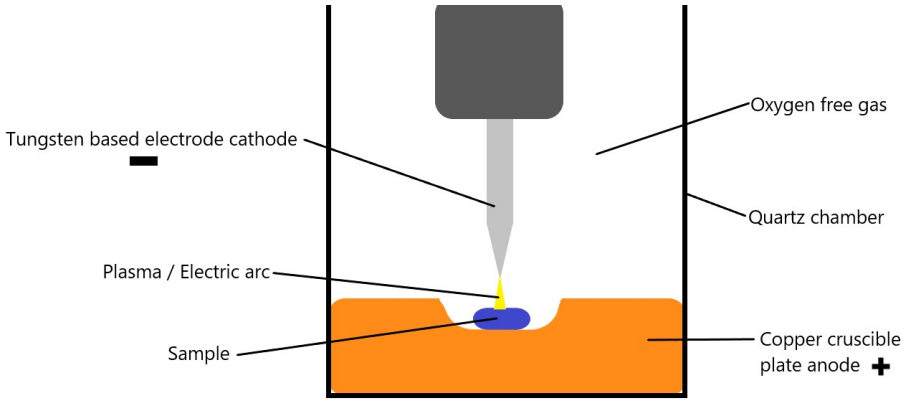


Figure 2.13: Schematic of an arc melter, the sample is melted by the electric arc formed between the chilled copper crucible and the tungsten cathode in a gas-controlled chamber.

It should be mentioned that relatively highly conductive $La_{0.1}Ba_{0.9}TiO_3$ has been made by Muta et al with a conductivity of 200 $S.cm^{-1}$ at 50°C, made by furnace sintering [160], discussed in more details from page 34. They used Ti metal as precursor, then as the three papers using an arc melter, the total O content in the precursors was smaller compared to using only TiO_2.

To sum up, the electronic compensation is responsible for the increase of the electrical conductivity of donor doped $BaTiO_3$ in reducing condition. In five works, highly La-doped were successfully synthesised, for all of them the oxygen concentration of the precursors was lowered (compared to TiO_2) by using Ti species with oxidation stats inferior to 4+. For the four publications using arc melting, the discrepancies in the structural results suggest that by optimising the parameters of the synthesis, different electrical properties could be achieved. Also, most of the thermoelectric properties are lacking and no thermal properties were reported, the Seebeck coefficient was only reported by Johnston et al and only at one temperature (the temperature of measurement is not mentioned in the paper, probably RT) and the electrical conductivity was not measured [155]. The absolute values of the resistivity were not communicated and measured only below RT by Sunstrom et al (only the resistivity normalised by the resistivity at 300K $\frac{\rho}{\rho_{300K}}$ from 15K to 300K was given) [156]. Eylem et al only communicated approximative values of the electrical conductivity

at RT, reproduced in Table 2.3 [158]. Muta et al published all the thermoelectric values, but only for the composition $La_{0.1}Ba_{0.9}TiO_3$ for the doped $BaTiO_3$ system [160].

Table 2.3: Table of the approximative conductivity of doped $BaTiO_3$ reproduced with permission from ref [158].

Sample	Approx resistivity at 298 K, ($\Omega.cm^{-1}$)	Approx conductivity at 298K ($S.cm^{-1}$)
$La_{0.2}Ba_{0.8}TiO_3$	0.4	2.5
$La_{0.33}Ba_{0.67}TiO_3$	0.05	20
$La_{0.4}Ba_{0.6}TiO_3$	0.008	125
$La_{0.5}Ba_{0.4}TiO_{2.9}$	0.003	333.33
$La_{0.6}Ba_{0.3}TiO_{2.9}$	0.001	1000
$la_{0.7}Ba_{0.2}TiO_{2.9}$	0.005	200
$La_{0.85}Ba_{0.15}TiO_3$	0.0002	5000
$Nd_{0.28}Ba_{0.72}TiO_3$	0.1	10
$Nd_{0.33}Ba_{0.67}TiO_3$	0.005	200
$Nd_{0.4}Ba_{0.6}TiO_3$	0.008	125
$Nd_{0.5}Ba_{0.5}TiO_3$	0.08	12.5
$Nd_{0.6}Ba_{0.4}TiO_3$	0.002	500
$Nd_{0.7}Ba_{0.3}TiO_3$	0.002	500
$Nd_{0.85}Ba_{0.15}TiO_3$	0.002	500
$Nd_{0.9}Ba_{0.1}TiO_3$	0.01	100
$Nd_{0.98}Ba_{0.02}TiO_3$	1.0	1
$NdTiO_3$	0.4	2.5
$Y_{0.2}Ba_{0.8}TiO_{2.85}$	0.05	20
$Y_{0.33}Ba_{0.67}TiO_{2.9}$	0.002	500
$Y_{0.4}Ba_{0.6}TiO_{2.9}$	0.005	200

Donor doped $CaTiO_3$ $CaTiO_3$ has a perovskite orthorhombic structure at room temperature, it transitions to tetragonal and then cubic when the temperature is increased [161]. While it has been widely studied for its photocatalytical [162–164] and photoluminescence properties [165–170], the total electrical conductivity of n-doped $CaTiO_3$ remains elusive as studies tend to focus more on the band gap of the material than the total electrical conductivity of the bulk material. It has been observed that Europium and Praseodymium doping increases the carrier concentration and reduces the Ti oxidation state from 4^+ to 3^+ [171, 172]. $CaTiO_3$ should share similar defect chemistry properties with $BaTiO_3$ [173]. Synthesized in air, La doped $CaTiO_3$ may form CaO layers to form a Ruddlesden-Popper phase while in a reducing atmosphere, the charge balance should be

compensated by oxygen vacancies [174,175]. Much of the informations concerning the thermolectric properties of $CaTiO_3$ are found in papers studying the $CaTiO_3 - SrTiO_3 - BaTiO_3$ system.
Li et al produced La-doped $CaTiO_3$ by a hydrothermal method followed by hot pressing in a graphite die under vacuum [176]. The synthesis produced dense ceramics with a grain size of 20 µm, as well as a Ti-rich and Ca poor nano precipitate secondary phase for samples with 20% or 25% of La. The interfaces between the main phase and the nano precipitates were approximately coherent, and could both scatter phonons and low energy carriers, thus decreasing the lattice thermal conductivity and increasing the absolute Seebeck coefficient. The high reducing condition produced oxygen vacancies. By measuring the carrier concentration by hall effect they estimated it to be about 2.37% for the undoped $CaTiO_3$, and this sample had an electrical conductivity of 50 $S.cm^{-1}$ at room temperature. The electrical conductivity increased with the La content until to $La_{0.2}Ca_{0.8}TiO_3$ with a value of 3383 $S.cm^{-1}$, sample $La_{0.25}Ca_{0.85}TiO_3$ in the opposite had an electrical conductivity between those of $La_{0.15}Ca_{0.85}TiO_3$ and $La_{0.2}Ca_{0.8}TiO_3$, in their opinion because the amount of secondary phase was too large. $La_{0.2}Ca_{0.8}TiO_3$ also shows the highest figure of merit with 0.4 at 1011K. No other work is found about the thermoelectric properties of La-doped $CaTiO_3$ and no work with x in $La_xCa_{1-x}TiO_3$ higher than 0.25 was published.
In the opposite of A-site deficient $La_xCa_{1-(3x/2)}TiO_3$, A-site deficient $La_{1-(2x/3)}Ca_xTiO_3$ sythesized in air has been studied [177, 178]. The electrical conductivity was not influenced by the A-site deficiency, a switch from n-type to p-type regim was observed depending on the oxygen partial pressure. $CaTiO_3$ was reported to have Pbnm space group, while the addition of La created three others crystal structures : transition to Imma was reported from $La_{0.267}Ca_{0.6}TiO_3$, I4/mcm from $La_{0.467}Ca_{0.3}TiO_3$, then Cmmm from $La_{0.553}Ca_{0.2}TiO_3$.

$CaTiO_3 - SrTiO_3 - BaTiO_3$ system $Sr_{1-x-y}Ba_xCa_yTiO_3$ forms a solid solution and the effect of the substitutions of Sr by Ca or Ba on the crystal structure is complex. Intermediate compositions of the system $Sr_{1-x}Ca_xTiO_3$ are controversial [179]. For example it was claimed that at RT the compositions between $Sr_{0.8}Ca_{0.2}TiO_3$ and $Sr_{0.65}Ca_{0.35}TiO_3$ were both a monoclinic distortion [180] or an orthorhombic structure [181,182]. Ca, Sr, and Ba can be substituted for one another to form

a solid solution. Muta et al studied the thermoelectric properties of $La_{0.1}Ba_{0.9-x}Sr_xTiO_3$ made by sintering under argon flow $BaTiO_3$, Ti metal, TiO_2, and La_2O_3 [160]. An increase in the Sr content decreased the absolute Seebeck coefficient and increased the electrical conductivity. They concluded that "the increase of the electrical conductivity is caused by the decrease of the Ti-Ti distance, which increases the overlap of Ti 3d orbital in the conduction band" and "Since the Sr substitution widens the conduction band, the effective mass of carriers is reduced and the Seebeck coefficient increases. Similar results are seen in other systems [183, 184]". The electrical conductivity of the sample with the composition $La_{0.1}Ba_{0.9}TiO_3$ was only 200 $S.cm^{-1}$ at room temperature whereas it was approximately 2500 $S.cm^{-1}$ for $La_{0.1}Sr_{0.9}TiO_3$ at room temperature. The power factor increased with the Sr concentration, however, the trend in the thermal conductivity is the opposite and the best figure of merit was slightly better for $La_{0.1}Ba_{0.3}Sr_{0.6}TiO_3$ compared to $Sr_{0.9}La_{0.1}TiO_3$. $La_{0.1}Ba_{0.9}TiO_3$ reached a maximum ZT of 0.125 at 873K.

Muta et al also produced a similar work for the Ca substitution [185], the substitution of Ca which generated lattice distortions and changes of structures that influenced the thermoelectric properties. Increasing the Ca decreased the electrical conductivity and increased the absolute Seebeck coefficient, e.g. at 330K $La_{0.1}Sr_{0.9}TiO_3$ had a conductivity of 2800 $S.cm^{-1}$ and a Seebeck coefficient of -83 $\mu V.K^{-1}$ whereas for $La_{0.1}Ca_{0.9}TiO_3$ the conductivity was 1100 $S.cm^{-1}$ and the Seebeck coefficient -109 $\mu V.K^{-1}$; the thermal conductivity decreased until $La_{0.6}Ca_{0.4}TiO_3$ and then remained similar whatever the concentration. The best power factor and figure of merit were obtained for $La_{0.1}Sr_{0.45}Ca_{0.45}TiO_3$ with an increase of 40% compared to $La_{0.1}Sr_{0.9}TiO_3$ for the power factor, whereas the figure of merit only slightly increased from around 0.2 to 0.22 at 873K. They postulated that the increase of the power factor is a result of the decrease of the dielectric constant because Wemple et al increased the carrier mobility of $SrTiO_3$ by hydrostatic pressure which also led to a decrease in the dielectric constant.

Somaily et al studied the structural and thermoelectric properties of the $Sr_{1-x-y}Ca_xNd_yTiO_3$ system and found a strong correlation between the electrical conductivity and the structural parameters, especially the average bond length $[A-O]$, $[B-O]$, and $[Ti-O]$, and the tilt angle, with $[A-O]$, $[B-O]$, and $[Ti-O]$ the bond length between the O anion and the cations A, B, or titanium. The

tilt angle is the difference between the angle of the bond Ti-O-Ti and 180°, 180° is the value for the perfect perovskite cubic structure. They defined a tolerance factor $\frac{[A-O]}{[B-O]}$, both the tilt angle and the tolerance factor are values of the structural deformation. The [Ti-O] bond length was largely influenced by the conversion of Ti^{4+} into larger Ti^{3+} in effect of the Nd doping. They observed that the lower the tilt angle, the lower the resistivity; the higher the tolerance factor, the higher the power factor. They measured the thermoelectric properties only up to 400K and found the highest ZT was 0.07 for $Nb_{0.08}Sr_{0.92}TiO_3$ but they predicted that at higher temperatures, after the transition to cubic structure, the composition $Ca_{0.16}Sr_{0.76}Nd_{0.08}TiO_3$ could have a ZT of 0.37 [179]. Yamamoto et al explored the $(Ba_xSr_yCa_z)_{0.8}Nb_{0.2}TiO_3$ phase diagram by thin film growing and concluded that the substitution of Sr by either Ca or Ba is detrimental for the power factor (according to the compositional mapping of the thermoelectric power factor they produced in their study) [186]. From Hall effect measurements, they observed in their study that the effective mass decreased linearly with Ca substitution and increased linearly with Ba substitution but the carrier mobility is much higher with the Sr-rich compositions which then led to a better power factor for the doped $SrTiO_3$. Zhang et al used a theoretical approach to study the $CaTiO_3-SrTiO_3-BaTiO_3$ system by using the Boltzmann transport equations and density functional theory calculations [187]. They compared the electrical conductivity, the power factor, and the electronic components of the thermal conductivity, all normalised by the relaxation time ($\frac{\sigma}{\tau}$, $\frac{S^2\sigma}{\tau}$, $\frac{K_e}{\tau}$) with different carrier concentrations. According to them making a "comparison of $\frac{\sigma}{\tau}$ of $CaTiO_3$, $SrTiO_3$ and $BaTiO_3$ is reasonable because they have similar structures and bonding properties and, then, τ have similar values for the three materials". Considering τ similar for the three oxides makes comparison much easier as τ can be removed from the equation to calculate σ by normalising it, however, the experimental values of τ measured by Yamamoto et al were different [186]. They measured 27.1 fs for $SrTi_{0.8}Nb_{0.2}O_3$, 1.5 fs for $CaTi_{0.8}Nb_{0.2}O_3$ and 0.47 fs $BaTi_{0.8}Nb_{0.2}O_3$. Their study suggests that the ratios $\frac{\sigma}{\tau}$ and $\frac{S^2\sigma}{\tau}$ are in the order $CaTiO_3 > SrTiO_3 > BaTiO_3$, the order is the opposite for that of the Seebeck coefficient and $\frac{K_e}{\tau}$. It should be noted that when the electronic thermal conductivity is compared to $\frac{\sigma}{\tau}$ and not the carrier concentration, the values are much more similar, their results may suggest that if we can achieve the same carrier concentration, then partial or full substitution

of Sr by Ba can increase the figure of merit. According to them, it is mainly the band narrowing caused by the changes of the lattice constant that modify the transport coefficients.
Based on the above studies, it could be concluded that for thermoelectric performance $SrTiO_3$ would be superior. However, the recent work of Li et al showed a ZT of a doped $CaTiO_3$ that is comparable to the best ZT obtained with $SrTiO_3$ for decades with many tried approaches. As mentioned above, Muta et al concluded that $La_{0.1}Sr_{0.9}TiO_3$ was more than ten times more conductive than $La_{0.1}Ba_{0.9}TiO_3$ because of the difference of Ti-Ti distance, leading to think that the structural properties of $BaTiO_3$ are responsible for this relatively low conductivity, however, they did not mention the difference of Ti oxidation stats between the two samples to be a possible explanation. The synthesis method they used is probably sufficient to reduce further the oxidation stats of $La_{0.1}Sr_{0.9}TiO_3$ but probably not $La_{0.1}Ba_{0.9}TiO_3$.

Summary At the present the best reported thermoelectric materials are metal based, the telluride and selenide are the two main families and the best ZT reported are higher than two [14]. For all of the materials, increasing the carrier concentration through doping was essential in order to achieve high enough electrical conductivity. SPS was often used as this special sintering technique is favorable to obtain microstructures that promote phonon scattering because the high heating and cooling rates are favorable to limit the particle size growth, while the applied pressure during the sintering allows high density. Oxide-based thermoelectrics are less performant but have the potential to be used at higher temperatures, thanks to their higher melting points, and to be more durable. P-type oxide materials are more mature than n-type oxide materials, especially the bismuth oxyselenides with ZT higher than one reported by several groups [64], in consequence, efforts of fundamental research and development should be carried out about n-type oxide materials in order to improve the performances of high temperature oxide thermoelectric generators.
Recently, the reported ZT of $SrTiO_3$ based material overpassed the highest ZT reported for ZnO based material [76, 78], it could be assumed that alkaline earth titanates are the most promising n-type oxide-based thermoelectric material. $SrTiO_3$ was the topic of numerous works to decrease its thermal conductivity or increase its power factor. The first main approche to increase the electrical

conductivity is by generating oxygen vacancies by using reducing conditions during the synthesis or post treatment, another well explored strategy is the n-type doping, many elements were tried in order to dope the material and La was the element that gave the best results when doping the A-site of $SrTiO_3$. The other alkaline earth titanates share a similar electronic structure with the $SrTiO_3$ and solid solutions mixing Ba, Ca, and Sr as the A-site of the perovskite structure were made [186]. However, the study of the thermoelectric properties of the other alkaline earth titanates did not receive the same interest by the scientific community. Researchers may have assumed that donor doped $BaTiO_3$ can not be a useful thermoelectric material as making it electrically conductive is challenging because inserting an element with 3+ valence in the Ba site is difficult if not impossible without ionic compensation, also works on the solid solution $CaTiO_3 - SrTiO_3 - BaTiO_3$ concluded to the superiority of $SrTiO_3$ for thermoelectric application. Another conclusion can be made after analysing the relevant publications, donor doped $BaTiO_3$ can be as electrically conductive as donor doped $SrTiO_3$, but the reduction of Ti^{4+} to Ti^{3+} is much more challenging than in the case of $SrTiO_3$. The issue can be addressed by using precursors with the Ti oxidation stats other than 4+ and using synthesis and post treatment methods that favour the electronic conpensation mechanism. As mixing elements of different atomic mass increased phonon scattering, the developement of new synthesis routes capable of making doped $BaTiO_3$ and $CaTiO_3$ with the same thermoelectric properties of doped $SrTiO_3$ could allow making doped $Ca_xSr_yBa_zTiO_3$ with even better performances than doped $SrTiO_3$. It is reasonable to say that with the current available publications, it can not be stated that $CaTiO_3$ based materials and $BaTiO_3$ materials are inferior to $SrTiO_3$ based materials, new approches to produce other alkaline earth titanate thermoelectric should be atempted. The current literature lack knowledge about conductive n-type doped $BaTiO_3$ and $CaTiO_3$ on several aspects sum up in the paragraph.

Data about the thermoelectric properties of donor doped $CaTiO_3$ are very limited, only one work focused on the thermoelectric properties of rare earth doped $CaTiO_3$ and in this work a secondary phase was reported. No publication reported the synthesis of doped $CaTiO_3$ with more than 25% of rare earth in the A-site, their is then no data available about the electric, thermal, and structural properties of highly rare earth doped doped $CaTiO_3$ and only one set of data for doping concen-

tration below 25%. Paper about rare eath doped $La_xCa_{1-(3x/2)}TiO_3$ with A-site vacancies are also nonexistent. The literature diverges about the crystallographic space group of $La_xBa_{1-x}TiO_3$, either cubic Pm3m or orthorhombic Ibmm for x between 0.15 and 0.8. The studies of the donor doped $BaTiO_3$ with electronic compensation with doping content over a few percent are very limited, the data are content in five works, in four an arc melter was used, in all of these works the electrical conductivity reported were much lower than the equivalent (in doping content) of the $SrTiO_3$. Most of the thermoelectric properties were not characterised, Muta et al did provide the full thermoelectric data for $La_{0.1}Ba_{0.9}TiO_3$ produced by furnace sintering but not for any other doped $BaTiO_3$ compositions, for the other four papers, the thermoelectric properties are very scarse. Then, the thermoelectric properties of highly conductive doped $BaTiO_3$ is almost fully vacant in the literature. Additionaly their is no reported values of conductivity over a few hundred of $S.cm^{-1}$ for La-doped $BaTiO_3$ when Ba is still the major element in the A-site (70% and over). For both La-doped $BaTiO_3$ and La-doped $CaTiO_3$, reducing the Ti oxidation state is an obligation to make the materials conductive by favoring the electronic conpensation. No paper has reported synthesis by arc melting and densification by SPS sintering, however, with their fast heating and cooling step, and capability to work in very low oxygen pressure, the arc melter and the SPS are appropriate for this work.

2.3 Aims and objectives

The aims of this PhD is to change the electrical properties of $BaTiO_3$ and $CaTiO_3$ to make them highly electrically conductive. While the doping mechanisms of the alkaline earth titanate have been studied extensively, published works about the series $La_xBa_{1-x}TiO_3$ and $La_xCa_{1-x}TiO_3$ with $0 \leq x \leq 1$ systems are still lacking. Additionally, studies of donor doping when the ionic compensation is not favoured are few, and no $BaTiO_3$ with conductivity in the magnitude of thousands of $S.cm^{-1}$ have been reported. The main approach of this work is the control the oxygen content in the final oxides by combining synthesis by arc melting and densification by spark plasma sintering. The structural, electrical, and thermal properties were then analysed.

For both $La_xBa_{1-x}TiO_3$ and $La_xCa_{1-x}TiO_3$:

- Dope the La in the A-site of the perovskite structure and collect evidences that the electronic compensation is favoured over ionic compensation :
  - Study the structural parameters by XRD. If the ionic compensation is favoured, the formation of a Ti rich secondary phase is expected. If the electronic compensation is favoured, it is expected that the modifications of the lattice constant will follow the Vegard's law.
  - Study the oxidation behaviour. If the electronic compensation is favoured, the concentration of Ti^{3+} should be proportional to the La doping; the difference of mass before and after oxidation would be proportional to the concentration of Ti^{3+} that changed to Ti^{4+}, it is then expected that the increase of mass would be proportional to the La doping. This behaviour is not compatible if the ionic compensation is favoured.
  - Study of the elemental composition. If the electronic compensation is favoured, the A/B ratio of the perovskite structure should be equal to one. If the ionic compensation is favoured, the A/B ratio would be inferior to one and decrease with the La doping.
- Study the influence of the La doping, successful donor doping would lead to an increase of the electrical conductivity by increasing the charge carrier concentration.
- Study the impact of the SPS parameters, the temperature of sintering, the heating and cooling rates, the applied pressure, and dweeling time could have an influence on the final density. The temperature of sintering could influence the oxygen vacancies concentration.
- Achieve a high electrical conductivity (superior to 1000 $S.cm^{-1}$) at room temperature for the samples with fewer than 30 % of La in the A-site.
- Measure the thermoelectric properties and achieve at least a power factor of 0.5 $mW.m^{-1}.K^{-2}$.

3 Methodology

3.1 Raw Materials

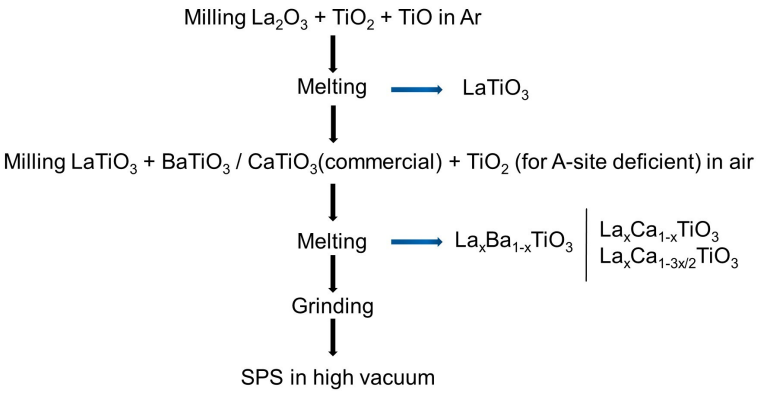


Figure 3.1: Synthesis flow diagram of the arc melting and SPS densification method used for the study of the $La_xBa_{1-x}TiO_3$, the $La_xCa_{1-x}TiO_3$, and the $La_xCa_{1-(3/2x)}TiO_3$ sytems.

Figure 3.1 is the flow diagram of the synthesis. Prior to its insertion in the glove box, the La_2O_3 (99.9%, Sigma-Aldrich) was dried at 1000°C in air for at least two hours. The TiO_2 (99.9% Sigma-Aldrich) was dried at 300°C in air for at least two hours. Once received from Sigma the TiO (99.9%, Sigma-Aldrich) was inserted in a glovebox. To produce $LaTiO_3$, the proper amount (according to the chemical equation 8 and Table 3.1) of La_2O_3, TiO, and TiO_2 was weighed in the glovebox.

$$0.5\,La_2O_3 + 0.5\,TiO_2 + 0.5\,TiO \longrightarrow LaTiO_3 \tag{8}$$

The oxides were mixed with an agate mortar in the glove box for 30 minutes, then filled in a pressing die of 13.5 mm of diameter inside the glovebox. The steps were done in a glovebox to avoid the lanthanum oxide absorbing the moisture in the air that would form hydroxides and would increase the O during the reaction. The die was taken out of the glove box and immediately pressed, such that the resultant pellets would be immediately placed into the arc melter chamber.

In early experiments, the $LaTiO_3$ was produced by using Ti metal granules (99.9% Fisher) and

mixing the oxides in air. The reasons for the optimisation of the synthesis methodology is discussed in subsection 4.2 (page 54) and the synthesis with the Ti metal granules is described below.
The proper amount (according to the chemical reaction equation 8' and Table 3.1) of La_2O_3 (99.9%, Sigma-Aldrich) and TiO_2 (99.9% Sigma-Aldrich) was mixed with an agate mortar and acetone for 30 minutes. The Ti metal was then added to the oxides and filled in the pressing die.

$$0.5\,La_2O_3 + 0.25\,TiO_2 + 0.75\,Ti \longrightarrow LaTiO_3 \tag{8'}$$

The pressed powder was then placed into the arc melter chamber. The next steps were the same regardless of whether Ti granules or Ti monoxide was used. A piece of Ti metal was place in one of the crusible of the arc melter to be used as a getter. The arc melter chamber was vacuumed and filled with argon at 1.1 atm three times. The piece of Ti was melted prior to the pellets to absorb any remaining O_2 in the chamber. The sample was flipped and polished to remove any potential Cu contamination from the Cu plate after each melting. The samples was melted four times. The $LaTiO_3$ was then ground into powder with an agate mortar and acetone for 30 minutes in air.

Table 3.1: Mass of precursors to produce 2.5 g of $LaTiO_3$

Sample composition	Mass of La_2O_3 (g)	Mass of TiO_2 (g)	Mass of TiO (g)	Mass of Ti (g)
$LaTiO_3$ (with Ti metal)	1.7348	0.7654	0	0.1529
$LaTiO_3$ (with TiO)	1.7348	0.4252	0.3401	0

3.2 Material preparation

Powder preparation for arc melting The $BaTiO_3$ (99.7% Fisher), $CaTiO_3$ (99+% Fisher), and TiO_2 (99.9% Sigma-Aldrich) were previously dried in a muffle furnace for at least two hours at 300°C. To produce La-doped $BaTiO_3$, the correct amount (according to the chemical reaction equation 9 and Table 3.2) of $BaTiO_3$ and $LaTiO_3$ (prepared by ourselves) powder was mixed with

an agate mortar and pestle for 30 minutes with acetone in air.

$$xLaTiO_3 + (1 - x)BaTiO_3 \longrightarrow La_xBa_{1-x}TiO_3 \quad (9)$$

Table 3.2 lists the $La_xBa_{1-x}TiO_3$ samples made by arc melting, the mass of precursors, and the SPS temperature used. Arc melting and SPS sintering are described later on. The samples SPS sintered at 1300°C and 1350°C were not investigated further as the conductivity at RT was low (below 300 $S.cm^{-1}$). Samples sintered at 1550°C and 1600°C were not investigated further as the pellets broke; partial melting was also suspected in the case of $BaTiO_3$.

Table 3.2: List of compositions and mass of precursors to produce 2.5 g of $La_xBa_{1-x}TiO_3$ by arc melting and the SPS sintering temperature used.

Sample composition	Mass of $LaTiO_3$ (g)	Mass of $BaTiO_3$ (g)	SPS sintering temperature (°C)
$BaTiO_3$			1300 /1350 / 1450 1500 / 1550 / 1600
$La_{0.05}Ba_{0.95}TiO_3$	0.1258	2.3742	1300 / 1350 / 1450 1500 / 1550 / 1600
$La_{0.1}Ba_{0.9}TiO_3$	0.2515	2.2485	1450
$La_{0.2}Ba_{0.8}TiO_3$	0.5027	1.9973	1450
$La_{0.3}Ba_{0.7}TiO_3$	0.7535	1.7464	1300 / 1350 / 1400 1450 /1500 / 1550 1600
$La_{0.4}Ba_{0.6}TiO_3$	1.0040	1.4959	1450
$La_{0.5}Ba_{0.5}TiO_3$	1.2542	1.2458	1450
$La_{0.6}Ba_{0.4}TiO_3$	1.5040	0.9960	1450
$La_{0.7}Ba_{0.3}TiO_3$	1.7535	0.7465	
$La_{0.8}Ba_{0.2}TiO_3$	2.0027	0.4973	1450
$La_{0.9}Ba_{0.1}TiO_3$	2.2515	0.2485	
$LaTiO_3$			1450

To produce La-doped $CaTiO_3$, the correct amount (according to the chemical reaction equation 10 and Table 3.3) of $CaTiO_3$ and $LaTiO_3$ (prepared by ourselves) powder was mixed with an agate mortar and pestle for 30 minutes with acetone in air.

$$xLaTiO_3 + (1 - x)CaTiO_3 \longrightarrow La_xCa_{1-x}TiO_3 \quad (10)$$

Table 3.3 lists the $La_xCa_{1-x}TiO_3$ samples made by arc melting, the mass of precursors used, and the SPS temperature used.

Table 3.3: List of compositions and mass of precursors to produce 2.5 g of $La_xCa_{1-x}TiO_3$ by arc melting and the SPS sintering temperatures used.

Sample composition	Mass of $LaTiO_3$ (g)	Mass of $CaTiO_3$ (g)	SPS sintering temperature (°C)
$CaTiO_3$			1450
$La_{0.05}Ca_{0.95}TiO_3$	0.2083	2.2917	1450
$La_{0.1}Ca_{0.9}TiO_3$	0.4025	2.0975	1400 / 1450 / 1500
$La_{0.2}Ca_{0.8}TiO_3$	0.7539	1.7461	1450
$La_{0.3}Ca_{0.7}TiO_3$	1.0633	1.4367	1400 / 1450 1500 / 1550
$La_{0.4}Ca_{0.6}TiO_3$	1.3379	1.1621	1450
$La_{0.5}Ca_{0.5}TiO_3$	1.5832	0.9168	1450 / 1500 / 1550
$La_{0.6}Ca_{0.4}TiO_3$	1.8037	0.6963	1450
$La_{0.7}Ca_{0.3}TiO_3$	2.0029	0.4971	1450
$La_{0.8}Ca_{0.2}TiO_3$	2.1839	0.3161	1450
$La_{0.9}Ca_{0.1}TiO_3$	2.3489	0.1511	1450
$LaTiO_3$			1450

To produce La-doped $CaTiO_3$ with A-site deficiency, the correct amount (according to the chemical reaction equation 11 and Table 3.4) of $LaTiO_3$ (prepared by ourselves), $CaTiO_3$, and TiO_2 powder were mixed with an agate mortar and pestle for 30 minutes with acetone in air. Table 3.4 lists the samples made by arc melting, the mass of precursors and the SPS temperature used.

$$xLaTiO_3 + (1 - 1.5\,x)CaTiO_3 + (0.5\,x)TiO_2 \longrightarrow La_xCa_{(1-1.5x)}TiO_{3-0.5x} \tag{11}$$

Table 3.4: List of compositions and mass of precursors to produce 2.5 g of $La_xCa_{1-3/2x}TiO_3$ by arc melting, and the SPS sintering temperatures used.

Sample composition	Mass of $LaTiO_3$ (g)	Mass of $CaTiO_3$ (g)	Mass of TiO_2 (g)	SPS sintering temperature (°C)
$La_{0.1}Ca_{0.85)}TiO_3$	0.4108	2.0222	0.0699	1450
$La_{0.2}Ca_{0.7)}TiO_3$	0.7790	1.5788	0.1325	1450
$La_{0.3}Ca_{0.55)}TiO_3$	1.1108	1.1792	0.1889	1450

Melting Immediately after the mixing, the powder was filled and pressed into the 13.5mm diameter die and placed in the arc melter chamber. A piece of Ti metal was place in one of the crusible of the arc melter to be used as a getter. The arc melter chamber was vacuumed three minutes and filled with argon at 1.1 atm three times. The piece of Ti was melted prior to the pellets to absorb any remaining O_2 in the chamber. The samples were flipped and polished to remove any potential Cu contamination from the Cu plate after each melting. The samples were melted four times then ground into powder with an agate mortar and acetone for 30 minutes in air.

SPS To make pellets by SPS, pieces of carbon paper of one mm of thickness were cut and placed to cover the inner surface of the graphite die and graphite punches of 13.5mm of diameter. The powder was then filled into the die (Figure 3.2). SPS sintering was achieved with a Agus-Pecs 630Sx (SUGA Co Ltd); the SPS parameters were the same except for when the influence of the parameters were studied: the sintering was made in a high vacuum mode, the applied pressure on the punches by the SPS electrodes was set on 40 MPa, the heating and cooling rate were set on 100°C per minute, and 10 minutes of dwelling at the set temperature. The temperature was controlled by a portable radiation thermometer (Chino model IR-AH). The sinterings were started when the gas pressure of the chamber was below $3 \cdot 10^{-3} Pa$. The sintered pellet was then polished to remove the stuck carbon layers which came from the carbon papers. On occasion, the sintered pellets would be broken; new pellets were sintered if the pieces could not be used for the analysis.

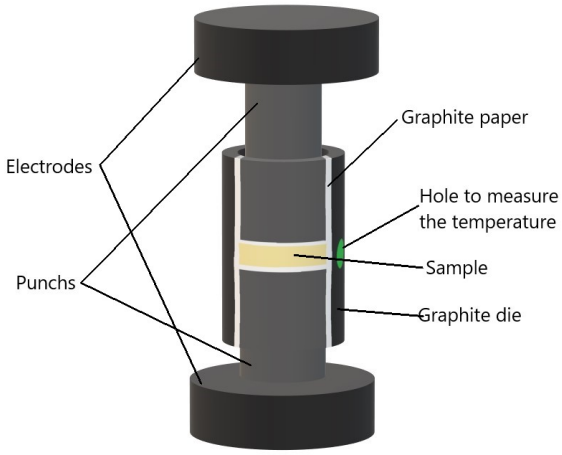


Figure 3.2: Schematic of a filled SPS die between two graphite electrodes. With graphite paper between the sample/die wall and sample/punches.

3.3 Microstructural characterisation

X-ray Diffraction Crystal structure and phases analysis were performed by powder X-Ray diffraction (XRD). Before analysis, the samples were ground by hand with an agate mortar. The powder was loaded flat into a Si powder sample holder (Bruker Corporation) and then scanned using a D8 advance diffractometer (Bruker Corporation) with a CuK$_\alpha$ ($\lambda = 0.15418$ nm) radiation. A tension of 40 kV and a current of 40 mA. 2θ from 10° to 70° with an increment of 0.0205°, and with 0.1 second per step. Phase analyses were done by using the Bragg's law as illustrated in Figure 3.3 and defined in eq (9).

$$2dsin(\theta) = n\lambda \tag{9}$$

With n as the diffraction order, θ the angle of incidence, λ the wavelength of the light emission, and d the grating period. The Bragg's law determines at which angles diffractions would happen. The angle made by the emitted x-ray, the sample, and the detector is 2θ. The phase analyses were done with DIFFRAC.EVA (Bruker). The lattice constants, lattice volumes, and full width at half maximum were calculated with JADE 6.0 (MDI).

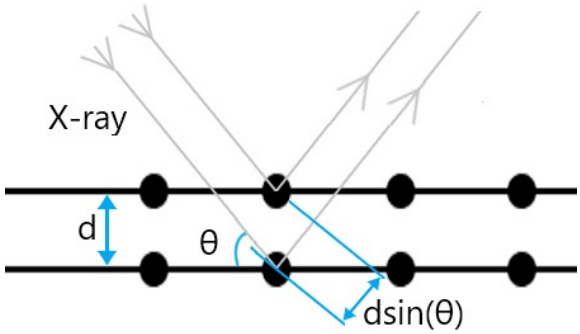


Figure 3.3: Schematic of incident X-ray diffraction by the atoms of a solid during an XRD experiment.

Density measurement Samples volume were measured with a calliper and the mass of the samples were measured with a precision scale. Density was calculated by:

$$D = \frac{m}{V} \tag{10}$$

With m the mass and V the volume of the sample. The theoretical densities ρ_{th} were calculated by dividing the sum of the elements by the lattice volume calculated from the XRD patterns with eq 11. The O loss was neglected.

$$\rho_{th} = \frac{\Sigma_{n=1}^{n} N_i A_i}{V_C N_A} \tag{11}$$

With N_i the number of atoms per unit cell of the element i, A_i the atomic mass of the atome i, V_C the volume per unit cell, and N_A the Avogadro's constant. The relative density was calculated by dividing the density by the theoretical density.

Preparation for microstructure characterisations Samples that were used for microstructure characterisations were mounted in epoxy. To avoid movement, the O-shaped mould was placed

on double sided tape, then the sample was placed into the mould (also in contact with the tape). Commercial epoxy and hardener (Struer) were mixed manually with a flat wood stick for five minutes in a disposable container. The mixture of the epoxy and hardener was poured into the mould until the mixture covered the sample and left overnight. The next day, another batch of mixture was made and poured into the mould until the height was approximately 3.5 cm and left overnight. The epoxy block was polished with a Tegramin station (Struer) using successively MD piano 220, MD piano 500, and MD piano 1200 disk (Struer), then with three polishing cloths loaded with abrasive particles of 9μm, 3μm, and 1μm. The block was inserted in the chamber of a Q150R carbon coater (Quorum) loaded with a new piece of carbon rope, carbon coating was done with the chamber under vacuum. Coatings were done in order to avoid accumulation of electric charges by making the sample and the mounting surfaces conductive. Carbon was chosen as metal coating does not allow chemical analysis. Scanning electron microscope (SEM) analysis were done with a 6490LV (JEOL) with an acceleration voltage of 20 kV. Secondary electron and backscattered images were obtained on the sample surface; the working distance was set around 10 mm and the contrast was adjusted manually. Energy-dispersive X-ray spectroscopy (EDX or EDS) were performed on the sample surface with the SEM 6490LV (JEOL). The main limitation to this technique is that many elements have similar X-ray characteristic emissions; in some cases, it was not possible to distinguish between the elements. Wavelength-dispersive X-ray spectroscopy (WDX) with an electron probe microanalyzer (EPMA) was performed to address this issue. EPMA analysis were done with a JXA-8200 Electron Microprobe (JEOL) and the elemental quantifications were done with four WDX detectors. The WDX differs to EDX as the X-Rays are splitted by monochromators and the specific wavelengths are analysed (Figure 3.4). Points of analysis and map positions were chosen with the EPMA's optical microscope by storing the X and Y positions, then the measurements were carried overnight.

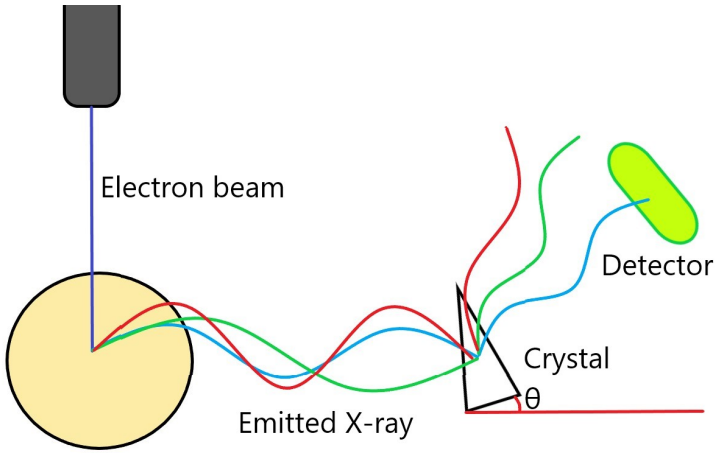


Figure 3.4: Schematic of the principle of the wavelength separation of the sample's emitted X-ray by a rotating crystal for WDX analysis.

Thermogravimetric analysis The thermogravimetric analysis (TGA) in air were done with a horizontal TGA-SDTQ600 (TA Instruments) (Figure 3.5). Before analysis the samples were ground by hand with an agate mortar. Samples between 20 and 40 mg were loaded in Al_2O_3 crucibles. For each crucible, a baseline run was done with an empty crucible. The air flow was set to 100 mL/min. The TGA was set with a five minutes isothermal at 30°C, a heating ramp and a cooling ramp set at the same rate without dwelling time at the maximum temperature.
The heating and cooling rate, and the maximum temperature were different:

- For the melted only $La_xBa_{1-x}TiO_3$ the heating and cooling rate was set to 10°C per minute, the maximum temperature was set to 1000°C.
- For the SPS sintered $La_xBa_{1-x}TiO_3$ the heating and cooling rate was set to 5°C per minute, the maximum temperature was set to 1250°C.
- For the melted only $La_xCa_{1-x}TiO_3$ the heating and cooling rate was set to 5°C per minute, the maximum temperature was set to 800°C.
- Fot the SPS sintered $La_xCa_{1-x}TiO_3$ the heating and cooling rate was set to 5°C per minute,

the maximum temperature was set to 1000°C.

The mass variations caused by the crucible, buoyancy and convection was removed with the manufacturer software Ta universal analysis (TA instrument).

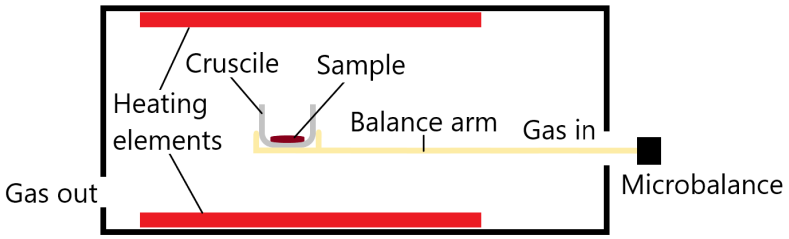


Figure 3.5: Schematic of a horizontal TGA, a crucible in a temperature-controlled chamber, sample holder on the sample arm connected to the microbalance.

3.4 Testing and evaluation of performance

Electrical tests A low speed diamond saw was used to cut the samples into bars with a length between 6 and 12 mm, with an approximate width of 1-4 mm. When the Seebeck coefficient was measured, samples of at least 10 mm of length were used, when only the electrical conductivity was measured, samples length were at least 6 mm. The two extremities were painted with silver paste and dried in air at RT for 30 minutes to avoid problems of contact between the sample and the two electrodes. The electrical conductivity and the Seebeck coefficient were measured by the four-point probes method in a temperature and gas controlled environment with a LSR-3 (Linseis) (Figure 3.6). When the Seebeck coefficient was measured (as well as the electrical conductivity), the chamber was vacuumed and filed with static He at 1.05 atm. The measurement of the Seebeck coefficent should be carry in static He to have a stable temperature gradient in the furnace and to produce a temperature gradient in the bulk of the sample, He is the gas of choice because of its high thermal conductivity. To measure the Seebeck coefficient, a gradient of 50°C was set, the gradient was created by the

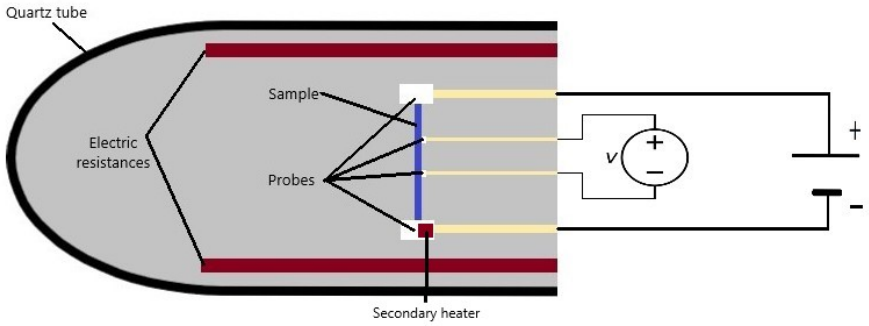


Figure 3.6: Schematic of a gas and temperature-controlled four points probes (LSR-3), with the top and bottom probes as the electrodes, the middle probes for the potentiometer, secondary heater at the bottom electrode to generate a temperature gradient.

secondary heater of the LSR-3, then the two points of the sample in contact with the probes were at different temperatures as illustrated in Figure 3.6. The maximum probes distance (8mm) was always used when measuring the Seebeck coefficient to maximise the temperature difference between the two probes. When only the electrical conductivity was measured, the chamber was vacuumed and filed just above 1 atm three times and the measurments were carried in flowing 5%H_2/95%. Ti granules (99.9% Fisher) were also present in the chamber to further reduce the O content of the gas. The equipment was calibrated manually by measuring the Seebeck coefficient of the constantan 55% Cu 45% Ni (Linseis) at a chosen temperature, then a numeric temperature bias was applied to one of the probs to correct the measured temperature difference, the steps was repeated until the measured value was satisfying : error below 5% for the temperature range of interest (200°C to 800°C). Figure 3.7 is the plot of the measured Seebeck coefficient of the reference sample before the corrections and after the corrections.

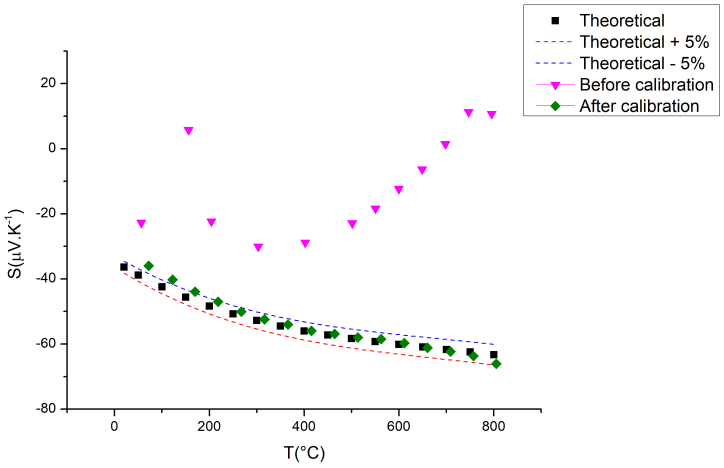


Figure 3.7: Plot of the Seebeck coefficient of the constantan reference sample before and after the calibration, the reference data, and the reference data +5% or -5%.

Thermal diffusivity The thermal diffusivity was measured with unbroken samples. The disk shape samples used to measured the thermal diffusivity were polished with a Target Holder (Buhler) manually in order to decrease their thickness and to have an homogeneous thickness. The thermal diffusivity was measured with an LFA 467 hyperflash (Netzsch) with a "standard" configuration (Figure 3.8) with the laser flash technique using disk shape sample holder of 12.7 mm of diameter. Before being placed in the the sample holder, the samples were coated with a graphite spray cane aerosol (Kontakt chemie) three times for both surfaces to increase the light absorbency. A delay of two minutes was taken between each coat for the solvent to evaporate. The chamber of the LFA was vacuumed and purged three times, the flow rate was set to 50 mL per minute. $H_2$5%/Ar95% gas mixture was used for the $La_xBa_{1-x}TiO_3$ samples and N_2 was used for the $La_xCa_{1-x}TiO_3$ samples. Before the measurements, shots were done at RT, shot parameters (e.g. the main gain) were modify to address undershooting, overshooting, too short duration, or too long duration, until a suitable curve was obtained (Figure 3.9 is a drawing of a suitable LFA shot). The thermal diffusivity was calculated with mathematical corrections by the manufacturer software.

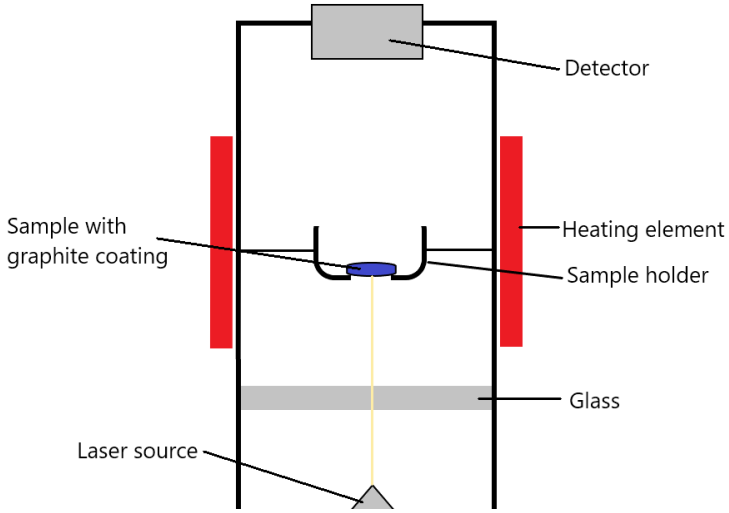


Figure 3.8: Schematic of a vertical LFA with a laser as the heat source at the bottom, the detector at the top, and the sample between. Sample placed in the gas and temperature controlled chamber.

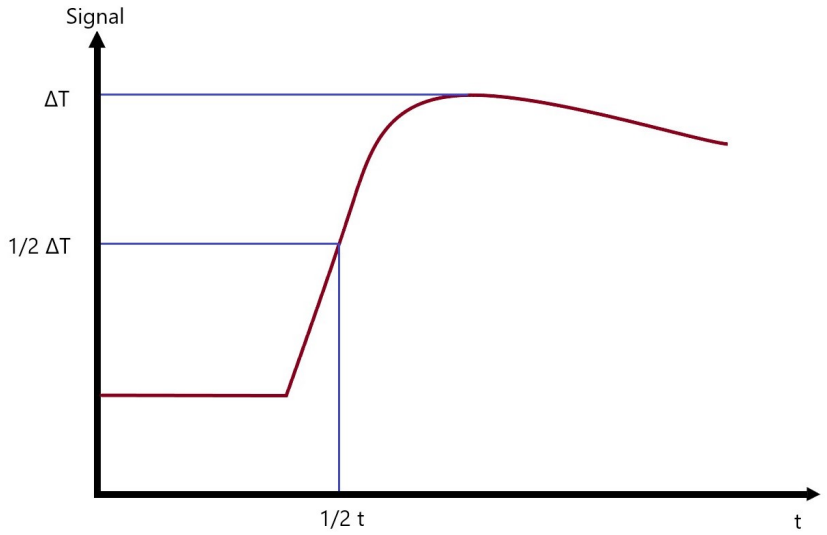


Figure 3.9: Draw of a suitable LFA signal curve after that the sample was heated up by a pulse of light.

4 Synthesis, structural, and thermoelectric properties of $La_xBa_{1-x}TiO_3$

4.1 Introduction

As discussed in subesection 2.2 (from page 27), three papers reported the synthesis of highly La-doped $BaTiO_3$ by using an arc melter ($0.5 \leq x \leq 1$ [156] and $0 \leq x \leq 1$ [155,158] for $La_xBa_{1-x}TiO_3$) but the electrical conductivity values were two orders of magnitude lower than reported values of La-doped $SrTiO_3$ with similar La concentrations. The results of these three papers suggest that it is possible to controll the Ti oxidation stats in $BaTiO_3$ with substitution of the Ba by La, thus increasing the number of electrons in the conduction band. Samples of La-doped $SrTiO_3$ with electrical conductivity of several thousand of $S.cm^{-1}$ at RT were reported in numerous papers [188]; $BaTiO_3$ and $SrTiO_3$ have similar electronic structure [187], it is then reasonable to think that making highly conductive doped $BaTiO_3$ should be possible. However their is no report of comparable conductivity of $BaTiO_3$ based material. As discussed in subsection 2.2, the electric properties of La-doped $SrTiO_3$ depends on the synthesis and post treatment conditions, as example, with the same cations compositions, La-doped $SrTiO_3$ can have a difference of electrical conductivity of five orders of magnitude [88].

Muta et al reported a sample of $La_{0.1}Ba_{0.9}TiO_3$ with an electrical conductivity of 200 $S.cm^{-1}$ at RT produced with Ti metal for precursor, sintered in Ar flow [160]. This conductivity is one order of magnitude higher than the one reported by Eylem et al (2.5 $S.cm^{-1}$ at RT) [158], but still an order of magnitute lower than La-doped $SrTiO_3$ [88]. Muta et al used a tubular furnace with Ar flow, with a lower oxygen pressure during the synthesis and during the post treatment, a much higher electrical conductivity could be achieved. Additionaly in their work they did not make other compositions of the series $La_xBa_{1-x}TiO_3$ and samples with different La concentration could have better electrical and thermoelectric properties.

In this section, the synthesis of $La_xBa_{1-x}TiO_3$ by arc melting and SPS sintering is investigated. Both arc melting and SPS sintering operate in strong reducing conditions, aiming to favour the electronic

compensation over the ionic compensation that lead to poorly conductive material [145, 146]. The aim of this methodology is to increase the charge carrier concentration. The study of the crystal structure, the microstructure and the oxidation behaviour (by TGA) was designed to observed what charge compensation mechanism is favoured. The electrical and thermal properties are described in the rest of the section. There are significant challenges in producing reproducible results in this and other similar systems investigated, a discussion of the approaches and difficulties are explored at the beginning of the section. The results presented in the rest of the section are for the optimised approach.

4.2 Influence of the synthesis route.

This subsection shows analyses about the $LaTiO_3$ when used as a raw material in the production of doped $CaTiO_3$ and doped $BaTiO_3$. These results highlight that great care is needed to ensure the conductive samples are repeatable and reproducible, particularly through taking great care during the synthesis steps and using high quality raw materials. This may explains the divergences in results from those yielded in previous studies, where the transition from insulating/semiconductor to metal were observed for higher La content (35%) [155–158], and BaO rich phase was observed [158]. Figure 4.1 shows the XRD patterns of different batches of $LaTiO_3$ produced in differents ways. A layered monoclinic perovskite $La_2Ti_2O_7$ formed with or without the presence of the orthorhombic Pbnm parovskite phase was observed, whenever Ti granules or titanium monoxide was used, when the milled powders were not immediately melted. This is likely due to the formation of hydroxides from the moisture and the raw materials. Single phase Pbnm orthorhombic perovskite $LaTiO_3$ was obtained in processing route either with the use of Ti granule and titanium monoxide powder and both produced identical XRD patterns (identical XRD pattern with the use of Ti granule not shown). Then the use of Ti granules, even problematic (for other reasons), was not the major source of the inconsistency of the phase and the final electrical conductivity.

From these preliminary studies it was decided that titanium monoxide would be used instead of Ti granules. The advantage of titanium monoxide is that it can be used in a powder form, then after the milling, supposing the milled powder is homogeneous, the inevitable loss of powder during the

pressing and melting process should not change the stoichiometry of the sample. Additionally the use of the Ti granules was found to damage the pressing die.

Figure 4.2 is the TGA of the $LaTiO_3$ in air with the same temperature profile that would be used to dry the raw material in a muffle furnace in air : a heating and cooling ramp of 5°C per minute from room temperature to 300°C with a dwelling time of two hours. Until 200°C, the mass slightly decreased, then increased until the end of the dwelling time. From the dwelling time the mass continues to increase at a lower rate, such that the final mass increased by more than 0.1 %. The decrease in mass from the start to 200°C was lower than 0.025%, so a decomposition of compounds such as hydroxides or evaporation of moisture is not strongly in evidence for temperature below 300°C. The final mass increase could be due to the absorption of O to form monoclinic $La_2Ti_2O_7$ or hydroxide. As single phase $LaTiO_3$ was observed on the XRD patterns (Figure 4.1), the vast majority of La ions should share liaison with Ti ions such that the formation of hydroxides is much less likely to occur when compared to raw TiO_2 or La_2O_3. However, the oxidation of Ti^{3+} is plausible. During the process, the decomposition of hydroxides and oxidation can occur, but the second has to be much more important. Thus it is then concluded that drying the $LaTiO_3$ in a muffle furnace in air prior to the reaction is not beneficial. Concisely, the choice and the preparation of the raw materials for the synthesis of the doped alkaline earth titanate is important, we observed the best repeatability for the $LaTiO_3$ synthesis by using titanium monoxide and preparing the powder in a glovebox.

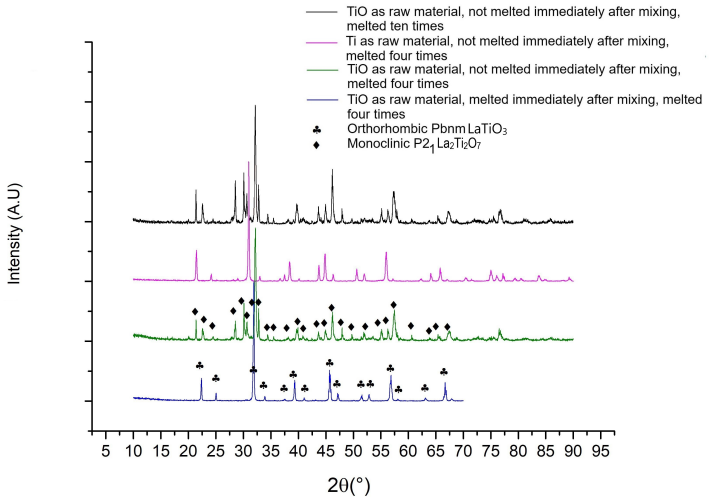


Figure 4.1: XRD patterns of different synthesis of $LaTiO_3$ with Ti or TiO precursors, with different delay after the melting, pattern of a sample that matched single phase $LaTiO_3$ and others with layered perovskite $La_2Ti_2O_7$.

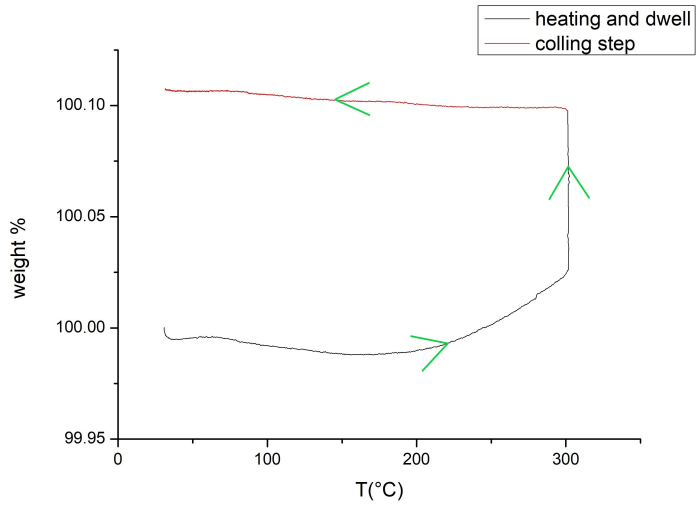


Figure 4.2: TGA plot of $LaTiO_3$ powder in air with a heating and cooling rate of 10°C per minute and a dwell of two hours.

4.3 Structure, microstructure, and oxidation properties

X-Ray diffraction data Figures 4.3 and 4.4 are the powder XRD patterns and expanded powder XRD patterns centred at 2θ value of 32.5° of the system $La_xBa_{1-x}TiO_3$ produced by arc melting. The plots include for comparison XRD data obtained from commercial undoped $BaTiO_3$ material that was synthesised in air. The undoped commercial $BaTiO_3$ synthesised in air was a white powder, and its XRD pattern matched with a tetragonal P4/mmm space group. However, the undoped samples after synthesizing in an arc melting in an argon atmosphere were dark blue/grey in comparison and were identified to have a hexagonal (P63mmc) structure. The influence of the Ti oxidation number on the colour is well established, and this modification of the O vacancies is attributed to the change of the crystal structure after the arc melting.

The introduction of doping induced a change to a space group of higher symmetry. Publications in the literature diverge whether the space group from doping is Ibmm orthorhombic or cubic Pm3m [156, 158]. As the Ibmm space group also has a high symmetry like cubic Pm3m, powder XRD can not easily distinguish between the two space groups. However we identified the doped composition to be cubic until $La_{0.8}Ba_{0.2}TiO_3$. In agreement with the former studies, $La_{0.8}Ba_{0.2}TiO_3$ and $LaTiO_3$ were identified as orthorhombic Pbnm. From $La_{0.05}Ba_{0.95}TiO_3$ to $La_{0.3}Ba_{0.7}TiO_3$, weak peaks of a hexagonal undoped $BaTiO_3$ were present with the cubic Pm3m peaks. These peaks formed a left shoulder to the [110] cubic peak. The intensity of these hexagonal peaks decreased with the La-doping. From $La_{0.8}Ba_{0.2}TiO_3$ to $LaTiO_3$, the space group was determined to be orthorhombic Pbnm, in agreement with the former studies [156, 158]. No layered perovskite phase was detected. If La could not be inserted in the Ba site (or only a few percent), it would result in an increase in the intensity of the peaks associated with undoped $BaTiO_3$ and/or a layered perovskite phase with the La content of the samples.

The peaks of all the XRD patterns (except the commercial $BaTiO_3$) were not sharp, exhibiting broadening. For Sunstrom et al, the broadness of the XRD peaks came from the Imma space group, the Imma space group is not cubic and induced a small peak splitting, the splitting is too small to be detected and on the XRD pattern and the splitted peaks merged in one broader peak.

This broadening could be associated with a smaller grain size, with the commercial sample being highly crystaline large graines while the samples produced by arc melting did not have sufficient time to grow. Values of the crystallite size calculated with the Scherrer equation [189]:

$$L = \frac{K\lambda}{\beta cos(\theta)} \tag{12}$$

Where L is the crystallite size, K the shape factor, λ the X-ray wavelength, β the full width at half maximum (FWHM), and θ the Bragg angle. With K = 0.89, the values obtained were below 100 nm, for example $La_{0.4}Ba_{0.6}TiO_3$, the calculated FWHM was 0.124 ± 0.0046 ° , giving crystallite a size of 66 ± 2.5 nm. These values do not make physical sense. An alternative explanation of this broadness is proposed in the SEM (page 75) and EPMA (page 81) parts. Briefly, on the microscopic scale, the chemical compositions were different to some extent, centered on the theoretical composition, making the XRD peak broader than if the composition of the grains were 100% homogenous.
From undoped $BaTiO_3$ to $La_{0.9}Ba_{0.1}TiO_3$, a shift in the position of the peaks to higher angles was observed. The shift was especially visible with the plot from 30 ° to 35° in Figure 4.4. This was the result of the decrease in the lattice constant which is an indication of the insertion of the La in the crystal structure; as La has a smaller ionic radius than Ba, a decrease is expected. However $LaTiO_3$ shifted back toward the lower angles, for that composition only a secondary non-perovskite phase was identified by SEM (Figures 5.16k, 5.16l, and 5.17f).

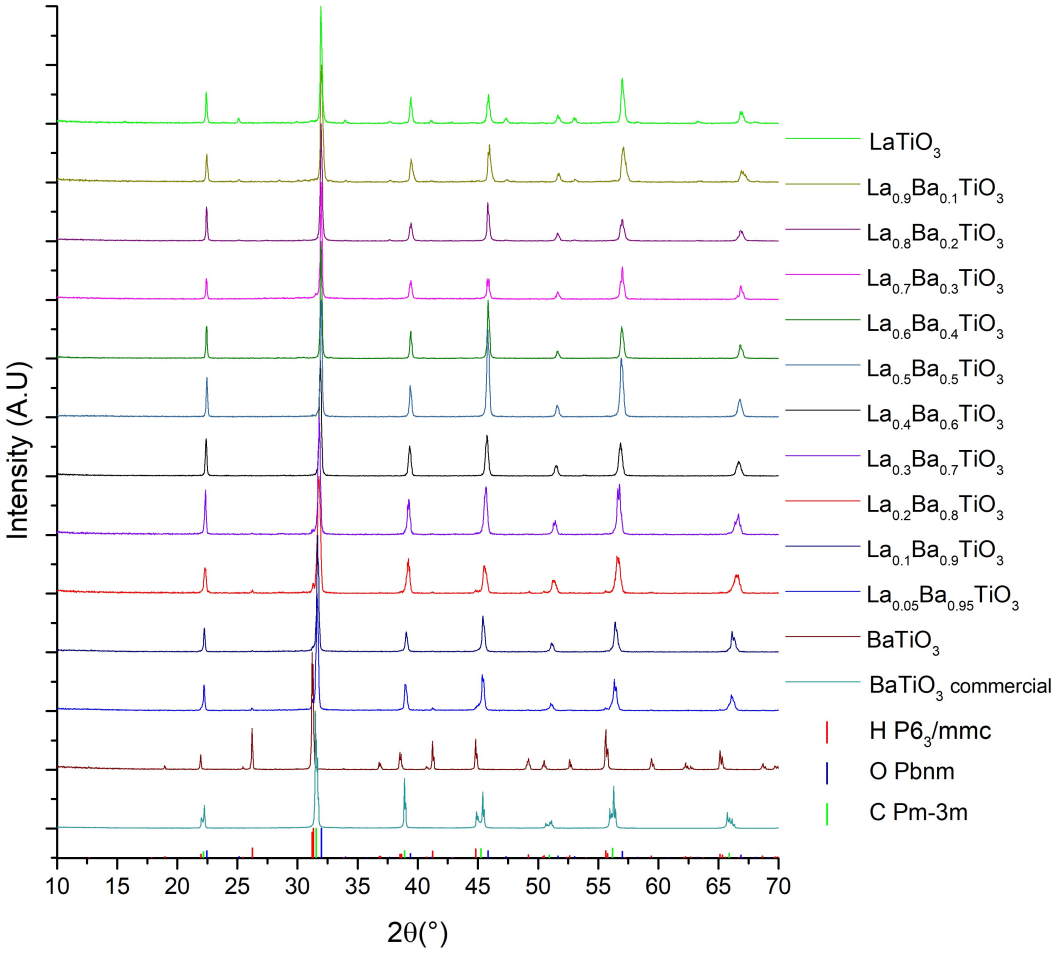


Figure 4.3: Powder XRD patterns of the system $La_xBa_{1-x}TiO_3$ produced by arc melting with argon atmosphere and commercial $BaTiO_3$.

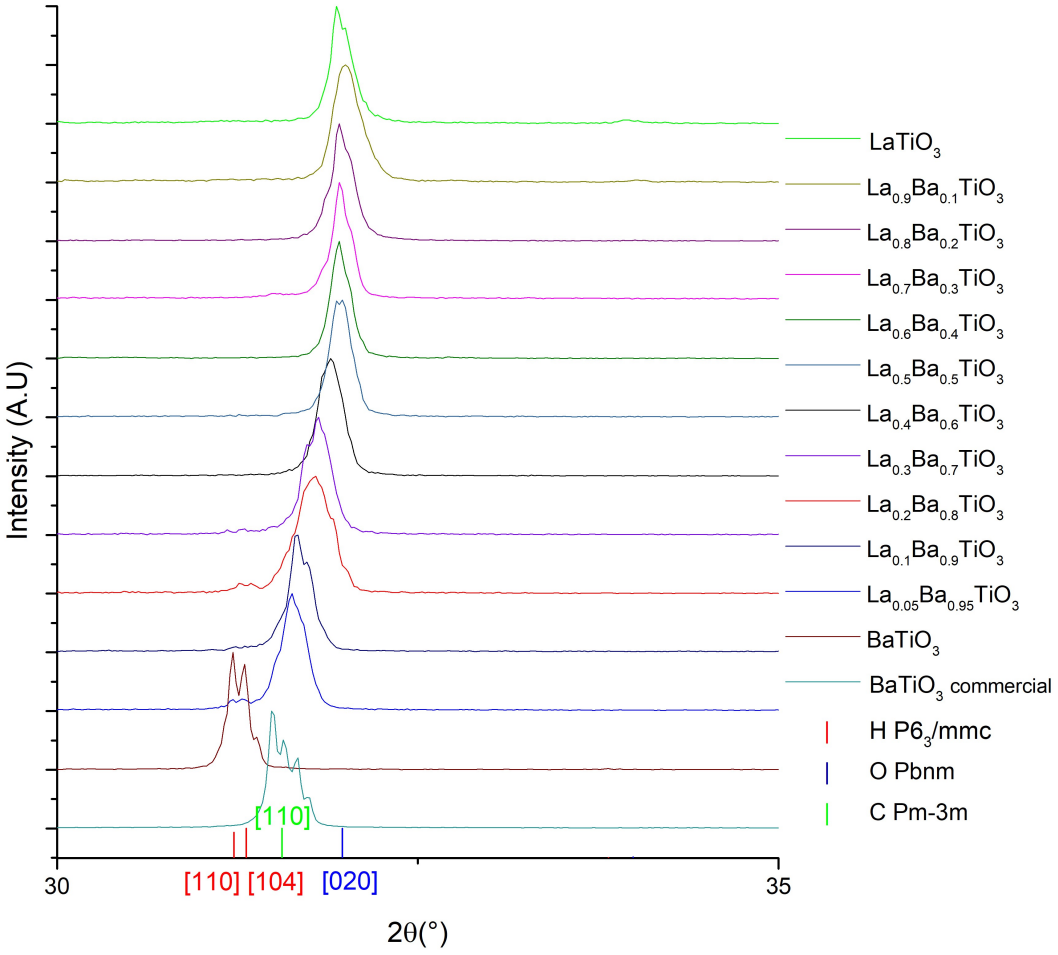


Figure 4.4: Expanded powder XRD patterns of the system $La_xBa_{1-x}TiO_3$ produced by arc melting with argon atmosphere and commercial $BaTiO_3$.

Figures 4.5 and 4.6 are respectively the plot of the lattice edge length and the lattice volume of the system $La_xBa_{1-x}TiO_3$ produced by arc melting and show the reduction of the lattice constant. The values were calculated from the powder XRD patterns. The decrease in the volume, even if not totally linear, follows the Vegard's law until $LaTiO_3$. For the samples identified as cubic, the volume decreases from 63.80 ± 0.01 Å^3 for $La_{0.05}Ba_{0.95}TiO_3$ to 61.76 ± 0.02 Å^3 for $La_{0.7}Ba_{0.3}TiO_3$. With the change of the space group, the volume is increased to 247.36 ± 0.08 Å^3 for $La_{0.8}Ba_{0.2}TiO_3$. These results indicate that the La was inserted in the A-site of the perovskite structure with no detectable non-perovskite phase. As observed with the angle shift, the lattice volume of $LaTiO_3$ (247.1 ± 0.14 Å^3) was slightly higher than $La_{0.9}Ba_{0.1}TiO_3$ (247.4 ± 0.08 Å^3), suggesting the presence of a non-perovskite phase in a too-small proportion to be detected by XRD.

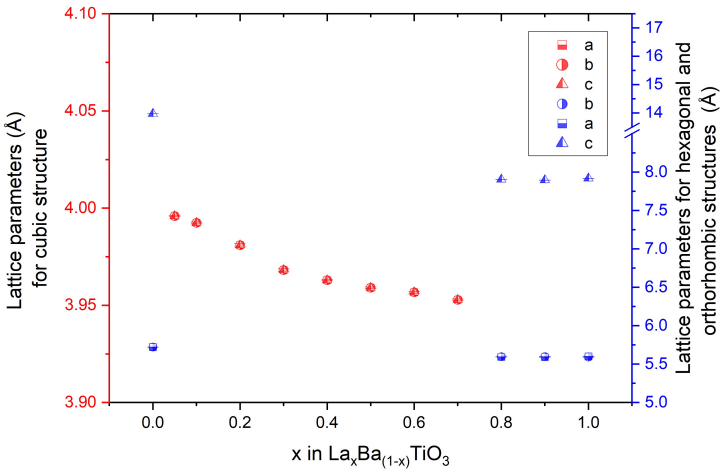


Figure 4.5: Plot of the lattice edge length of the system $La_xBa_{1-x}TiO_3$ produced by arc melting, calculated from the XRD patterns. Error bars are smaller than the symbol size.

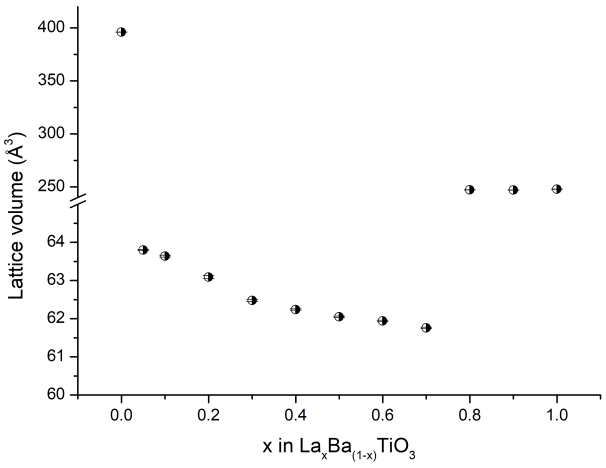


Figure 4.6: Plot of the lattice volume of the system $La_xBa_{1-x}TiO_3$ produced by arc melting, calculated from the XRD patterns. Error bars are smaller than the symbol size.

Figures 4.7 and 4.8 are respectively the powder XRD patterns and powder XRD patterns centered on 2θ value of 32.5° of the system $La_xBa_{1-x}TiO_3$ produced by arc melting and followed by a SPS sintering. Overall the powder XRD patterns were similar. For lightly La-doped samples the intensity of the peaks identified to $BaTiO_3$ slightly decreased. As with the melted sample a shift to the lower angle is present, highlighted in Figure 4.8. The FWHM decreased after the SPS sintering, as shown in Figure 4.11, which could mean larger crystallite sizes, however, SEM observations showed an increase in the grain size. Additionally the calculated crystallite sizes were below 100nm, for example the calculated FWHM of $La_{0.4}Ba_{0.6}TiO_3$ was 0.106 ± 0.0039 °, which gives a crystallite size of D = 77 ± 2.9 nm, which does not make physical sense. However, with the alternative explanation discussed in the SEM and EPMA parts, the decrease of the FWHM indicates a higher homogeneity of the chemical composition of the grains. For both arc melted and SPS sintered samples, the FWHM was the highest for the samples $La_{0.2}Ba_{0.8}TiO_3$, and the smallest for the samples $La_{0.6}Ba_{0.4}TiO_3$.

Figures 4.9 is the plot of the lattice edge length of the $La_xBa_{1-x}TiO_3$ produced by arc melting

followed by SPS sintering. Lattice volume after the arc melting and after the SPS is plot in Figure 4.10. The volume decreased with the La content following the Vegard's law, from 63.93 ± 0.01 $Å^3$ for $La_{0.05}Ba_{0.95}TiO_3$ to 62.13 ± 0.02 $Å^3$ for $La_{0.6}Ba_{0.4}TiO_3$. With the change of the space group the volume increased to 247.1 ± 0.31 $Å^3$ for $La_{0.8}Ba_{0.2}TiO_3$. The lattice volume of $LaTiO_3$ was higher than $La_{0.8}Ba_{0.2}TiO_3$ with 248.8 ± 0.06 $Å^3$, suggesting the presence of a non-perovskite phase in a too-small proportion to be detected by XRD. The lattice volumes of the SPS sintering samples were close to the arc melted samples, the highest difference was 0.34 ± 0.05 $Å^3$ for the samples $La_{0.3}Ba_{0.7}TiO_3$. The variations of volume between the arc melted and SPS sintered samples may be because of a higher homogeneity of the La in the sample during the SPS sintering or the loss of oxygen during the SPS sintering, resulting of a higher amount of Ti^{3+} that have a higher ionic radius than Ti^{4+} [190]. XRD data showed that arc melting followed by an SPS sintering is a suitable way to produce La doped $BaTiO_3$.

While with conventional furnace sintering, the solubility of La in $BaTiO_3$ is as low as 0.3% [191], by reacting the oxides with an arc melter, the full series can be achieved. In their work, Eylem et al successfully doped $BaTiO_3$ with La and obtained a perovskite phase but observed BaO when $0.5 \leq x \leq 0.8$, in our case no such impurities were observed. In their work, they could not obtain a perovskite phase when doped with Gd for $x > 0.2$ and when doped with Y for $x > 4$. As explained in the subsection 4.2, improper control of the raw materials can lead to significantly different results, it is possible that a higher solubility limit for Gd and Y can be achieved by taking more care of the raw materials before the melting.

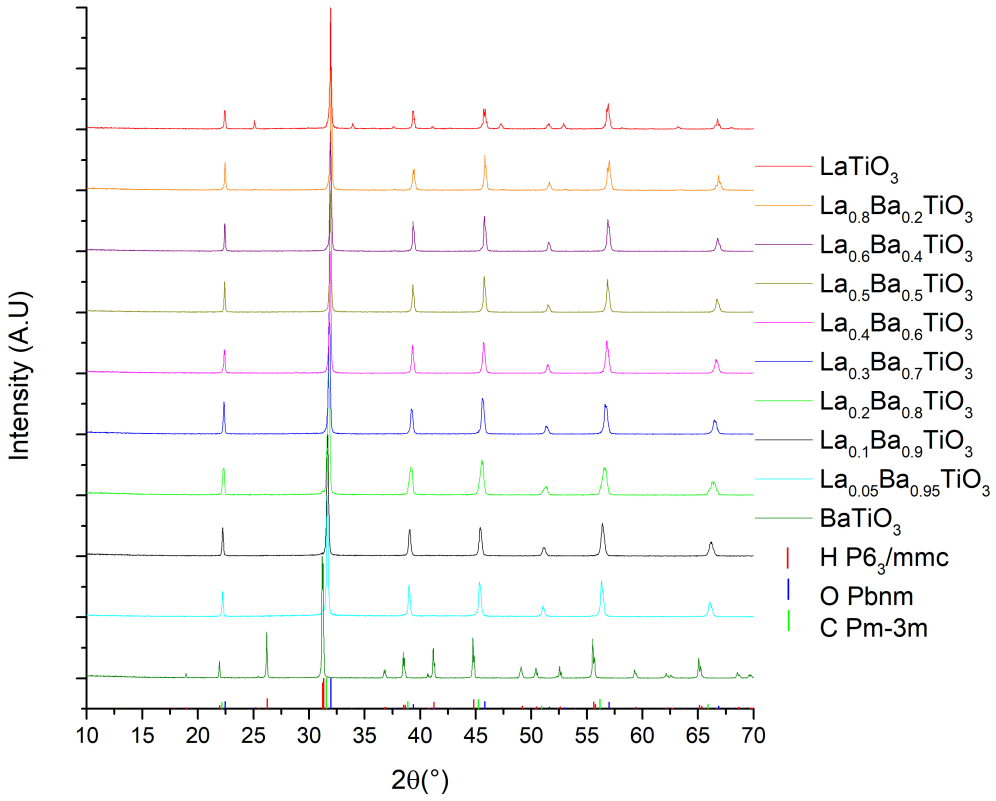


Figure 4.7: XRD pattern of the system $La_xBa_{1-x}TiO_3$ produced by arc melting with argon atmosphere followed by a SPS sintering at 1450°C for 10 minutes in high vacuum (diffusion pump) with a heating and cooling rate of 100°C/min and an applied pressure of 40 MPa.

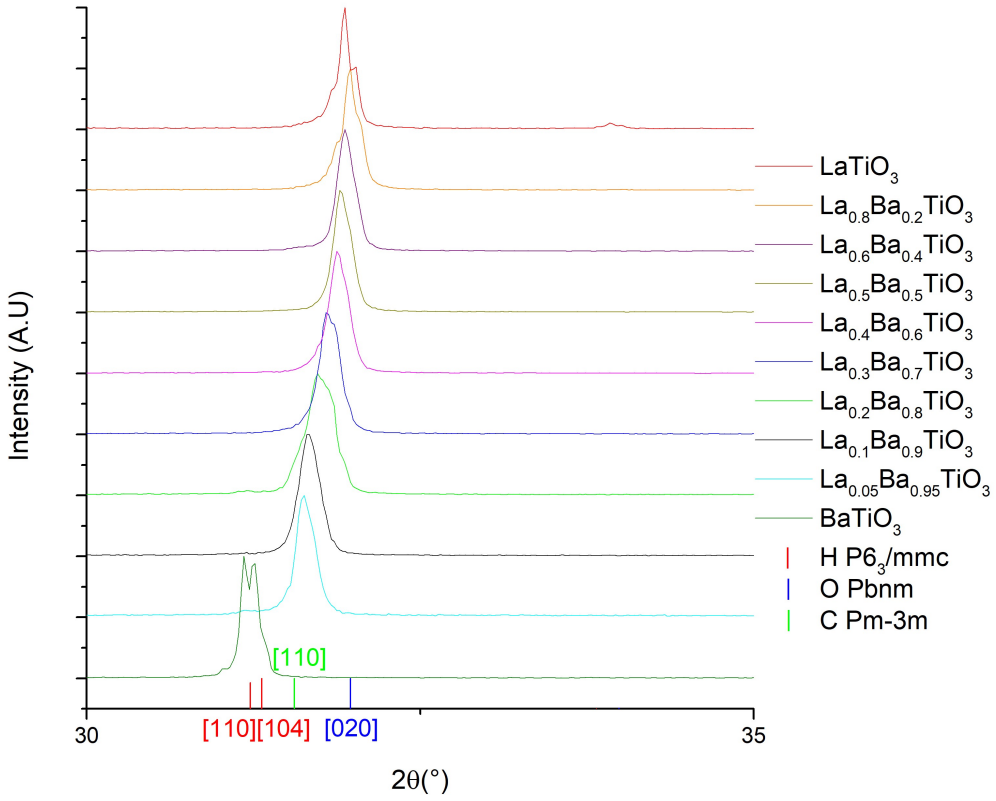


Figure 4.8: Expanded XRD pattern of the system $La_xBa_{1-x}TiO_3$ produced by arc melting with argon atmosphere followed by a SPS sintering at 1450°C for 10 minutes in high vacuum (diffusion pump) with a heating and cooling rate of 100°C/min and an applied pressure of 40 MPa.

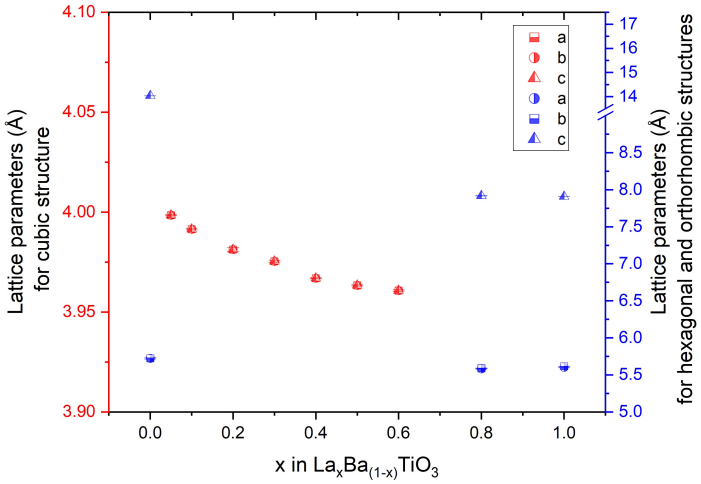


Figure 4.9: Plot of the lattice edge length of the system $La_xBa_{1-x}TiO_3$ produced by arc melting with argon atmosphere followed by a SPS sintering at 1450°C for 10 minutes in high vacuum (diffusion pump) with a heating and cooling rate of 100°C/min and an applied pressure of 40 MPa. Error bars are smaller than the symbol size.

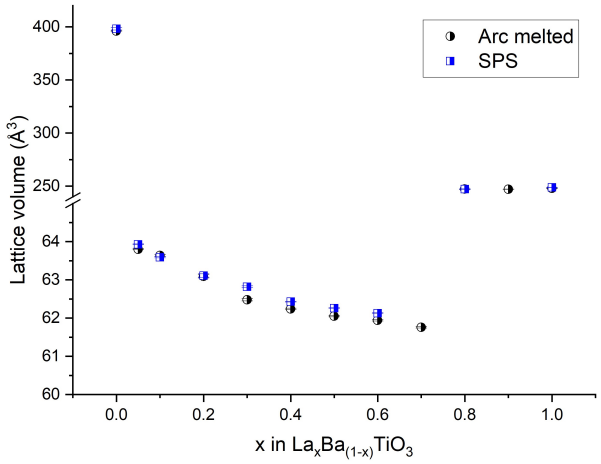


Figure 4.10: Plot of the lattice volume of the system $La_xBa_{1-x}TiO_3$ after the arc melting with argon atmosphere and after the SPS sintering at 1450°C for 10 minutes in high vacuum (diffusion pump) with a heating and cooling rate of 100°C/min and an applied pressure of 40 MPa. Error bars are smaller than the symbol size.

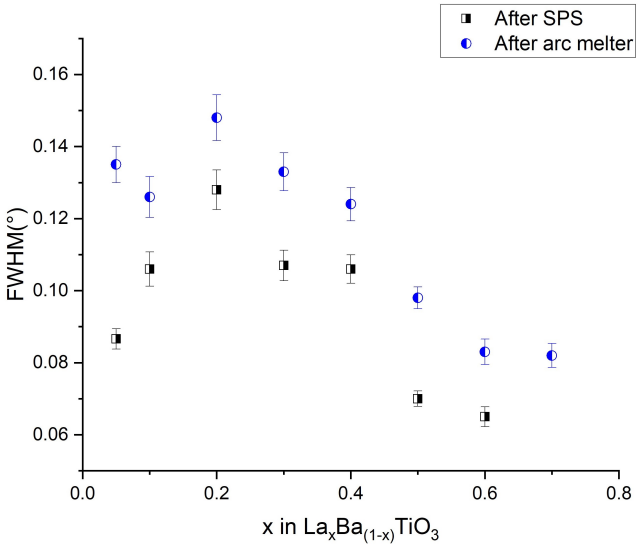


Figure 4.11: Full width at half maximum of the samples $La_xBa_{1-x}TiO_3$ produced by arc melting with argon atmosphere, and produced by arc melting with argon atmosphere followed by a SPS sintering at 1450°C for 10 minutes in high vacuum (diffusion pump) with a heating and cooling rate of 100°C/min and an applied pressure of 40 MPa.

TGA By heating the samples in an oxygen rich atmosphere, the doping mechanisme in eq 3 (page 20) and eq 7 (page 27) should be reversed, oxygen would then be absorbed by the sample resulting in an irreversible increase of the mass. Figure 4.12 is the plot of the TGA curves in air of the series $La_xBa_{1-x}TiO_3$ produced by arc melting in argon. The TGA were set for two ramps with a heating and cooling rate of 10°C per minute from room temperature to 1000°C in a air flow of 100 $mL.min^{-1}$. The profiles of all the analysed samples are similar, in which around 250-300°C the sample's weight increase. The difference between the starting mass and the final mass increases proportionaly with the La content, as the stoichiometry of La increases, the ratio Ti^{3+}/Ti^{4+} is higher. These Ti ions can then be oxidized at high temperature resulting in a mass increase during the TGA experiment. The TGA data indicates that the La doping induces Ti reduction and then increases the charge carrier concentration of the doped $BaTiO_3$. Figure 4.13 is the plot of the final mass increase for different doping level, also plot the final mass increase normalised by the

ratio $\frac{M_O}{M_{La_xBa_{1-x}TiO_3}}$ to take into account the change of molar mass with the doping level. The trend is linear, indicating that the oxidation stats of the Ti is proportional to the La content, then the doping mechanisme remains similar over the whole range of doping. The TGA are consistent with the results of Eylem et al, they observed a correlation between the oxygen uptake and the La doping [158].

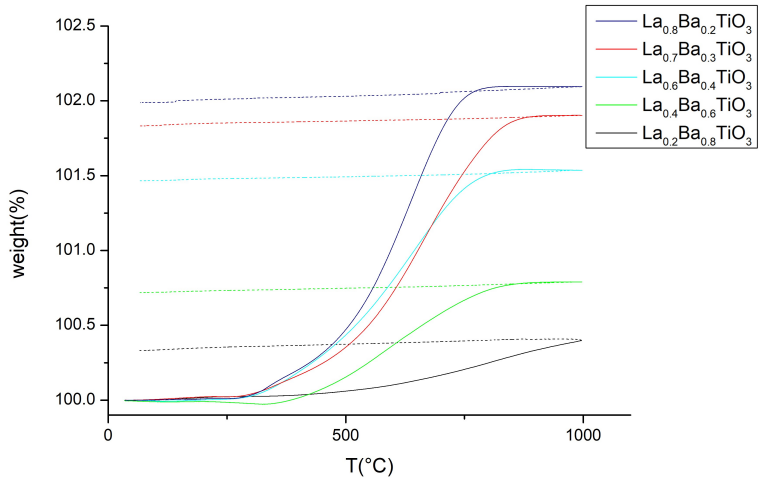


Figure 4.12: TGA plot of $La_xBa_{1-x}TiO_3$ in air from room temperature to 1000°C, with a heating and cooling rate of 10°C per minute, heating step plotted in solid line, cooling step plotted in dash line. Powder from crushed pellets produced by arc melting in argon.

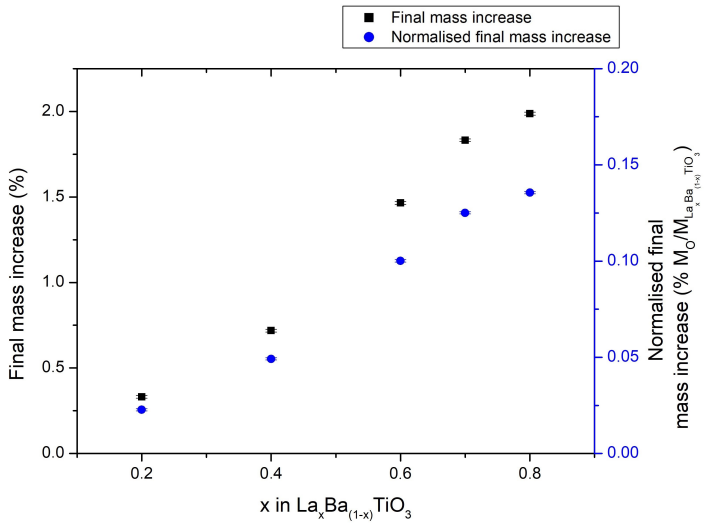


Figure 4.13: Influence of the doping level on the difference of mass after the TGA for the series $La_xBa_{1-x}TiO_3$, plot in Figure 4.12. Powder from crushed pellets produced by arc melting in argon.

Figure 4.14 is the plot of the TGA in air from RT to 1250°C of the SPS sintered samples. All of the samples plateaued during the TGA indicating that they were fully oxidised. The temperature at which they plateaued was correlated to the La content. At first, La doping increased the oxidising temperature, but decreased it with more doping, around for example 350°C for $La_{0.4}Ba_{0.6}TiO_3$ and 250°C for $La_{0.8}Ba_{0.2}TiO_3$. The temperature at the end of the oxidation also decreased, for example 1050°C for $La_{0.2}Ba_{0.8}TiO_3$ and 725°C for $La_{0.8}Ba_{0.2}TiO_3$. $La_{0.05}Ba_{0.95}TiO_3$ is a special, the mass increased at two different temperatures, around 100°C and 500°C. This behaviour is explained by the presence of undoped $BaTiO_3$ grains in the sample. The undoped $BaTiO_3$ oxidised at a lower temperature than the La-doped $BaTiO_3$, resulting in two slops. Figure 4.15 is the plot of the final mass for the different doping levels after the SPS step, also plot the mass increased normalised by the ratio $\frac{M_O}{M_{La_xBa_{1-x}TiO_3}}$ to take into account the change of molar mass with the doping level. The final mass was proportional to the La content linearly. In the absence of a donor doping mechanism, the oxygen vacancy concentration would not be proportional to the La content, then it indicates that electronic compensations (eq 7 in page 27) occurred without ionic compensation.

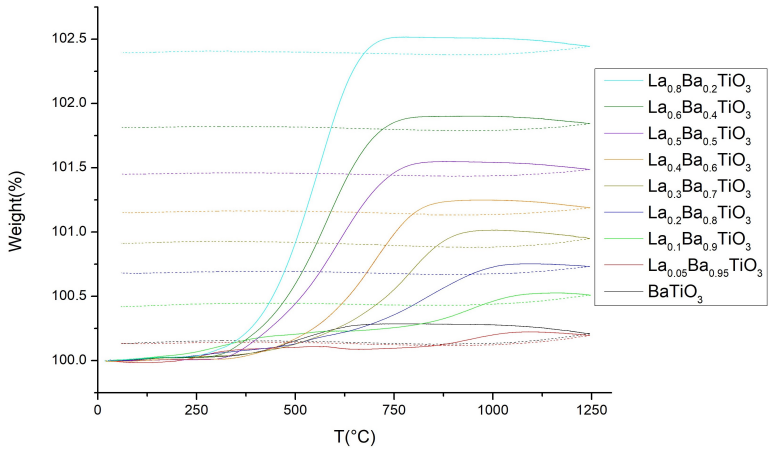


Figure 4.14: TGA of $La_xBa_{1-x}TiO_3$ powders in air from RT to 1000°C, with heating and cooling rate of 5°C/min with a flow of 100 mL/min, heating step plotted in solid line, cooling step in dash line. Powders from the crushed pellets SPS sintered at 1450°C in high vacuum (diffusion pump) for 10 minutes with a heating and cooling rate of 100°C/min and applied pressure of 40 MPa.

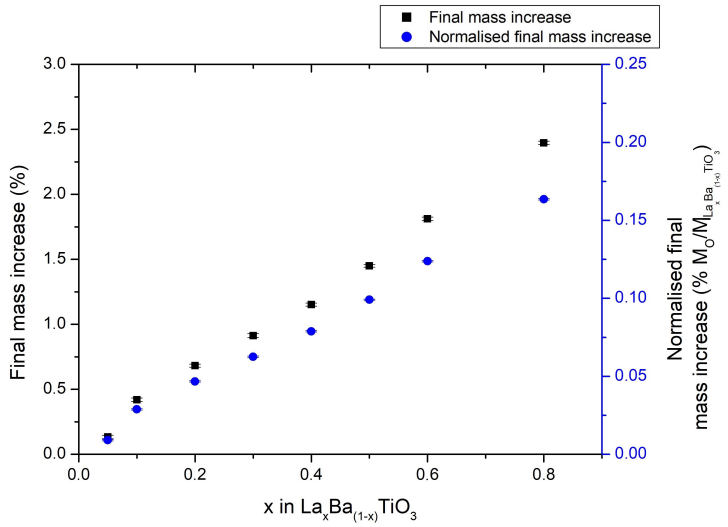


Figure 4.15: Influence of the doping level on the difference of mass after the TGA for the series $La_xBa_{1-x}TiO_3$, plot in Figure 4.14. Powders from the crushed pellet SPS sintered at 1450°C in high vacuum (diffusion pump) for 10 minutes with heating and cooling rate of 100°C/min and applied pressure of 40 MPa.

Figure 4.16 is the powder XRD patterns of the powder after the TGA run for two compositions. The amount of powder used was small, thus the signal to noise ratio is relatively poor, and the scan was repeated with a longer time for $La_{0.2}Ba_{0.8}TiO_3$. No change of the powder XRD pattern has been observed for $La_{0.1}Ba_{0.9}TiO_3$. For $La_{0.2}Ba_{0.8}TiO_3$ no new peaks have been detected, the left shoulder of the peak at 32° is not visible anymore and the peak splitting is smaller. This change of the XRD pattern may be due to allowing diffusion of the La ion resulting of a better homogeneity of the chemical composition. However the time of the TGA run was "short" and the powder not pressed before the TGA, in that condition a diffusion of the La ion is not probable. The other possibility is a change of the crystal structure because of the O absorbtion. Because the perovskite phase is the only observed after the TGA, it is concluded that the weight increase during the TGA is only because of the O absorbtion in consequence of the "reversal" of the doping mechanisme in eq 3 (page 20), 4 (page 21), and 7 (page 20). These results are comparable to those obtained by Lu et al, the values of the weight gain increased with the doping content while the electrical conductivity at 473K reached the maximum for x=0.175 for the $La_xSr_{1-3x/2}TiO_3$ system [100].

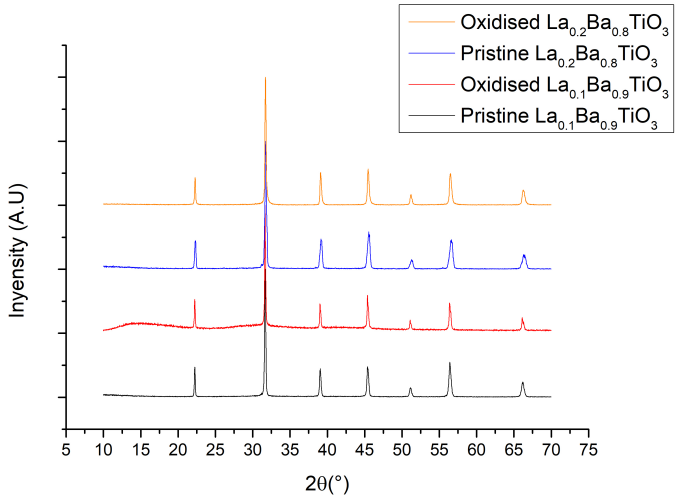


Figure 4.16: Powder XRD patterns of the powder after the TGA run in air at 1250°C, XRD scan of 30 minutes for $La_{0.2}Ba_{0.8}TiO_3$, XRD scan of 6 minutes for $La_{0.1}Ba_{0.9}TiO_3$.

Density The influence of the main SPS parameters on the density was observed for the $La_{0.2}Ba_{0.8}TiO_3$ composition. The theoretical density was defined from the lattice parameters calculated from the XRD patterns. The influence of the O vacancy on the mass was neglected. The densities were measured by direct measurement of the masses and volumes with a precision balance and a caliper. Respectively, Figures 4.17, 4.18, 4.19, and 4.20 are the influence of the temperature, applied pressure, cooling rate and heating rate on the final density of the sample for $La_{0.2}Ba_{0.8}TiO_3$. The sample sintered with a cooling rate of 200°C per minute was less dense than the other (Figure 4.19) but no significant difference was observed between the samples with the cooling rates of $50°C.min^{-1}$ and $100°C.min^{-1}$. With a higher cooling rate, the time during the sample is at a high temperature is longer, leading to a higher sintering time. The heating rate, the cooling rate, and the applied pressure did not have a significant influence on the final density of the samples. The temperature played an important role, the higher the temperature of sintering, the higher the density. Densities were higher than 90% from 1350°C. A higher density would result in higher electrical conductivity. However, we concluded that the difference in density induced by a higher SPS sintering temperature was not drastic enough to generate an important increase in the electrical conductivity.

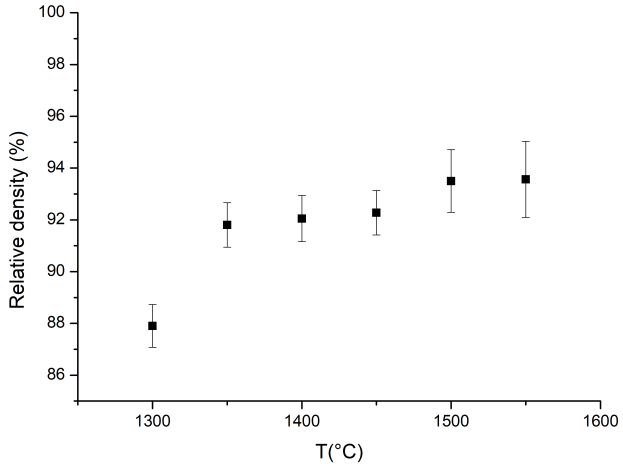


Figure 4.17: Relative density of the SPS sintered pellets for different sintering temperatures for $La_{0.2}Ba_{0.8}TiO_3$ under vacuum, and an applied pressure of 40 MPa.

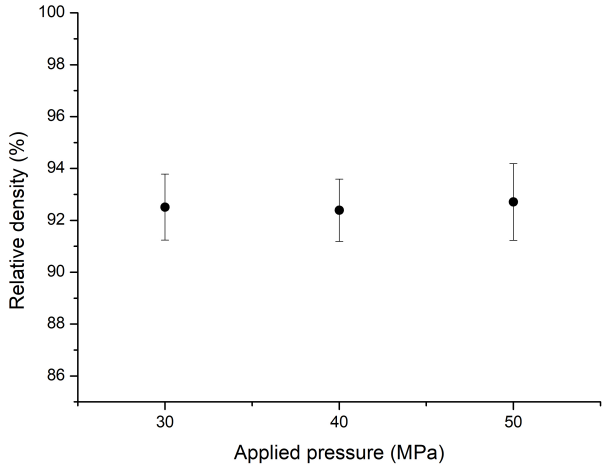


Figure 4.18: Relative density of the SPS sintered pellets for different applied pressures for $La_{0.2}Ba_{0.8}TiO_3$ at 1400°C under vacuum.

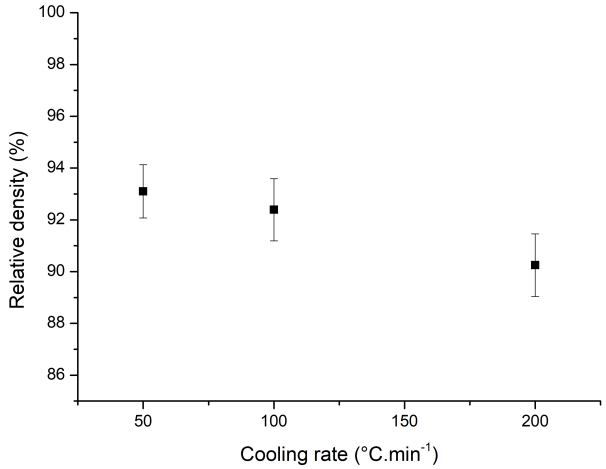


Figure 4.19: Relative density of the SPS sintered pellets for different cooling rates for $La_{0.2}Ba_{0.8}TiO_3$ at 1400°C under vacuum, with an applied pressure of 40 MPa.

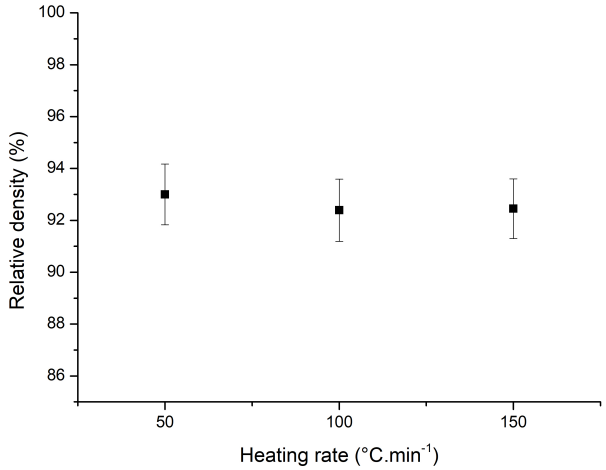


Figure 4.20: Relative density of the SPS sintered pellets for different heating rates for $La_{0.2}Ba_{0.8}TiO_3$ at 1400°C under vacuum, with an applied pressure of 40 MPa.

Figure 4.21 is the plot of the relative density for the samples $La_xBa_{1-x}TiO_3$ sintered by SPS at 1450°C. The proportion of La was a determinant of the sinterability of the material. Samples at the lower end of the La content was more than 90% dense. From $La_{0.4}Ba_{0.6}TiO_3$, the relative densities of the samples were below 90%. TGA data showed that the O vacancy concentration was proportional to the La content (Figure 4.13) and the underestimations of the relative masse of the samples were proportional to the La content (oxygen vacancies were neglected to calculate the theoretical mass from the XRD patterns). However, the drop in the density with the La concentration was much higher than the effect of the O loss. So, the decrease in the measured relative density was caused by higher porosity. An increase in the porosity with the La content was consistent with the SEM observations (Figure 4.22).

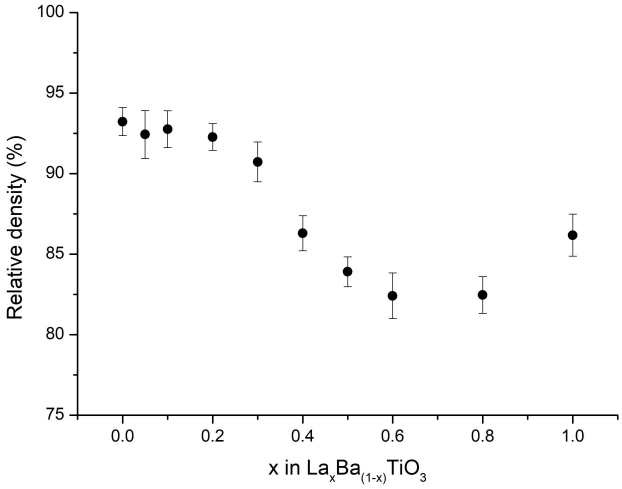
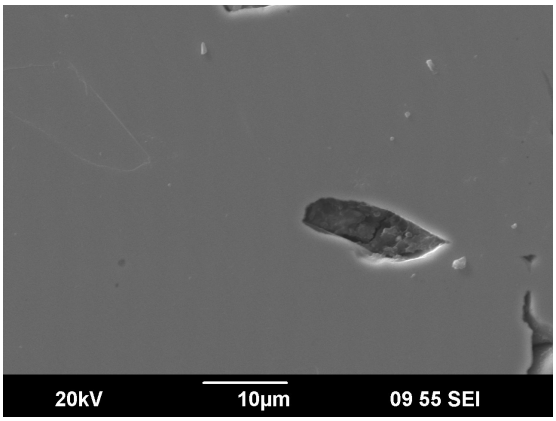


Figure 4.21: Relative density of the samples $La_xBa_{1-x}TiO_3$ produced by arc melting in argon and sintered by SPS at different temperature in high vacuum (diffusion pump) for 10 minutes with a heating and cooling rate of 100°C per minute and an apllied pressure of 40MPa.

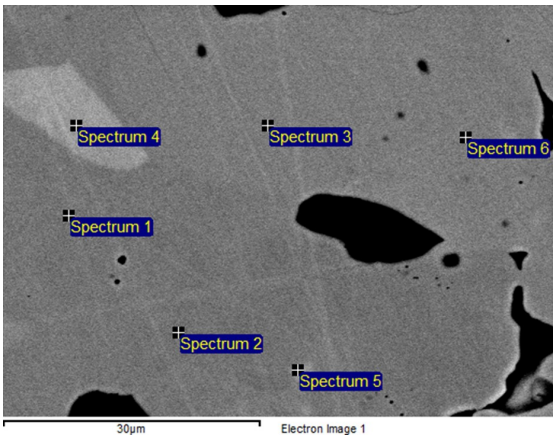
SEM Figures 4.22 are a selection of secondary electron images and backscattered electron images with the EDX target positions of the $La_xBa_{1-x}TiO_3$ SPS sintered pellets. Table 4.1 shows the EDX results. Figure 4.23 is an EDX spectra of the sample $La_{0.2}Ba_{0.8}TiO_3$ with the labelled X-ray energy of the Ba, La, and Ti. The overlap between the X-ray energy of the three elements is important,

such that the information of the element quantification should be considered with caution. Unlike the samples after the arc melting, the microstructure of the sample were similar to a conventional sintering with a relative homogeneous microstructure after the SPS sintering [192]. The number of pores and their sizes tended to increase with the La content, suggesting a higher porosity, which is in agreement with the measured density (Figure 4.21). The relatively high porosity of the samples with a high concentration of La was highlighted in Figure 4.22i. No difference in contrast was observed for the undoped $BaTiO_3$ in backscattered mode (Figure 4.22n) showing a dense single phase material. However, the surface of the doped samples showed zones of different contrast. For example, in Figure 4.22d (sample $La_{0.2}Ba_{0.8}TiO_3$), a large dark area was visible. Note the very dark area around the target five was likely to be an artefact as the result of the spectrum five in Table 4.1b was not sufficiently different from the others darkened areas. Additionally, two unidentified objects were present on the Figure 4.22c at the same positions. These may be particles deposited after the carbon coating, resulting in a charge accumulation that disturbed the electron beam around these particles. It could also be an artefact from melted epoxy, epoxy melted by the electron flow were visible through the optical microscope, then melted epoxy could be present in Figure 4.22l. A brighter zone was detected for the sample $La_{0.1}Ba_{0.1}TiO_3$, (Figures 4.22a and 4.22b) the EDX detected La, but it is likely to be a La-poor phase, possibly undoped $BaTiO_3$ which is compatible with the XRD observations. It appeared that the central members of the series had less areas with different contrast. This may indicates a higher homogeneity of the chemical composition for these samples.

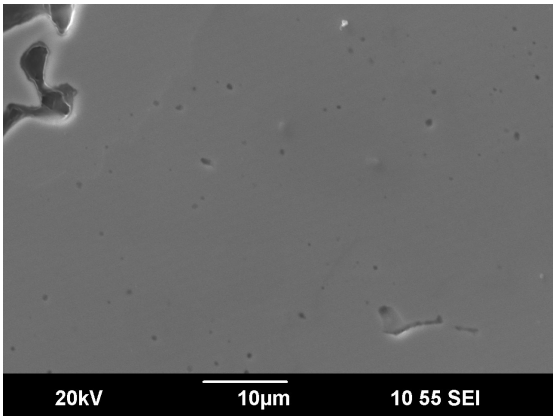
All the EDX analyses showed a Ba concentration higher than 50 atm%, which was very likely to be an overestimation as B-site vacancies in undoped $BaTiO_3$ is not reported in the literature. For all the targets, the three elements were detected, and for each sample, the concentration of Ba was in the same order of magnitude. That indicates the formation of the perovskite phase at all the analyzed zones, which is in agreement with the XRD data.



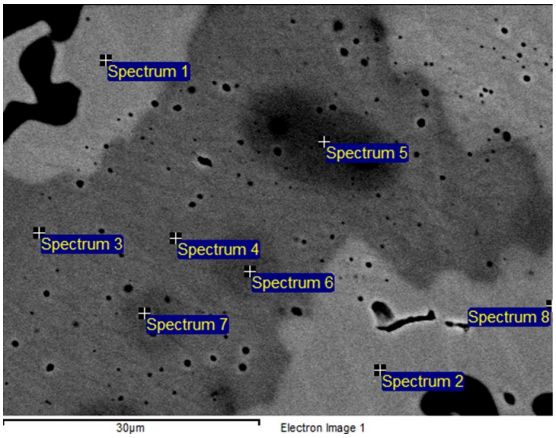
(a) $La_{0.1}Ba_{0.9}TiO_3$, secondary electron mode.



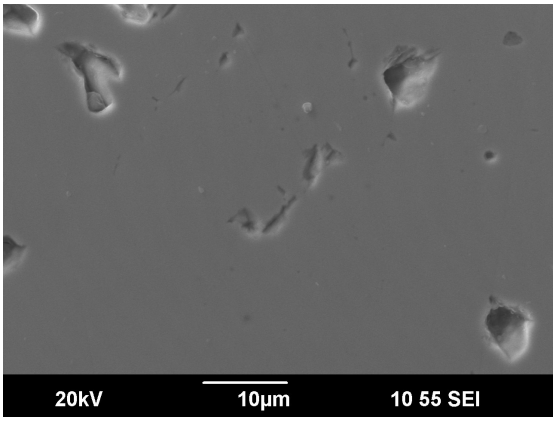
(b) $La_{0.1}Ba_{0.9}TiO_3$, backscattered electron mode with EDX targets, results in Table 4.1a.



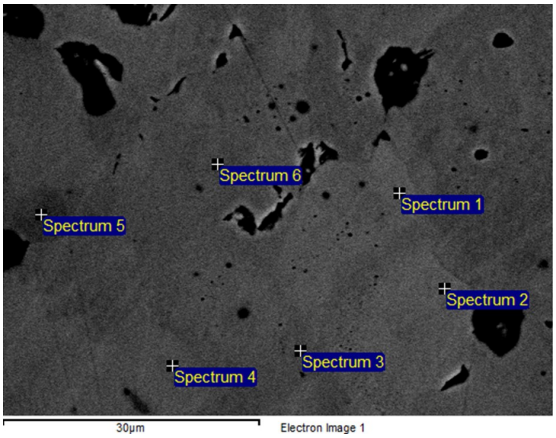
(c) $La_{0.2}Ba_{0.8}TiO_3$, secondary electron mode.



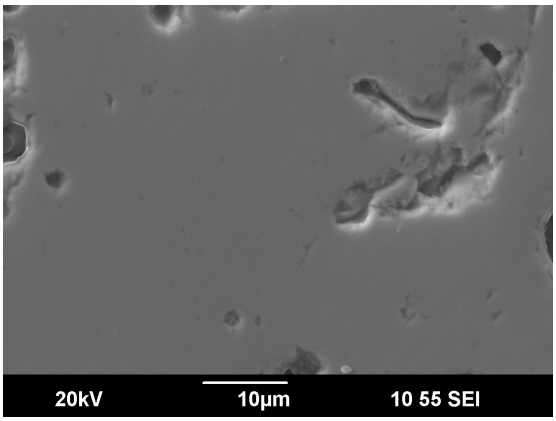
(d) $La_{0.2}Ba_{0.8}TiO_3$, backscattered electron mode with EDX targets, results in Table 4.1b.



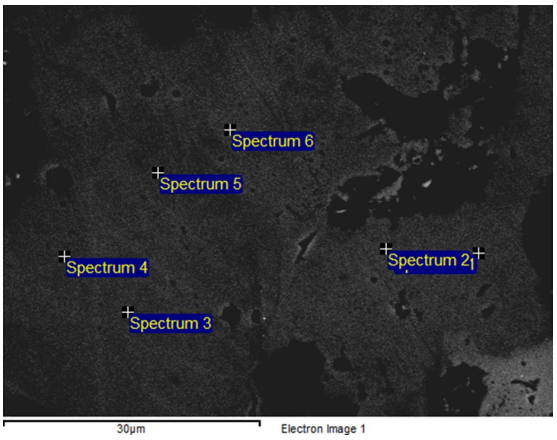
(e) $La_{0.3}Ba_{0.7}TiO_3$, secondary electron mode.



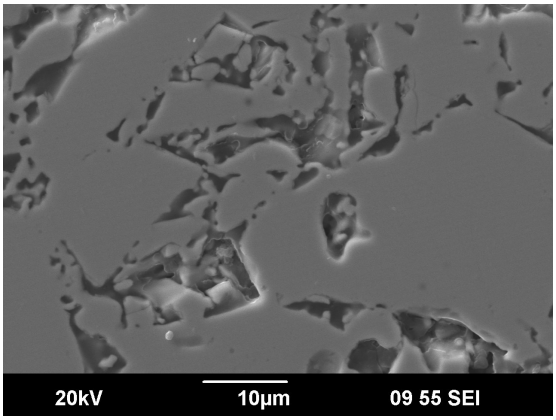
(f) $La_{0.3}Ba_{0.7}TiO_3$, backscattered electron mode with EDX targets, results in Table 4.1c.



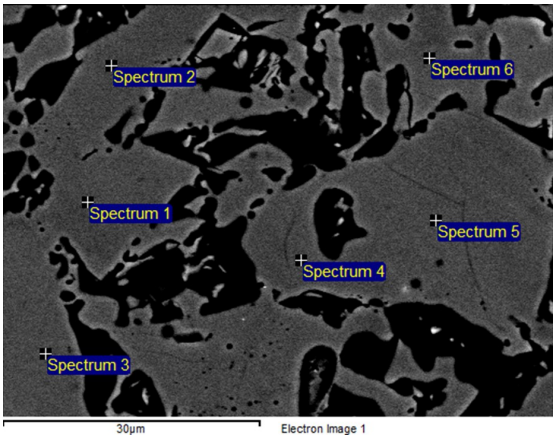
(g) $La_{0.4}Ba_{0.6}TiO_3$, secondary electron mode.



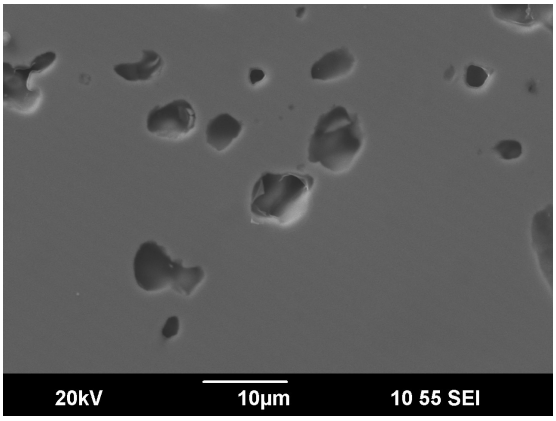
(h) $La_{0.4}Ba_{0.6}TiO_3$, backscattered electron mode with EDX targets, results in Table 4.1d.



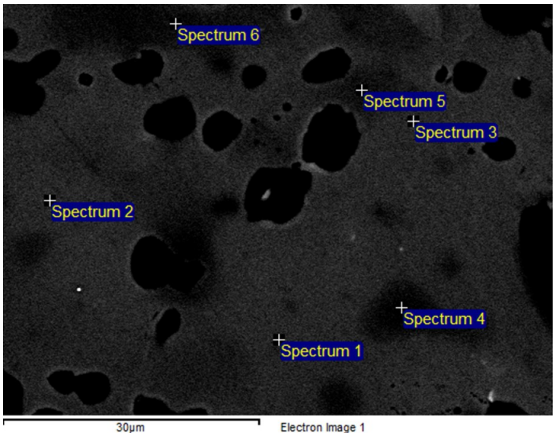
(i) $La_{0.6}Ba_{0.4}TiO_3$, secondary electron mode.



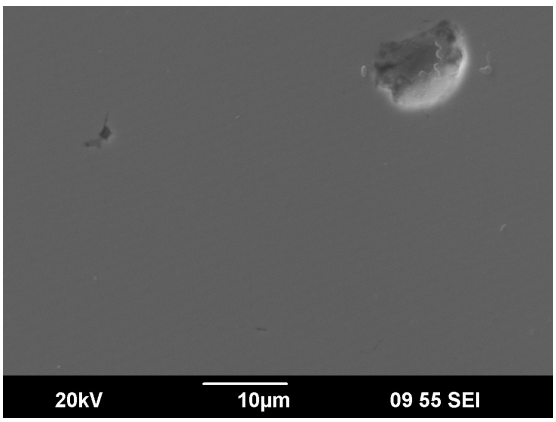
(j) $La_{0.6}Ba_{0.4}TiO_3$, backscattered electron mode with EDX targets, results in Table 4.1e.



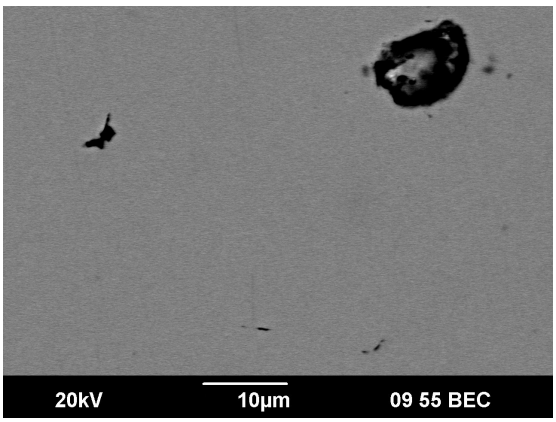
(k) $La_{0.8}Ba_{0.2}TiO_3$, secondary electron mode.



(l) $La_{0.8}Ba_{0.2}TiO_3$, backscattered electron mode with EDX targets, results in Table 4.1f.



(m) $BaTiO_3$, secondary electron mode.



(n) $BaTiO_3$, backscattered electron mode.

Figure 4.22: SEM images of $La_xBa_{1-x}TiO_3$ melted in argon and sintered by SPS at 1450°C in high vacuum (diffusion pump), with a heating and cooling rate of 100°C per minute and an applied pressure of 40MPa.

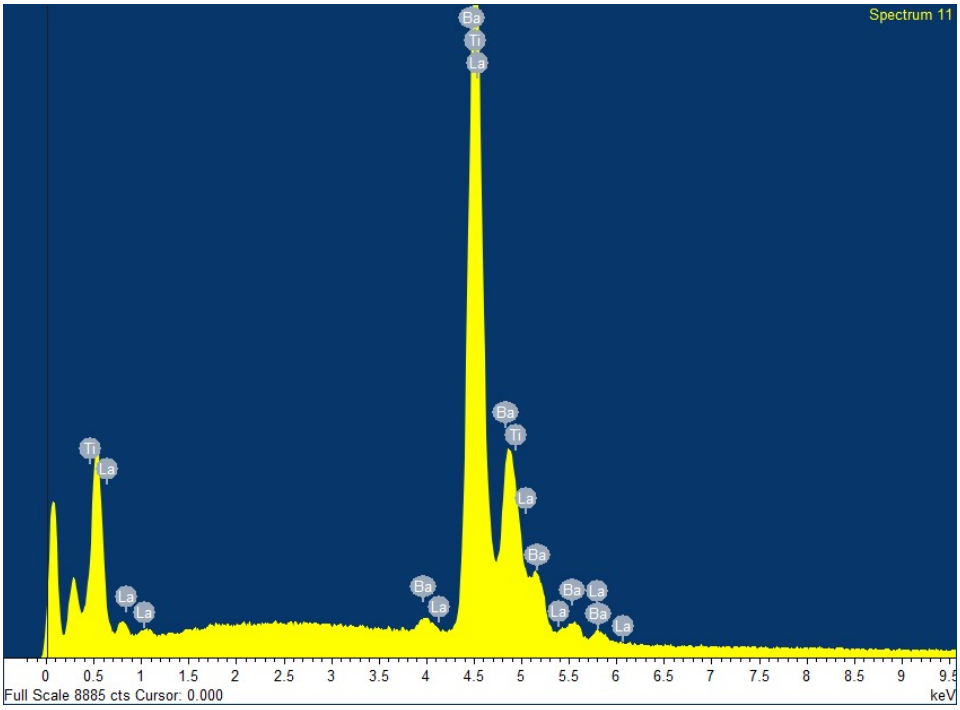


Figure 4.23: EDX spectra of $La_{0.2}Ba_{0.8}TiO_3$ sintered by SPS at 1450°C in high vacuum (diffusion pump) for 10 minutes with a heating and cooling rate of 100°C/min and an applied pressure of 40 MPa of the powder synthesized by arc melting in argon.

Table 4.1: EDX targets results of Figures 4.22.

(a) EDX results of $La_{0.1}Ba_{0.9}TiO_3$ in atomic percent, targets position in Figure 4.22b.

Target	Ti	Ba	La	La + Ba
1	56.9	40.4	2.7	43.1
2	56.3	40.0	3.7	43.7
3	57.0	40.4	2.6	43.0
4	57.5	40.4	2.1	42.5
5	55.0	41.9	3.1	45.0
6	56.4	40.5	3.1	43.6
Theorectical	50	45	5	50

(b) EDX results of $La_{0.2}Ba_{0.8}TiO_3$ in atomic percent, targets position in Figure 4.22d.

Target	Ti	Ba	La	La + Ba
1	55.5	38.6	5.9	44.5
2	57.2	39.8	3.0	42.8
3	54.7	33.6	11.7	45.3
4	54.1	36.3	9.7	46.0
5	56.2	32.1	11.7	43.8
6	54.3	38.7	7.0	45.7
7	56.0	32.4	11.6	44.0
8	56.1	34.8	9.2	44.0
Theorectical	50	40	10	50

(c) EDX results of $La_{0.3}Ba_{0.7}TiO_3$ in atomic percent, targets position in Figure 4.22f.

Target	Ti	Ba	La	La + Ba
1	54.7	19.1	26.2	45.3
2	54.1	22.9	23.0	45.9
3	55.4	31.3	13.3	44.6
4	54.0	21.7	24.4	46.1
5	56.0	33.4	10.6	44.0
6	56.7	34.0	9.3	43.3
Theoretical	50	35	15	50

(d) EDX results of $La_{0.4}Ba_{0.6}TiO_3$ in atomic percent, targets position in Figure 4.22h.

Target	Ti	Ba	La	La + Ba
1	53.5	20.0	26.5	46.5
2	54.3	19.0	26.7	45.7
3	53.7	23.7	22.6	46.3
4	51.3	23.7	25.0	48.7
5	55.0	28.1	16.9	45.0
6	53.9	22.0	24.1	46.1
Theoretical	50	30	20	50

(e) EDX results of $La_{0.6}Ba_{0.4}TiO_3$ in atomic percent, targets position in Figure 4.22j.

Target	Ti	Ba	La	La + Ba
1	54.3	17.3	28.4	45.7
2	54.1	19.7	26.2	45.9
3	53.6	14.8	31.6	46.4
4	51.7	19.3	29.0	48.3
5	54.5	15.4	30.2	45.6
6	54.8	19.5	25.7	45.2
Theoretical	50	20	30	50

(f) EDX results of $La_{0.8}Ba_{0.2}TiO_3$ in atomic percent, targets position in Figure 4.22l.

Target	Ti	Ba	La	La + Ba
1	52.7	8.5	38.8	47.3
2	53.5	9.5	37.1	46.6
3	53.6	7.4	39.0	46.4
4	52.0	9.6	38.5	48.1
5	53.4	7.5	39.2	46.7
6	51.5	8.0	40.5	48.5
Theoretical	50	10	40	50

EPMA, samples after arc melting Figures 4.24 to 4.29 and 10.1 to 10.11 (in appendice from page 180) are the elemental maps and the EPMA backscattered images of the arc melted $La_xBa_{1-x}TiO_3$ samples. The location of the point elemental analysis were manually located. Tables 4.2 to 4.4 and 10.1 to 10.5 (in appendice) are the results of the WDX. These analyses were conducted during early experiments without the use of a glove box throughout the entire procedure and when Ti metal was used as raw materials to produce the $LaTiO_3$. The polished pieces of ceramics were the remaining parts of the samples used for other characterisations. However, this resulted in the samples not coming from comparable areas of the melted samples, so the resultant images could not be used to compare the morphology of each sample. The morphologies greatly varied from those obtained through conventional sintering, likely due to the result of the very fast cooling rate induced by the arc melting process. All of the samples contained some features that were larger than 100 µm. Such features can lead to a slight variation of incidence angle from the electron beam. This can lead to a variation in contrast of the backscattered images as the EPMA is much more sensitive to these angles than a SEM.

The O contents were directly measured and the values were not normalized, except for tables 10.3 (page 183) and 10.5 (page 187). For these tables, the element values in atomic % were normalised (sum of the atomic values set to 100%) but the total values are in weight % and not normalised (the file with the value in atm % was corrupted). The sums of the elements give informations about the precision of the analysis of each point; a value too far away from 100 would indicate inaccurate data. Here, most of the points have a sum = 100 ± 2% and no points overpass 100 ± 3%. O is a light element that is difficult to quantify even with a WDX, the samples would be expected to be reduced during the synthesis, so the average O concentration should be lower than the theoretical (60%). However, all of the points were found to be greater than 60%. All of the samples can be split in three groups, the first being $0.1 \leq x \leq 0.3$; the chemical composition of the phases were not the same. The second being $0.3 \leq x \leq 0.7$; one dominant main phase with homogeneous chemical compositions. The last being $x > 0.7$; La-rich phases were observed as small dots or lines. An exemplar sample from each of these groups will be further elaborated on below. The data of the others composition are in appendice.

Some of the maps were based on areas of interest (for example, the presence of secondary phases) and are not fully representative. However, it does provide some qualitative informations on the chemical composition of areas where it was not possible to process a point analysis. Figure 4.24 are the elemental maps of O, Ti, Ba, and La all in weight%. The maps of O and Ti show a homogeneous distribution of these elements on all of the surfaces of the sample except at the pores which give rise to incorrect values. The map of Ba shows areas with different concentrations of Ba. The surfaces are coloured in red around 60W%, yellow around 50W%, and green around 40W%. The red areas on the Ba map coincided with the brighter zone on the backscattered image. The map of the La shows areas with high differences of concentration, red-magenta with a concentration around 13W%, blue-green around 6W%, and dark blue with no detection of La. The blue areas coincide with the bright white areas on the backscattered image. It was concluded that these areas were undoped $BaTiO_3$. On the elemental map, a lack of Ba was compensated by a higher concentration of La and vice versa.

Figure 4.25 is the backscattered EPMA images of $La_{0.1}Ba_{0.9}TiO_3$ with the targets of the point analysis; the results of the analysis are in Table 4.2. No La was observed for the points 25, 26, 27, and 28 in Figure 4.25; the bright areas should correspond to phases with an absence of La. Darker areas seemed to contain La in a few %, such as 1.71% for target 19. However, it is not possible to use the colour contrast of the image to estimate the amount of La. This is because a large part of the contrast came from the small differences of angles between the gun, the beamed area, and the detector. Due to this, a smaller proportion of the contrast came from the chemical composition when compared to a SEM. For example, the points 19 and 23 demonstrated there was a large contrast on the backscattered image, but the chemical compositions were very close, La : 1.71% vs 1.70% Ba : 16.71% vs 16.62% Ti : 19.21% vs 19.00% O : 62.37% vs 62.67%. This effect was observable for all of the images, so no qualitative interpretation of a possible difference of atomic composition between two areas with a different contrast can be performed without a chemical analysis. The variation in the concentration of La was high compared to the theoretical value (2%), from a total absence of La, such as points 28, to more than 5% for point 29. The variation of the Ba was relatively large as well, from 13% for points 29 to 19% for point 28. The concentration of both La and Ba, which

are in theory the elements at the A-site of the required perovskite structure, was stable between 18% and 19% at all of the points. While the concentrations of La and Ba varied, the concentration of Ti was consistent for all points as all of them are between 19% and 20 %. The concentration of O was also very stable, between 61% and 63% for all of the points.

Table 4.2: Element composition of several points of $La_{0.1}Ba_{0.9}TiO_3$ by EPMA of Figure 4.25, concentration in atomic %.

Target	La	Ba	La+Ba	Ti	O	Total
16	2.08	16.28	18.36	19.21	62.42	100.25
17	3.69	14.80	18.49	19.06	62.45	101.10
18	2.18	16.45	18.63	19.17	62.20	100.17
19	1.71	16.71	18.42	19.21	62.37	99.98
20	1.57	16.92	18.49	19.01	62.50	100.93
21	0.68	17.71	18.39	19.20	62.41	99.84
22	1.02	17.46	18.49	19.22	62.29	100.03
23	1.70	16.62	18.33	19.00	62.67	99.98
24	3.78	14.69	18.47	19.31	62.22	99.88
25	0.00	18.19	18.19	19.00	62.81	100.50
26	0.00	18.50	18.50	19.27	62.23	100
27	0.00	18.29	18.29	19.23	62.48	99.89
28	0.00	19.05	19.05	19.47	61.48	99.71
29	5.39	13.12	18.51	19.12	62.37	101.13
Theoritical	2	18	20	20	60	100

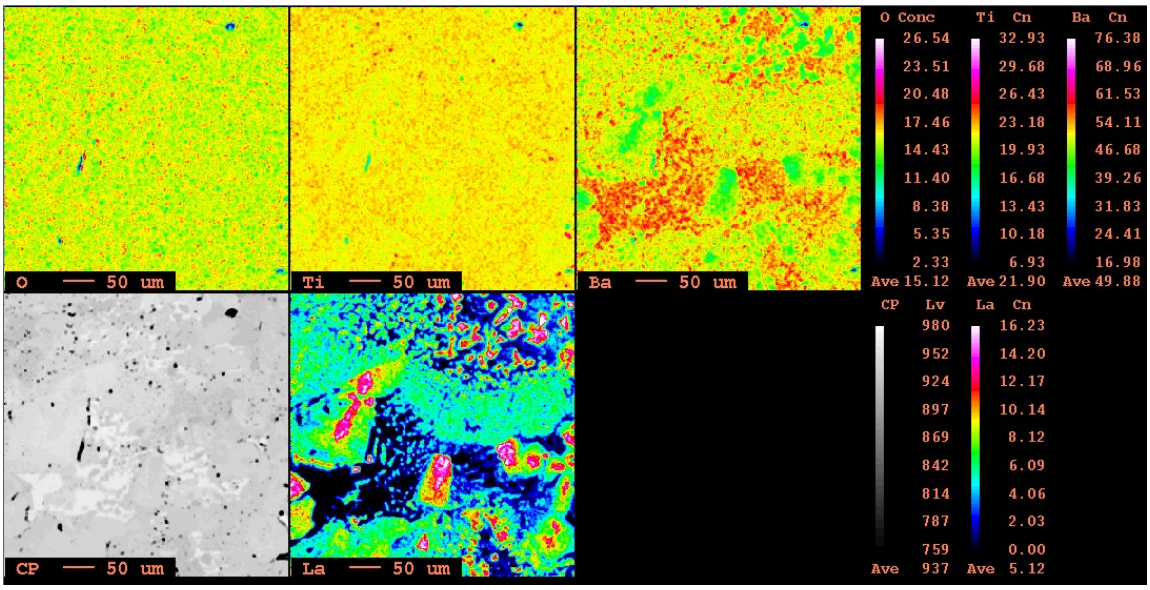


Figure 4.24: WDX element map fox $La_{0.1}Ba_{0.9}TiO_3$, concentration in weight%.

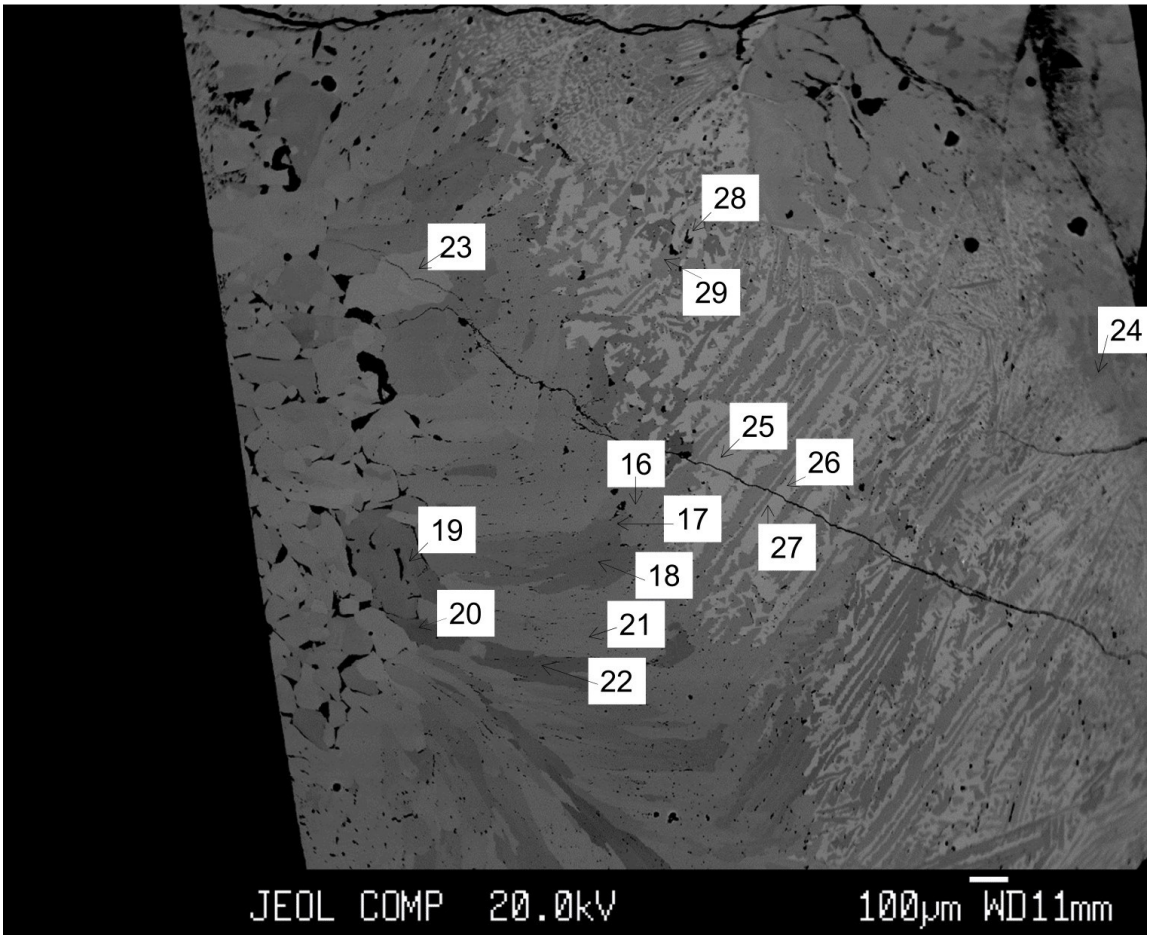


Figure 4.25: EPMA backscattered electrons image of $La_{0.1}Ba_{0.9}TiO_3$, element composition in Table 4.2.

Figure 4.27 is a backscattered image of the sample $La_{0.4}Ba_{0.6}TiO_3$ with the targets chosen randomly, the results of the element points analysis are given in table 4.3. We can identify three kinds of morphologies. Big structures that were dominant at the upper left of the image, medium size structures with a smaller width, and those that are separated by thin white phases. The element compositions of the first two are all similar and in agreement with the theoretical composition, with an amount of La always being slightly higher than the theoretical and an amount of Ba always being slightly lower than the theoretical. For example, La : 8.77% Ba : 9.87% Ti : 19.22% O : 62.14% for target one, when the theoretical is La : 8% Ba : 12% Ti : 20% O : 60%. The chemical compositions of these white phases were Ba-rich with an absence of La according to the element point analysis, e.g. target 10 : La : 0% Ba : 18.77% Ti : 19.5% and O : 61.73%. For all points analysed, the sum of the La and the Ba were very similar, between 18% and 19%, which is consistent with the theoretical value.

The elemental maps of this sample are showed in Figure 4.26. The spot was chosen to observe the smaller structures with some white phases between them. The maps of the O and Ba were both homogeneous and coloured in green-yellow which gives values around 15W% for O and approximately 22W% for Ba compared with the respective theoretical values : 20.52W% and 20.47W%. The Ba map shows that the white phases, coloured in red, were rich in Ba with a concentration around 60W% which is the theoretical value of the sum of the La and Ba in weight percent. The medium-sized structure was mainly in dark blue around 22W% with a transition in blue-cyan-green toward the white phases. This gradient of the concentration of Ba is not visible on the backscattered image. The map of the La showed the quasi identical of what would be the complementary (opposite) colours of the Ba's map; the white phases were coloured in dark blue, which corresponds to an absence of La, and the medium-sized structure was mainly coloured in red which is an approximate value of 32W%.

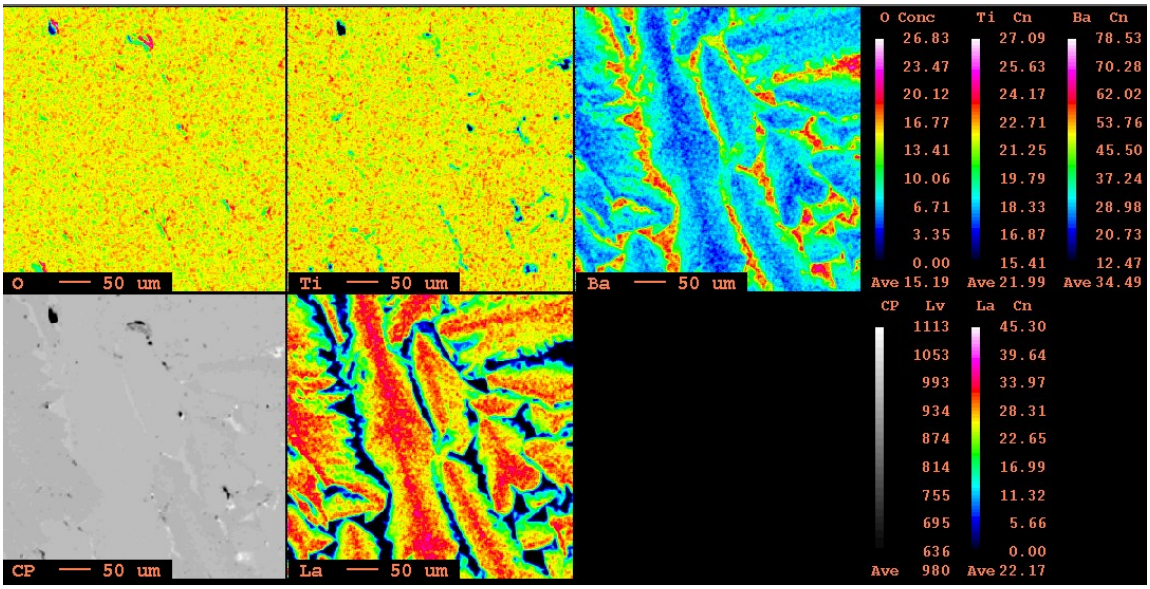


Figure 4.26: WDX element map of $La_{0.4}Ba_{0.6}TiO_3$, concentration in weight%.

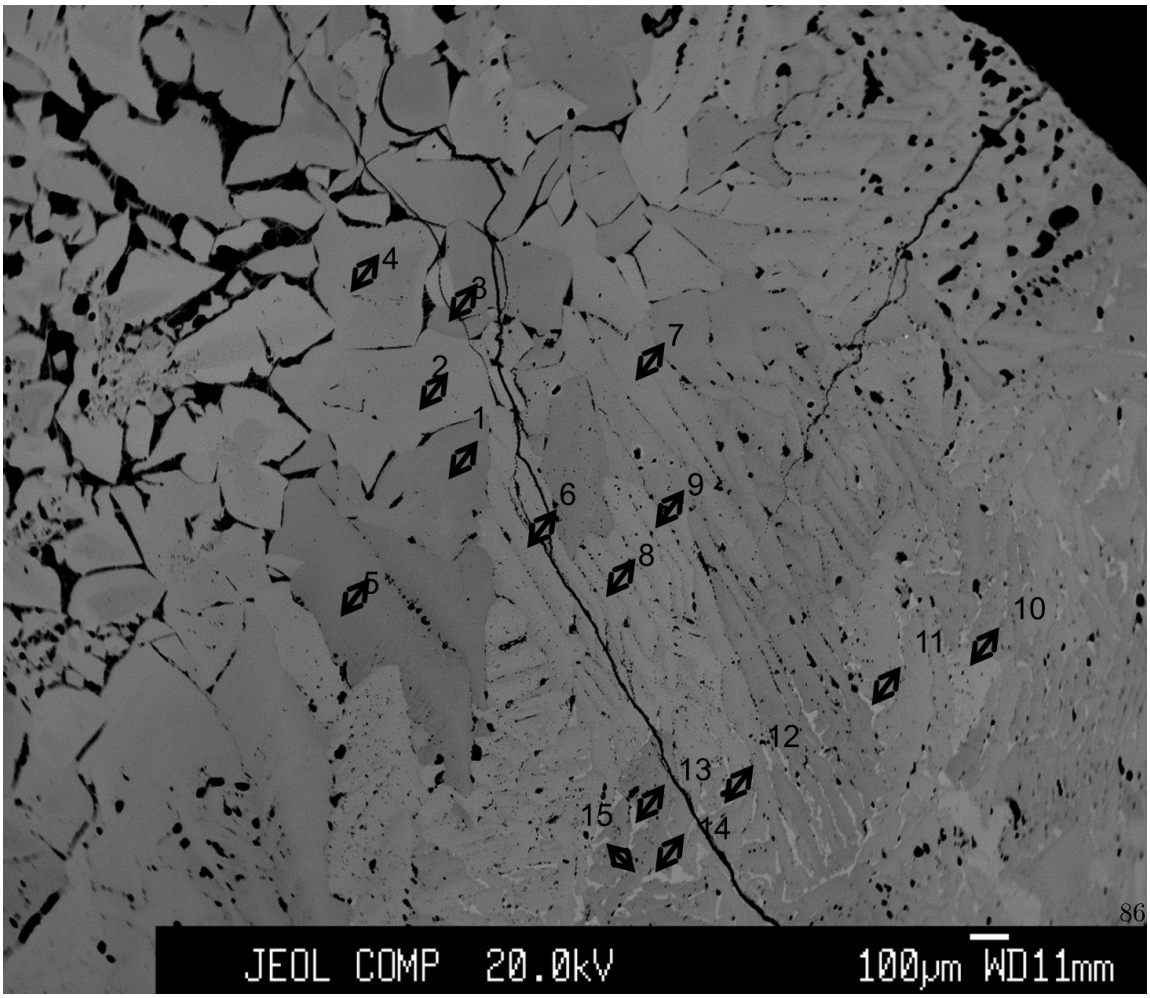


Figure 4.27: EPMA backscattered electrons image of $La_{0.4}Ba_{0.6}TiO_3$, element composition of the points in Table 4.3.

Table 4.3: Element composition of several points of $La_{0.4}Ba_{0.6}TiO_3$ by EPMA of Figure 4.27, concentration in atomic%.

Target	La(%)	Ba(%)	La+Ba(%)	Ti(%)	O(%)	Total(%)
1	8.77	9.87	18.63	19.22	62.14	101.06
2	8.27	10.35	18.62	18.92	62.46	101.50
3	8.09	10.57	18.66	18.74	62.60	101.85
4	7.82	11.03	18.85	18.79	62.37	101.73
5	8.81	9.97	18.79	19.36	61.85	101.60
6	9.11	9.62	18.73	19.21	62.05	101.29
7	8.67	10.31	18.99	19.21	61.80	101.37
8	10.01	8.94	18.96	19.28	61.76	101.11
9	9.40	9.32	18.72	19.16	62.12	101.83
10	10.88	7.89	18.77	19.17	62.06	101.24
11	0.00	18.77	18.77	19.5	61.73	100.88
12	0.00	18.87	18.87	19.63	61.50	100.54
13	0.00	18.36	18.36	19.24	62.39	100.74
14	0.00	19.01	19.01	19.09	61.89	98.93
15	9.11	9.72	18.83	19.19	61.98	101.57
Theoritical	8	12	20	20	60	100

Backscattered image of the sample $La_{0.7}Ba_{0.3}TiO_3$ is given in Figure 4.28, with the results of the analysis in table 4.4. White dots and lines located at the grain boundaries were visible. Unfortunately, it was not possible to do a chemical analysis on these points because their widths are too small to be targeted. The points for chemical analysis were randomly selected; the results are given in table 4.4. All points showed very similar chemical compositions such as La : 13% Ba : 5.5%, Ti : 19.1% O : 62.3% for target number 33, which is in agreement with the theoretical value which is La : 14% Ba : 16% Ti : 20% and O : 60%. This suggests that a main phase was present for most of the surface of the sample with a probable second phase that was not possible to analyse by point analysis.

The elemental maps of $La_{0.7}Ba_{0.3}TiO_3$ is shown in Figure 4.29. The spot was chosen to analyse for the white phase visible on the backscattered image. A main phase and a brighter white second phase with nets like patterns (grain boundaries) were visible. The concentration of La in the main phase coloured in green seemed to be homogenous around 54W%, but the concentration in the second phase coloured in red-magenta was higher, being approximately 67W%. The concentration of Ba is slightly variable in the main phases coloured in green-red, being approximately 4W% to

Table 4.4: Element composition of several points of $La_{0.7}Ba_{0.3}TiO_3$ by EPMA of Figure 4.29. Concentration in atomic%.

Target	La	Ba	La+Ba	Ti	O	Total
30	13.28	5.48	18.76	19.14	62.10	102.47
31	12.48	6.28	18.76	19.30	61.94	101.66
32	13.01	5.40	18.41	19.12	62.47	101.86
33	13.00	5.51	18.51	19.12	62.37	101.95
34	13.33	5.42	18.75	19.03	62.22	101.84
35	13.61	5.22	18.82	19.22	61.95	102.43
36	13.63	5.47	19.11	19.49	61.40	101.64
37	13.20	5.43	18.63	19.13	62.24	102.52
38	13.54	5.25	18.78	19.28	61.94	101.86
39	13.34	5.46	18.80	19.27	61.93	102
Theoritical	14	16	20	20	60	100

6W%. In the second phase, coloured in dark blue, no Ba was detected. The concentration of Ti was also not homogenous, the concentration in that second phase in navy blue was about 15W%. The the atomic ratio La/Ti in the second phase was about 1.6 instead of $\frac{La+Ba}{Ti} = 1$ for the theoretical stoichiometry. The lack of Ba in the second phase cannot balance the very high amount of La to conserve the theoretical stoichiometry of the A-site of the perovskite structure. The concentration of O was homogeneous in the main phase, but not at the net like patterns. The O concentrations were higher at the zones coloured in yellow-red, that gives a concentration around 17%, instead of around 14% for the main phase areas coloured in green.

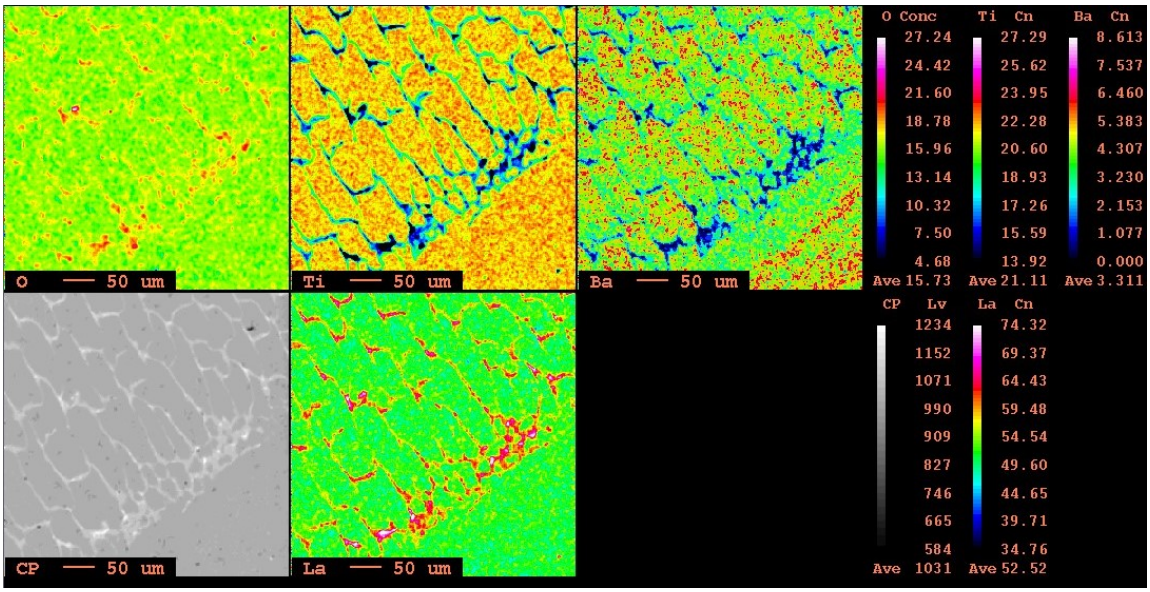


Figure 4.28: WDX element map of $La_{0.7}Ba_{0.3}TiO_3$, concentration in weight%.

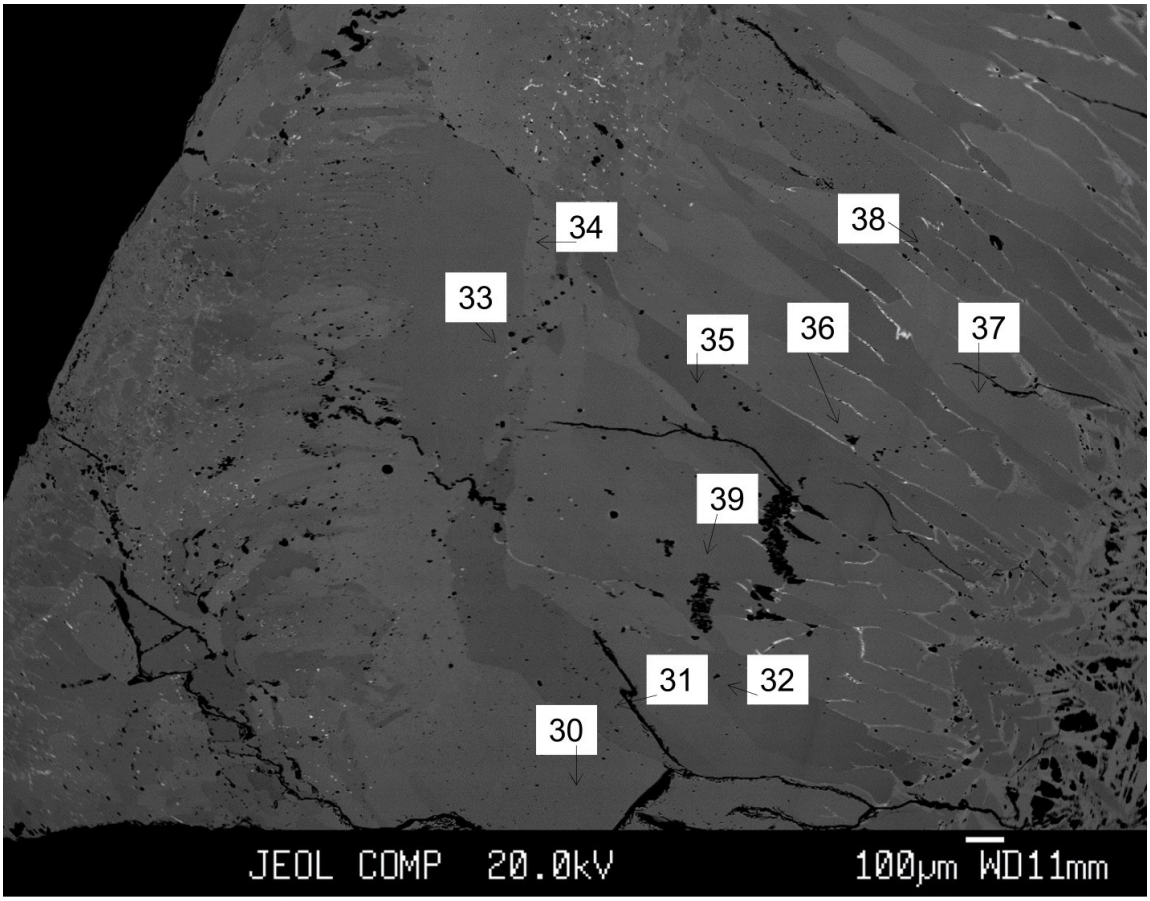


Figure 4.29: EPMA backscattered electrons image of $La_{0.7}Ba_{0.3}TiO_3$, element composition of the points in Table 4.4.

Figure 4.30 is the ternary diagram of all of the normalised elemental composition in Ba, La, and Ti except of point three of table 10.3 (page 183). The black dots represent the theoretical composition of the samples; the black line represent all of the possible compositions of the series $La_xBa_{1-x}TiO_3$ which correspond to a A/B ratio equal to one. It can be visually observed that while the samples did not have a chemical composition very close to their theoretical one, they are still centred on it, and with a few exceptions, all of the dots were close to the black line which shows that perovskite structures with a A/B ratio = 1 were dominant. The EPMA data were in agreement with the XRD data. The detection of $BaTiO_3$ explains the left shoulder of the [110] peak. Except for the small La-rich secondary phase in $La_{0.7}Ba_{0.3}TiO_3$, perovskite phases were formed for all of the compositions. As a result of the insertion of the La in the Ba site, there was an increase in the lattice volume and the distribution of the La was non-homogeneous so should have resulted in peaks broadness. The grain sizes observed on the SEM images are well over 1 μm, then the values of the crystallite calculated in the XRD part did not describe the reality, another explanation of the width of the peaks is needed.

Regarding the non-perovskite phase observed for samples with a high La content, unlike the results of Eylem et al, no BaO rich phase was observed although they also only identified cubic perovskite by XRD, and the change of the lattice constant followed the Vegard's Law [158]. We partially agree with Sunstrom et al as they identified the secondary phase as La_2O_3 [156], however, the WDX detected a small amount of Ti as well. Sunstrom et al did not use WDX but EDX to analyse the chemical composition of the La-rich phase and may not have detected the small amount of Ti. Thus it is evident that we found this unreported La-rich compound in the samples with high La content. Additionaly, we observed La-rich phase with Ti detected by SEM/EDX with measured cation chemical composition of : La 88.3% - Ti 11.7%, and La 95% - Ti 5% (data in Table 5.1f at page 128 in section 5).

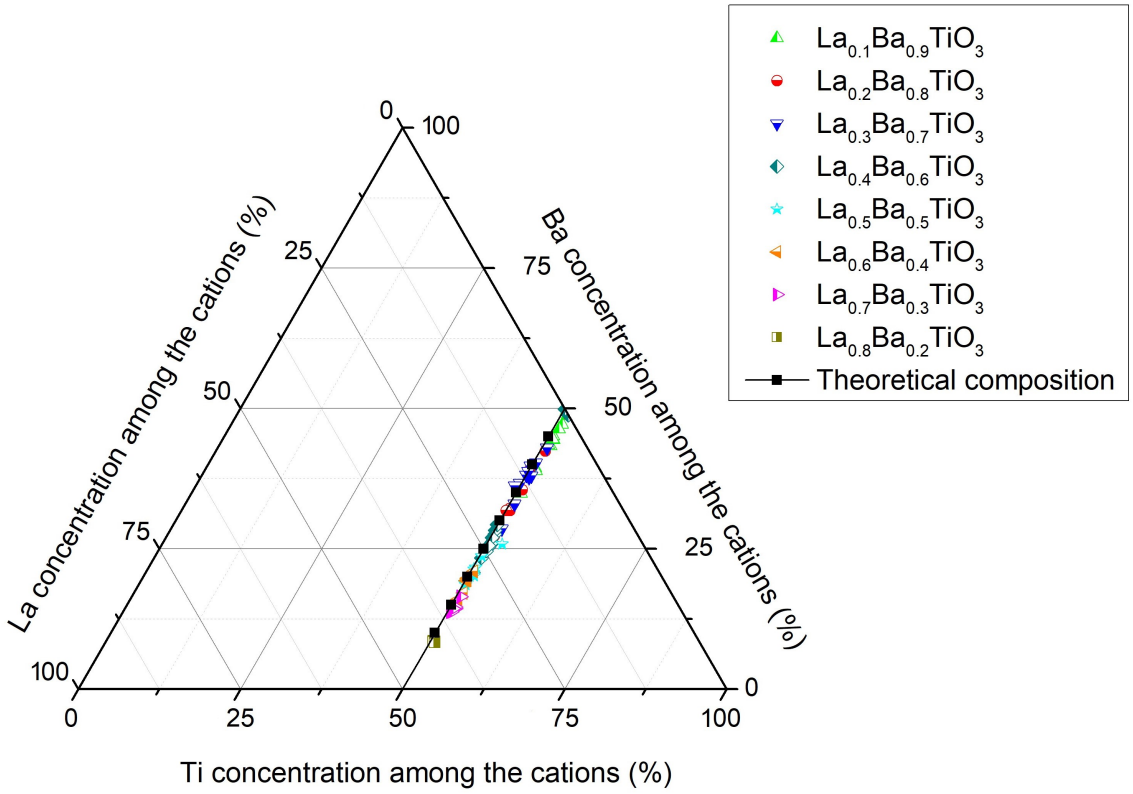
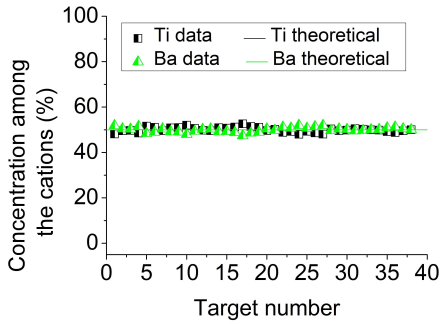
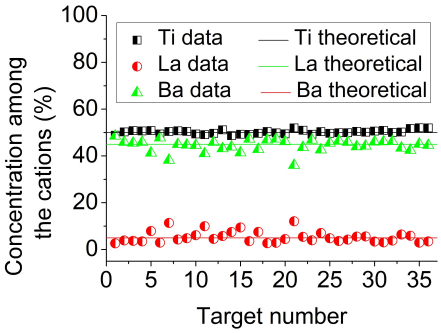


Figure 4.30: Ternary diagramme of the normalised concentration of La, Ti and Ba detected by the WDX of $La_xBa_{1-x}TiO_3$ produced by arc melting in argon.

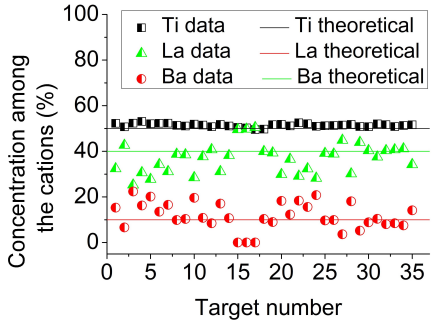
EPMA, samples after SPS Figure 4.31 is the plots of the cations' chemical composition detected by WDX with an EPMA. Figure 4.32 is the ternary plot of these chemical compositions. The grain sizes of the samples SPS sintered from the powder of the crushed arc melted samples were smaller than the sample after arc melting. As the grain sizes of the SPS sintered samples were much smaller than the samples that were only melted, the magnification of the optical microscope was not enough to do observations without difficulties, then the targets have been taken randomly with the care of avoiding holes. Still, the relatively high number of points provides extensive informations about the chemical composition of these ceramics. It has been chosen not to calculate the average chemical composition as the value would be misleading, indeed it would not take into account the size of the analysed grain and only areas away from holes have been analysed. At both ends of the series, undoped $BaTiO_3$ and undoped $LaTiO_3$ show very homogenous compositions. The sample $La_{0.8}Ba_{0.2}TiO_3$ shows very stable chemical compositions and very close to the theoretical one. It seems that $La_{0.3}Ba_{0.7}TiO_3$ and $La_{0.4}Ba_{0.6}TiO_3$ are the samples with widest range of compositions, for $La_{0.3}Ba_{0.7}TiO_3$ the minimum and maximum of La detected among the cations are respectively 11.8% and 29.1%, for $La_{0.4}Ba_{0.6}TiO_3$ they are respectively 7.5% and 26.7%. $La_{0.2}Ba_{0.8}TiO_3$ is the only sample where undoped $BaTiO_3$ has been detected. La deficient values have been detected in the other samples, as for example target one of $La_{0.2}Ba_{0.8}TiO_3$ has 5.9% of La cations concentration, and in the other way target 25 has 48.5% of La among the cations. Except for $La_{0.8}Ba_{0.2}TiO_3$ all the analysed samples show a range of cation distributions centred in their theoretical composition. All the analysed points show a (La+Ba)/Ti ratio very close to the unity as the La-rich areas are Ba poor and La-rich areas are Ba rich. For all the analysed points no undoped $LaTiO_3$ phase has been detected. These results strongly indicate that the perovskite structure was formed for all the made samples, the formation of non-perovkite phase has not been detected and if present it is in very small quantities. The insertion of the La in the Ba site, even if not done homogeneously, is very well highlighted by the results of the WDX, which suggestes that the arc melting followed by SPS is a suitable method to produce donor doped $BaTiO_3$. The crushing, milling, and short SPS sintering improved the homogeneity of the cation's distribution compared to the arc melted only samples. SPS dwelling time longer than ten minutes may improve further the homogeneity.



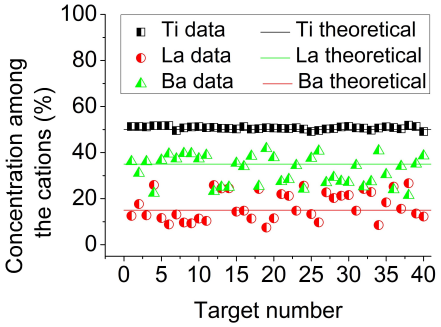
(a) $BaTiO_3$.



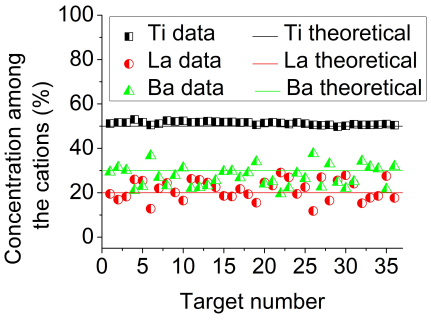
(b) $La_{0.1}Ba_{0.9}TiO_3$.



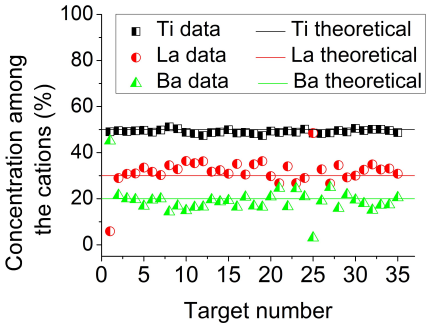
(c) $La_{0.2}Ba_{0.8}TiO_3$.



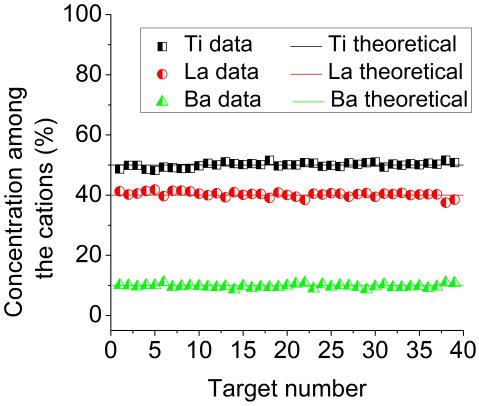
(d) $La_{0.3}Ba_{0.7}TiO_3$.



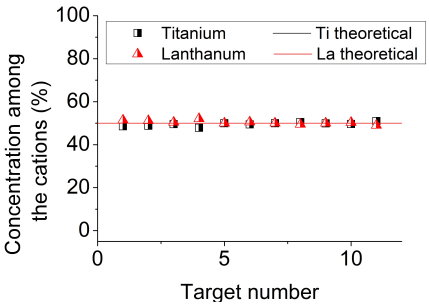
(e) $La_{0.4}Ba_{0.6}TiO_3$.



(f) $La_{0.6}Ba_{0.4}TiO_3$.



(g) $La_{0.8}Ba_{0.2}TiO_3$.



(h) $LaTiO_3$.

Figure 4.31: Normalised concentration of La, Ti and Ba detected by the WDX of $La_xBa_{1-x}TiO_3$ melted in argon and sintered by SPS at 1450°C in high vacuum (diffusion pump), with a heating and cooling rate of 100°C per minute and an applied pressure of 40MPa.

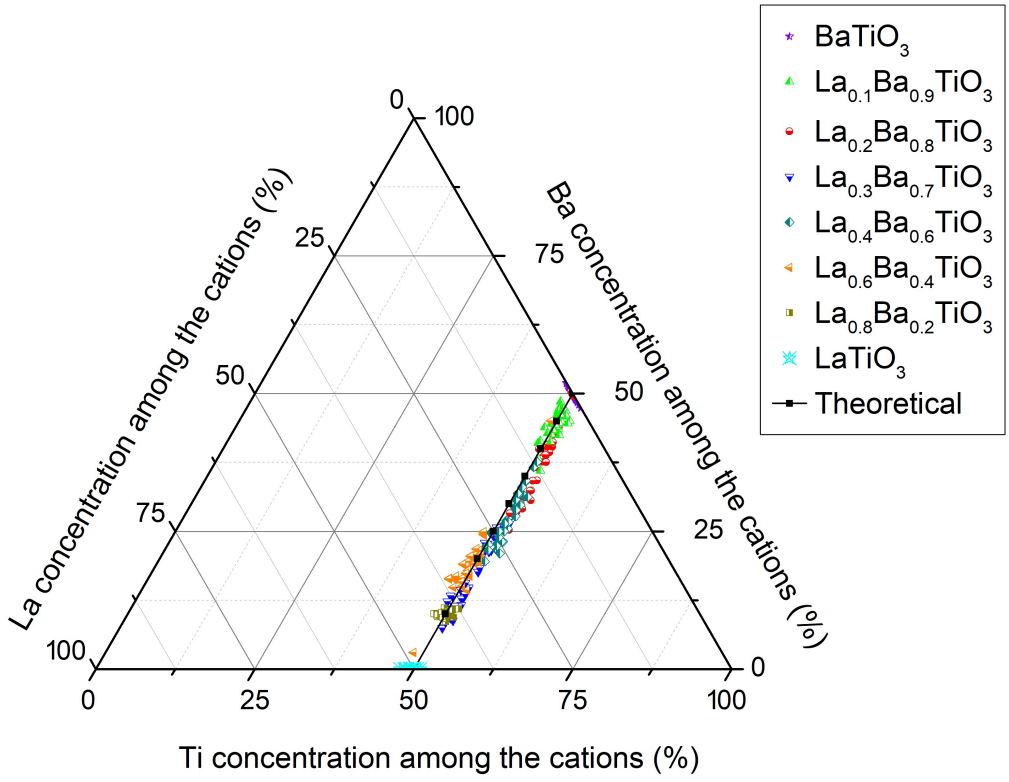


Figure 4.32: Ternary diagramme of the normalised concentration of La, Ti and Ba detected by the WDX of $La_xBa_{1-x}TiO_3$ produced by arc melting in argon and sintered by SPS at 1450°C in high vacuum (diffusion pump) for 10 minutes with a heating and cooling rate of 100°C per minute and applied pressure of 40MPa.

4.4 Evaluation of the thermoelectric performances.

Electrical properties Figure 4.33 is the plot of the electrical conductivity from RT to 800°C measured in static He atmosphere for the series $La_xBa_{1-x}TiO_3$ sintered by SPS at 1450°C, the undoped $BaTiO_3$ has been plot separately in Figure 4.34 for clarity. Until oxidised, all of the doped samples showed a metallic behaviour, with their electrical conductivity decreasing with the temperature, the undoped samples showed a semiconductor behaviour as its conductivity increased with the temperature and reached the maximum around 550°C with 17 $S.cm^{-1}$. The metallic behaviour was an intrinsic property of the materials and not because of the expected oxidation during the measurement because the drop of the conductivity was already in place before the temperature of oxidation observed with the TGA in air (Figure 4.14 in page 70). The electrical behavior could not be explained by contamination as the amount of impurity needed to be the source of the increase of conductivity would be too high to not be detected by XRD and SEM.

Previous works observed a change from insulator/semiconductor to metal from $La_{0.33}Ba_{0.67}TiO_3$ with a conductivity about 20 $S.cm^{-1}$ at RT [157, 158], whereas we observed metal conductivity for all of the doped samples and a conductivity of 3700 ± 100 $S.cm^{-1}$ at RT for $La_{0.3}Ba_{0.7}TiO_3$. For a point of comparison, La deficient $La_{0.15}Sr_{0.775}TiO_3$ at 473K was around 2335 $S.cm^{-1}$ [100] and $La_{0.08}Sr_{0.92}TiO_3$ produced by solution combustion and SPS was around 3025 $S.cm^{-1}$ at RT [119]. The electrical conductivity at RT was increased with the La content until $La_{0.4}Ba_{0.6}TiO_3$ because of the increase of the charge carrier concentration. With further increases of the La content, the electrical conductivity decreased in a non-regular way. TGA data (Figure 4.14 at page 70) suggested that the carrier concentration continued to be increased, however, this was counterbalanced by the decrease of the density of the sintered samples.

With the rise of the measuring temperature, the sensitivity to oxidation was also a key parameter. All of the compositions had their electrical conductivity decreased after the measurement, the differences before/after measurements were proportional to the La content. Because the oxidation depends on the total surface of the sample, the gas purity and the time of the measurement, the values obtained at high temperature did not only depend of the intrinsic properties of the bulk

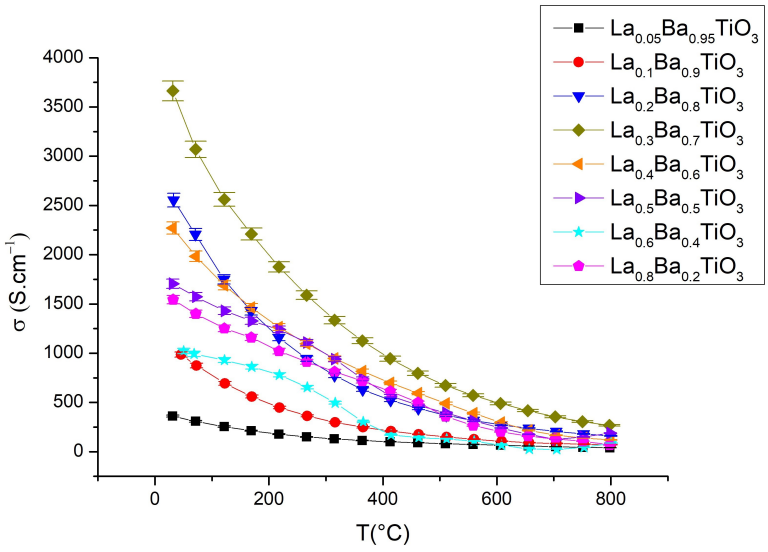


Figure 4.33: Temperature dependence of the electrical conductivity of $La_xBa_{1-x}TiO_3$ melted in argon and sintered by SPS at 1450°C in high vacuum (diffusion pump) for 10 minutes with a heating and cooling rate of 100°C per minute and applied pressure of 40MPa, measurement carried in static He with a heating rate of 10°C per minute.

materials. At all of the measurement's temperature $La_{0.3}Ba_{0.7}TiO_3$ remained the most conductive, at 800°C the conductivity was 267 $S.cm^{-1}$. In the work of Muta et al the conductivity of $La_{0.1}Ba_{0.9}TiO_3$ was 75 $S.cm^{-1}$ at 873K [160], while in our case the conductivity of $La_{0.1}Ba_{0.9}TiO_3$ was 106 $\pm$ 2.9 $S.cm^{-1}$ at around 610°C. At room temperature the difference is more important, they observed 200 $S.cm^{-1}$ at 50°C, while we measured 990 $\pm$ 27 $S.cm^{-1}$. For a point of comparison, La deficient $La_{0.15}Sr_{0.775}TiO_3$ at 973K was around 404 $S.cm^{-1}$ and $La_{0.08}Sr_{0.92}TiO_3$ produced by solution combustion and SPS was around 166 $S.cm^{-1}$ at 1045K.

Samples $La_{0.5}Ba_{0.5}TiO_3$, $La_{0.6}Ba_{0.4}TiO_3$, and $La_{0.8}Ba_{0.2}TiO_3$ switched from metal to semiconductor during the measurements resulting in an increase of their conductivity at 800°C compared to 750°C. Figure 4.35 is the plot of the electrical conductivity during the cooling step of a few representative compositions, during that step less data points were taken, from that time the samples were already oxidised. The conductivity continued to decrease during the cooling step as at that point they

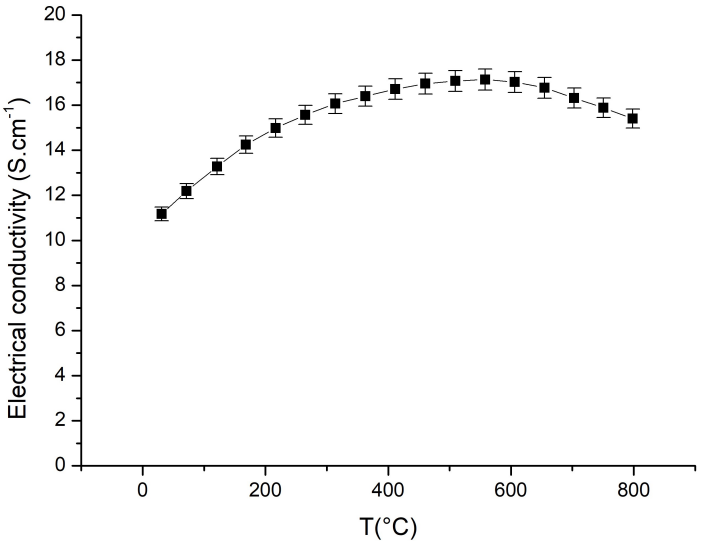


Figure 4.34: Temperature dependence of the electrical conductivity of undoped $BaTiO_3$ melted in argon and sintered by SPS at 1450°C in high vacuum (diffusion pump) for 10 minutes with a heating and cooling rate of 100°C per minute and applied pressure of 40MPa, measurement carried in static He with a heating rate of 10°C per minute.

were semiconductors, whereas others samples like $La_{0.1}Ba_{0.9}TiO_3$ maintained a metal conductivity. In order to confirm these atypical conductivity curves, another piece (from the same pellet) of $La_{0.5}Ba_{0.5}TiO_3$ was cut to repeat the electrical properties measurement, the results were similar as those reported.

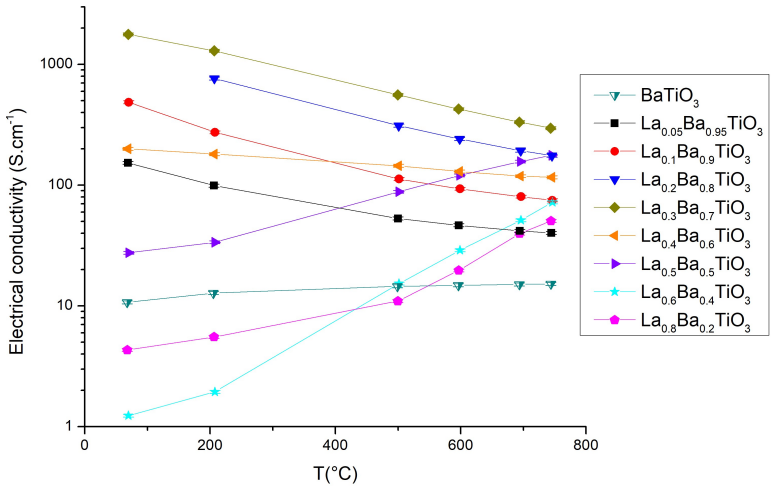


Figure 4.35: Temperature dependence of the electrical conductivity during the cooling step of $La_xBa_{1-x}TiO_3$ melted in argon and sintered by SPS at 1450°C in high vacuum (diffusion pump) for 10 minutes with a heating and cooling rate of 100°C per minute and applied pressure of 40MPa, measurement carried in static He with a cooling rate of 10°C per minute.

Figure 4.36 is the plot of the temperature dependence of the absolute Seebeck coefficient for the series $La_xBa_{1-x}TiO_3$. The absolute values decreased with the La content, the highest measured value was -250 ± 4.9 $\mu V.K^{-1}$ for the sample $La_{0.05}Ba_{0.95}TiO_3$ at 800°C. For each sample the absolute value of the Seebeck coefficient increased with the temperature because fewer charge carriers were free to move for the still metallic sample due to the decrease of the carrier concentration because of the oxidation. The sample $La_{0.1}Ba_{0.9}TiO_3$ by Muta et al had around -222 $\mu V.K^{-1}$ at 873K [160], while in our case the Seebeck coefficient of $La_{0.1}Ba_{0.9}TiO_3$ was -191 ± 3.7 $\mu V.K^{-1}$ at around 610 °C. In our case the synthesis lead to a higher carrier concentration. For a point of comparison, La deficient $La_{0.15}Sr_{0.775}TiO_3$ at 1013 was around -168 $\mu V.K^{-1}$ [100], and $La_{0.08}Sr_{0.92}TiO_3$ produced by solution combustion and SPS was around -238 $\mu V.K^{-1}$ at 1045K [119].

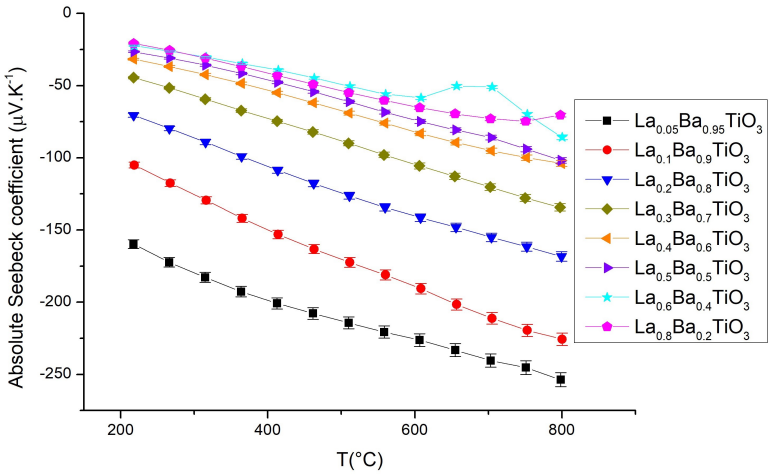


Figure 4.36: Temperature dependence of the absolute Seebeck coefficient of $La_xBa_{1-x}TiO_3$ melted in argon and sintered by SPS at 1450°C in high vacuum (diffusion pump) for 10 minutes with a heating and cooling rate of 100°C per minute and applied pressure of 40MPa, measurement carried in static He with a heating rate of 10°C per minute.

Figure 4.37 is the temperature dependence of the power factor, $La_{0.2}Ba_{0.8}TiO_3$ achieved the highest value with 0.62 ± 0.024 $W.m^{-1}.K^{-1}$ at 365°C. At the highest measured temperature it was $La_{0.3}Ba_{0.7}TiO_3$ that had the highest value with 0.48 ± 0.019 $W.m^{-1}.K^{-1}$ at 800°C. The sample $La_{0.1}Ba_{0.9}TiO_3$ by Muta et al had around 0.37 $W.m^{-1}.K^{-1}$ at 873K [160], while we measured 0.39 ± 0.015 for $La_{0.1}Ba_{0.9}TiO_3$ at 610°C. For a point of comparison, La deficient $La_{0.15}Sr_{0.775}TiO_3$ at 1013 was around 1.14 $W.m^{-1}.K^{-1}$ [100], and $La_{0.08}Sr_{0.92}TiO_3$ produced by solution combustion and SPS was around 0.94 $W.m^{-1}.K^{-1}$ at 1045K [119].

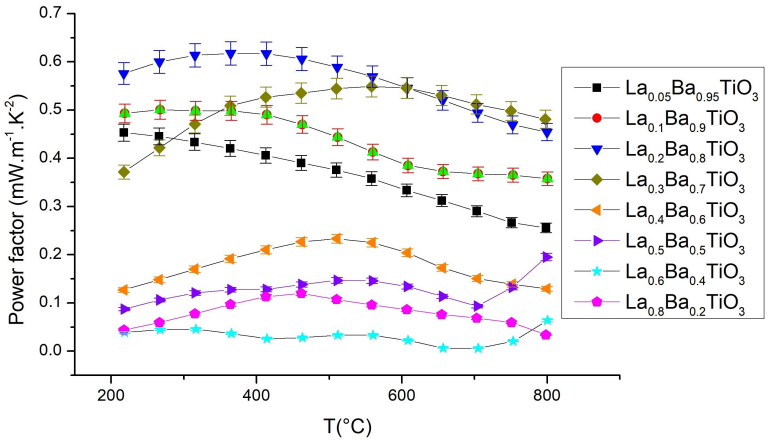


Figure 4.37: Temperature dependence of the power factor of $La_xBa_{1-x}TiO_3$ melted in argon and sintered by SPS at 1450°C in high vacuum (diffusion pump) for 10 minutes with a heating and cooling rate of 100°C per minute and applied pressure of 40MPa, measurement carried in static He with a heating rate of 10°C per minute.

Figure 4.38 is the plot of the temperature dependence of the electrical conductivity measured in air or $H_2$5%/Ar95% of selected samples made in the early experiments. The conductivities were similar to those in Figure 4.33, showing that the results can be repeated. To achieve repeatable results, the parameters of the synthesis need to be controlled. In earlier experiments, samples with much lower electrical conductivity were made, the colors of these samples were not as dark as the highly conductive more recent one. For some of them, differences could be seen with the XRD patterns. The use of TiO instead of Ti metal granules, and the preparation of the $LaTiO_3$ in the glovebox improved this repeatability.

In addition to the La content, the electrical conductivity was influenced by the SPS sintering temperature probably as a higher SPS sintering temperature creates more oxygen vacancies. The conductivities of the samples $La_{0.05}Ba_{0.95}TiO_3$ sintered at 1400°C, 1450°C, and 1500°C were measured respectively at 190 ± 6 $S.cm^{-1}$, 310 ± 9 $S.cm^{-1}$, and 480 ± 13 $S.cm^{-1}$ at RT. The same effect was present for $La_{0.2}Ba_{0.8}TiO_3$ and the maximum electrical conductivity was achieved by sintering

at 1550°C with 3500 ± 132 $S.cm^{-1}$ at RT. While for samples sintered at 1300°C the conductivity was below 300 $S.cm^{-1}$ at RT.

For $La_{0.2}Ba_{0.8}TiO_3$ the maximum electrical conductivity was achieved for the sample sintered at 1550°C. However, a higher amount of fractures (samples were broken more often and into more pieces) after the sintering was noticed for $La_{0.05}Ba_{0.95}TiO_3$, $La_{0.2}Ba_{0.8}TiO_3$, and undoped $BaTiO_3$. Attempts to reduce the number of fractures and broken samples by modifying the SPS parameters (the cooling rate, the heating rate, the applied pressure, and the time during the sintering when the applied pressure was removed) were unsuccessful. Making samples with a larger die was also explored but did not permit to have bigger pieces to be shaped when samples broke (more cracks were present). Making bar samples longer than 5-6 mm was not possible for the samples sintered at 1550°C and 1600°C. In practice, 5-6 mm was sufficient to measure the electrical conductivity, however, to measure the Seebeck coefficient a bar of at least 9 mm was needed. The samples sintered at 1300°C made in earlier experiments were all crack-free, but with conductivities under 100 $S.cm^{-1}$. Making crack-free samples sintered at 1500°C was possible but needed more attempts as the proportion of crack-free samples sintered at 1400°C and 1450°C was higher. Therefore it was decided to SPS sinter all the series at 1450°C. For some of them, a second sample had to be done to have a long enough sample bar.

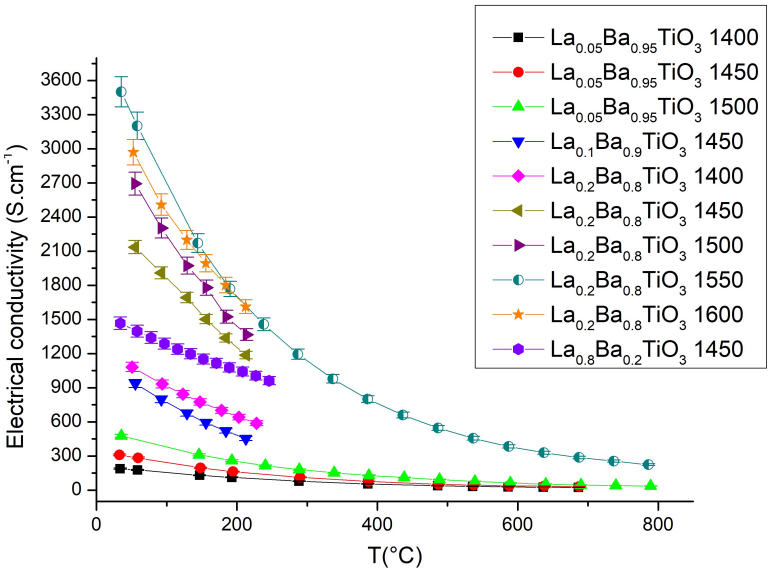


Figure 4.38: Temperature dependence of the electrical conductivity of $La_xBa_{1-x}TiO_3$ melted in argon and sintered by SPS at different temperature in high vacuum (diffusion pump) for 10 minutes with a heating and cooling rate of 100°C per minute and applied pressure of 40MPa, carried in static air for measurements under 250°C, carried in flowing $H_2$5%/Ar95% for measurement over 250°C with a heating rate of 5°C per minute.

Thermal properties Figure 4.39 is the temperature dependence of the thermal diffusivity measured with a LFA. Except for the sample $La_{0.3}Ba_{0.7}TiO_3$ at temperatures higher than 600°C, the thermal diffusivity decreased with the temperature for all of the samples as phonon and electron scattering increased with the temperature. More La increased the thermal diffusivity, as it also increased the electrical conductivity (Figures 4.33 and 4.34 at page 96), and then the electronic component of the thermal conductivity was also significantly increased. As mentioned above, from 600°C, $La_{0.3}Ba_{0.7}TiO_3$ did not follow a normal behaviour with the thermal diffusivity decreasing with a new slope. Figure 4.40 is the Arrhenius plot of the thermal diffusivity, the thermal diffusivity increases linearly with $\frac{1000}{T}$ except with $La_{0.3}Ba_{0.7}TiO_3$ that followed two slopes showing the oxidation of the sample.

After the measurements from 50°C to 800°C were performed (heating stage), a few measurements

were also made during the cooling stage of the samples/LFA chamber. The values during the heating and cooling stage are in Figure 4.41. Comparing the values before and after the samples reached 800°C gives information about the stability of the samples during the measurements. The thermal diffusivity of the samples $BaTiO_3$, $La_{0.05}Ba_{0.95}TiO_3$, $La_{0.1}Ba_{0.9}TiO_3$, and $La_{0.2}Ba_{0.8}TiO_3$ were identical before and after having reached 800°C. The values for $La_{0.3}Ba_{0.7}TiO_3$ were different : 2.0 ± 0.1 $mm^2.s^{-1}$ / 1.4 ± 0.07 $mm^2.s^{-1}$ at 150°C and 1.3 ± 0.07 $mm^2.s^{-1}$ / 0.92 ± 0.05 $mm^2.s^{-1}$ at 400°C. This drop in the thermal diffusivity showed that the sample was not stable at high temperatures in these experimental conditions.

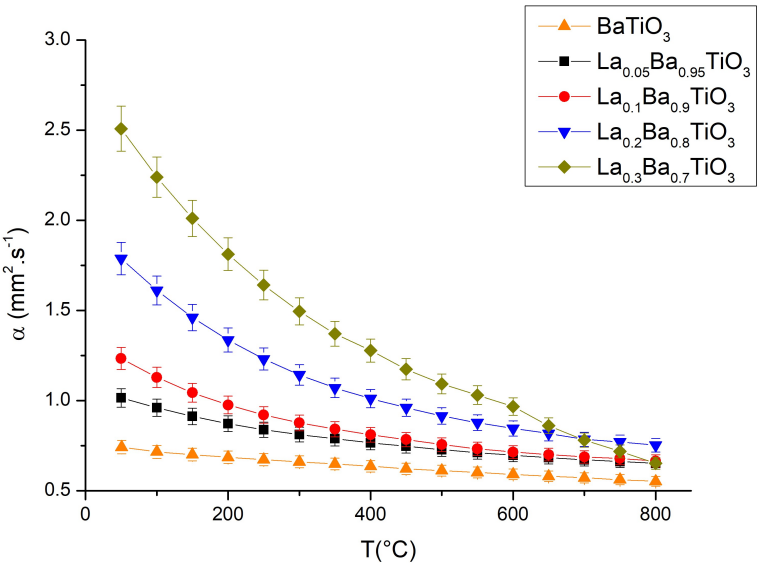


Figure 4.39: Temperature dependence of the thermal diffusivity of $La_xBa_{1-x}TiO_3$ melted in argon and sintered by SPS at different temperature in high vacuum (diffusion pump) for 10 minutes with a heating and cooling rate of 100°C per minute and applied pressure of 40MPa. Measurements carried in flowing $H_2$5%/Ar95%.

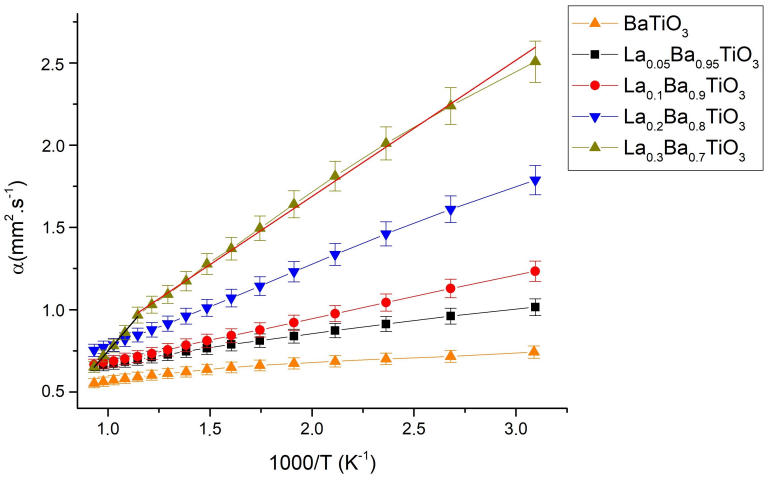


Figure 4.40: Arrhenius plot of the temperature dependence of the thermal diffusivity of $La_xBa_{1-x}TiO_3$ melted in argon and sintered by SPS at different temperature in high vacuum (diffusion pump) for 10 minutes with a heating and cooling rate of 100°C per minute and applied pressure of 40MPa. Measurements carried in flowing $H_2$5%/Ar95%. Linear fits for $La_{0.3}Ba_{0.7}TiO_3$.

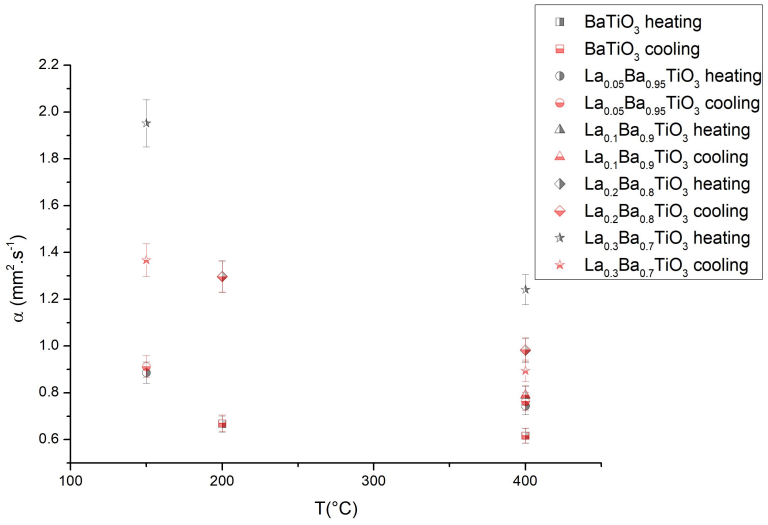


Figure 4.41: Thermal diffusivity before and after measurements up to 800°C of $La_xBa_{1-x}TiO_3$ melted in argon and sintered by SPS at different temperature in high vacuum (diffusion pump) for 10 minutes with a heating and cooling rate of 100°C per minute and applied pressure of 40MPa. Measurements carried in flowing $H_2$5%/Ar95%.

4.5 Summary

In summary, perovskite $La_xBa_{1-x}TiO_3$ with x from 0 to 1 was synthesised by a combination of arc melting and SPS. XRD, TGA, and EPMA experiments showed that La was inserted in the Ba site for the whole series of $La_xBa_{1-x}TiO_3$ ($0 \leq x \leq 1$) following the electronic compensation doping mechanism. WDX results showed that the distributions of La and Ba in the grains are not homogeneous, though the atomic ratio of the total A-site cations (Ba^{2+}+La^{3+}) to the B-site Ti cation is homogeneous and close to the nominal ratio of 1:1. The influence of the doping level and the SPS parameters on the final electrical and thermoelectric properties were studied. Exceptionally high electrical conductivity was achieved by increasing the carrier concentration via both donor doping and creation of oxygen vacancies due to the extremely high synthesis temperature, high cooling rate and low oxygen partial pressure associated with the arc melting and SPS. An unprecedented high electrical conductivity of 3,700 $S.cm^{-1}$ at room temperature was observed in the composition $La_{0.3}Ba_{0.7}TiO_3$, which is the first and highest electrical conductivity obtained to date for La-doped $BaTiO_3$. The composition $La_{0.2}Ba_{0.8}TiO_3$ produced a high power factor of 0.6 $mW.m^{-1}.K^{-2}$ at 365°C, which is lower than the typical high temperature (600-800°C) required to achieve high power factor. This demonstrates that La-doped $BaTiO_3$ fabricated by arc melting and SPS is a promising thermoelectric material to cover applications in the intermediate temperature range.

5 Synthesis, structural, and thermoelectric properties of $La_xCa_{1-x}TiO_3$

5.1 Introduction

As shown in section 4, arc melting followed by SPS sintering is a suitable approach to favour electronic compensation when doping La in the A-site of the $BaTiO_3$ perovskite. Because the alkaline earth titanates have a similar electronic structures [187], the approach should also be efficient with others alkaline earth titantes. While reports of the synthesis of perovskites $La_xBa_{1-x}TiO_3$ and $La_xSr_{1-x}TiO_3$ for $0 \leq x \leq 1$ exist [158, 159], it is not the case for the $La_xCa_{1-x}TiO_3$ system. The composition with the highest concentration of La reported is $La_{0.25}Ca_{0.75}TiO_3$ by Li et al [176]. In their work they obtained with the sample $La_{0.2}Ca_{0.8}TiO_3$ 3383 $S.cm^{-1}$ at RT and ZT = 0.4 at 1011K, but observed a Ti rich secondary phase, there is then a lack of data of the intrinsic properties of La-doped $La_xCa_{1-x}TiO_3$, especially for more heavily doped compositions. In this section the same methodology used in section 4 was applied for the study of the $La_xCa_{1-x}TiO_3$ system. Strong reducing conditions were used to increase the electrical conductivity in order to improve the power factor. The thermoelectric properties were studied with the samples with $x \leq 0.3$ as they were those with the superior properties, furthermore the compositions with more La were sensitive to oxidation which makes them difficult to characterise at high temperature. This section is the first study of the full series $La_xCa_{1-x}TiO_3$ for $0 \leq x \leq 1$. The study of the crystal structure, the microstructure and the study of the oxidation (by TGA) was designed to observed what charge compensation mechanism was favoured. The electrical and thermal properties are described in the rest of the section.

5.2 Structure, microstructure, and oxidation properties

X-Ray diffraction data Prior to the SPS sintering, a series of $La_xCa_{1-x}TiO_3$ samples were melted and analyzed to clarify if arc melting was a suitable method to insert La into the Ca site. Figure 5.1 is the plot of the powder XRD patterns of these samples. Also plotted in red stripes

the XRD reflection rays of Pnma $CaTiO_3$ of the PDF card 22-0153. Figure 5.2 is the plot of the powder XRD patterns between 2θ values of 30° and 35°. No secondary phase was detected and the intensity of the [101] peak was variable. With the increase of the La content, the peaks splitting decreased, this is especially visible in Figure 5.2, suggesting a higher symmetry of the crystal structure with La doping with only a shoulder remaining. Ca ion in $CaTiO_3$ is too small to have ideal cubic ABO_3 structure [193]. La has an ionic radius slightly higher than Ca [190], then La insertion in the Ca site would increase the symmetry of the crystal structure. The peaks shifted to the lower angles, indicating an increase of the lattice constants with the La content, the shift was highlighted in Figure 5.2. Figure 5.3 is the plot of the lattice constant; the values were calculated from the powder XRD patterns. With the increase of the La content, the ratio a/c was closer to one, as examples a/c for $La_{0.05}Ca_{0.95}TiO_3$ was $1.012 \pm (6.19 \cdot 10^{-4})$ and was $1.001 \pm (2.18 \cdot 10^{-4})$ for $La_{0.4}Ca_{0.6}TiO_3$ suggesting an increase in the symmetry of the crystal structure. Figure 5.4 is the plot of the lattice volume of the arc melted $La_xCa_{1-x}TiO_3$. The lattice volume increased, from 223.1 ± 0.03 Å^3 for $CaTiO_3$ to 238.6 ± 0.05 Å^3 for $La_{0.6}Ca_{0.4}TiO_3$, following the Vegard's law. Such increase in the lattice volume is consistent with an insertion of the La in the Ca site as the ionic radius of La is higher than Ca [190]. Overall, the XRD results of these samples showed that the La was inserted in the Ca site, and that arc melting was a suitable method to synthesize single phase La-doped $CaTiO_3$.

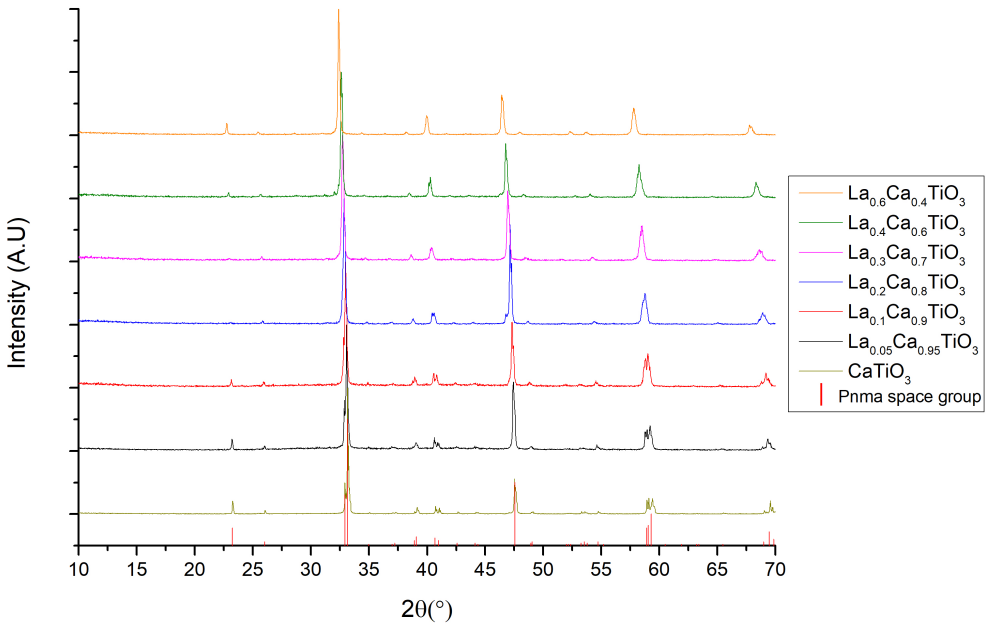


Figure 5.1: Powder XRD patterns of melted $La_xCa_{1-x}TiO_3$.

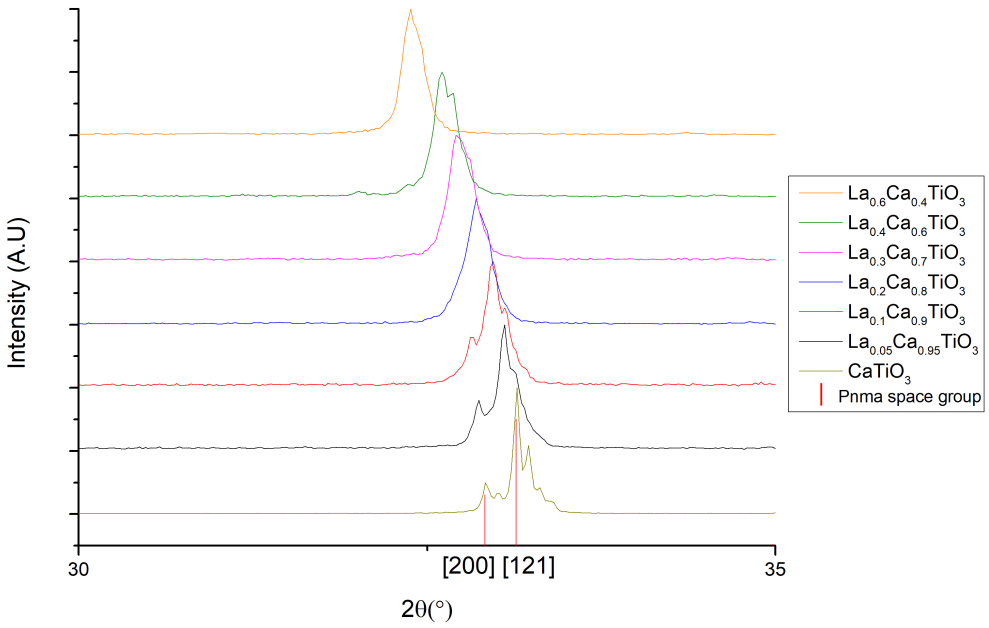


Figure 5.2: Expanded powder XRD patterns of melted $La_xCa_{1-x}TiO_3$.

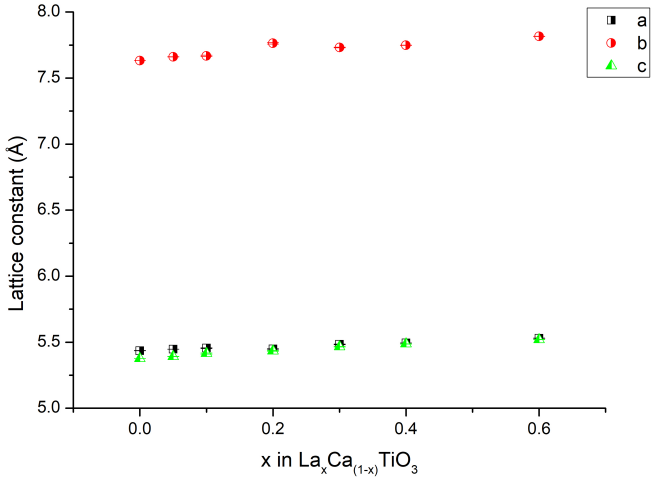


Figure 5.3: Plot of the lattice constants of $La_xCa_{1-x}TiO_3$ arc melted in argon. Error bars are smaller than the symbol size.

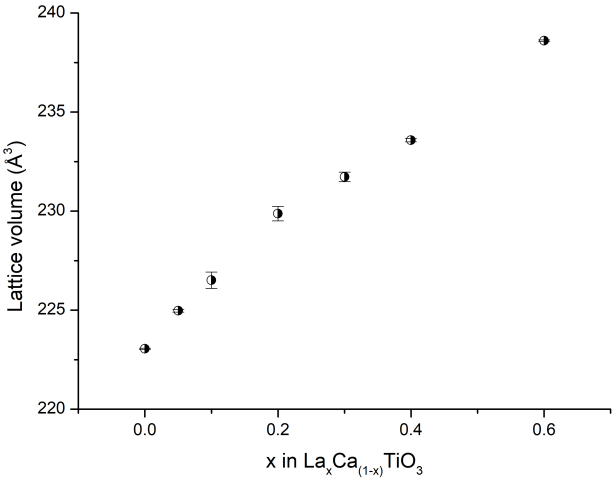


Figure 5.4: Plot of the lattice volume of $La_xCa_{1-x}TiO_3$ arc melted in argon. Error bars are smaller than the symbol size.

Figure 5.5 is the plot of the powder XRD patterns of $La_xCa_{1-x}TiO_3$ after the SPS sintering. Except for $LaTiO_3$, no secondary phase were observed for all of the samples. Like as reported in the literature for undoped $CaTiO_3$ [194], all peaks were attributed to the orthorhombic space group number 62 (Pnma or Pbnm). With the increase of the La content, the patterns shifted to the lower angles, indicating an increase of the lattice volume. Figure 5.6 is the expanded powder XRD patterns between 30° and 35°, highlighting the shift toward the lower angles. The intensity of the peak [101], between 22.5° and 25°, decreased and then increased with the La concentration. The peak was hardly visible for $La_{0.2}Ca_{0.8}TiO_3$ and $La_{0.3}Ca_{0.7}TiO_3$ although the others peaks that characterized the space group number 62 were present. At first, the splitting of the peaks decreased but increased again with La concentration, this was easily visible for peaks [132], [024], and [312] between 57.5° and 60°, indicating a higher symmetry of the structure around $La_{0.5}Ca_{0.5}TiO_3$.
With the increase of the La content, the ratio a/c was closer to one, for example $1.0109 \pm (1.17 \cdot 10^{-4})$ for $La_{0.05}Ca_{0.95}TiO_3$, $0.9997 \pm (8.5 \cdot 10^{-5})$ for $La_{0.9}Ca_{0.1}TiO_3$, suggesting a higher symetry. The calculated unit cell constants from the XRD patterns and the lattice volumes are respectively plotted in Figure 5.7 and 5.8, the lattice constant increased with the increase of the La content from 223.3 ± 0.07 $Å^3$ for $CaTiO_3$ to 248.9 ± 0.07 $Å^3$ for $LaTiO_3$, following the Vegard's law. For the doped samples the lattice volume decreased after the SPS sintering, such as 231.7 ± 0.24 $Å^3$ after melting and, 230.5 ± 0.29 $Å^3$ after the SPS for $La_{0.3}Ca_{0.7}TiO_3$. The decrease may be because of the oxygen loss leading to a distortion of the lattice or a difference in the homogeneity of the La in the sample.
In the litterature there is no report of the substitution of La in the Ca site for the all series $La_xCa_{1-x}TiO_3$ from x = 0 to x = 1. In their work Li et al made sample up to x = 0.25 but observed a second phase at the grain boundary from $La_{0.25}Ca_{0.75}TiO_3$. The XRD data indicated that our synthesis method produce a total or near-total insertion of the La in the A-site of the $CaTiO_3$ structure without formation of non-perovskite secondary phase.

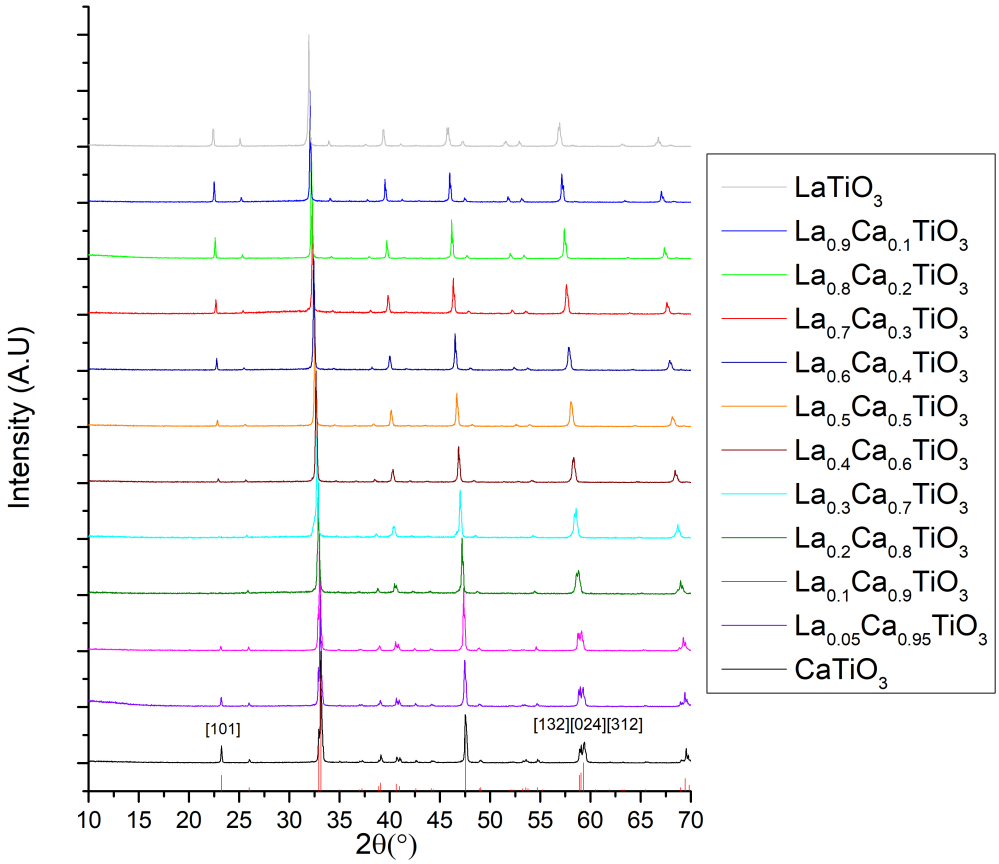


Figure 5.5: Powder XRD patterns of $La_xCa_{1-x}TiO_3$ melted in argon and sintered by SPS at 1450°C in high vacuum (diffusion pump) for 10 minutes with a heating and cooling rate of 100°C per minute and applied pressure of 40MPa.

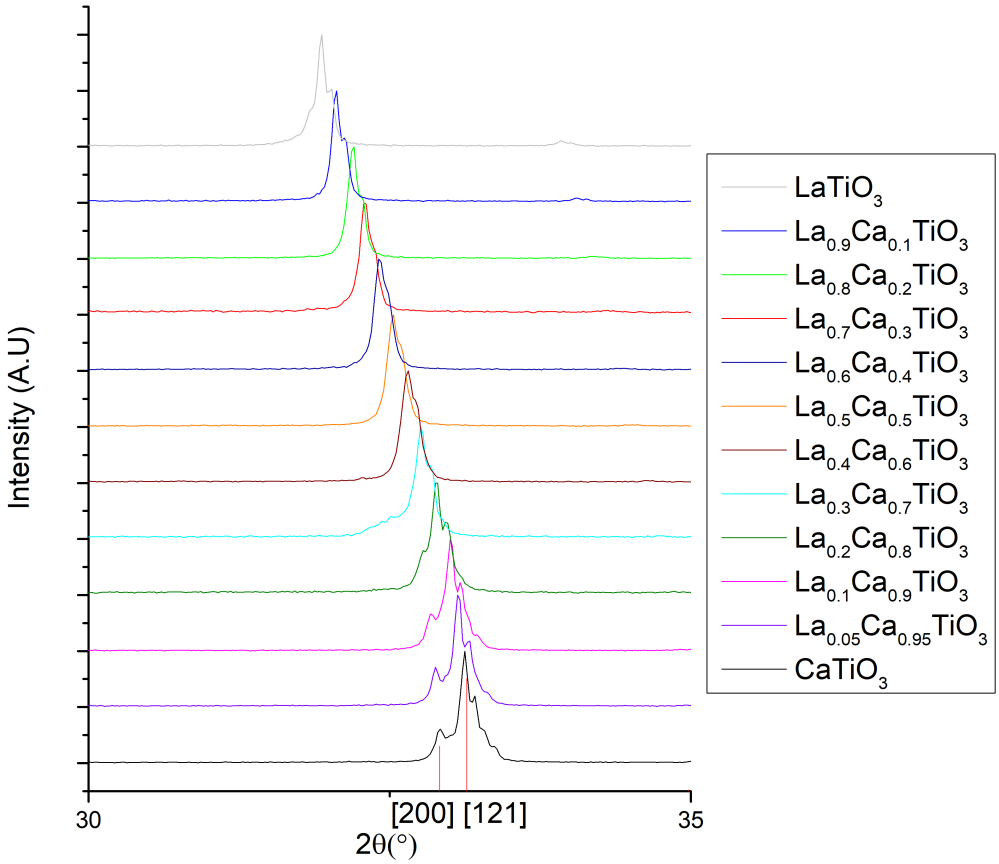


Figure 5.6: Expanded powder XRD patterns of $La_xCa_{1-x}TiO_3$ melted in argon and sintered by SPS at 1450°C in high vacuum (diffusion pump) for 10 minutes with a heating and cooling rate of 100°C per minute and applied pressure of 40MPa.

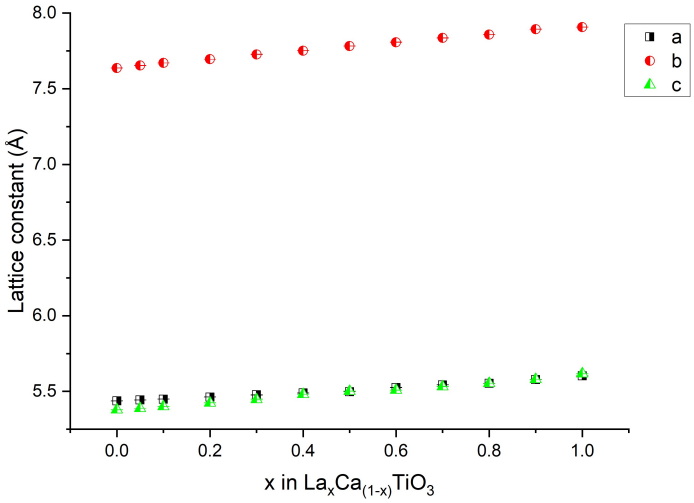


Figure 5.7: Plot of the lattice edge length of the system $La_xCa_{1-x}TiO_3$ melted in argon and sintered by SPS at 1450°C in high vacuum (diffusion pump) for 10 minutes with a heating and cooling rate of 100°C per minute and applied pressure of 40MPa, calculated from the XRD patterns. Error bars are smaller than the symbol size.

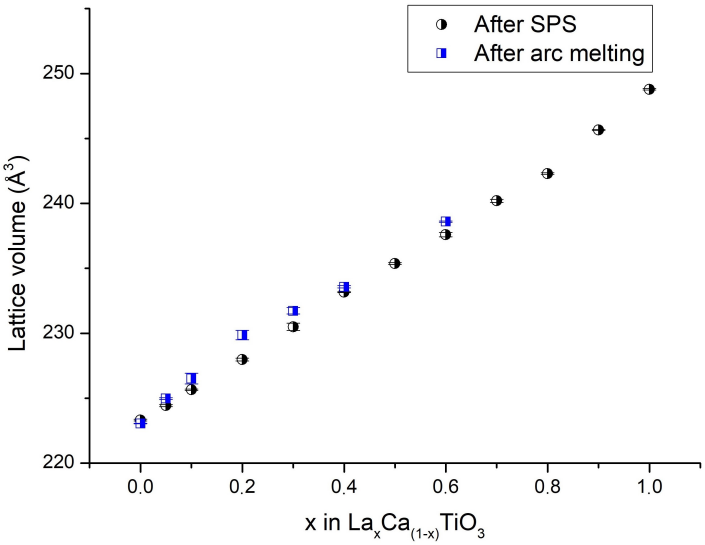


Figure 5.8: Plot of the lattice volume of the system $La_xCa_{1-x}TiO_3$ after arc melting with argon and after sintering by by SPS at 1450°C in high vacuum (diffusion pump) for 10 minutes with a heating and cooling rate of 100°C per minute and an apllied pressure of 40MPa, calculated from the XRD patterns. Error bars are smaller than the symbol size.

TGA Prior to the SPS sintering, a series of $La_xCa_{1-x}TiO_3$ were melted and analysed to help elucidate if the arc melting method was suitable to insert the La into the Ca site. Figure 5.9 is the plot of the TGA in air of $La_xCa_{1-x}TiO_3$ after the melting synthesis. The final mass of the samples were higher than the starting mass. The mass difference between the final mass and the starting mass was proportional to the amount of La at the A-site. This indicates that La doped $CaTiO_3$ has a doping mechanism similar to the La doped $BaTiO_3$ (in eq 7 in page 27) and described as follows:

$$La_2O_3 + 2\,TiO_2 \longrightarrow 2\,La^{\bullet}_{Ca} + 6\,O^{\times}_{O} + \frac{1}{2}\,O_2 + 2\,Ti^{\times}_{Ti} + 2\,e' \tag{12}$$

Figure 5.10 is the plot of the difference in mass before and after the oxidation, also plot the mass increased normalised by the ratio $\frac{M_O}{M_{La_xCa_{1-x}TiO_3}}$ to take into account the change of the molar mass with the doping level. The influence of the La on the final mass increase was linear, indicating that the doping mechanism remained the same for all of the analysed samples. The starting temperatures of oxidation was also correlated to the La doping as composition with more La started to oxidise at a lower temperature. For example, the starting temperature of oxidation for $La_{0.4}Ca_{0.6}TiO_3$ was approximately 350°C while for $La_{0.2}Ca_{0.8}TiO_3$ it was between 500°C and 600°C. For all the samples the mass did not reach a plateau, indicating the samples were not fully oxidised.

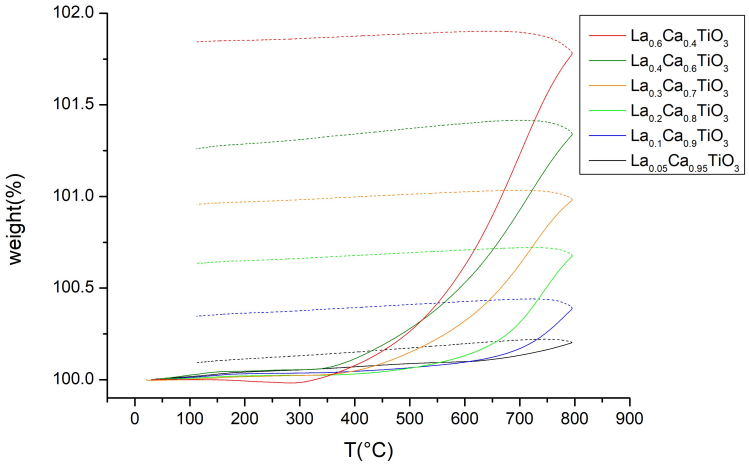


Figure 5.9: TGA plot of $La_xCa_{1-x}TiO_3$ in air from room temperature to 800°C, with a heating and cooling rate of 10°C per minute, heating step plotted in solid line, cooling step plotted in dash line. Powder from crushed pellets produced by arc melting in argon.

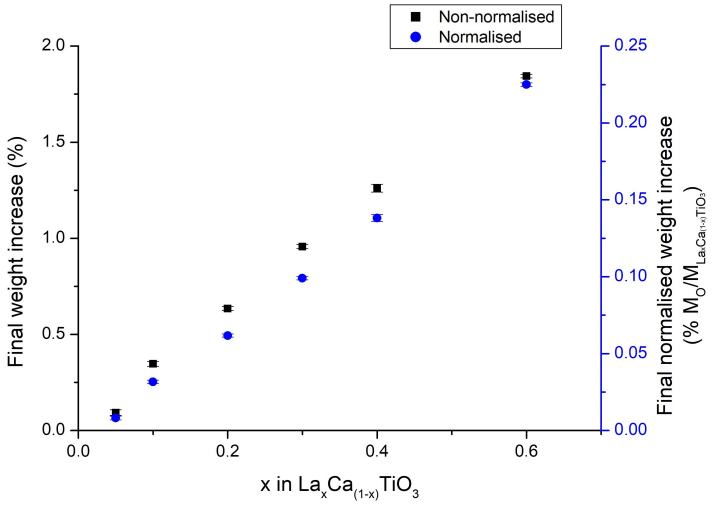


Figure 5.10: Influence of the doping level on the difference of mass after the TGA for the series $La_xCa_{1-x}TiO_3$, plot in Figure 5.9. Powder from crushed pellets produced by arc melting in argon.

Figures 5.11 is the plot of the TGA in air of the samples after the SPS sintering. For all of the samples, the mass reached a plateau before 900°C, indicating that the samples were fully oxidised during the TGA run. Undoped $CaTiO_3$ started to oxidise at the lowest temperature around 175°C, the mass increase stopped and the powder fully oxidized around 300°C. For the doped compositions, the temperature of oxidation was correlated to the La content, as examples $La_{0.2}Ca_{0.8}TiO_3$ started to oxidise around 450°C while for $La_{0.7}Ca_{0.3}TiO_3$ the temperature was around 250°C. The temperature of the end of the oxidation also decreased with the doping level, as for example the temperature was around 775°C for $La_{0.2}Ca_{0.8}TiO_3$ and around 675°C for $La_{0.7}Ca_{0.3}TiO_3$. Contrary to the other doped samples, $La_{0.05}Ca_{0.95}TiO_3$ showed a hybride behavior, it did not plateau before a high slop increase, but started with a slight increase of the mass until around 600°C. This increase was in the limit of the resolution of the TGA, however that behavior was visible for the three samples SPS sintered at different temperature (Figure 5.13a). This is indicative that $La_{0.05}Ca_{0.95}TiO_3$ was less resistant to the oxidation than the samples with a higher doping content. The sensitivity toward oxidation of the compositions with a high La content makes the characterisation of the electrical and thermal properties at high temperature challenging. The increase in mass after the TGA run was also correlated to the La content.

Figure 5.12 is the plot of the weight increase at the end of the TGA run against the doping level, also plotted the mass increased normalised by the ratio $\frac{M_O}{M_{La_xCa_{1-x}TiO_3}}$ to take into account the change of the molar mass with the doping level. The increase of mass was linearly proportional to the doping level, indicating that the doping mechanism described in eq 12 (page 115) remained the same for all of the compositions. For the doping mechanism to remain the same, the La ion has to be inserted in the Ca site without forming other phases, thus the TGA data was in agreement with the XRD results.

Figure 5.13 is the plot of the TGA of the four compositions that were sintered at different SPS temperatures. For all of the samples, the temperature of oxidation were dependent of the SPS sintering temperature. For all of the samples, the mass increase was correlated to the sintering temperature. The difference was the highest for the composition $La_{0.1}Ca_{0.9}TiO_3$. Because the divergence of mass increase between the samples were close to the resolution of the TGA, quantitative analysis was

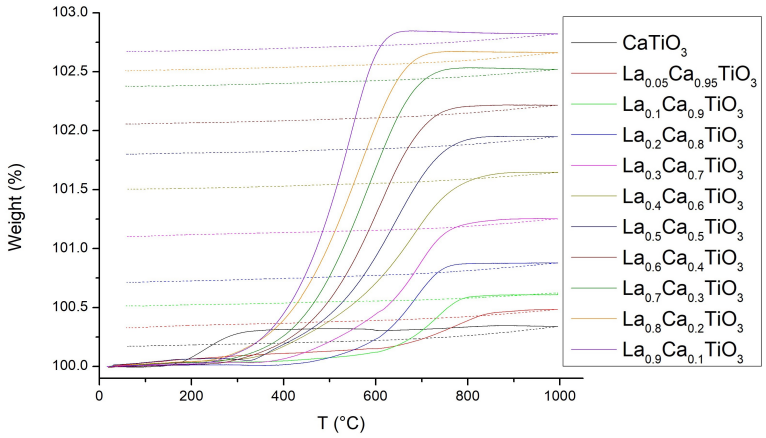


Figure 5.11: TGA of $La_xCa_{1-x}TiO_3$ powders carried in air from room temperature to 1000°C, with a heating and cooling rate of 5°C per minute, gas flow of 100 $mL.min^{-1}$, heating step plotted in solid line, cooling step plotted in dash line. Powders from the crushed pellet SPS sintered at 1450°C in high vacuum (diffusion pump) for 10 minutes.

not possible. However, the TGA data indicates that a higher SPS sintering temperature leads to a higher reduction of the Ti oxidation stats by the creation of O vacancies as described in eq 3 (page 20) and eq 4 (page 21), in addition to the donor doping mechanism. It is then expected that a higher SPS sintering temperature should results in higher charge carrier concentration and electrical conductivity.

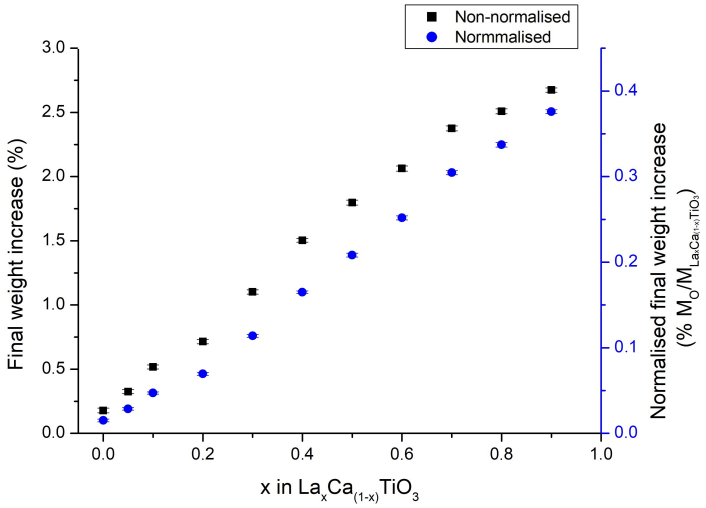
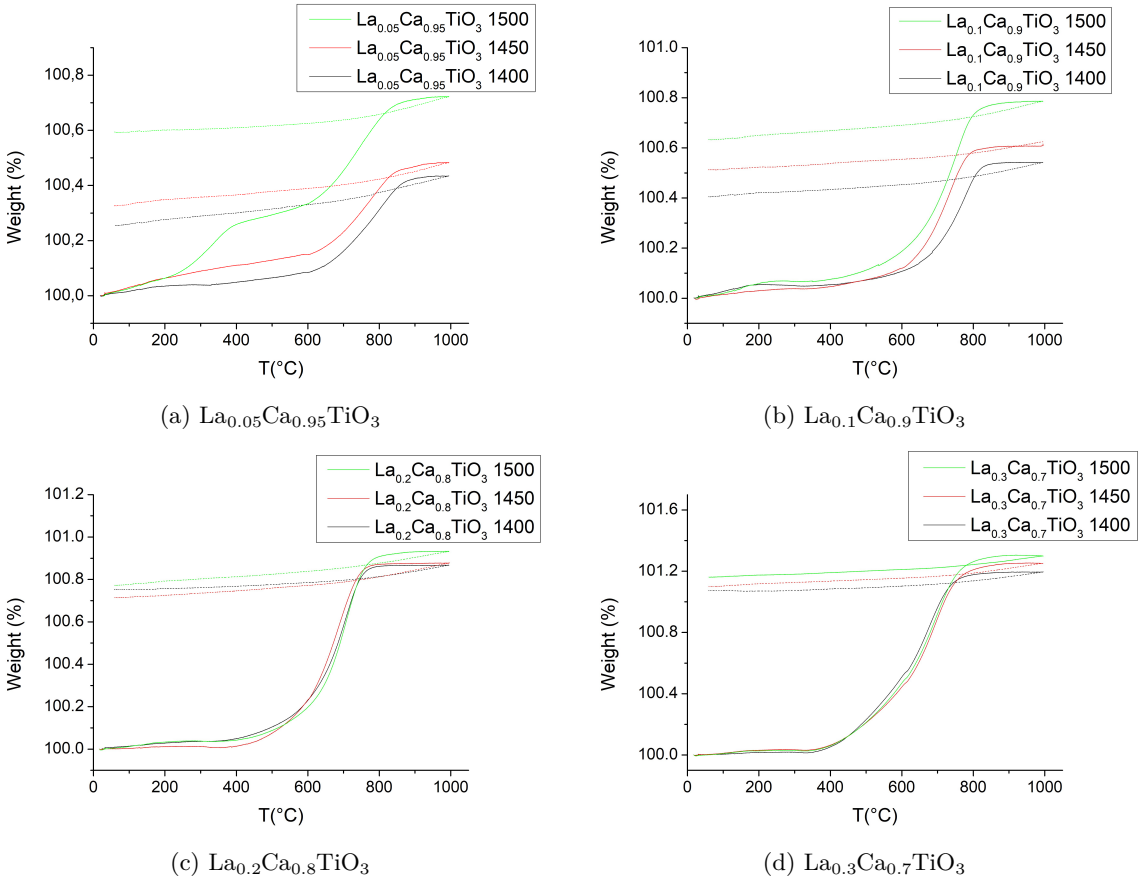


Figure 5.12: Influence of the doping level on the difference of mass after the TGA for the series $La_xCa_{1-x}TiO_3$, plot in Figure 5.11. Powders from the crushed pellet SPS sintered at 1450°C in high vacuum (diffusion pump) for 10 minutes.



(a) $La_{0.05}Ca_{0.95}TiO_3$ (b) $La_{0.1}Ca_{0.9}TiO_3$

(c) $La_{0.2}Ca_{0.8}TiO_3$ (d) $La_{0.3}Ca_{0.7}TiO_3$

Figure 5.13: TGA of $La_xCa_{1-x}TiO_3$ powders carried in air from room temperature to 1000°C, with a heating and cooling rate of 5°C per minute, gas flow of 100 $mL.min^{-1}$, heating step plotted in solid line, cooling step plotted in dash line. Powders from the crushed pellet SPS sintered at different temperature in high vacuum (diffusion pump) for 10 minutes.

Figure 5.14 is the powder XRD patterns of two compositions after beeing heated up in air in a muffle furnace with the same temperature profile compared with the TGA experiments. The low intensity peaks were not visible anymore and the high intensity peaks were wider. No distinctive phases were identified. Formation of numerous secondary phases was probable with possible amorphous phases. It was clear that these compositions were not stable after oxidation.

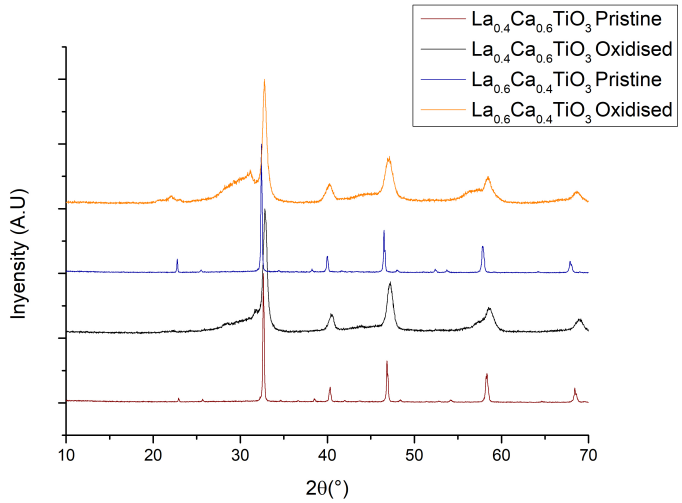


Figure 5.14: Powder XRD patterns of $La_{0.4}Ca_{0.6}TiO_3$ and $La_{0.6}Ca_{0.4}TiO_3$ SPS sintered at 1450°C. Powders oxidised in a muffle furnace at 1000°C, heating and cooling rate of 5°C per minute. XRD scan of 30 minutes.

Density Figure 5.15 is the plot of the relative density of the $La_xCa_{1-x}TiO_3$ samples after SPS sintering. The measurements were taken with a microbalance and a caliper. The theoretical lattice volumes were calculated from the powder XRD patterns, and the theoretical lattice mass was calculated with three anions for two cations. The proportion of La was the main determinant of the sinterability of the material. It should be noted that by neglecting the O vacancies, the relative densities were underestimated by an unknown value, potentially similar to the mass increase after oxidation in air, (Figure 5.12 in page 119). Because the final mass increase was proportional to the La content, the underestimation of the relative mass was also proportional to the La content. However, this underestimation is much smaller than the decrease of the relative density with the La doping. Additionally, it was observed that the melted (before SPS sintering) materials as well as SPS sintered materials were easier to crush when the La content was higher, indicative of a higher porosity. In addition it can be visually observed on SEM images (Figure 5.16a to 5.16l from page 125) that the number of pores increased with the La content. When at above 1400°C, the SPS sintering temperature did not have an significant influence on the density of the samples, the same

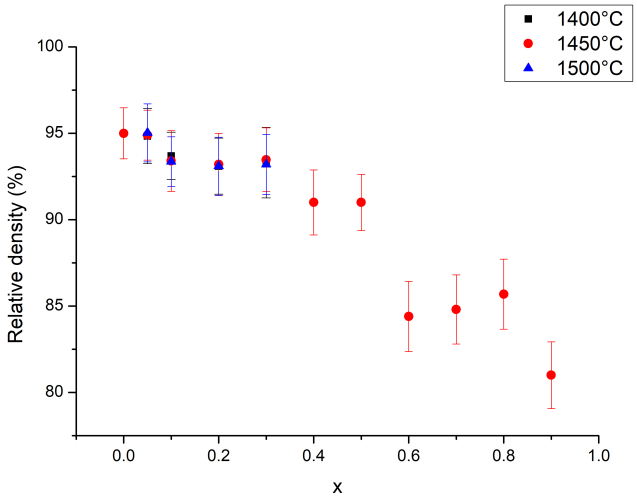


Figure 5.15: Relative density of the samples $La_xCa_{1-x}TiO_3$ produced by arc melting in argon and sintered by SPS at different temperature in high vacuum (diffusion pump) for 10 minutes with a heating and cooling rate of 100°C per minute and an applied pressure of 40MPa

was observed for the La-doped $BaTiO_3$ (Figure 4.17 in page 73).

The samples from $La_{0.6}Ca_{0.4}TiO_3$ to $LaTiO_3$ were less than 90% dense, and so their electrical characterisations did not fully represent their bulk properties. In an attempt to increase the relative density of the final samples, a batch of $La_{0.2}Ca_{0.8}TiO_3$ and $La_{0.5}Ca_{0.5}TiO_3$ powder were ball milled (yttria-stabilized zirconia bowl and balls) before the SPS sintering. However, the results showed there was no increase in the measured densities when compared to the samples that were hand milled.

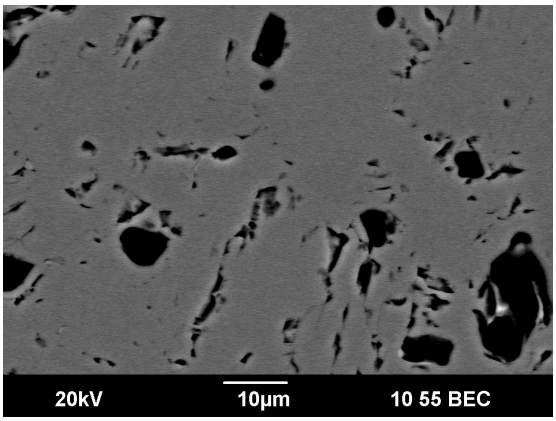
SEM Figures 5.16 are a selection of backscattered and secondary electron images of SPS sintered pellets of the series $La_xCa_{1-x}TiO_3$. Figures 5.17 and Tables 5.1 are the maps of the points where EDX analysis were carried out and the normalised results of the EDX analysis, respectively. A qualitative trend can be drawn from the SEM observation and it is consistent with the measured bulk density (Figure 5.15) in which the number of pores and their sizes increased with the La content. No difference in contrast was observed on the backscattered image (Figure 5.16a) nor

during the rest of the SEM observation of the undoped $CaTiO_3$, indicating a single-phase material. The EDX data is presented in Table 5.1a. The values of all the points were consistent, in agreement with the backscattered images observations. The largest difference was only 0.4 % (between target one and four). For all the points observed, the concentration of Ca was lower than the concentration of Ti. The average ratio of Ca/Ti was 0.9 instead of 1 in theory. The Ca losses during the melting steps, which would be due to the Ca sublimation, cannot be excluded. However, the amount lost would have been visible on the Cu plate of the arc melter. Since the perovskite structure was clearly identified with the XRD patterns, the hypothesis of the Ca sublimation would mean that the A-site deficient $CaTiO_3$ was formed. The second hypothesis and the most likely is that the EDX overestimated the Ti amount, wrong quantifications occur with standardless EDX [195], errors can be increase for other reasons such as a drift in the beam current [195]. This hypothesis is also supported by the more accurate WDX results (Figure 5.19a in page 131) where stoichiometry between Ca and Ti was observed.

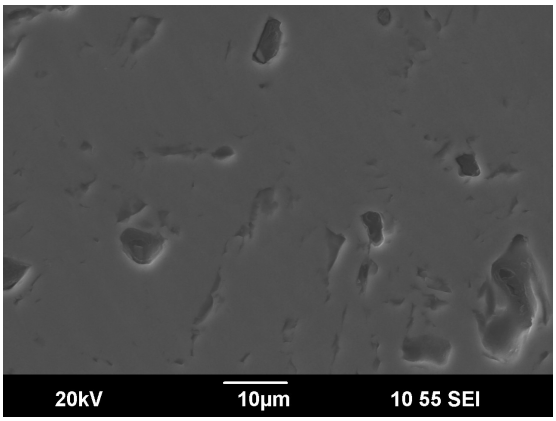
With the doped samples, namely, $La_{0.2}Ca_{0.8}TiO_3$, $La_{0.4}Ca_{0.6}TiO_3$, $La_{0.6}Ca_{0.4}TiO_3$, and $La_{0.8}Ca_{0.2}TiO_3$ (Figures 5.16c to 5.16j) zones with different contrasts were observed in backscattered mode. No clear distinct phases were observed, but rather a mixture with a gradient of contrast. As an example, in Figure 5.16j ($La_{0.8}Ca_{0.2}TiO_3$) a darker zone was present at the left of the image, however, it was not clear where was the "boundary" between the dark zone and the rest of the surface. Additionally, the contrast of this dark zone is not totally homogeneous as slightly lighter zones were visible within it. The distinction of contrast on the backscattered images were not visible on the secondary mode for example, Figure 5.16c versus Figure 5.16d. La and Ca have very different atomic numbers, so the variations in the La/Ca ratio (without change of Ti and O) should result in high contrast. The contrast between the areas then indicated a difference in chemical composition but not necessarily a dramatic one. The analysis of the backscattered images indicate that the chemical compositions were less homogeneous for the $La_{0.4}Ca_{0.6}TiO_3$ and $La_{0.6}Ca_{0.4}TiO_3$ samples. EDX analysis confirmed that the brighter zones corresponded to a higher La content and the darker areas to high Ca content. For all the points of the doped samples, the Ti concentration was very stable, with variation lower than 1%. For all the points, the ratio (La+Ca)/Ti was close to one

and was very stable. This indicated that no non-perovskite or layered perovskites phases were in place. The ratio La/Ca was more variable. La/Ca were more stable for the samples $La_{0.2}Ca_{0.8}TiO_3$ (La between 10% and 13%) and $La_{0.8}Ca_{0.2}TiO_3$ (La between 38% and 42%). In agreement with the observations on the backscattered images, the ranges of concentration of La in $La_{0.4}Ca_{0.6}TiO_3$ $La_{0.6}Ca_{0.4}TiO_3$ were wider, respectively, from 16% to 32% and from 25% to 39%. The data of the EPMA/WDX analysis was then performed to provide more accurate quantifications (Figures 5.19 and 5.20). For $LaTiO_3$, small bright regions were present with a main phase in Figures 5.16k and 5.16l. No darker regions were observed. The EDX (Figures 5.17 and Table 5.17f) indicate that the main phase was $LaTiO_3$. The bright regions were a La-rich phase such as target 2 on the figure with only a small amount of Ca (5%).

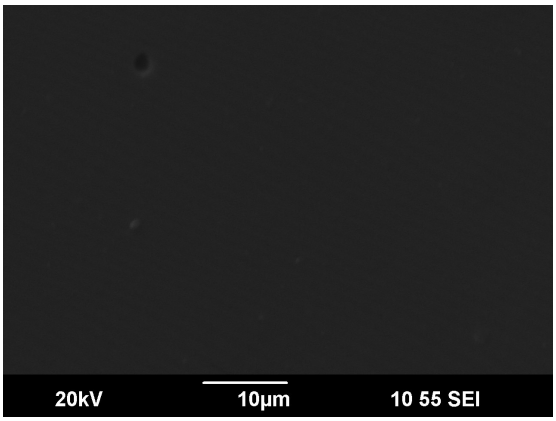
Figure 5.18 is an EDX spectrum of the sample $La_{0.4}Ca_{0.6}TiO_3$ which shows Ca and La overlapping at approximately 4.05 keV in addition to Ti and La overlapping at approximately 4.3 keV and 5 eV. Between 0 and 1 keV, the three elements possess distinguishable X-ray energies, but they can be disturbed by C or O and cannot alone provide very accurate quantification of the elements. Ca and La have distinguishable peaks at more than 3 keV energy, even if those of La are not very intense. Ti does not have well distinguished peaks at energies higher than 3 keV. Overall, the EDX results, while reproducible, should be calibrated and referenced to the more accurate methods such as WDX for the quantification.



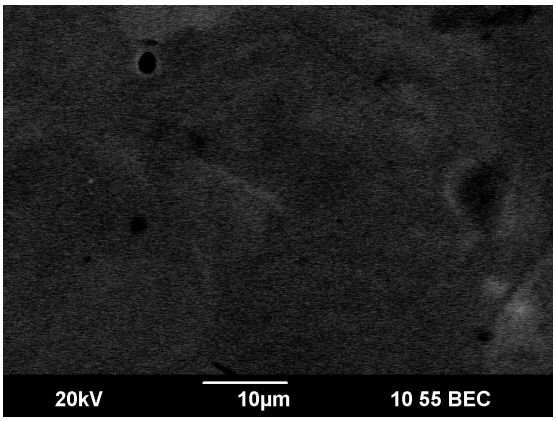
(a) $CaTiO_3$, backscattered electron mode.



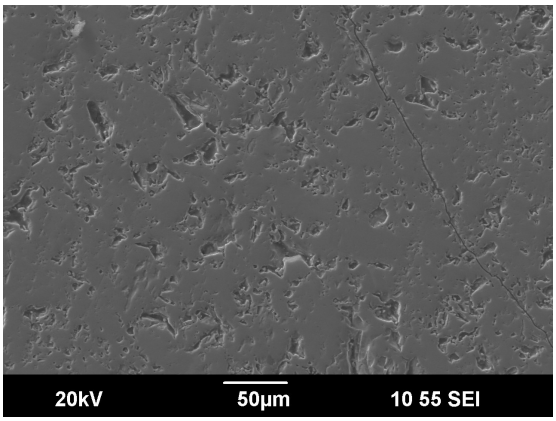
(b) $CaTiO_3$, secondary electron mode.



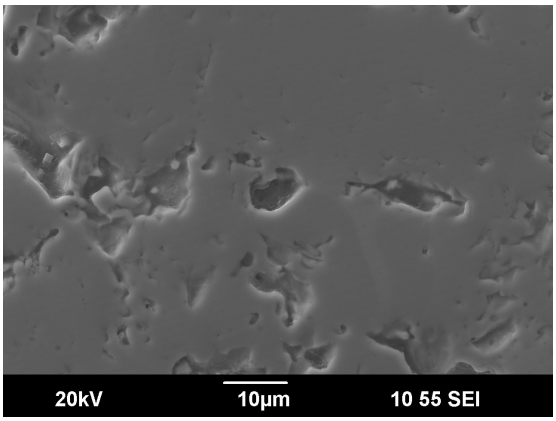
(c) $La_{0.2}Ca_{0.8}TiO_3$, secondary electron mode.



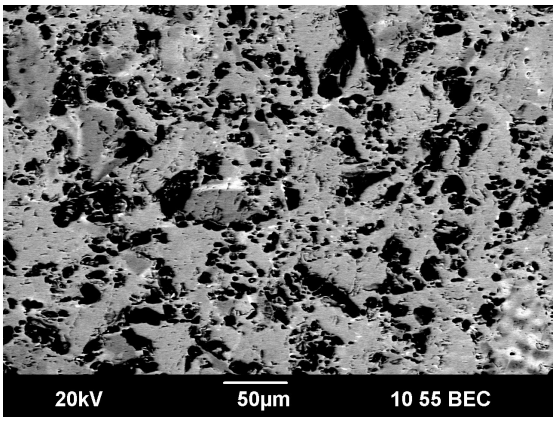
(d) $La_{0.2}Ca_{0.8}TiO_3$, backscattered electron mode.



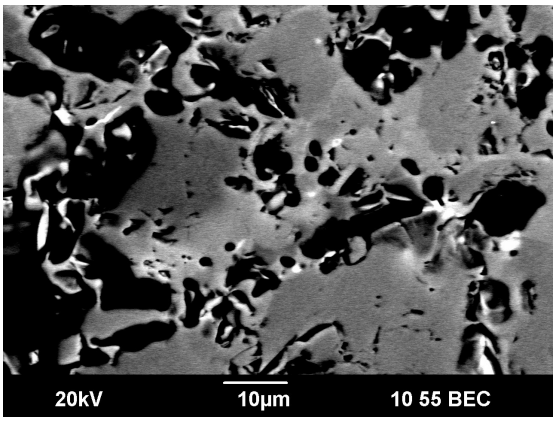
(e) $La_{0.4}Ca_{0.6}TiO_3$, backscattered electron mode.



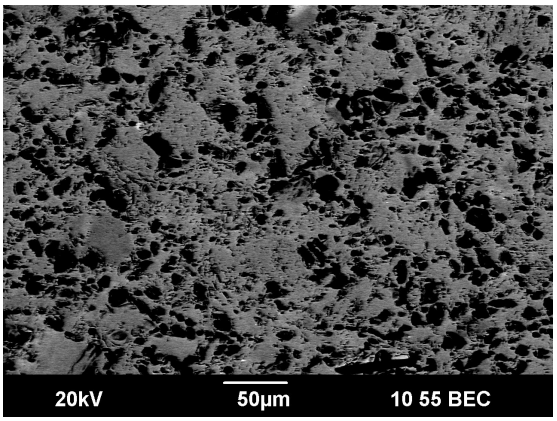
(f) $La_{0.4}Ca_{0.6}TiO_3$, backscattered electron mode.



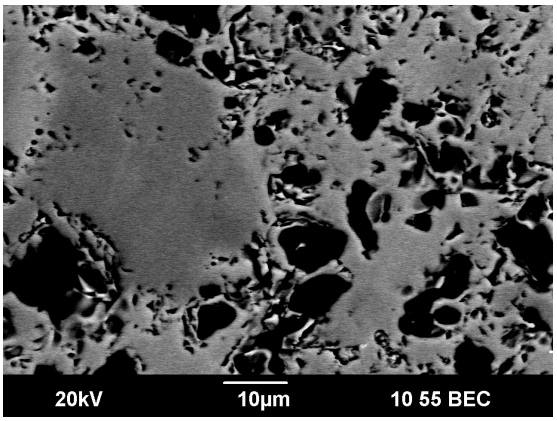
(g) $La_{0.6}Ca_{0.4}TiO_3$, backscattered electron mode.



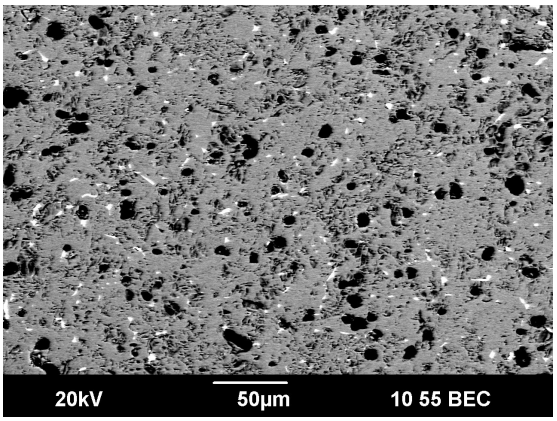
(h) $La_{0.6}Ca_{0.4}TiO_3$, backscattered electron mode.



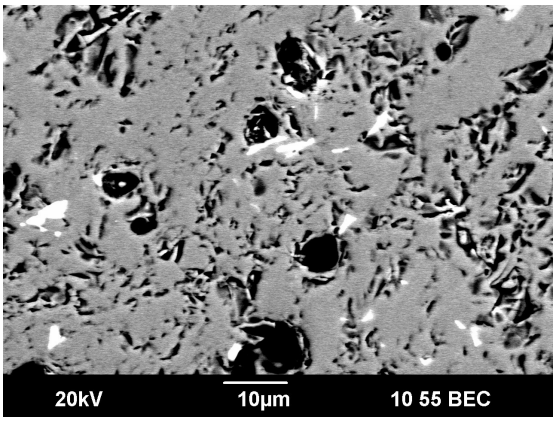
(i) $La_{0.8}Ca_{0.2}TiO_3$, backscattered electron mode.



(j) $La_{0.8}Ca_{0.2}TiO_3$, backscattered electron mode.

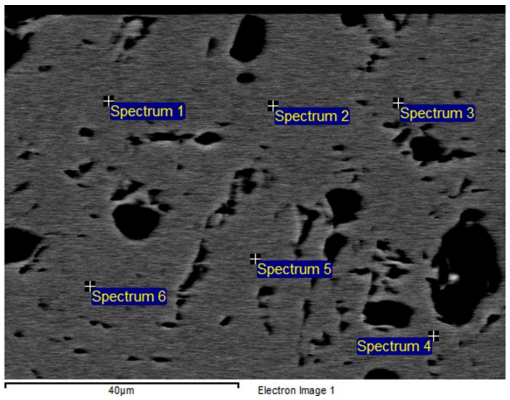


(k) $LaTiO_3$, backscattered electron mode.

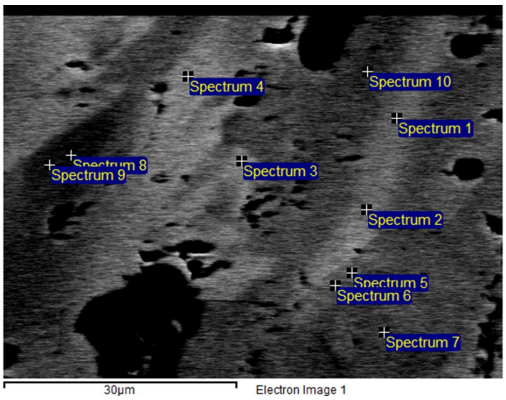


(l) $LaTiO_3$, backscattered electron mode.

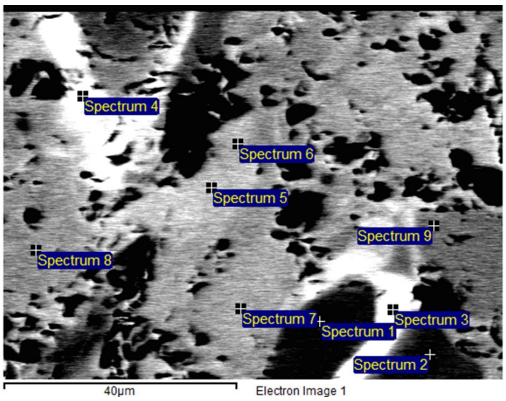
Figure 5.16: SEM images of $La_xCa_{1-x}TiO_3$ melted in argon and sintered by SPS at 1450°C in high vacuum (diffusion pump), with a heating and cooling rate of 100°C per minute and an applied pressure of 40MPa.



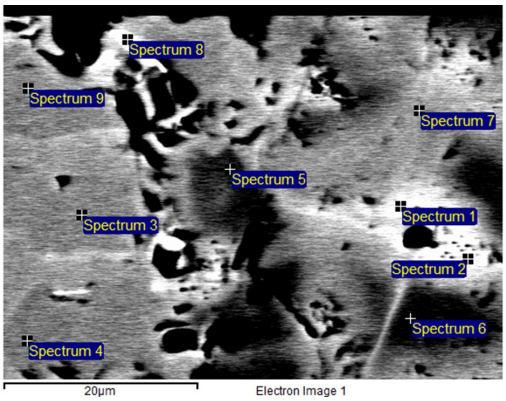
(a) $CaTiO_3$, backscattered electron mode with EDX target positions, results in Table 5.1a.



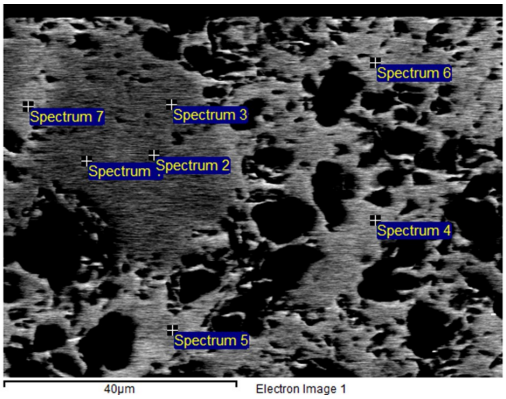
(b) $La_{0.2}Ca_{0.8}TiO_3$, backscattered electron mode with EDX target positions, results in table 5.1b.



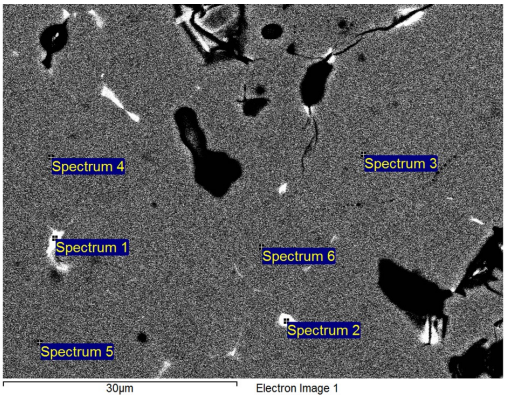
(c) $La_{0.4}Ca_{0.6}TiO_3$, backscattered electron mode with EDX target positions, results in Table 5.1c.



(d) $La_{0.6}Ca_{0.4}TiO_3$, backscattered electron mode EDX with target positions, results in Table 5.1d. The result of point 8 is not in the table because it was unreliable (sulfur detected).



(e) $La_{0.8}Ca_{0.2}TiO_3$, backscattered electron mode with EDX target positions, results in Table 5.1e.



(f) $LaTiO_3$, backscattered electron mode with EDX target positions, results inf Table 5.1f.

Figure 5.17: SEM images with EDX targets of $La_xCa_{1-x}TiO_3$ melted in argon and sintered by SPS at 1450°C in high vacuum (diffusion pump), with a heating and cooling rate of 100°C per minute and an applied pressure of 40MPa. EDX results in Tables 5.1

Table 5.1: EDX targets results of Figures 5.17.

(a) EDX results of $CaTiO_3$ in atomic percent, targets position in Figure 5.17a.

Target	Ca	Ti
1	47.6	52.4
2	47.2	52.8
3	47.2	52.8
4	47.3	52.7
5	47.5	52.5
6	47.4	52.6
Theorectical	50	50

(b) EDX results of $La_{0.2}Ca_{0.8}TiO_3$ in atomic percent, targets position in Figure 5.17b.

Target	Ca	Ti	La	La + Ca
1	36.7	51.3	12.0	48.7
2	36.3	51.3	12.4	48.7
3	35.9	51.4	12.7	48.6
4	35.8	51.4	12.8	48.6
5	37.2	51.5	11.3	48.5
6	37.1	51.5	11.3	48.4
7	37.7	51.6	10.8	48.5
8	38.9	51.4	9.8	48.7
9	38.7	51.4	9.9	48.6
10	38.2	51.3	10.6	48.6
Theorectical	40	50	10	50

(c) EDX results of $La_{0.4}Ca_{0.6}TiO_3$ in atomic percent, targets position in Figure 5.17c.

Target	Ca	Ti	La	La + Ca
1	33.2	51.0	15.9	49.1
2	33.0	51.0	16.0	49.0
3	18.5	51.5	30.0	48.5
4	16.9	50.7	32.3	49.2
5	26.7	50.9	22.4	49.1
6	27.4	51.1	21.6	49.0
7	27.6	51.0	21.5	49.1
8	28.0	51.1	21.0	49.0
9	29.8	51.1	19.1	48.9
Theorectical	30	50	20	50

(d) EDX results of $La_{0.6}Ca_{0.4}TiO_3$ in atomic percent, targets position in Figure 5.17d.

Target	Ca	Ti	La	La + Ca
1	13.6	50.0	36.4	50.0
2	13.6	50.0	36.4	50.0
3	19.1	50.0	30.9	50.0
4	19.3	50.1	30.5	49.8
5	23.3	50.2	26.4	49.7
6	24.2	50.4	25.4	49.6
7	18.4	50.4	31.2	49.6
9	19.3	49.6	31.0	50.3
Theorectical	20	50	30	50

(e) EDX results of $La_{0.8}Ca_{0.2}TiO_3$ in atomic percent, targets position in Figure 5.17e.

Target	Ca	Ti	La	La + Ca
1	11.4	50.2	38.4	49.8
2	11.3	50.2	38.4	49.7
3	11.5	50.0	38.6	50.1
4	9.3	49.5	41.3	50.6
5	9.7	49.6	40.7	50.4
6	7.9	50.0	42.2	50.1
7	8.2	50.3	41.5	49.7
Theorectical	10	50	40	50

(f) EDX results of $LaTiO_3$ in atomic percent, targets position in Figure 5.17f.

Target	Ti	La
1	11.7	88.3
2	5.0	95.0
3	48.1	51.9
4	49.6	50.4
5	49.6	50.4
6	49.8	50.2
Theorectical	50	50

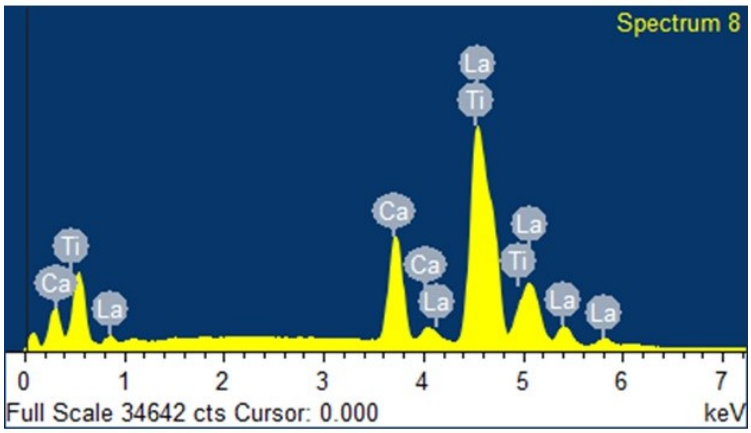
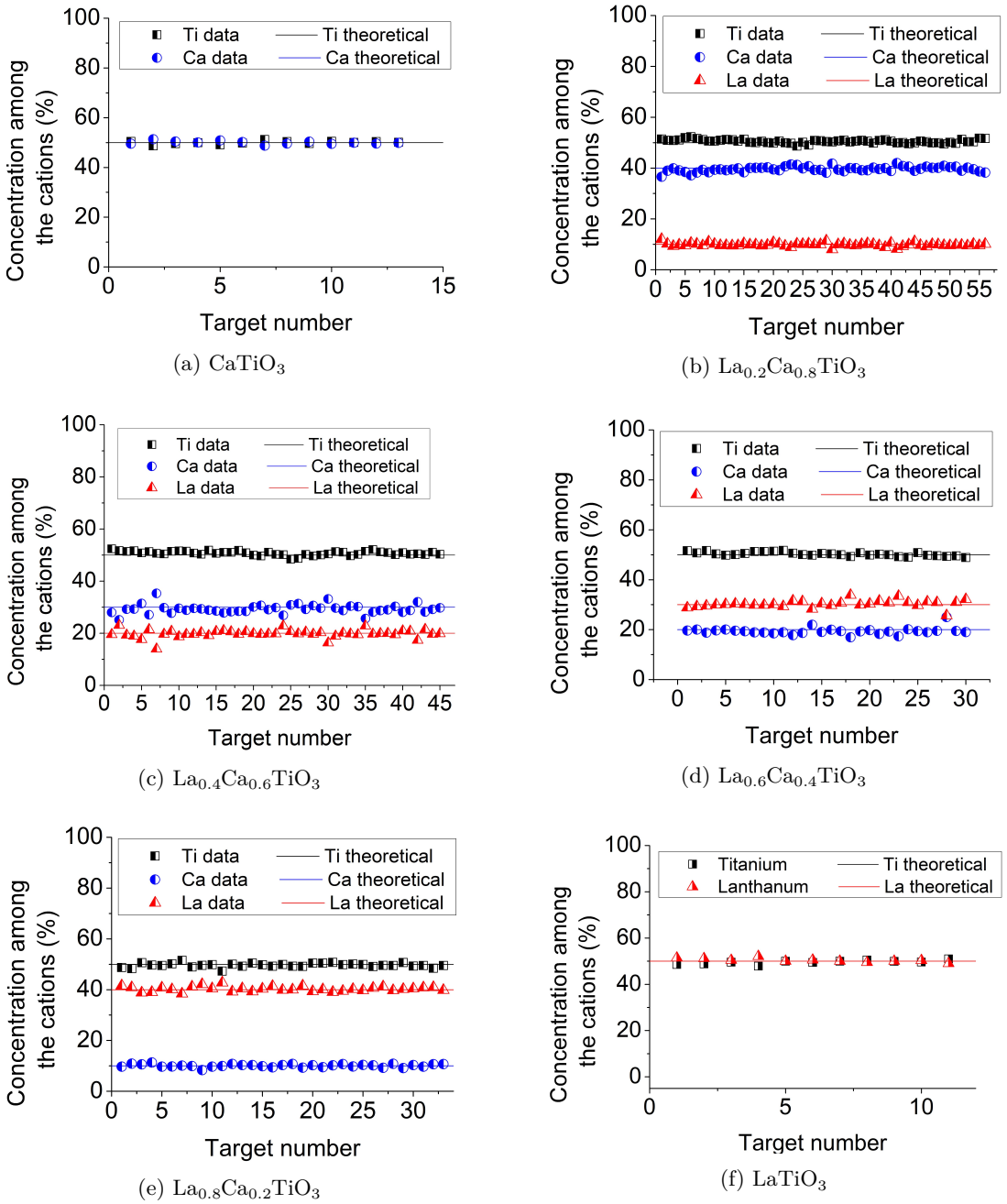


Figure 5.18: EDX spectra of the target number 8 of the sample $La_{0.4}Ca_{0.6}TiO_3$ melted in argon and sintered by SPS at 1450°C in high vacuum (diffusion pump)), with a heating and cooling rate of 100°C per minute and an applied pressure of 40MPa.

EPMA data Figures 5.19 are the plots of the cation chemical compositions of the samples $La_xCa_{1-x}TiO_3$ after the SPS sintering analysed by WDX with an EPMA. Figure 5.20 is the plot of these data in a ternary diagram. The targets for analysis were chosen randomly with the care of avoiding pores as the optical microscope was not powerful enough to do fine analyses of the surfaces. At both ends of the series, undoped $CaTiO_3$ and $LaTiO_3$, the detected chemical compositions were close to the theoretical ones. Samples $La_{0.8}Ca_{0.2}TiO_3$ and $La_{0.2}Ca_{0.6}TiO_3$ showed homogeneous cations concentration with only small variations. For sample $La_{0.6}Ca_{0.4}TiO_3$ variations were small apart from target 28 which had a La concentration among the cations of 25.6%, when the theoretical concentration is 30%. Sample $La_{0.4}Ca_{0.6}TiO_3$ showed the lowest chemical homogeneity, at the farthest of the theoretical composition was target 7 with 14% of La among the cations instead of

20% for the theoretical compositions. However, the chemical compositions of these samples were considered relatively homogeneous as they were close to the theoretical composition. For all of the analysed points, a lower concentration of La was balanced by a higher concentration of Ca, then the sum of La + Ca was always close to the theoretical 50%. For all of the analysed points of all of the samples, the Ca concentration among the cations was very close to the theoretical 50%. These results are in agreement with the SEM observations: no other phase than the perovskite structure was detected, the sample had a relatively homogeneous chemical composition that was centred in the theoretical one. It is then concluded that the La was well inserted in the Ca site for all the $La_xCa_{1-x}TiO_3$ series, while Li et al observed insertion of La in the Ca site, but formation of a Ti rich secondary phase for x higher than 0.2 [176]. Then arc melting followed by an SPS sintering is a suitable method to synthesise donors doped $CaTiO_3$.



(a) $CaTiO_3$

(b) $La_{0.2}Ca_{0.8}TiO_3$

(c) $La_{0.4}Ca_{0.6}TiO_3$

(d) $La_{0.6}Ca_{0.4}TiO_3$

(e) $La_{0.8}Ca_{0.2}TiO_3$

(f) $LaTiO_3$

Figure 5.19: Normalised concentration of La, Ca and Ti detected by the WDX of $La_xCa_{1-x}TiO_3$ melted in argon and sintered by SPS at 1450°C in high vacuum (diffusion pump), with a heating and cooling rate of 100°C per minute and an applied pressure of 40MPa.

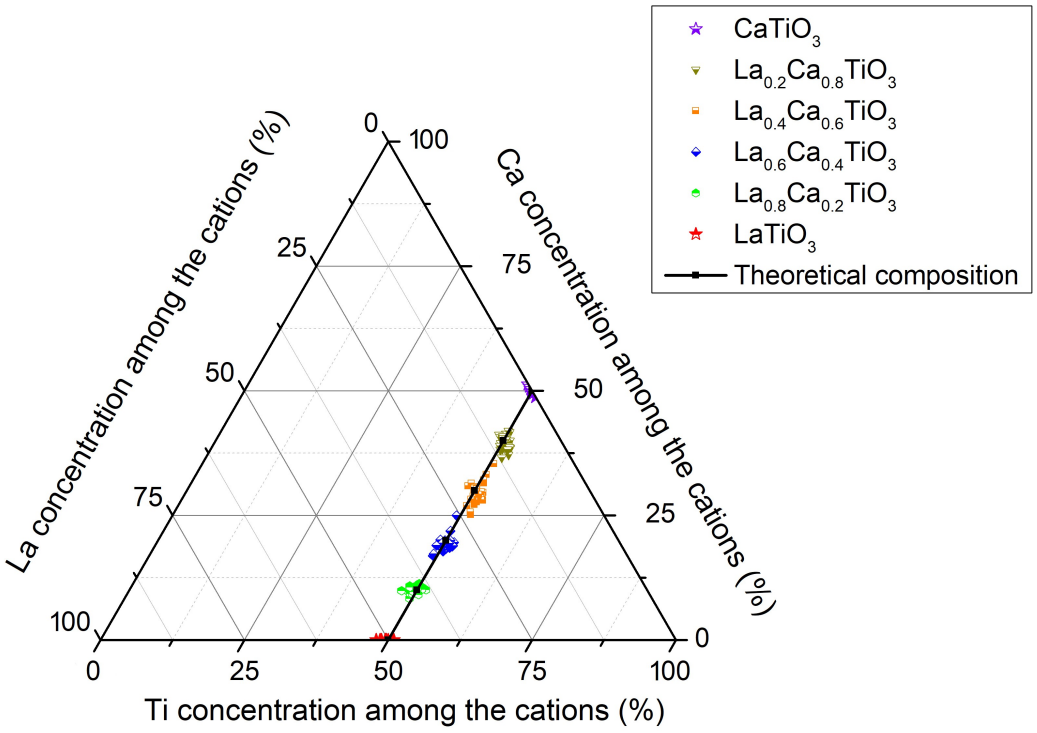


Figure 5.20: Ternary diagramme of the normalised concentration of La, Ca and Ti detected by the WDX of $La_xCa_{1-x}TiO_3$ melted in argon and sintered by SPS at 1450°C in high vacuum (diffusion pump), with a heating and cooling rate of 100°C per minute and an applied pressure of 40MPa.

5.3 Evaluation of the thermoelectric performances

Electrical properties Figures 5.21, 5.22, and 5.23 show respectively the temperature dependence of the electrical conductivity, the temperature dependence of the absolute Seebeck coefficient, and the temperature dependence of the power factor of the samples $La_xCa_{1-x}TiO_3$ for x=0.05, x=0.1, x=0.2, and x=0.3 at different sintering temperatures. The measurements were performed in static He to measure the Seebeck coefficient. For each of these four compositions the SPS sintering temperature played a key role in the electrical conductivity. For example, at ≈ 220°C the samples $La_{0.05}Ca_{0.95}TiO_3$ sintered at 1400°C, 1450°C, or 1500°C, respectively had an electrical conductivity of 68 ± 1.9 $S.cm^{-1}$, 119 ± 3.3 $S.cm^{-1}$, and 251 ± 6.9 $S.cm^{-1}$. At 30°C samples $La_{0.3}Ca_{0.7}TiO_3$ sintered at 1400°C, 1450°C, and 1500°C respectively had an electrical conductivity of 1850 ± 51 $S.cm^{-1}$, 2280 ± 63 $S.cm^{-1}$, and 2880 ± 79 $S.cm^{-1}$. As the processing did not significantly affect the density (Figure 5.15 at page 122), it indicates that O vacancies are created during the SPS sintering and create charge carriers as describes in equation 3 and 4 (page 20). This effect was also observed for La doped $SrTiO_3$ [196]. The values obtained were lower than those reported by Li et al, for example they reported 3383 $S.cm^{-1}$ at RT for $La_{0.2}Ca_{0.8}TiO_3$ [176]. Their samples were more conductive because of the higher relative density (96.7%) and the sintering was done (by hot pressing) at a higher temperature (1500°C) and for longer time (two hours). Likewise, La deficient $La_{0.15}Sr_{0.775}TiO_3$ at 473K was around 2335 $S.cm^{-1}$ [100], and $La_{0.08}Sr_{0.92}TiO_3$ produced by solution combustion and SPS was around 3025 $S.cm^{-1}$ at RT [119].

The La content also greatly influences the electrical conductivity by acting as a donor dopant thus increasing the charge carrier concentration, then increasing the electrical conductivity. In this temperature range, all of the samples showed a metal conductor behaviour as the electrical conductivity decreased with the increase of the temperature. Interestingly below 125°C sample $La_{0.2}Ca_{0.8}TiO_3$ sintered at 1450°C had a lower electrical conductivity than $La_{0.1}Ca_{0.9}TiO_3$ sintered at 1450°C and 1500°C but its conductivity decreased to a lower rate and then stayed higher than these two. The undoped $CaTiO_3$ had a different behaviour because of its higher sensitivity toward oxidation, as shown in Figure 5.11 (page 118), indicating that the electrical conductivity decreased

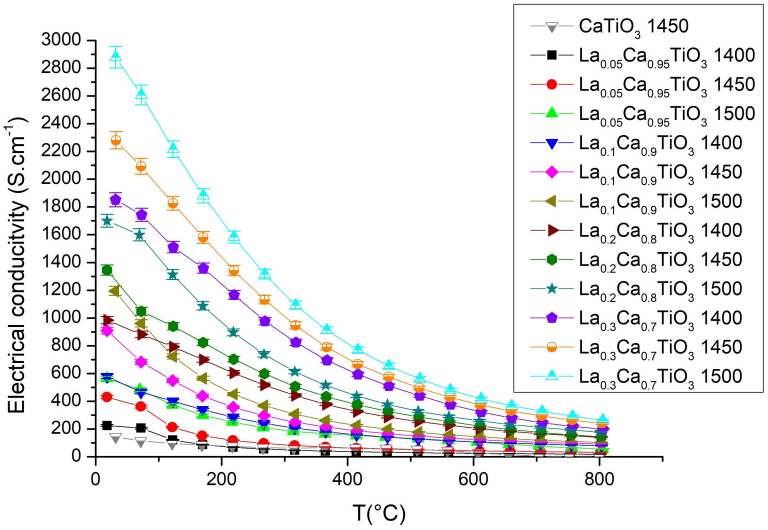


Figure 5.21: Temperature dependence of the electrical conductivity of $La_xCa_{1-x}TiO_3$ after different SPS sintering in high vacuum (diffusion pump), measurement carried in static He with a heating rate of 10°C per minute.

not only because of the increase of temperature.

The values of the absolute Seebeck coefficient, shown in Figure 5.22, increased with the temperature as expected for each sample. The results also show that the Seebeeck coefficient decreased with the increase of the La concentration and by the increase of the SPS sintering temperature. This is because the increase of the charge carrier is detrimental for the Seebeck coefficient. The highest value measured is -287 ± 5.6 µ$V.K^{-1}$ at 800°C for $La_{0.05}Ca_{0.95}TiO_3$ sintered at 1400°C which was also the sample with the lowest conductivity. The sample $La_{0.2}Ca_{0.8}TiO_3$ by Li et al had around -199 $\mu V.K^{-1}$ at 1011K [176]. For a point of comparison, La deficient $La_{0.15}Sr_{0.775}TiO_3$ at 1013 was around -168 $\mu V.K^{-1}$ [100] and $La_{0.08}Sr_{0.92}TiO_3$ produced by solution combustion and SPS was around -238 $\mu V.K^{-1}$ at 1045K [119].

The undoped $CaTiO_3$ behaved differently, in terms of its electrical conductivity. At 700°C the measured Seebeck values switched from negative to positive. It is known that $CaTiO_3$ is either n-type or p-type conductor depending on the oxygen partial pressure [197]. Therefore it is likely that

this change was because of the oxidation during the measurement. The data is not plotted directly as the switch happened during the measurements at 700°C (first measurement : -154 $\mu V.K^{-1}$, second measurement -85 $\mu V.K^{-1}$, third measurement +87 $\mu V.K^{-1}$). All of the data of the sample is plotted in Figure 10.12 in appendice (page 189).

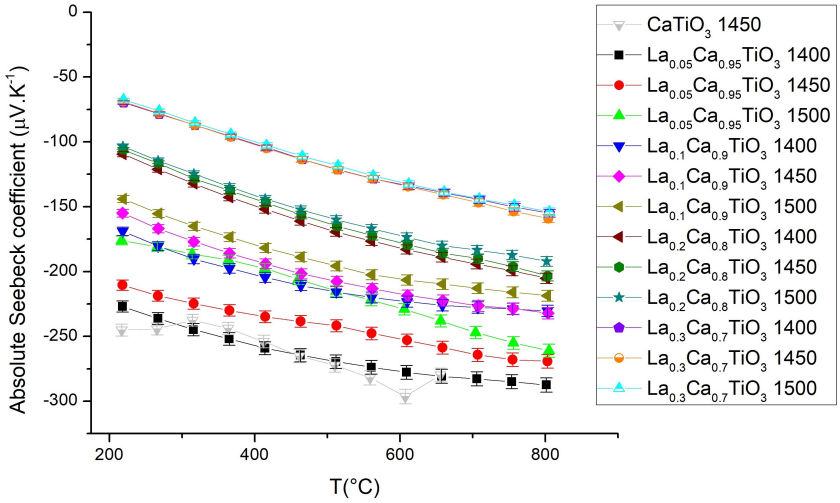


Figure 5.22: Temperature dependence of the Seebeck coefficient of $La_xCa_{1-x}TiO_3$ after different SPS sintering temperature, sintering made in high vacuum (diffusion pump), measurement carried in static He with a heating rate of 10°C per minute and a set gradient of 50°C.

One group of samples, such as the three $La_{0.05}Ca_{0.95}TiO_3$, showed PF continuously decreasing with the temperature. A different group of samples, such as $La_{0.3}Ca_{0.7}TiO_3$ sintered at 1450°C had a quadratic like PF curves, that reached a maximum around 465°C. For high temperature thermoelectric, the figure of merit increases with the temperature, then the PF at the highest temperature is an important characteristic. Considering the power factor at 800°C for the samples sintered at 1500°C the PF increased with the La content until it reached the maximum for $La_{0.2}Ca_{0.8}TiO_3$ with 0.66 $\pm$ 0.03 $mW.m^{-1}.K^{-2}$. Overhall within the temperatures measured, the highest power factor was achieved by $La_{0.2}Ca_{0.8}TiO_3$ sintered at 1500°C with a value of 0.97 $\pm$ 0.05 $mW.m^{-1}.K^{-2}$ around

270°C. In comparison the sample $La_{0.2}Ca_{0.8}TiO_3$ by Li et al reported around 1.04 $W.m^{-1}.K^{-1}$ at 1013K and around 0.98 $W.m^{-1}.K^{-1}$ at 540K [176], while La deficient $La_{0.15}Sr_{0.775}TiO_3$ at 1013K was reported around 1.14 $W.m^{-1}.K^{-1}$ [100], and $La_{0.08}Sr_{0.92}TiO_3$ produced by solution combustion and SPS it was 0.94 $W.m^{-1}.K^{-1}$ at 1045K [119]. The power factor we obtained is comparable to the values of other oxides thermoelectrics but lower than the best oxides thermoelectrics reported.

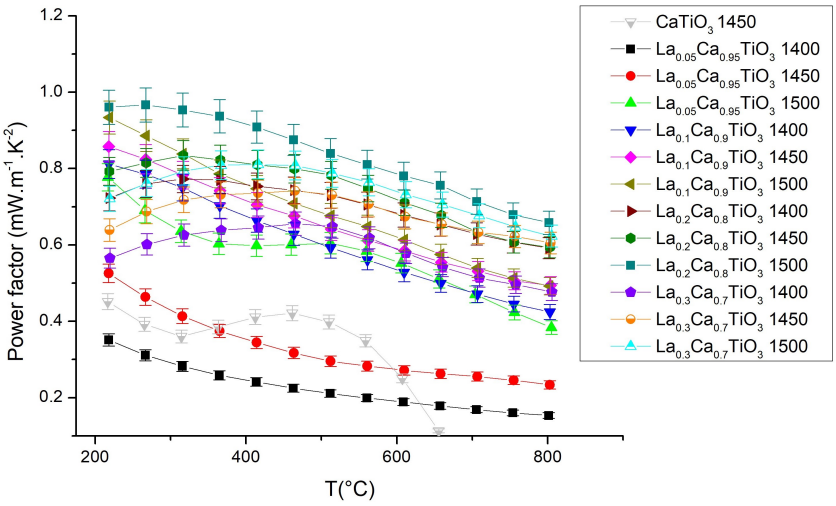


Figure 5.23: Temperature dependence of the power factor of $La_xCa_{1-x}TiO_3$ after a SPS sintering at 1450°C in high vacuum (diffusion pump) for 10 minutes with a heating and cooling rate of 100°C/min and an applied pressure of 40 MPa of the powder synthesized by arc melting in argon, measurement carried in static He with a heating rate of 10°C per minute and a set gradient of 50°C.

Figure 5.24 presents the temperature dependence of the electrical conductivity of the series of $La_xCa_{1-x}TiO_3$ after a SPS sintering at 1450°C. The measurements were performed in flowing 5% H_2/95%Ar to limit the oxidation of the samples during the measurement. Until x=0.5 the increase of the La content increased the electrical conductivity at room temperature. More La induced a decrease in the conductivity but not in a consistent way. More specificly at RT the electrical conductivities were in the following order : $La_{0.8}Ca_{0.2}TiO_3 \approx La_{0.7}Ca_{0.3}TiO_3 < La_{0.6}Ca_{0.4}TiO_3 <$

$La_{0.9}Ca_{0.1}TiO_3$, which is consistent with the measured relative density (Figure 5.15 in page 122). The TGA data indicated that the carrier concentration to be proportional to the La content for all of the compositions, however, this was acompanied by a decrease of the sinterability with the La content. At higher temperature their electrical condutivity was also determined by their resistance to oxidation. Because samples with a lower La content were more resistant to oxidation, they keept a relatively high electrical conductivity at high temperature, while samples with a high La content became poorly conductive. Sample $La_{0.5}Ca_{0.5}TiO_3$ illustrated this trend the most, while it was the most conductive at RT with 3200 ± 90 $S.cm^{-1}$, its measured conductivity at 800°C was lower than $La_{0.05}Ca_{0.95}TiO_3$.

The influence of the sintering temperature from 1450°C was limited. For example a sample of $La_{0.5}Ca_{0.5}TiO_3$ was SPS sintered at 1500°C and the same electrical conductivity at room temperature was measured compared to the sample sintered at 1450°C. In addition $La_{0.2}Ca_{0.8}TiO_3$ and $La_{0.5}Ca_{0.5}TiO_3$ sintered at 1550°C resulted in a brittle and partially melted sample, with a poor electrical conductivity. This led to the decision to sinter all of the other compositions at 1450°C only. As mentioned in the previous subsection, samples of $La_{0.2}Ca_{0.8}TiO_3$ and $La_{0.5}Ca_{0.5}TiO_3$ were made with a ball milling steps in an attempt to increase further the density of the samples. However their electrical conductivity at RT were much lower than the hand milled samples, respectively 700 ± 21 $S.cm^{-1}$ and 50 ± 2 $S.cm^{-1}$. Ball milling involved more steps in the powder preparation, then it significantly increased the risk of impurity introduction. Ball milling steps are associated with contaminations [198], as an example, Bumrungpon et al observed YSZ contamination by SEM in $Bi_{0.3}Sb_{0.7}Te_3$ ball milled at 150 rpm [199]. In our case the addition of YSZ grains in the bulk or the inclusion of YSZ at the grain boundaries could decrease the electrical conductivity. Y could be inserted in the B-site of the perovskite structure [200], in that case Y would act as an acceptor and would decrease the charge carrier concentration. At the moment it is unknown what exactly was the reason of that low electrical conductivity.

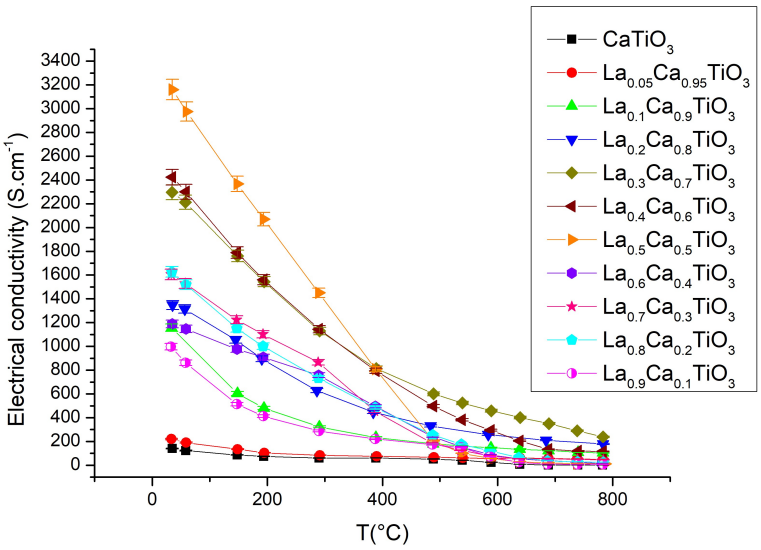


Figure 5.24: Temperature dependence of the electrical condutivity of $La_xCa_{1-x}TiO_3$ after a SPS sintering at 1450°C in high vacuum (diffusion pump) for 10 minutes with a heating and cooling rate of 100°C/min and an applied pressure of 40 MPa of the powder synthesized by arc melting in argon, measurement carried in 5% H_2/95%Ar with a heating rate of 5°C per minute.

Thermal properties Figures 5.25 is the plot of the temperature dependence of the thermal diffusivity of $La_xCa_{1-x}TiO_3$ SPS sintered at different temperatures. As expected the thermal diffusivity decreased with the temperature for all of the samples. Figure 5.26 is the thermal diffusivity in a Arrhenius plot, the thermal diffusivity decreased linearly with $\frac{1000}{T}$. The overall thermal diffusivity increased with the La content and the sintering temperature as the electrical conductivity was increased by both (Figure 5.21), then the electronic component of the thermal conductivity was significantly increased. This is the opposite of what was observed by Li et al for $La_xCa_{1-x}TiO_3$, in their case the thermal diffusivity decreased with the doping level, according to them, because of the increase of the Ti-rich secondary phase. They measured a thermal diffusivity around 0.84 $mm^2.s^{-1}$ for $La_{0.2}Ca_{0.8}TiO_3$ at 750°C [176]. A lower thermal diffusivity was measured in our case for $La_{0.2}Ca_{0.8}TiO_3$ with 0.79 ± 0.039 $mm^2.s^{-1}$.

Similar to the electrical conductivity the influence of the SPS sintering temperature was the highest

for $La_{0.3}Ca_{0.7}TiO_3$. With the increase of the temperature, the differences of thermal diffusivity between the samples were smaller, at 800°C they were contained between 0.89 ± 0.05 $mm^2.s^{-1}$ and 0.76 ± 0.04 $mm^2.s^{-1}$ instead of 2.1 ± 0.1 $mm^2.s^{-1}$ and 1.29 ± 0.07 $mm^2.s^{-1}$ at 50°C.

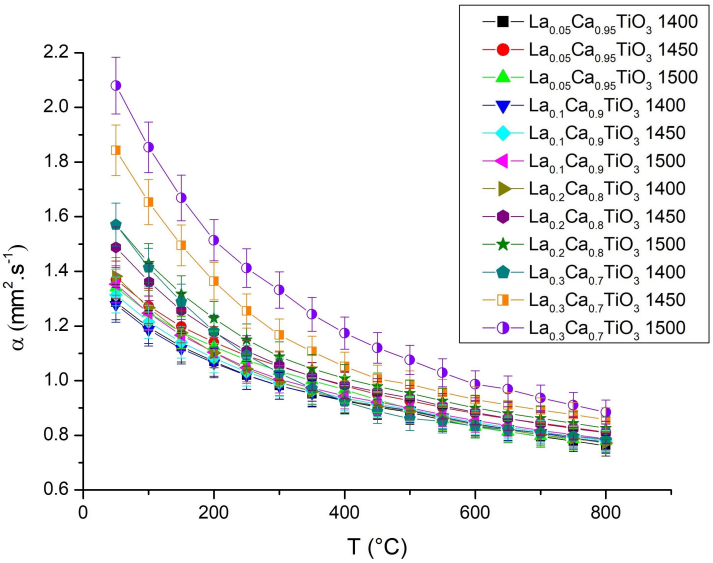


Figure 5.25: Temperature dependence of the thermal diffusivity of $La_xCa_{1-x}TiO_3$ after a SPS sintering different temperature in high vacuum (diffusion pump) for 10 minutes with a heating and cooling rate of 100°C/min and an applied pressure of 40 MPa of the powder synthesized by arc melting in argon, measurement carried in N_2 flow.

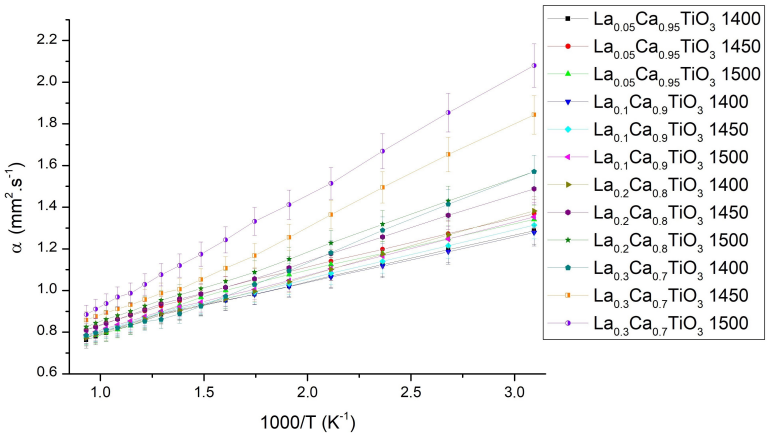


Figure 5.26: Arrhenius plot of the temperature dependence of the thermal diffusivity of $La_xCa_{1-x}TiO_3$ after a SPS sintering different temperature in high vacuum (diffusion pump) for 10 minutes with a heating and cooling rate of 100°C/min and an applied pressure of 40 MPa of the powder synthesized by arc melting in argon, measurement carried in N_2 flow.

5.4 Summary

In conclusion, for the first time, the complete solid solution of the perovskite $La_xCa_{1-x}TiO_3$ ($0 \leq x \leq 1$) was successfully fabricated by a combination of arc melting and SPS and the functional properties were studied. XRD, TGA, and EPMA experiments showed that La was inserted in the Ca site for the whole series of $La_xCa_{1-x}TiO_3$ ($0 \leq x \leq 1$) following the electronic compensation doping mechanism. WDX data showed that the atomic ratio of the total A-site cations (Ca^{2+}+La^{3+}) to the B-site Ti cation is homogeneous and close to the nominal ratio of 1:1. The distribution of La and Ca in the grains are more homogeneous than that of La and Ba in $La_xBa_{1-x}TiO_3$. The influence of the doping level and the SPS parameters on the electrical and thermoelectric properties were studied. Similar to that observed in $La_xBa_{1-x}TiO_3$, arc melting and SPS enhanced the reactions of donor doping and oxygen loss, creating electrons and high electrical conductivity. A high electrical conductivity of 3,200 $S.cm^{-1}$ at room temperature was observed in the composition $La_{0.5}Ca_{0.5}TiO_3$. The high power factor of 0.97 $mW.m^{-1}.K^{-2}$, obtained at 270°C in the sample $La_{0.2}Ca_{0.8}TiO_3$ sintered at 1500°C, is comparable to the highest values among existing n-type thermoelectric materials but at

a much higher temperature (∼740°C). This work shows significant potential of using arc melting and SPS to fabricate highly conductive $La_xCa_{1-x}TiO_3$ to fill the gap of thermoelectric materials in the intermediate temperature range.

6 Synthesis, structural, and thermoelectric properties of $La_xCa_{1-(3/2x)}TiO_3$

6.1 Introduction

In their work, Lu et al made A-site deficient La-doped $SrTiO_3$ with actual A-site vacancies [100]. Some of the $La_xSr_{1-(3x/2)}TiO_3$ they made had high thermoelectric performances, with a figure of merit higher than 0.3 at 973K for x from 0.1 to 0.175, and were relatively resistant against oxidation in air at high temperatures. Other studies also showed that making A-site deficient $SrTiO_3$ could increase the performance of the doped $SrTiO_3$ [98,99,136]. Therefore it was decided that La-doped $CaTiO_3$ with A-site deficient would be produced by arc melting and SPS sintering to try to improve its thermoelectric properties. This section shows the main results obtained so far. There was no data collected on the thermal properties as no suitable measurements could have been made with the equipment available.

6.2 Investigation of the doping mechanism by structural and microstructural analysis.

XRD Figures 6.1 and 6.2 are, respectively, the powder XRD patterns and the expanded powder XRD patterns centred between 45° and 50° of the system $La_xCa_{1-(3/2x)}TiO_3$ produced by arc melting and SPS sintering. A shift to the lower angle is easily observed indicating an insertion of the La in the A-site, for x=0.1 and x=0.2 in which only the perovskite phase was observed, the symmetry of the crystal structure decreased with La content as the peak splitting is more visible, another peak at the right of [040] is visible, probably [230] or [212]. However, for x=0.3 a peak at approximately 25.24° was also present and this peak can be attributed to a TiO_2 secondary phase that indicates that the creation of cation vacancies may not have been achived.

For x=0.1 and x=0.2, with the hypothesis that all the excesses of Ti compare to the sum of (Ca + La) was forming a secondary phase, then the chemical composition of the main phase would be respectively $La_{0.10588}Ca_{0.8941}TiO_3$ and $La_{0.2118}Ca_{0.7882}TiO_3$ and TiO_2 for the secondary phase.

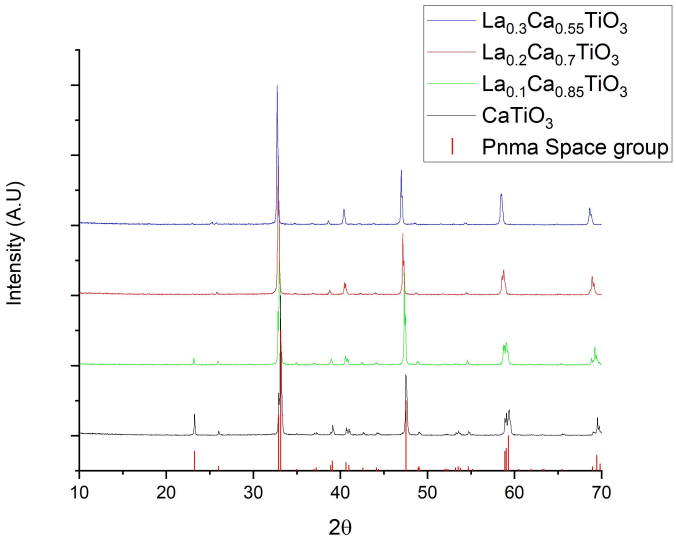


Figure 6.1: XRD patterns of $La_xCa_{1-(3/2x)}TiO_3$ melted in argon and sintered by SPS at 1450°C in high vacuum (diffusion pump), with a heating and cooling rate of 100°C per minute and an applied pressure of 40MPa.

These two compositions were similar to the one for one doping $La_xCa_{(1-x)}TiO_3$ with a slightly higher ratio of La/Ca. If A-site vacancies were generated, then it would be expected that the lattice volume would be smaller compared to the one to one doping. On the other hand, if no cation vacancies were generated then an increase of the lattice volume would be expected as the ratio La/Ca is higher. Figure 6.3 is Figure 6.2 with the addition of the powder XRD patterns of the samples $La_{0.1}Ca_{0.9}TiO_3$ and $La_{0.2}Ca_{0.8}TiO_3$. It can be seen that the peak positions of $La_xCa_{1-(3/2x)}TiO_3$ were shifted to the smaller angle indicating a higher lattice volume compared to $La_xCa_{(1-x)}TiO_3$. Thus the creation of A-site vacancies was unlikely or in a small concentration compared to the TiO_2 secondary phase.

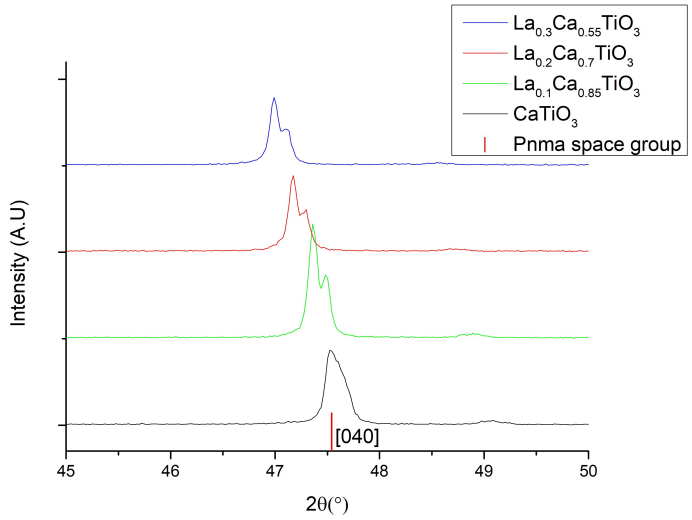


Figure 6.2: Expanded XRD patternd of $La_xCa_{1-(3/2x)}TiO_3$ melted in argon and sintered by SPS at 1450°C in high vacuum (diffusion pump), with a heating and cooling rate of 100°C per minute and an applied pressure of 40MPa.

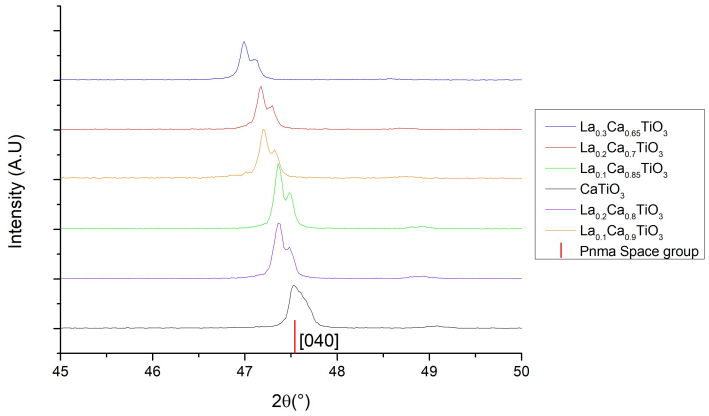
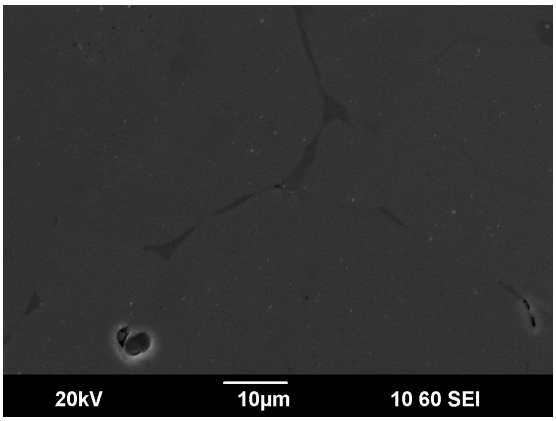


Figure 6.3: Expanded XRD patterns of $La_xCa_{1-(3/2x)}TiO_3$ and $La_xCa_{(1-x)}TiO_3$ melted in argon and sintered by SPS at 1450°C in high vacuum (diffusion pump), with a heating and cooling rate of 100°C per minute and an applied pressure of 40MPa.

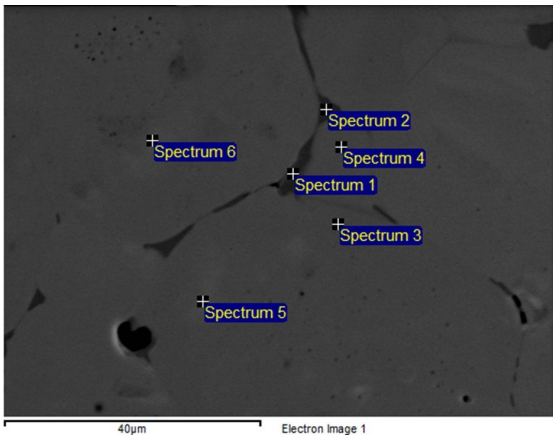
SEM Figures 6.4a to 6.4f are a selection of SEM images of the samples $La_xCa_{1-(3/2x)}TiO_3$ for x=0.1, x=0.2 and x=0.3 in backscattered or secondary electron mode. Grain boundary shapes like zones with darker contrast than the main area can be seen on Figure 6.4a. The main area was very likely to be the perovkite phase detected by the XRD in Figure 6.1. Secondary electron mode is known to have the contrast mostly determined by the topography, then these darker zones should be at a different z position (z-axis) than the main area. Figure 6.4b was at the same location than Figure 6.4a but in backscattered electron mode. Small variations of contrast was observed in the main zone, the contrast between the two zones was more pronounced, indicating a different chemical composition. The results of the EDX are in Table 6.1, but while the main phase showed a chemical composition approaching the theoretical one, the secondary phase was a very Ti-rich phase with a small content of aluminium. The images of the secondary electron mode (Figures 6.4a and 6.4c) suggested that the secondary phase had a lower height than the main phase, making small accumulations of aluminium from the aluminium colloid solution used for the sample preparation possible. No aluminium was detected in the main phase. As single phase $CaTi_{0.9}Al_{0.1}$ has been achieved [201], then it would be expected that aluminium contamination during the synthesis or the SPS sintering lead to a detectable presence of aluminium in the main phase as well. It seems more probable that the aluminium came from the colloid solution used for the polishing, thus the secondary phase was likely to be only titanium oxide.

Within the main phase, patches of brighter zones were present, such as target 5 in Figure 6.4b, but the chemical analysis (Table 6.1) did not show a different chemical composition. These zones were more present in the sample $La_{0.3}Ca_{0.7}TiO_3$ and can be easily observed in Figure 6.4d. The EDX results indicated that the brighter zones had a higher content in La and a lower content of Ca, which was similar to the $La_xCa_{1-x}TiO_3$ system. The secondary phase was also present and can be seen at the top of the Figure 6.4d but no EDX has been carried out. The amount of secondary phase was more visible for sample $La_{0.3}Ca_{0.55}TiO_3$. The theoretical ratio (La+Ca)/Ti for x=0.1, x=0.2 and x=0.3 are respectively 0.95, 0.9, and 0.85; excluding the Ti rich phase, the EDX gave respectively 0.93, 0.92, and 0.90, whereas the average for the undoped $CaTiO_3$ was 0.90 (Table 5.1a).

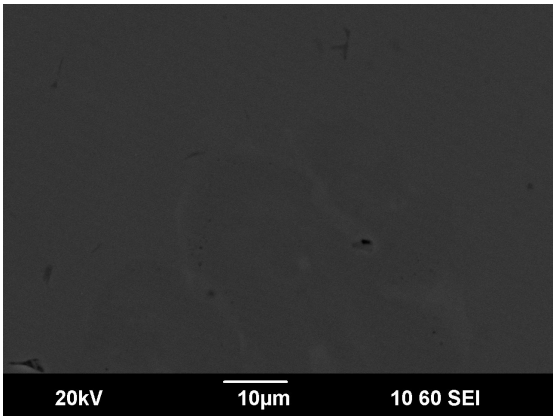
While the A/B ratio was decreasing with x increasing, this diminution was far from the theoretical one. The accuracy of the EDX does not allow us to state that A-site vacancies were not formed because the measured A/B ratio was not compatible, but when combined with the detection of a Ti rich phase by SEM and an attributed TiO_2 peak in the XRD pattern (Figure 6.1), the indication of the formation of a main perovskite phase with a A/B ratio close to one and the formation of a TiO_2 phase with the excess of Ti was very strong. It was unknown if it was only the restricted amount of O in the reaction that leads to the formation of a secondary phase, the repartition of the O content (and so the Ti oxidation stats of the perovkite phase) of the TiO_2 phase and of the main phase was also unknown. It has been observed that the brittleness of the samples increased with the La content, and all the sintered $La_{0.3}Ca_{0.55}TiO_3$ broke into many small pieces while handling, making the measurement of the electrical properties not possible, while the other composition (x=0.1 and x=0.2) broke in bigger pieces making the electrical measurement possible but not the thermal diffusivity measurment. The secondary TiO_2 phase was likely responsible for this behaviour.



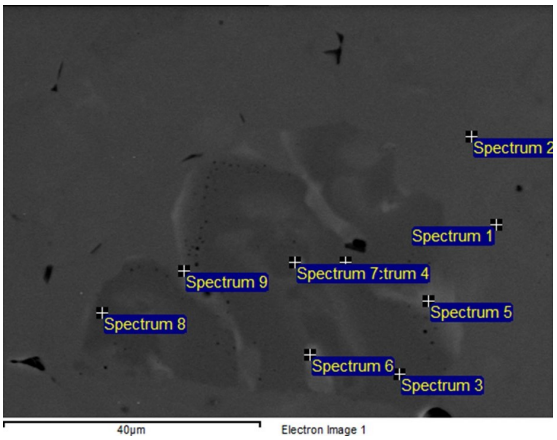
(a) $La_{0.1}Ca_{0.85}TiO_3$, secondary electron mode.



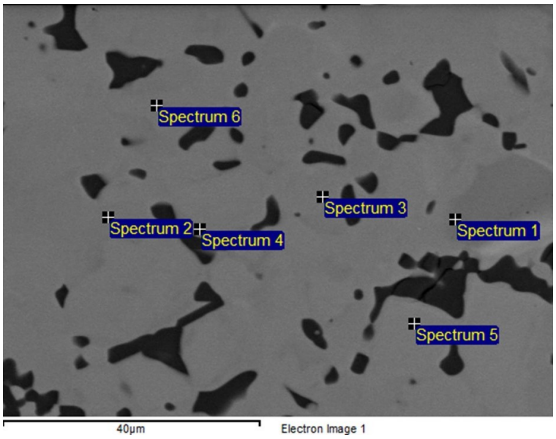
(b) EDX targets of $La_{0.1}Ca_{0.85}TiO_3$, results in Table 6.1, backscattered electron mode.



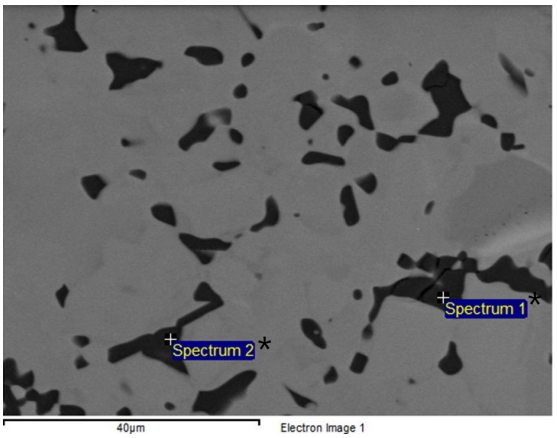
(c) $La_{0.2}Ca_{0.7}TiO_3$, secondary electron mode.



(d) EDX targets of $La_{0.2}Ca_{0.7}TiO_3$, results in Table 6.2, backscattered electron mode.



(e) $La_{0.3}Ca_{0.55}TiO_3$, results in Table 6.3, backscattered electron mode.



(f) $La_{0.3}Ca_{0.55}TiO_3$, results in Table 6.3, backscattered electron mode.

Figure 6.4: Selection of SEM images of $La_xCa_{1-(3/2x)}TiO_3$ melted in argon and sintered by SPS at 1450°C in high vacuum (diffusion pump), with a heating and cooling rate of 100°C per minute and an applied pressure of 40MPa.

Table 6.1: EDX targets result of $La_{0.1}Ca_{0.85}TiO_3$ of Figure 6.4b.

Target	Ca (atm%)	Ti (atm%)	La (atm%)	Al (atm%)
1	16.8	77.9	2.1	3.2
2	3.2	92.5	0.6	3.7
3	42.4	51.8	5.8	0
4	42.3	51.9	5.8	0
5	41.4	51.7	6.9	0
6	41.7	51.6	6.7	0
Theoretical	43.59	51.28	5.13	0

Table 6.2: EDX targets result of $La_{0.2}Ca_{0.7}TiO_3$ of Figure 6.4d.

Target	Ca (atm%)	Ti (atm%)	La (atm%)
1	36.4	51.9	11.7
2	36.4	52.1	11.5
3	38.3	51.9	9.8
4	38.3	52.0	9.7
5	32.5	52.2	15.4
6	31.4	52.2	16.4
7	33.6	51.6	14.8
8	38.5	52.1	9.4
9	33.6	52.1	14.4
Theoretical	36.84	52.6	10.53

Table 6.3: EDX targets result of $La_{0.3}Ca_{0.55}TiO_3$ of Figures 6.4e and 6.4f.

Target	Ca (atm%)	Ti (atm%)	La (atm%)	Al (atm%)
1	32.2	52.4	15.4	0
2	29.9	52.3	17.7	0
3	30.2	52.2	17.7	0
4	29.2	53.3	17.5	0
5	28.8	52.4	18.9	0
6	29.9	52.5	17.6	0
1⋆	1.4	97.3	0	1.4
2⋆	1.5	97.1	0	1.4
Theoretical	29.73	54.05	16.22	0

6.3 Evaluation of the electrical performances

Figure 6.5, 6.6, and 6.7 represent the temperature dependence of the electrical conductivity, the Seebeck coefficient, and the power factor of the system $La_xCa_{1-(3/2x)}TiO_3$ respectively. Compared to the one to one doping $La_xCa_{1-x}TiO_3$ SPS sintered at the same temperature, for x=0.1 at 800°C, the electrical conductivity is increase by 9 ± 5.7 %. The Seebeck coefficient was also increased by 3 ± 3.84 % which is within the margin of error and the power factor was increased by 14 ± 9.48 %. For x=0.2, the electrical conductivity at 800°C was increased by 12 ± 5.61 % and the absolute Seebeck coefficient reduced by 6 ± 3.84 %, leading to an almost identical power factor, approximately 0.59 ± 0.03 $mW.m^{-1}.K^{-2}$. The increase of the power factor for x=0.1 may be the results of a lower O content or a more optimal La concentration. It was reported that reduced TiO_2 is a thermoelectric material [202–204], then the presence of a TiO_2 secondary phase could increase the electrical conductivity without reducing the absolute Seebeck coefficient compared to $La_xCa_{1-x}TiO_3$. However the amount of secondary phase in the samples x=0.1 and x=0.2 were different. Additionally, the O content of the secondary phase could also be different in these two samples. Thus, the presence of a TiO_2 secondary phase could either be beneficial, neutral or detrimental to the thermoelectric performances, depending on each sample's chemical composition.

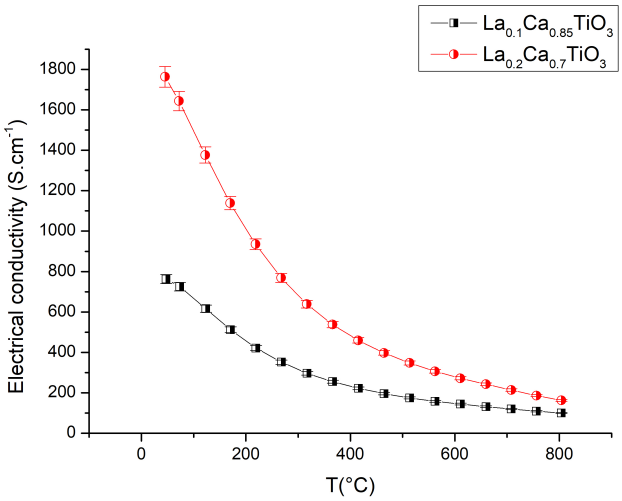


Figure 6.5: Temperature dependence of the electrical conductivity of $La_xCa_{1-(3/2x)}TiO_3$ melted in argon and sintered by SPS at 1450°C in high vacuum (diffusion pump) for 10 minutes with a heating and cooling rate of 100°C per minute and applied pressure of 40MPa, measurement carried in static He with a heating rate of 10°C per minute and a set gradient of 50°C.

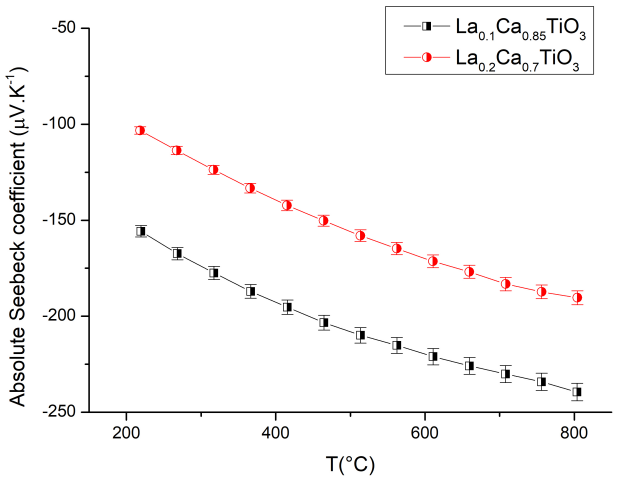


Figure 6.6: Temperature dependence of the Seebeck coefficient of $La_xCa_{1-(3/2x)}TiO_3$ melted in argon and sintered by SPS at 1450°C in high vacuum (diffusion pump) for 10 minutes with a heating and cooling rate of 100°C per minute and applied pressure of 40MPa, measurement carried in static He with a heating rate of 10°C per minute and a set gradient of 50°C.

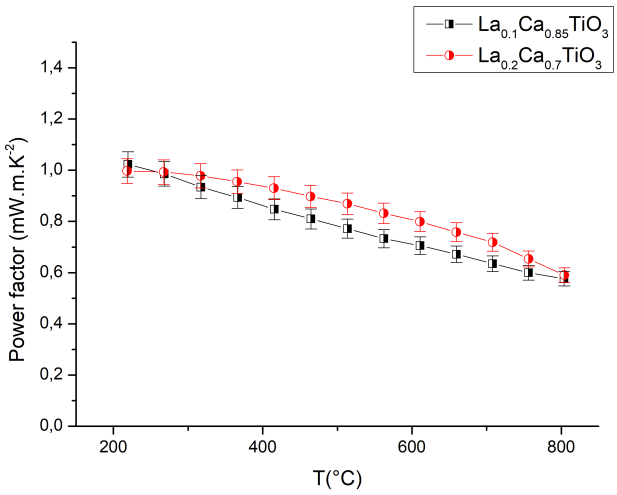


Figure 6.7: Temperature dependence of the power factor of $La_xCa_{1-(3/2x)}TiO_3$ melted in argon and sintered by SPS at 1450°C in high vacuum (diffusion pump) for 10 minutes with a heating and cooling rate of 100°C per minute and applied pressure of 40MPa, measurement carried in static He with a heating rate of 10°C per minute and a set gradient of 50 °C.

6.4 Summary

In conclusion, in addition to the electronic compensation doping mechanism studied in section 4 and section 5 for $La_xBa_{1-x}TiO_3$ and $La_xCa_{1-x}TiO_3$, attempts were made to synthesise a series of compositions following the ionic compensation doping mechanism based on the general formula $La_xCa_{1-(3/2x)}TiO_3$. This doping mechanism inherently carries A-site deficiency. The aim was to test whether this doping mechanism exists and if so, how does A-site deficiency influences the oxygen loss and the electrical conductivity. The XRD and SEM results revealed the formation of a Ti-rich secondary phase, indicating that it is very unlikely that A-site vacancies were created. Despite the existence of secondary phases, the two compositions $La_{0.1}Ca_{0.85}TiO_3$ and $La_{0.2}Ca_{0.7}TiO_3$ showed both slightly higher electrical conductivity and Seebeck coefficient when compared to the compositions with the same doping La doping level in $La_xCa_{1-x}TiO_3$ ($La_{0.1}Ca_{0.9}TiO_3$ and $La_{0.2}Ca_{0.8}TiO_3$, respectively), giving rise to a high power factor of about 1.0 $mW.m^{-1}.K^{-2}$ at 200°C.

7 Conclusion

In conclusion, the approach of a combination of synthesising metal oxides using the arc melting method and using titanium suboxide (titanium monoxide, TiO) raw material was successful to produce the complete solid solutions of both $La_xBa_{1-x}TiO_3$ with $0 \leq x \leq 1$, and for the first time $La_xCa_{1-x}TiO_3$ with $0 \leq x \leq 1$. Sintering of the as-prepared powders by SPS produced dense ceramics suitable for electrical and thermal characterisations. The XRD, SEM, EPMA, WDX, and TGA data all converged toward the same suggestion that La was inserted in the A-site of the perovskite structure for the both alkaline earth titanates systems studied.

No non-perovskite phase was observed by XRD and SEM and the lattice volume changed with the La content following the Vegard's law. The lattice constants decreased proportionally with the La doping content for $La_xBa_{1-x}TiO_3$ and increased proportionally with the La content for $La_xCa_{1-x}TiO_3$ as the ionic size of La is smaller than Ba and bigger than Ca. The ratios A/B of the chemical composition of the grains (A is the sum of cations at the A-site and B is the Ti cation), measured by WDX were close to one, consistent with the stoichiometry. The distributions of cations at the A-site (La and Ba for $La_xBa_{1-x}TiO_3$, La and Ca for $La_xCa_{1-x}TiO_3$) are inhomogeneous. The degree of inhomogeneity was higher for the $La_xBa_{1-x}TiO_3$ than for the $La_xCa_{1-x}TiO_3$. This inhomogeneity may explain the broadness of the XRD peaks for $La_xBa_{1-x}TiO_3$ and disagreements about the space groups reported in the literature. The mass increase after oxidation measured by TGA was proportional to the La content. This suggests that the Ti oxidation state at RT was proportional to the La doping level for both $La_xBa_{1-x}TiO_3$ and $La_xCa_{1-x}TiO_3$ which is in line with the electronic compensation mechanism. All these results suggest that electronic compensation was the favoured doping mechanism. The ionic compensation mechanism, which has been widely considered as the favourable doping mechanism for samples prepared in air using normal furnaces, was not favoured under the sample preparation conditions used in this study.

For both systems the temperature of oxidation in air was lowered proportionally to the La doping content, making characterisation of the thermoelectric properties at high temperature difficult for samples with high La concentration.

In both systems high electrical conductivity of several thousands $S.cm^{-1}$ were achieved at RT, which has not been achieved before for a $BaTiO_3$ based system. Additionally all compositions exhibited metallic behaviour, which was not the case for similar previous works. For both systems, the electrical conductivity increased with the La doping content. At RT it peaked at x = 0.3 for $La_xBa_{1-x}TiO_3$ and at x = 0.5 for $La_xCa_{1-x}TiO_3$. The electrical conductivity increased because of the increase in the charge carrier concentration, until overpassed by the decrease of the relative density of the ceramic pellets as the relative density decreased with the La doping, which affected the carrier mobility. In both cases, the SPS temperature influenced the electrical conductivity of the sintered pellets as more O vacancies were produced at higher temperatures. For both systems the values of the Seebeck coefficient lowered with the doping content, in line with an electronic compensation mechanism and increase of the charge carrier concentration. The high electrical conductivity led to high power factors, 0.6 $mW.m^{-1}$ for $La_{0.2}Ba_{0.8}TiO_3$ at 365°C and 0.97 $mW.m^{-1}$ for $La_{0.2}Ca_{0.8}TiO_3$ at 270°C.

For the $La_xCa_{1-(3/2x)}TiO_3$ system, a Ti rich secondary phase was observed by XRD and SEM, indicating that the formation of A-site vacancies is not the favoured mechanism for La-doped $CaTiO_3$ when synthesised by the approach developed in this work, instead an additional ionic compensation occurred caused by the deficient stoichiometry in A-site elements (Ca and La) in the raw materials. The electrical conductivity and Seebeck coefficient were not significantly improved compared to $La_xCa_{1-x}TiO_3$ samples.

8 Future work

For both $La_xBa_{1-x}TiO_3$ and $La_xCa_{1-x}TiO_3$

- Differential scanning calorimetry in innert gas to measure the heat capacity C_p from RT to 800°C in order to calculate the figure of merit ZT with the already measured thermal diffusivity α and density ρ.
- TGA in an inert gas to characterise the modification that happened to the materials during the thermoelectric characterization, especially the oxidation because of the O_2 impurity in

the chamber.

- X-Ray photoelectron spectrometry to quantify the ratio Ti^{3+}/Ti^{4+}, to confirm or not the connection between the electrical conductivity, the oxygen loss, the dopant concentration, and the Ti oxidation stats.
- Find a method to make cracks-free samples at a temperature higher than 1450°C, in order to characterize all the thermoelectric properties of $La_xBa_{1-x}TiO_3$ at the highest electrical conductivity.
- UV Vis to quantify the modification of the bandgap with the doping level and the SPS sintering temperature. Tuning the bandgap of oxides is important for applications such as the photocatalytic water splitting.
- Van der Pauw measurement to quantify the modification of the carrier concentration and the carrier mobility with the doping level, and the SPS sintering temperature.
- Increase the relative density of the final sample and identify the reason why the ball-milled samples were less conductive.

For $La_xBa_{1-x}TiO_3$

- Neutron diffraction and transmission electron microscopy to determine the space group as it is not possible with XRD.
- TGA in flowing $H_2$5%/Ar95% to characterise the modification that happened to the materials during the thermoelectric characterization, especially the oxidation because of the O_2 impurity in the chamber.

9 References

[1] Clemens Forman, Ibrahim Kolawole Muritala, Robert Pardemann, and Bernd Meyer. Estimating the global waste heat potential. *Renewable and Sustainable Energy Reviews*, 57:1568–1579, 2016.

[2] Sarah Brueckner, Rene Arbter, Martin Pehnt, and Eberhard Laevemann. Industrial waste heat potential in GermanyA bottom-up analysis. *Energy Efficiency*, 10(2):513–525, 2017.

[3] Hayati Mamur and Rasit AHISKA. A review: Thermoelectric generators in renewable energy. *International Journal of Renewable Energy Research*, 4(1):128–136, 2014.

[4] Peng Li, Lanlan Cai, Pengcheng Zhai, Xinfeng Tang, Qingjie Zhang, and M Niino. Design of a concentration solar thermoelectric generator. *Journal of Electronic Materials*, 39(9):1522–1530, 2010.

[5] RC OBrien, RM Ambrosi, NP Bannister, SD Howe, and Helen V Atkinson. Safe radioisotope thermoelectric generators and heat sources for space applications. *Journal of Nuclear Materials*, 377(3):506–521, 2008.

[6] DM Rowe. Applications of nuclear-powered thermoelectric generators in space. *Applied Energy*, 40(4):241–271, 1991.

[7] Mohamed S El-Genk, Hamed H Saber, and Thierry Caillat. Efficient segmented thermoelectric unicouples for space power applications. *Energy Conversion and Management*, 44(11):1755–1772, 2003.

[8] James D Patterson and Bernard C Bailey. *Solid-State Physics*. Springer, 2007.

[9] Maurice Gerl and Jean-Paul Issi. *Traite des materiaux*. Presses polytechniques et universitaires romandes, 1997.

[10] HoSung Lee. The Thomson effect and the ideal equation on thermoelectric coolers. *Energy*, 56:61–69, 2013.

[11] Jian He and Terry M Tritt. Advances in thermoelectric materials research: Looking back and moving forward. *Science*, 357(6358):eaak9997, 2017.

[12] Kefan Yu, Yanjie Zhou, Yulun Liu, Fusheng Liu, Lipeng Hu, Weiqin Ao, Chaohua Zhang, Yu Li, Junqin Li, and Heping Xie. Near-room-temperature thermoelectric materials and their application prospects in geothermal power generation. *Geomechanics and Geophysics for Geo-Energy and Geo-Resources*, 6(1):1–25, 2020.

[13] Joseph P Heremans, Vladimir Jovovic, Eric S Toberer, Ali Saramat, Ken Kurosaki, Anek Charoenphakdee, Shinsuke Yamanaka, and G Jeffrey Snyder. Enhancement of thermoelectric efficiency in PbTe by distortion of the electronic density of states. *Science*, 321(5888):554–557, 2008.

[14] Xiao Zhang and Li-Dong Zhao. Thermoelectric materials: Energy conversion between heat and electricity. *Journal of Materiomics*, 1(2):92–105, 2015.

[15] Cristina V Manzano, Begoña Abad, Miguel Muñoz Rojo, Yee Rui Koh, Stephen L Hodson, Antonio M Lopez Martinez, Xianfan Xu, Ali Shakouri, Timothy D Sands, Theodorian Borca-Tasciuc, et al. Anisotropic effects on the thermoelectric properties of highly oriented electrodeposited Bi_2Te_3 films. *Scientific Reports*, 6(1):1–8, 2016.

[16] Ananya Banik, Tanmoy Ghosh, Raagya Arora, Moinak Dutta, Juhi Pandey, Somnath Acharya, Ajay Soni, Umesh V Waghmare, and Kanishka Biswas. Engineering ferroelectric instability to achieve ultralow thermal conductivity and high thermoelectric performance in $Sn_{1-x}Ge_xTe$. *Energy & Environmental Science*, 2019.

[17] Yanzhong Pei, Xiaoya Shi, Aaron LaLonde, Heng Wang, Lidong Chen, and G Jeffrey Snyder. Convergence of electronic bands for high performance bulk thermoelectrics. *Nature*, 473(7345):66, 2011.

[18] Kanishka Biswas, Jiaqing He, Ivan D Blum, Chun-I Wu, Timothy P Hogan, David N Seidman, Vinayak P Dravid, and Mercouri G Kanatzidis. High-performance bulk thermoelectrics with all-scale hierarchical architectures. *Nature*, 489(7416):414, 2012.

[19] Liangwei Fu, Meijie Yin, Di Wu, Wei Li, Dan Feng, Li Huang, and Jiaqing He. Large enhancement of thermoelectric properties in n-type PbTe via dual-site point defects. *Energy & Environmental Science*, 10(9):2030–2040, 2017.

[20] Kuei Fang Hsu, Sim Loo, Fu Guo, Wei Chen, Jeffrey S Dyck, Ctirad Uher, Tim Hogan, E Kanatzidis Polychroniadis, and Mercouri G Kanatzidis. Cubic $AgPbmSbTe_{2+m}$: bulk thermoelectric materials with high figure of merit. *Science*, 303(5659):818–821, 2004.

[21] Li-Dong Zhao, Shih-Han Lo, Yongsheng Zhang, Hui Sun, Gangjian Tan, Ctirad Uher, Christopher Wolverton, Vinayak P Dravid, and Mercouri G Kanatzidis. Ultralow thermal conductivity and high thermoelectric figure of merit in SnSe crystals. *Nature*, 508(7496):373, 2014.

[22] Anh Tuan Duong, Van Quang Nguyen, Ganbat Duvjir, Suyong Kwon, Jae Yong Song, Jae Ki Lee, Ji Eun Lee, SuDong Park, Taewon Min, Jaekwang Lee, et al. Achieving ZT= 2.2 with Bi-doped n-type SnSe single crystals. *Nature Communications*, 7:13713, 2016.

[23] Cheng Chang, Minghui Wu, Dongsheng He, Yanling Pei, Chao-Feng Wu, Xuefeng Wu, Hulei Yu, Fangyuan Zhu, Kedong Wang, Yue Chen, et al. 3D charge and 2D phonon transports leading to high out-of-plane ZT in n-type SnSe crystals. *Science*, 360(6390):778–783, 2018.

[24] Tin selenide (SnSe): growth, properties, and applications, author=Shi, Weiran and Gao, Minxuan and Wei, Jinping and Gao, Jianfeng and Fan, Chenwei and Ashalley, Eric and Li, Handong and Wang, Zhiming. *Advanced Science*, 5(4):1700602, 2018.

[25] Xiaolei Shi, Angyin Wu, Tianli Feng, Kun Zheng, Weidi Liu, Qiang Sun, Min Hong, Sokrates T Pantelides, Zhi-Gang Chen, and Jin Zou. High Thermoelectric Performance in p-type Polycrystalline Cd-doped SnSe Achieved by a Combination of Cation Vacancies and Localized Lattice Engineering. *Advanced Energy Materials*, 9(11):1803242, 2019.

[26] Min Jin, Jun Jiang, Rongbin Li, Xianghu Wang, Yunxia Chen, Rulin Zhang, and Yuqi Chen. Growth of large size snse single crystal and comparison of its thermoelectric property with polycrystal. *Materials Research Bulletin*, 114:156–160, 2019.

[27] Chan-Chieh Lin, R Lydia, Jae Hyun Yun, Ho Seong Lee, and Jong Soo Rhyee. Extremely low lattice thermal conductivity and point defect scattering of phonons in Ag-doped $(SnSe)_{1-x}(SnS)_x$ compounds. *Chemistry of Materials*, 29(12):5344–5352, 2017.

[28] Cheng Chang, Qing Tan, Yanling Pei, Yu Xiao, Xiao Zhang, Yue-Xing Chen, Lei Zheng, Shengkai Gong, Jing-Feng Li, Jiaqing He, et al. Raising thermoelectric performance of n-type SnSe via Br doping and Pb alloying. *RSC Advances*, 6(100):98216–98220, 2016.

[29] Huili Liu, Xun Shi, Fangfang Xu, Linlin Zhang, Wenqing Zhang, Lidong Chen, Qiang Li, Ctirad Uher, Tristan Day, and G Jeffrey Snyder. Copper ion liquid-like thermoelectrics. *Nature Materials*, 11(5):422, 2012.

[30] AA Olvera, NA Moroz, P Sahoo, P Ren, TP Bailey, AA Page, C Uher, and PFP Poudeu. Partial indium solubility induces chemical stability and colossal thermoelectric figure of merit in Cu_2Se. *Energy & Environmental Science*, 10(7):1668–1676, 2017.

[31] Bin Zhong, Yong Zhang, Weiqian Li, Zhenrui Chen, Jingying Cui, Wei Li, Yuandong Xie, Qing Hao, and Qinyu He. High superionic conduction arising from aligned large lamellae and large figure of merit in bulk $Cu_{1.94}Al_{0.02}Se$. *Applied Physics Letters*, 105(12):123902, 2014.

[32] Huili Liu, Xun Yuan, Ping Lu, Xun Shi, Fangfang Xu, Ying He, Yunshan Tang, Shengqiang Bai, Wenqing Zhang, Lidong Chen, et al. Ultrahigh Thermoelectric Performance by Electron and Phonon Critical Scattering in $Cu_2Se_{1-x}I_x$. *Advanced Materials*, 25(45):6607–6612, 2013.

[33] Bernard L Cohen. Anomalous behavior of tellurium abundances. *Geochimica et Cosmochimica Acta*, 48(1):203–205, 1984.

[34] Anjum Ara, Jawed Ahmad Usmani, et al. Lead toxicity: a review. *Interdisciplinary toxicology*, 8(2):55, 2015.

[35] Nikolai Fedotovich Izmerov, IV Sanotsky, and KK Sidorov. *Toxicometric parameters of industrial toxic chemicals under single exposure*, volume 35. Moscow, 1982.

[36] SJ Peppiatt. The melting of small particles. II. Bismuth. *Proceedings of the Royal Society of London. A. Mathematical and Physical Sciences*, 345(1642):401–412, 1975.

[37] CJ Coombes. The melting of small particles of lead and indium. *Journal of Physics F: Metal Physics*, 2(3):441, 1972.

[38] Bernhard Wunderlich and Hua-Cheng Shu. The crystallization and melting of selenium. *Journal of Crystal Growth*, 48(2):227–239, 1980.

[39] CRM Wronski. The size dependence of the melting point of small particles of tin. *British Journal of Applied Physics*, 18(12):1731, 1967.

[40] Frank Carl Kracek. The melting point of tellurium. *Journal of the American Chemical Society*, 63(7):1989–1990, 1941.

[41] Ichiro Terasaki, Yoshitaka Sasago, and Kunimitsu Uchinokura. Large thermoelectric power in $NaCo_2O_4$ single crystals. *Physical Review B*, 56(20):R12685, 1997.

[42] Vincent Thoréton, Y Hu, I Kehal, X Flandre, Da Huo, C Pirovano, A Rolle, E Capoen, N Nuns, AS Mamede, et al. Oxide Ion Transport in promising Cobaltites for SOC. *Procedia Engineering*, 98:115–120, 2014.

[43] Kazunori Takada, Hiroya Sakurai, Eiji Takayama-Muromachi, Fujio Izumi, Ruben A Dilanian, and Takayoshi Sasaki. Superconductivity in two-dimensional CoO_2 layers. *Nature*, 422(6927):53, 2003.

[44] Jeffrey W Fergus. Oxide materials for high temperature thermoelectric energy conversion. *Journal of the European Ceramic Society*, 32(3):525–540, 2012.

[45] Yang Wang, Yu Sui, Jinguang Cheng, Xianjie Wang, and Wenhui Su. Comparison of the high temperature thermoelectric properties for Ag-doped and Ag-added $Ca_3Co_4O_9$. *Journal of Alloys and Compounds*, 477(1-2):817–821, 2009.

[46] O-Jong Kwon, Wook Jo, Kyeong-Eun Ko, Jae-Yeol Kim, Sung-Hwan Bae, Hyun Koo, Seong-Min Jeong, Jin-Sang Kim, and Chan Park. Thermoelectric properties and texture evaluation

of $Ca_3Co_4O_9$ prepared by a cost-effective multisheet cofiring technique. *Journal of Materials Science*, 46(9):2887–2894, 2011.

[47] Yoshinobu Fujishiro, Motoyuki Miyata, Masanobu Awano, and Kunihiro Maeda. Characterization of Thermoelectric Metal Oxide Elements Prepared by the Pulse Electric-Current Sintering Method. *Journal of the American Ceramic Society*, 87(10):1890–1894, 2004.

[48] Tomoya Nagira, Mikio Ito, Shigeru Katsuyama, Kazuhiko Majima, and Hiroshi Nagai. Thermoelectric properties of $(Na_{1-y}M_y)_xCo_2O_4$ (M= K, Sr, Y, Nd, Sm and Yb; y= 0.01 0.35). *Journal of Alloys and Compounds*, 348(1-2):263–269, 2003.

[49] Mikio Ito and Daisuke Furumoto. Microstructure and thermoelectric properties of $Na_xCo_2O_4$/Ag composite synthesized by the polymerized complex method. *Journal of Alloys and Compounds*, 450(1-2):517–520, 2008.

[50] Yoichi Kamihara, Takumi Watanabe, Masahiro Hirano, and Hideo Hosono. Iron-based layered superconductor $La[O_{1-x}F_x]FeAs$ (x=0.05-0.12) with T_c = 26 K. *Journal of the American Chemical Society*, 130(11):3296–3297, 2008.

[51] S Arsenijević, R Gaál, AS Sefat, Michael A McGuire, Brian C Sales, David Mandrus, and Laszlo Forró. Pressure effects on the transport coefficients of $Ba(Fe_{1-x}Co_x)_2As_2$. *Physical Review B*, 84(7):075148, 2011.

[52] Loreynne Pinsard-Gaudart, David Bérardan, Julien Bobroff, and Nita Dragoe. Large Seebeck coefficients in iron-oxypnictides: a new route towards n-type thermoelectric materials. *physica status solidi (RRL)–Rapid Research Letters*, 2(4):185–187, 2008.

[53] Ismail Ijjaali, Bin Deng, and James A Ibers. Seven new rare-earth transition-metal oxychalcogenides: Syntheses and characterization of Ln_4MnOSe_6 (Ln= La, Ce, Nd), Ln_4FeOSe_6 (Ln= La, Ce, Sm), and La_4MnOS_6. *Journal of Solid State Chemistry*, 178(5):1503–1507, 2005.

[54] Yan-Ling Pei, Jiaqing He, Jing-Feng Li, Fu Li, Qijun Liu, Wei Pan, Celine Barreteau, David Berardan, Nita Dragoe, and Li-Dong Zhao. High thermoelectric performance of oxyselenides:

intrinsically low thermal conductivity of Ca-doped BiCuSeO. *NPG Asia Materials*, 5(5):e47, 2013.

[55] Fu Li, Jing-Feng Li, Li-Dong Zhao, Kai Xiang, Yong Liu, Bo-Ping Zhang, Yuan-Hua Lin, Ce-Wen Nan, and Hong-Min Zhu. Polycrystalline BiCuSeO oxide as a potential thermoelectric material. *Energy & Environmental Science*, 5(5):7188–7195, 2012.

[56] Fei Xu, Anmin Li, ZhuoFang Huang, Yu Rao, Bo Lu, and Yu Wu. Effect of Al doping and Cu deficiency on the microstructures and thermoelectric properties of BiCuSeO-based thermoelectric materials. *Journal of Electronic Materials*, 50:3580–3591, 2021.

[57] Celine Barreteau, David Berardan, Emilie Amzallag, LiDong Zhao, and Nita Dragoe. Structural and electronic transport properties in Sr-doped BiCuSeO. *Chemistry of Materials*, 24(16):3168–3178, 2012.

[58] Yong Liu, Li-Dong Zhao, Yaochun Liu, Jinle Lan, Wei Xu, Fu Li, Bo-Ping Zhang, David Berardan, Nita Dragoe, Yuan-Hua Lin, et al. Remarkable enhancement in thermoelectric performance of BiCuSeO by Cu deficiencies. *Journal of the American Chemical Society*, 133(50):20112–20115, 2011.

[59] Céline Barreteau, David Bérardan, LiDong Zhao, and Nita Dragoe. Influence of Te substitution on the structural and electronic properties of thermoelectric BiCuSeO. *Journal of Materials Chemistry A*, 1(8):2921–2926, 2013.

[60] Jing Li, Jiehe Sui, Yanling Pei, Celine Barreteau, David Berardan, Nita Dragoe, Wei Cai, Jiaqing He, and Li-Dong Zhao. A high thermoelectric figure of merit ZT>1 in Ba heavily doped BiCuSeO oxyselenides. *Energy & Environmental Science*, 5(9):8543–8547, 2012.

[61] LD Zhao, D Berardan, YL Pei, C Byl, L Pinsard-Gaudart, and N Dragoe. $Bi_{1-x}Sr_xCuSeO$ oxyselenides as promising thermoelectric materials. *Applied Physics Letters*, 97(9):092118, 2010.

[62] Jin-Le Lan, Yao-Chun Liu, Bin Zhan, Yuan-Hua Lin, Boping Zhang, Xun Yuan, Wenqing Zhang, Wei Xu, and C-W Nan. Enhanced thermoelectric properties of Pb-doped BiCuSeO ceramics. *Advanced Materials*, 25(36):5086–5090, 2013.

[63] Jiehe Sui, Jing Li, Jiaqing He, Yan-Ling Pei, David Berardan, Haijun Wu, Nita Dragoe, Wei Cai, and Li-Dong Zhao. Texturation boosts the thermoelectric performance of BiCuSeO oxyselenides. *Energy & Environmental Science*, 6(10):2916–2920, 2013.

[64] Li-Dong Zhao, Jiaqing He, David Berardan, Yuanhua Lin, Jing-Feng Li, Ce-Wen Nan, and Nita Dragoe. BiCuSeO oxyselenides: new promising thermoelectric materials. *Energy & Environmental Science*, 7(9):2900–2924, 2014.

[65] Vedentam Srikant and David R Clarke. On the optical band gap of zinc oxide. *Journal of Applied Physics*, 83(10):5447–5451, 1998.

[66] ZE Vakulov, EG Zamburg, DA Khakhulin, and OA Ageev. Thermal stability of ZnO thin films fabricated by pulsed laser deposition. *Materials Science in Semiconductor Processing*, 66:21–25, 2017.

[67] Joana Loureiro, Nuno Neves, Raquel Barros, Tiago Mateus, Rafael Santos, Sergej Filonovich, Sebastian Reparaz, Clivia M Sotomayor-Torres, Frederic Wyczisk, Laurent Divay, et al. Transparent aluminium zinc oxide thin films with enhanced thermoelectric properties. *Journal of Materials Chemistry A*, 2(18):6649–6655, 2014.

[68] Li Han, Ngo Van Nong, Le Thanh Hung, Tim Holgate, Nini Pryds, Michitaka Ohtaki, and Søren Linderoth. The influence of α-and γ-Al_2O_3 phases on the thermoelectric properties of Al-doped ZnO. *Journal of Alloys and Compounds*, 555:291–296, 2013.

[69] N Ma, J-F Li, BP Zhang, YH Lin, LR Ren, and GF Chen. Microstructure and thermoelectric properties of $Zn_{1-x}Al_xO$ ceramics fabricated by spark plasma sintering. *Journal of Physics and Chemistry of Solids*, 71(9):1344–1349, 2010.

[70] Paolo Mele, S Saini, H Honda, K Matsumoto, K Miyazaki, H Hagino, and A Ichinose. Effect of substrate on thermoelectric properties of Al-doped ZnO thin films. *Applied Physics Letters*, 102(25):253903, 2013.

[71] Xiurong Qu, Wen Wang, Shuchen Lv, and Dechang Jia. Thermoelectric properties and electronic structure of Al-doped ZnO. *Solid State Communications*, 151(4):332–336, 2011.

[72] K Park, JK Seong, and GH Kim. NiO added $Zn_{1-x}Ni_xO$ ($0 \leq x \leq 0.05$) for thermoelectric power generation. *Journal of Alloys and Compounds*, 473(1-2):423–427, 2009.

[73] K Park, JK Seong, and Sahn Nahm. Improvement of thermoelectric properties with the addition of Sb to ZnO. *Journal of Alloys and Compounds*, 455(1-2):331–335, 2008.

[74] K Park and JK Seong. Influence of simultaneous addition of Sb_2O_3 and SnO_2 on thermoelectric properties of $Zn_{1-x-y}Sb_xSn_yO$ prepared by tape casting. *Journal of Alloys and Compounds*, 464(1-2):1–5, 2008.

[75] K Park, KY Ko, W-S Seo, W-S Cho, J-G Kim, and JY Kim. High-temperature thermoelectric properties of polycrystalline $Zn_{1-x-y}Al_xTi_yO$ ceramics. *Journal of the European Ceramic Society*, 27(2-3):813–817, 2007.

[76] Michitaka Ohtaki, Kazuhiko Araki, and Kiyoshi Yamamoto. High thermoelectric performance of dually doped ZnO ceramics. *Journal of Electronic Materials*, 38(7):1234–1238, 2009.

[77] Jun Wang, Bo-Yu Zhang, Hui-Jun Kang, Yan Li, Xinba Yaer, Jing-Feng Li, Qing Tan, Shuai Zhang, Guo-Hua Fan, Cheng-Yan Liu, et al. Record high thermoelectric performance in bulk $SrTiO_3$ via nano-scale modulation doping. *Nano Energy*, 35:387–395, 2017.

[78] Megha Acharya, Subhra Sourav Jana, Mani Ranjan, and Tanmoy Maiti. High performance ($ZT > 1$) n-type oxide thermoelectric composites from earth abundant materials. *Nano Energy*, 84:105905, 2021.

[79] Gang Ou, Dongke Li, Wei Pan, Qinghua Zhang, Ben Xu, Lin Gu, Cewen Nan, and Hui Wu. Arc-melting to narrow the bandgap of oxide semiconductors. *Advanced Materials*, 27(16):2589–2594, 2015.

[80] Victor Moritz Goldschmidt. Die gesetze der krystallochemie. *Naturwissenschaften*, 14(21):477–485, 1926.

[81] Subir Sachdev. Handbook of magnetism and advanced magnetic materials. 2006.

[82] Lusann Yang, Stephen Dacek, and Gerbrand Ceder. Proposed definition of crystal substructure and substructural similarity. *Physical Review B*, 90(5):054102, 2014.

[83] Y Fujishiro, M Miyata, M Awano, and K Maeda. Thermoelectric characterization of $Na_xM_{x/2}Ti_{1-x/2}O_2$(M=Co, Ni and Fe) polycrystalline materials. *Ceramics International*, 28(8):841–845, 2002.

[84] T Okuda, K Nakanishi, S Miyasaka, and Y Tokura. Large thermoelectric response of metallic perovskites: $Sr_{1-x}La_xTiO_3$ (0<x<0.1). *Physical Review B*, 63(11):113104, 2001.

[85] Thomas F Soules, Edward J Kelly, David M Vaught, and James W Richardson. Energy-band structure of $SrTiO_3$ from a self-consistent-field tight-binding calculation. *Physical Review B*, 6(4):1519, 1972.

[86] K Ueda, H Yanagi, H Hosono, and H Kawazoe. Study on electronic structure of $CaTiO_3$ by spectroscopic measurements and energy band calculations. *Journal of Physics: Condensed Matter*, 11(17):3535, 1999.

[87] J Liu, CL Wang, WB Su, HC Wang, P Zheng, JC Li, JL Zhang, and LM Mei. Enhancement of thermoelectric efficiency in oxygen-deficient $Sr_{1-x}La_xTiO_{3-\delta}$ ceramics. *Applied Physics Letters*, 95(16):162110, 2009.

[88] Takashi Teranishi, Yusuke Ishikawa, Hidetaka Hayashi, Akira Kishimoto, Misaki Katayama, and Yasuhiro Inada. Thermoelectric efficiency of reduced $SrTiO_3$ ceramics modified with La and Nb. *Journal of the American Ceramic Society*, 96(9):2852–2856, 2013.

[89] Deepanshu Srivastava, Colin Norman, Feridoon Azough, Marion C Schäfer, Emmanuel Guilmeau, Demie Kepaptsoglou, Quentin M Ramasse, Giuseppe Nicotra, and Robert Freer. Tuning the thermoelectric properties of A-site deficient $SrTiO_3$ ceramics by vacancies and carrier concentration. *Physical Chemistry Chemical Physics*, 18(38):26475–26486, 2016.

[90] M Upadhyay Kahaly and Udo Schwingenschlögl. Thermoelectric performance enhancement of $SrTiO_3$ by Pr doping. *Journal of Materials Chemistry A*, 2(27):10379–10383, 2014.

[91] Mikio Ito and Tomoaki Matsuda. Thermoelectric properties of non-doped and Y-doped $SrTiO_3$ polycrystals synthesized by polymerized complex process and hot pressing. *Journal of Alloys and Compounds*, 477(1-2):473–477, 2009.

[92] YF Yamada, A Ohtomo, and M Kawasaki. Parallel syntheses and thermoelectric properties of Ce-doped $SrTiO_3$ thin films. *Applied Surface Science*, 254(3):768–771, 2007.

[93] Cong Chen, Mohamed Bousnina, Fabien Giovannelli, and Fabian Delorme. Influence of Bi on the thermoelectric properties of $SrTiO_{3-\delta}$. *Journal of Materiomics*, 5(1):88–93, 2019.

[94] Hiroaki Muta, Ken Kurosaki, and Shinsuke Yamanaka. Thermoelectric properties of rare earth doped $SrTiO_3$. *Journal of Alloys and Compounds*, 350(1-2):292–295, 2003.

[95] J Liu, CL Wang, Y Li, WB Su, YH Zhu, JC Li, and LM Mei. Influence of rare earth doping on thermoelectric properties of $SrTiO_3$ ceramics. *Journal of Applied Physics*, 114(22):223714, 2013.

[96] Srinivasa Rao Popuri, AJM Scott, RA Downie, MA Hall, Emmanuelle Suard, Rodolphe Decourt, Michaël Pollet, and J-WG Bos. Glass-like thermal conductivity in $SrTiO_3$ thermoelectrics induced by A-site vacancies. *Rsc Advances*, 4(64):33720–33723, 2014.

[97] AV Kovalevsky, AA Yaremchenko, S Populoh, A Weidenkaff, and JR Frade. Effect of A-site cation deficiency on the thermoelectric performance of donor-substituted strontium titanate. *The Journal of Physical Chemistry C*, 118(9):4596–4606, 2014.

[98] Feridoon Azough, Samuel S Jackson, Dursun Ekren, Robert Freer, Marco Molinari, Stephen R Yeandel, Pooja M Panchmatia, Stephen C Parker, David Hernandez Maldonado, Demie M Kepaptsoglou, et al. Concurrent La and A-site vacancy doping modulates the thermoelectric response of $SrTiO_3$: experimental and computational evidence. *ACS applied materials & interfaces*, 9(48):41988–42000, 2017.

[99] Jiao Han, Qiu Sun, and Ying Song. Enhanced thermoelectric properties of La and Dy co-doped, Sr-deficient $SrTiO_3$ ceramics. *Journal of Alloys and Compounds*, 705:22–27, 2017.

[100] Zhilun Lu, Huairuo Zhang, Wen Lei, Derek C Sinclair, and Ian M Reaney. High-figure-of-merit thermoelectric La-doped A-site-deficient $SrTiO_3$ ceramics. *Chemistry of Materials*, 28(3):925–935, 2016.

[101] Dragos Neagu and John TS Irvine. Structure and properties of $La_{0.4}Sr_{0.4}TiO_3$ ceramics for use as anode materials in solid oxide fuel cells. *Chemistry of Materials*, 22(17):5042–5053, 2010.

[102] Dragos Neagu, George Tsekouras, David N Miller, Hervé Ménard, and John TS Irvine. In situ growth of nanoparticles through control of non-stoichiometry. *Nature Chemistry*, 5(11):916, 2013.

[103] Ning Wang, Li Han, Hongcai He, Yaoshuai Ba, and Kunihito Koumoto. Effects of mesoporous silica addition on thermoelectric properties of Nb-doped $SrTiO_3$. *Journal of Alloys and Compounds*, 497(1-2):308–311, 2010.

[104] Ning Wang, Hongcai He, Xiao Li, Li Han, and Chunqiu Zhang. Enhanced thermoelectric properties of Nb-doped $SrTiO_3$ polycrystalline ceramic by titanate nanotube addition. *Journal of Alloys and Compounds*, 506(1):293–296, 2010.

[105] Pinku Roy, Vijyeta Pal, and Tanmoy Maiti. Effect of Spark Plasma Sintering (SPS) on the thermoelectric properties of $SrTiO_3$: 15 at% Nb. *Ceramics International*, 43(15):12809–12813, 2017.

[106] Olena Okhay, Sebastian Zlotnik, Wenjie Xie, Krzysztof Orlinski, Maria J Hortiguela Gallo, Gonzalo Otero-Irurueta, Antonio JS Fernandes, Dorota A Pawlak, Anke Weidenkaff, and Alexander Tkach. Thermoelectric performance of Nb-doped $SrTiO_3$ enhanced by reduced graphene oxide and Sr deficiency cooperation. *Carbon*, 143:215–222, 2019.

[107] Shingo Ohta, Takashi Nomura, Hiromichi Ohta, Masahiro Hirano, Hideo Hosono, and Kunihito Koumoto. Large thermoelectric performance of heavily Nb-doped $SrTiO_3$ epitaxial film at high temperature. *Applied Physics Letters*, 87(9):092108, 2005.

[108] Ning Wang, Hongcai He, Yaoshuai Ba, Chunlei Wan, and Kunihito Koumoto. Thermoelectric properties of Nb-doped $SrTiO_3$ ceramics enhanced by potassium titanate nanowires addition. *Journal of the Ceramic Society of Japan*, 118(1383):1098–1101, 2010.

[109] Shingo Ohta, Takashi Nomura, Hiromichi Ohta, and Kunihito Koumoto. High-temperature carrier transport and thermoelectric properties of heavily La-or Nb-doped $SrTiO_3$ single crystals. *Journal of Applied Physics*, 97(3):034106, 2005.

[110] Subhra Sourav Jana and Tanmoy Maiti. Enhanced Thermoelectric Performance in Oxide Composites of La and Nb Codoped $SrTiO_3$ by Using Graphite as the Electron Mobility Booster. *ACS Applied Materials & Interfaces*, 14(12):14174–14181, 2022.

[111] Jayakanth Ravichandran, Wolter Siemons, D-W Oh, Justin T Kardel, Arvind Chari, Herman Heijmerikx, Matthew L Scullin, Arun Majumdar, Ramamoorthy Ramesh, and David G Cahill. High-temperature thermoelectric response of double-doped $SrTiO_3$ epitaxial films. *Physical Review B*, 82(16):165126, 2010.

[112] Yuan-Hua Lin, Ce-Wen Nan, Yuheng Liu, Jingfeng Li, T Mizokawa, and Zhijian Shen. High-Temperature Electrical Transport and Thermoelectric Power of Partially Substituted $Ca_3Co_4O_9$-Based Ceramics. *Journal of the American Ceramic Society*, 90(1):132–136, 2007.

[113] Yuheng Liu, Yuanhua Lin, Zhan Shi, Ce-Wen Nan, and Zhijian Shen. Preparation of $Ca_3Co_4O_9$ and improvement of its thermoelectric properties by spark plasma sintering. *Journal of the American Ceramic Society*, 88(5):1337–1340, 2005.

[114] JJ Petrovic and RE Honnell. Partially stabilized ZrO_2 particle-$MoSi_2$matrix composites. *Journal of Materials Science*, 25(10):4453–4456, 1990.

[115] IJ Shon, ZA Munir, K Yamazaki, and K Shoda. Simultaneous Synthesis and Densification of $MoSi_2$ by Field-Activated Combustion. *Journal of the American Ceramic Society*, 79(7):1875–1880, 1996.

[116] T Nishimura, M Mitomo, H Hirotsuru, and M Kawahara. Fabrication of silicon nitride nanoceramics by spark plasma sintering. *Journal of Materials Science Letters*, 14(15):1046–1047, 1995.

[117] Hiroyuki Shimizu, Masaru Yoshinaka, Ken Hirota, and Osamu Yamaguchi. Fabrication and mechanical properties of monolithic $MoSi_2$ by spark plasma sintering. *Materials Research Bulletin*, 37(9):1557–1563, 2002.

[118] Lihua Zhang, Tsuyoshi Tosho, Noriyuki Okinaka, and Tomohiro Akiyama. Thermoelectric Properties of Combustion Synthesized and Spark Plasma Sintered $Sr_{1-x}R_xTiO_3$. *Materials Transactions*, 48(8):2088–2093, 2007.

[119] Asami Kikuchi, Noriyuki Okinaka, and Tomohiro Akiyama. A large thermoelectric figure of merit of La-doped $SrTiO_3$ prepared by combustion synthesis with post-spark plasma sintering. *Scripta Materialia*, 63(4):407–410, 2010.

[120] Kunsu Park, Jae Sung Son, Sung Ill Woo, Kwangsoo Shin, Min-Wook Oh, Su-Dong Park, and Taeghwan Hyeon. Colloidal synthesis and thermoelectric properties of La-doped $SrTiO_3$ nanoparticles. *Journal of Materials Chemistry A*, 2(12):4217–4224, 2014.

[121] Ihtesham Chowdhury, Ravi Prasher, Kelly Lofgreen, Gregory Chrysler, Sridhar Narasimhan, Ravi Mahajan, David Koester, Randall Alley, and Rama Venkatasubramanian. On-chip cooling by superlattice-based thin-film thermoelectrics. *Nature Nanotechnology*, 4(4):235–238, 2009.

[122] Woo Seok Choi, Hyang Keun Yoo, and Hiromichi Ohta. Polaron Transport and Thermoelectric Behavior in La-Doped $SrTiO_3$ Thin Films with Elemental Vacancies. *Advanced Functional Materials*, 25(5):799–804, 2015.

[123] Kyu Hyoung Lee, Akihiro Ishizaki, Sung Wng Kim, Hiromichi Ohta, and Kunihito Koumoto. Preparation and thermoelectric properties of heavily Nb-doped $SrO(SrTiO_3)_1$ epitaxial films. *Journal of Applied Physics*, 102(3):033702, 2007.

[124] SR Sarath Kumar, Anas I Abutaha, Mohamed N Hedhili, and Husam N Alshareef. Effect of oxygen vacancy distribution on the thermoelectric properties of La-doped $SrTiO_3$ epitaxial thin films. *Journal of Applied Physics*, 112(11):114104, 2012.

[125] SR Sarath Kumar, Abeer Z Barasheed, and Husam N Alshareef. High temperature thermoelectric properties of strontium titanate thin films with oxygen vacancy and niobium doping. *ACS Applied Materials & Interfaces*, 5(15):7268–7273, 2013.

[126] Y Kozuka, M Kim, H Ohta, Y Hikita, C Bell, and HY Hwang. Enhancing the electron mobility via delta-doping in $SrTiO_3$. *Applied Physics Letters*, 97(22):222115, 2010.

[127] Al Jumlat Ahmed, Md Shahriar A Hossain, Sheik Mohammad Kazi Nazrul Islam, Frank Yun, Guangsai Yang, Ridwone Hossain, Aslam Khan, Jongbeom Na, Miharu Eguchi, Yusuke Yamauchi, et al. Significant Improvement in Electrical Conductivity and Figure-of-merit of Nanoarchitectured Porous $SrTiO_3$ by La Doping Optimization. *ACS Applied Materials & Interfaces*, 2020.

[128] Mengjie Qin, Feng Gao, Gaogao Dong, Jie Xu, Maosen Fu, Yu Wang, Mike Reece, and Haixue Yan. Microstructure characterization and thermoelectric properties of $Sr_{0.9}La_{0.1}TiO_3$ ceramics with nano-sized Ag as additive. *Journal of Alloys and Compounds*, 762:80–89, 2018.

[129] Chang-Sun Park, WooJe Han, Dong Il Shim, Hyung Hee Cho, and Hyung-Ho Park. The effect of mesoporous structure on the thermoelectric properties of nonstoichiometric La-doped $SrTiO_3$. *Journal of The Electrochemical Society*, 163(6):E155, 2016.

[130] Chang-Sun Park, Min-Hee Hong, Hyung Hee Cho, and Hyung-Ho Park. Enhancement of seebeck coefficient of mesoporous $SrTiO_3$ with v-group elements V,Nb, and Ta substituted for Ti. *Journal of the European Ceramic Society*, 38(1):125–130, 2018.

[131] Daquan Liu, Yuwei Zhang, Huijun Kang, Jinling Li, Zongning Chen, and Tongmin Wang. Direct preparation of La-doped $SrTiO_3$ thermoelectric materials by mechanical alloying with carbon burial sintering. *Journal of the European Ceramic Society*, 38(2):807–811, 2018.

[132] Ning Wang, Haijun Chen, Hongcai He, Wataru Norimatsu, Michiko Kusunoki, and Kunihito Koumoto. Enhanced thermoelectric performance of nb-doped $SrTiO_3$ by nano-inclusion with low thermal conductivity. *Scientific Reports*, 3:3449, 2013.

[133] Da-Quan Liu, Yu-Wei Zhang, Hui-Jun Kang, Jin-Ling Li, Xiong Yang, and Tong-Min Wang. Effect of nb doping on microstructures and thermoelectric properties of $SrTiO_3$ ceramics. *Chinese Physics B*, 27(4):047205, 2018.

[134] Enzhu Li, Ning Wang, Hongcai He, and Haijun Chen. Improved thermoelectric performances of $SrTiO_3$ ceramic doped with nb by surface modification of nanosized titania. *Nanoscale Research Letters*, 11(1):188, 2016.

[135] Deepanshu Srivastava, Colin Norman, Feridoon Azough, Marion C Schäfer, Emmanuel Guilmeau, and Robert Freer. Improving the thermoelectric properties of $SrTiO_3$-based ceramics with metallic inclusions. *Journal of Alloys and Compounds*, 731:723–730, 2018.

[136] Jiao Han, Qiu Sun, Wenxu Li, and Ying Song. Microstructure and thermoelectric properties of $La_{0.1}Dy_{0.1}Sr_xTiO_3$ ceramics. *Ceramics International*, 43(7):5557–5563, 2017.

[137] Ke-Xian Wang, Jun Wang, Yan Li, Tao Zou, Xiao-Huan Wang, Jian-Bo Li, Zheng Cao, Wen-Jing Shi, and Xinba Yaer. Enhancement of thermoelectric properties of $SrTiO_3$/LaNb−$SrTiO_3$ composite by different doping levels. *Chinese Physics B*, 27(4):048401, 2018.

[138] Daquan Liu, Yanxia Wang, Xue Jiang, Huijun Kang, Xiong Yang, Xiaoying Zhang, and Tongmin Wang. Ultrahigh electrical conductivities and low lattice thermal conductivities of

La,Dy, and Nb co-doped $SrTiO_3$ thermoelectric materials with complex structures. *Journal of Materials Science & Technology*, 2020.

[139] J Petzelt. Soft mode behavior in cubic and tetragonal $BaTiO_3$ crystals and ceramics: review on the results of dielectric spectroscopy. *Ferroelectrics*, 375(1):156–164, 2008.

[140] Dillon D Fong, G Brian Stephenson, Stephen K Streiffer, Jeffrey A Eastman, Orlando Auciello, Paul H Fuoss, and Carol Thompson. Ferroelectricity in ultrathin perovskite films. *Science*, 304(5677):1650–1653, 2004.

[141] Lucie Mazet, Sang Mo Yang, Sergei V Kalinin, Sylvie Schamm-Chardon, and Catherine Dubourdieu. A review of molecular beam epitaxy of ferroelectric $BaTiO_3$ films on Si, Ge and GaAs substrates and their applications. *Science and Technology of Advanced Materials*, 16(3):036005, 2015.

[142] Ryan R McQuade and Michelle R Dolgos. A review of the structure-property relationships in lead-free piezoelectric $Na_{0.5}Bi_{0.5}TiO_3$−(x)$BaTiO_{3-x}$. *Journal of Solid State Chemistry*, 242:140–147, 2016.

[143] Hideki Ogihara, Clive A Randall, and Susan Trolier-McKinstry. High-energy density capacitors utilizing 0.7 $BaTiO_3$-$BiScO_3$ ceramics. *Journal of the American Ceramic Society*, 92(8):1719–1724, 2009.

[144] Helen M Chan, Martin R Harmer, and Donald Ml Smyth. Compensating defects in highly donor-doped $BaTiO_3$. *Journal of the American Ceramic Society*, 69(6):507–510, 1986.

[145] Finlay D Morrison, Derek C Sinclair, and Anthony R West. An Alternative Explanation for the Origin of the Resistivity Anomaly in La-Doped $BaTiO_3$. *Journal of the American Ceramic Society*, 84(2):474–76, 2001.

[146] Finlay D Morrison, Alison M Coats, Derek C Sinclair, and Anthony R West. Charge compensation mechanisms in La-doped $BaTiO_3$. *Journal of Electroceramics*, 6(3):219–232, 2001.

[147] T Kolodiazhnyi, A Petric, M Niewczas, C Bridges, A Safa-Sefat, and JE Greedan. Thermoelectric power, Hall effect, and mobility of n-type $BaTiO_3$. *Physical Review B*, 68(8):085205, 2003.

[148] Soonil Lee, Gaiying Yang, Rudeger HT Wilke, Susan Trolier-McKinstry, and Clive A Randall. Thermopower in highly reduced n-type ferroelectric and related perovskite oxides and the role of heterogeneous nonstoichiometry. *Physical Review B*, 79(13):134110, 2009.

[149] CN Berglund and WS Baer. Electron transport in single-domain, ferroelectric barium titanate. *Physical Review*, 157(2):358, 1967.

[150] M Nasir Khan, Hyun-Tak Kim, Hidetoshi Minami, and Hiromoto Uwe. Thermoelectric properties of niobium doped hexagonal barium titanate. *Materials Letters*, 47(1-2):95–101, 2001.

[151] Xingxing Xiao, Marc Widenmeyer, Wenjie Xie, Tianhua Zou, Songhak Yoon, Marco Scavini, Stefano Checchia, Zhicheng Zhong, Philipp Hansmann, Stefan Kilper, et al. Tailoring the structure and thermoelectric properties of $BaTiO_3$ via Eu 2+ substitution. *Physical Chemistry Chemical Physics*, 19(21):13469–13480, 2017.

[152] Peter B Hitchcock, Michael F Lappert, Laurent Maron, and Andrey V Protchenko. Lanthanum does form stable molecular compounds in the +2 oxidation state. *Angewandte Chemie*, 120(8):1510–1513, 2008.

[153] Simon Cotton. *Lanthanide and actinide chemistry*. John Wiley & Sons, 2013.

[154] Km Rubi and R Mahendiran. Large thermoelectric response of B-site doped ferroelectrics: $Ba_{0.7}Eu_{0.3}Ti_{1-x}Nb_xO_3$ (x= 0 to 0.1). *Journal of Solid State Chemistry*, 281:121050, 2020.

[155] WD Johnston and D Sestrich. The $La_xBa_{1-x}TiO_3$ System. *Journal of Inorganic and Nuclear Chemistry*, 20(1-2):32–38, 1961.

[156] IV Joseph E. Sunstrom and Susan M. Kauzlarich'. Synthesis, Magnetisme, and Electrical properties of $La_{1-x}Ba_xTiO_3(0.0<x<0.5)$. *Chemistry of Materials*, 5:1539–1544, 1993.

[157] Veronika Fritsch, Joachim Hemberger, Manuel Brando, A Engelmayer, S Horn, Matthias Klemm, Georg Knebel, Frank Lichtenberg, Prabhat Mandal, Franz Mayr, et al. Metal-to-insulator transition in $La_{1-x}Ba_xTiO_3$. *Physical Review B*, 64(4):045113, 2001.

[158] Cahit Eylem, Gotthard Saghi-Szabo, Bai Hao Chen, Bryan Eichhorn, Jian Liang Peng, Richard Greene, Lourdes Salamanca-Riba, and Sahn Nahm. Structural, Magnetic, and Transport Properties of $R_xBa_{1-x}TiO_{3-\delta}$ Solid solutions, where R= La, Nd, Gd, Er, and Y: Rare-Earth-Dependent Metal-to-Semiconductor Transitions. *Chemistry of Materials*, 4(5):1038–1046, 1992.

[159] Joseph E Sunstrom IV, Susan M Kauzlarich, and Peter Klavins. Synthesis, structure, and properties of lanthanum strontium titanate $La_{1-x}Sr_xTiO_3$ (0.l $\leq$x $\leq$1). *Chemistry of Materials*, 4(2):346–353, 1992.

[160] Hiroaki Muta, Ken Kurosaki, and Shinsuke Yamanaka. Thermoelectric properties of doped $BaTiO_3$−$SrTiO_3$ solid solution. *Journal of Alloys and Compounds*, 368(1-2):22–24, 2004.

[161] Roushown Ali and Masatomo Yashima. Space group and crystal structure of the perovskite $CaTiO_3$ from 296 to 1720 k. *Journal of Solid State Chemistry*, 178(9):2867–2872, 2005.

[162] Byung-Geon Park. Photoluminescence of Eu^{3+}-doped $CaTiO_3$ perovskites and their photocatalytic properties with a metal ion loading. *Chemical Physics Letters*, 722:44–49, 2019.

[163] Ruinan Wang, Shuang Ni, Gang Liu, and Xiaoxiang Xu. Hollow $CaTiO_3$ cubes modified by La/Cr co-doping for efficient photocatalytic hydrogen production. *Applied Catalysis B: Environmental*, 225:139–147, 2018.

[164] LM Lozano-Sánchez, MG Méndez-Medrano, C Colbeau-Justin, JL Rodríguez-López, DB Hernández-Uresti, and S Obregón. Long-lived photoinduced charge-carriers in Er^{3+} doped $CaTiO_3$ for photocatalytic H_2 production under uv irradiation. *Catalysis Communications*, 84:36–39, 2016.

[165] Guanping Huang, Wen Dong, Liang Fang, Fengang Zheng, and Mingrong Shen. Effects of Eu-doping site on structural and photoluminescent properties of $CaTiO_3$ particles. *Journal of Advanced Dielectrics*, 1(02):215–221, 2011.

[166] Yuexiao Pan, Qiang Su, Huifang Xu, Tianhu Chen, Weikun Ge, Chunlei Yang, and Mingmei Wu. Synthesis and red luminescence of Pr^{3+}-doped $CaTiO_3$ nanophosphor from polymer precursor. *Journal of Solid State Chemistry*, 174(1):69–73, 2003.

[167] Yibing Wu, Zhuo Sun, Kaibin Ruan, Yong Xu, and Hong Zhang. Enhancing photoluminescence with Li-doped $CaTiO_3$: Eu^{3+} red phosphors prepared by solid state synthesis. *Journal of Luminescence*, 155:269–274, 2014.

[168] Yibing Wu, Fengyang Zhao, Xianqing Piao, and Kaibin Ruan. Zn-doped $CaTiO_3$: Eu^{3+} red phosphors for enhanced photoluminescence in white leds by solid-state reaction. *Luminescence*, 31(1):152–157, 2016.

[169] Yoshiyuki Inaguma, Takeshi Tsuchiya, Yuki Mori, Yuki Imade, Nobuhisa Sato, Tetsuhiro Katsumata, and Daisuke Mori. Temperature dependence of luminescence properties of praseodymium-doped perovskite $CaTiO_3$:Pr^{3+}. *Thermochimica Acta*, 532:168–171, 2012.

[170] Hua Zou, Dengfeng Peng, Guangheng Wu, Xusheng Wang, Dinghua Bao, Jun Li, Yanxia Li, and Xi Yao. Polarization-induced enhancement of photoluminescence in Pr^{3+} doped ferroelectric diphase $BaTiO_3$−$CaTiO_3$ ceramics. *Journal of Applied Physics*, 114(7):073103, 2013.

[171] Muhammad Rizwan, Zahid Usman, Muhammad Shakil, SSA Gillani, S Azeem, HB Jin, CB Cao, Rana Farhat Mehmood, Ghulam Nabi, and Muhammad Adnan Asghar. Electronic and optical behaviour of lanthanum doped $CaTiO_3$ perovskite. *Materials Research Express*, 7(1):015920, 2020.

[172] Duong Thi Mai Huong, Nguyen Hoang Nam, Nguyen Ngoc Long, et al. Preparation and optical characterization of Eu3+-doped $CaTiO_3$ perovskite powders. *Journal of Alloys and Compounds*, 537:54–59, 2012.

[173] Janusz Nowotny and Mieczysław Rekas. Defect chemistry of $BaTiO_3$. *Solid State Ionics*, 49:135–154, 1991.

[174] MF Zhou, T Bak, J Nowotny, M Rekas, CC Sorrell, and ER Vance. Defect chemistry and semiconducting properties of calcium titanate. *Journal of Materials Science: Materials in Electronics*, 13(12):697–704, 2002.

[175] U Balachandran and NG Eror. Self-compensation in lanthanumdoped calcium titanate. *Journal of Materials Science*, 17(6):1795–1800, 1982.

[176] Jianbo Li, Yanxia Wang, Xiong Yang, Huijun Kang, Zhiqiang Cao, Xue Jiang, Zongning Chen, Enyu Guo, and Tongmin Wang. Processing bulk insulating $CaTiO_3$ into a high-performance thermoelectric material. *Chemical Engineering Journal*, 428:131121, 2022.

[177] V Vashook, Jens Zosel, Wolfgang Preis, Werner Sitte, and Ulrich Guth. A-deficient chromites–titanates with the perovskite-type structure: synthesis and electrical conductivity. *Solid State Ionics*, 175(1-4):441–444, 2004.

[178] V Vashook, L Vasylechko, N Trofimenko, M Kuznecov, P Otchik, J Zosel, and U Guth. A-site deficient perovskite-type compounds in the ternary $CaTiO_3$-$LaCrO_3$-$La_{2/3}TiO_3$ system. *Journal of Alloys and Compounds*, 419(1-2):271–280, 2006.

[179] H Somaily, S Kolesnik, B Dabrowski, and O Chmaissem. Thermoelectric and structural correlations in $(Sr_{1-x-y}Ca_xNd_y)TiO_3$ perovskites. *Physical Review B*, 96(6):064105, 2017.

[180] DI Woodward, PL Wise, WE Lee, and IM Reaney. Space group symmetry of $Ca_xSr_{1-x}TiO_3$ determined using electron diffraction. *Journal of Physics: Condensed Matter*, 18(8):2401, 2006.

[181] Shahid Anwar and NP Lalla. Effect of oxygenation on the structural and dielectric properties of $Sr_{1-x}Ca_xTiO_3$ with 0.20 x 0.40. *Applied Physics Letters*, 92(21):212901, 2008.

[182] Shahid Anwar and NP Lalla. Occurrence of a new superlattice phase across the antiferroelectric phase transition in $Sr_{1-x}Ca_xTiO_3$ (x= 0.30 and 0.40). *Journal of Physics: Condensed Matter*, 20(32):325231, 2008.

[183] Kazuyuki Isawa, Yuji Yaegashi, Seiya Ogota, Mitsugu Nagano, Shiroshi Sudo, Kazuyoshi Yamada, and Hisao Yamauchi. Thermoelectric power of delafossite-derived compounds, $RCuO_{2+\delta}$ (R=Y, La, Pr, Nd, Sm, and Eu). *Physical Review B*, 57(13):7950, 1998.

[184] Shiqiang Hui and Anthony Petric. Electrical properties of yttrium-doped strontium titanate under reducing conditions. *Journal of the Electrochemical Society*, 149(1):J1, 2001.

[185] Hiroaki Muta, Akihiro Ieda, Ken Kurosaki, and Shinsuke Yamanaka. Substitution effect on the thermoelectric properties of alkaline earth titanate. *Materials Letters*, 58(30):3868–3871, 2004.

[186] Masahiro Yamamoto, Hiromichi Ohta, and Kunihito Koumoto. Thermoelectric phase diagram in a $CaTiO_3$−$SrTiO_3$−$BaTiO_3$ system. *Applied Physics Letters*, 90(7):072101, 2007.

[187] Rui-zhi Zhang, Xiao-yun Hu, Ping Guo, and Chun-lei Wang. Thermoelectric transport coefficients of n-doped $CaTiO_3$, $SrTiO_3$ and $BaTiO_3$: A theoretical study. *Physica B: Condensed Matter*, 407(7):1114–1118, 2012.

[188] Xiao-Lei Shi, Hao Wu, Qingfeng Liu, Wei Zhou, Siyu Lu, Zongping Shao, Matthew Dargusch, and Zhi-Gang Chen. $SrTiO_3$-based thermoelectrics: Progress and challenges. *Nano Energy*, 78:105195, 2020.

[189] Bernard Dennis Cullity. *Elements of X-ray Diffraction*. Addison-Wesley Publishing, 1956.

[190] Robert D Shannon. Revised effective ionic radii and systematic studies of interatomic distances in halides and chalcogenides. *Acta Crystallographica Section A: Foundation*, 32(5):751–767, 1976.

[191] Ki Hyun Yoon, Chul Han Kwon, and Tae Heui Kim. Photoeffects in La^{3+}-doped $BaTiO_3$ ceramic electrodes. *Journal of applied physics*, 67(2):868–872, 1990.

[192] Mohamed N Rahaman. *Ceramic processing and sintering*. CRC press, 2017.

[193] RH Buttner and EN Maslen. Electron difference density and structural parameters in $CaTiO_3$. *Acta Crystallographica Section B: Structural Science*, 48(5):644–649, 1992.

[194] Philippe Gillet, François Guyot, Geoffrey D Price, Benoit Tournerie, and Andrée Le Cleach. Phase changes and thermodynamic properties of $CaTiO_3$. spectroscopic data, vibrational modelling and some insights on the properties of $MgSiO_3$ perovskite. *Physics and Chemistry of Minerals*, 20(3):159–170, 1993.

[195] Dale E Newbury and Nicholas WM Ritchie. Is scanning electron microscopy/energy dispersive x-ray spectrometry (SEM/EDS) quantitative? *Scanning*, 35(3):141–168, 2013.

[196] Peng-Peng Shang, Bo-Ping Zhang, Jing-Feng Li, and Ning Ma. Effect of sintering temperature on thermoelectric properties of La-doped $SrTiO_3$ ceramics prepared by sol–gel process and spark plasma sintering. *Solid State Sciences*, 12(8):1341–1346, 2010.

[197] U Balachandran, B Odekirk, and NG Eror. Electrical conductivity in calcium titanate. *Journal of Solid State Chemistry*, 41(2):185–194, 1982.

[198] Shi Yeon Kim, Dong Kyu Choi, Dong-Hun Yeo, Hyo Soon Shin, and Ho Gyu Yoon. Influence of ball milling contamination on properties of sintered AlN substrates. *Journal of the European Ceramic Society*, 40(15):5349–5356, 2020.

[199] Mongkol Bumrungpon, Kenji Hirota, Katsuhiro Takagi, Kenichi Hanasaku, Toshiharu Hirai, Issei Morioka, Ryusuke Yasufuku, Masato Kitamura, and Kazuhiro Hasezaki. Synthesis and thermoelectric properties of bismuth antimony telluride thermoelectric materials fabricated at various ball-milling speeds with yttria-stabilized zirconia ceramic vessel and balls. *Ceramics International*, 46(9):13869–13876, 2020.

[200] Pengrong Ren, Qian Wang, Xin Wang, Lu Wang, Jing Wang, Huiqing Fan, and Gaoyang Zhao. Effects of doping sites on electrical properties of yttrium doped $BaTiO_3$. *Materials Letters*, 174:197–200, 2016.

[201] AA Murashkina, AN Demina, AK Demin, VI Maragou, and PE Tsiakaras. The influence of Fe, Cu, Al-doping on the crystal structure, thermal and electrical properties of calcium titanate. *Solid State Ionics*, 179(27-32):1615–1619, 2008.

[202] Yun Lu, Liang Hao, Katsuhiro Sagara, Hiroyuki Yoshida, and Yingrong Jin. Improvement in Thermoelectric Properties of Non-Stoichiometric Titanium Dioxide by Reduction Treatment. *Materials Transactions*, 54(10):1981–1985, 2013.

[203] Yun Lu, Mitsuji Hirohashi, and Kenkichi Sato. Thermoelectric properties of non-stoichiometric titanium dioxide TiO_{2-x} fabricated by reduction treatment using carbon powder. *Materials Transactions*, 47(6):1449–1452, 2006.

[204] Yun Lu, Katsuhiro Sagara, Liang Hao, Ziwu Ji, and Hiroyuki Yoshida. Fabrication of non-stoichiometric titanium dioxide by spark plasma sintering and its thermoelectric properties. *Materials Transactions*, 53(7):1208–1211, 2012.

10 Appendice

Table 10.1: Element composition of several points of $La_{0.2}Ba_{0.8}TiO_3$ by EPMA of Figure 10.2, concentration in atomic%.

Target	La	Ba	La+Ba	Ti	O	Total
60	3.56	15.48	19.04	19.36	61.60	99.89
61	5.16	13.98	19.15	18.97	61.88	100.76
62	3.97	15.22	19.19	19.11	61.70	99.95
63	4.55	14.67	19.22	19.71	61.07	100.23
64	5.56	13.82	19.39	18.79	61.83	100.45
65	4.29	14.60	18.90	19.56	61.54	100.60
66	4.55	14.59	19.14	19.15	61.71	100.26
67	6.24	12.66	18.90	19.51	61.59	100.67
68	7.80	10.89	18.69	19.45	61.86	100.69
69	0.00	18.94	18.94	19.49	61.56	100.40
70	0.00	18.99	18.99	19.57	61.44	100.22
71	4.24	14.69	18.93	18.925	62.14	99.79
72	2.42	16.57	18.99	19.594	61.42	100.32
Theoritical	4	16	20	20	60	100

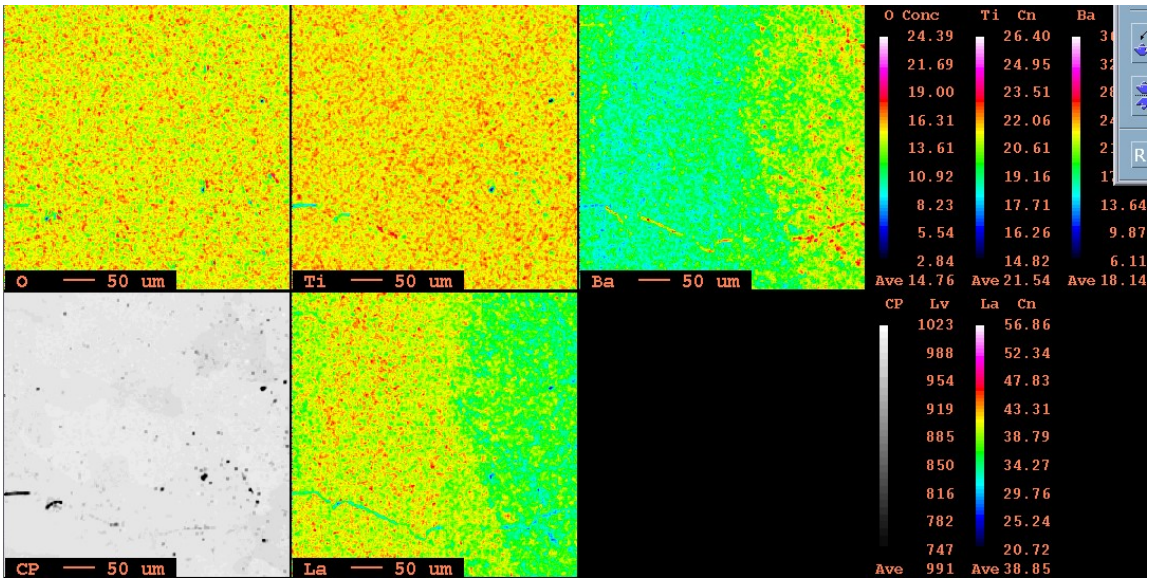


Figure 10.1: WDX element map of $La_{0.2}Ba_{0.8}TiO_3$, concentration in weight%.

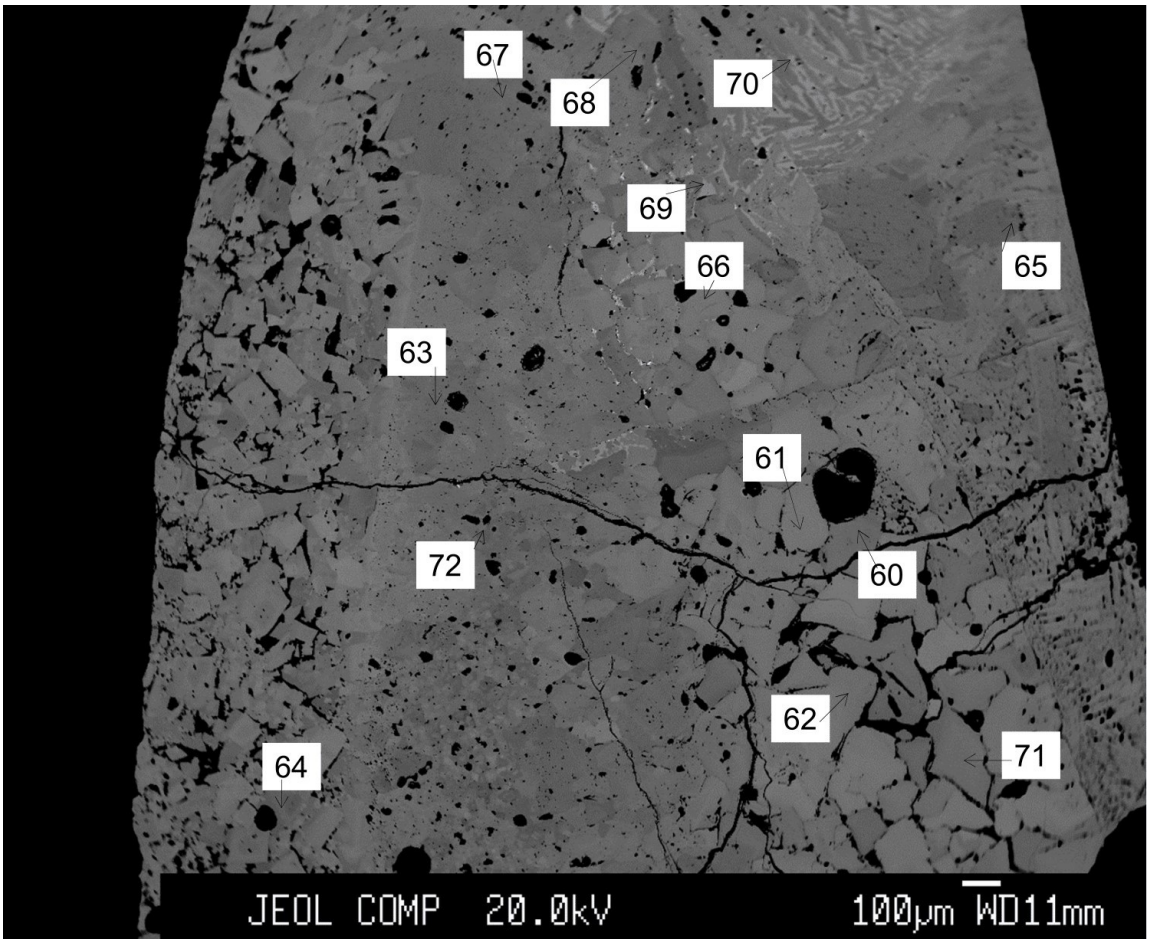


Figure 10.2: EPMA backscattered electrons image of $La_{0.2}Ba_{0.8}TiO_3$, element composition of the points in Table 10.1.

Table 10.2: Element composition of several points of $La_{0.3}Ba_{0.7}TiO_3$ by EPMA of Figure 10.4. Concentration in atomic%.

Target	La	Ba	La+Ba	Ti	O	Total
48	0.00	18.63	18.63	19.55	61.82	100.36
49	0.00	18.79	18.79	19.42	61.78	100.84
50	2.62	16.41	19.04	19.68	61.28	100.22
51	8.25	10.86	19.11	19.48	61.41	101.23
52	0.00	18.86	18.86	19.53	61.60	100.27
53	6.72	12.42	19.14	19.48	61.38	100.78
54	4.18	14.97	19.15	19.23	61.62	100.34
55	6.72	12.19	18.91	19.40	61.69	101.04
56	8.95	10.06	19.01	19.45	61.54	101.32
57	6.93	12.18	19.11	19.20	61.69	101.64
58	5.31	13.68	18.98	19.52	61.49	100.46
59	8.48	10.51	18.99	19.37	61.64	101.38
Theoritical	6	14	20	20	60	100

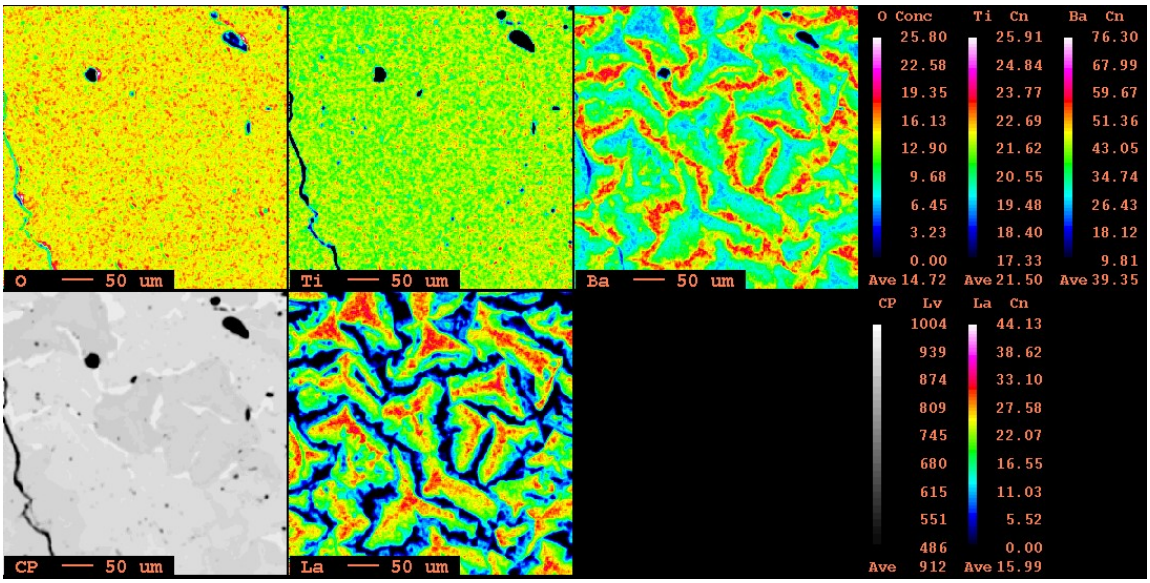


Figure 10.3: WDX element map of $La_{0.3}Ba_{0.7}TiO_3$, concentration in weight%.

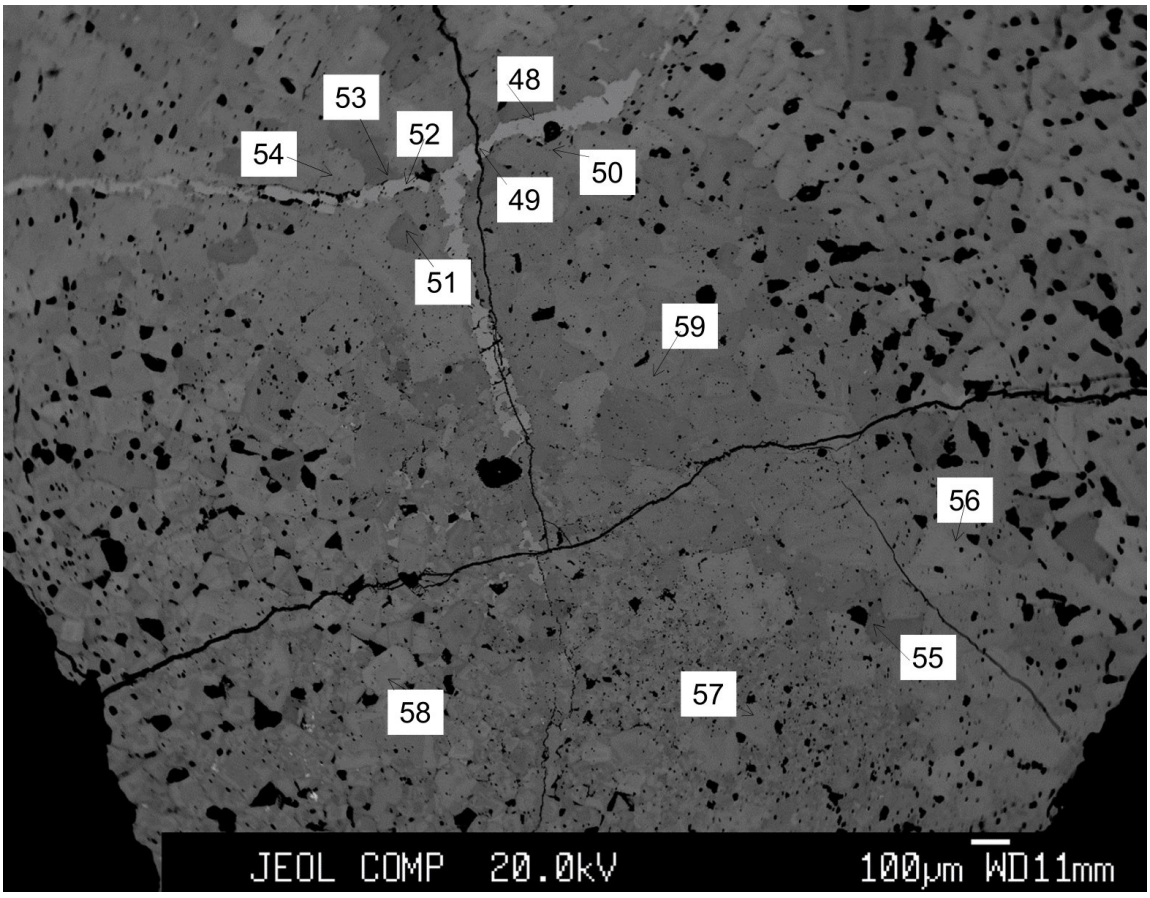


Figure 10.4: EPMA backscattered electrons image of $La_{0.3}Ba_{0.7}TiO_3$, element composition of the points in Table 10.2.

Table 10.3: Normalised element composition of several points of $La_{0.5}Ba_{0.5}TiO_3$ by EPMA of Figure 10.6, total not normalised.

Target	La (atm %)	Ba (atm %)	La +Ba (atm %)	Ti (atm%)	O (atm %)	Total (weight % , not normalised)
1	10.17	9.28	19.44	19.75	60.81	100.81
2	11.04	7.98	19.03	19.5	61.47	100.93
3	0.79	20.25	21.05	20.75	58.21	111.91
4	10.98	8.53	19.51	19.86	60.62	102.17
5	8.60	10.23	18.83	20.75	60.42	98.92
6	10.1	9.24	19.34	19.59	61.07	101.52
7	11.16	7.80	18.95	19.67	61.38	100.46
8	11.93	7.29	19.23	19.28	61.49	102.19
9	11.07	8.35	19.43	19.66	60.91	101.27
10	12.15	7.29	19.44	19.77	60.79	101.38
11	11.51	7.82	19.34	19.55	61.11	101.49
Theoretical	10	10	20	20	60	100

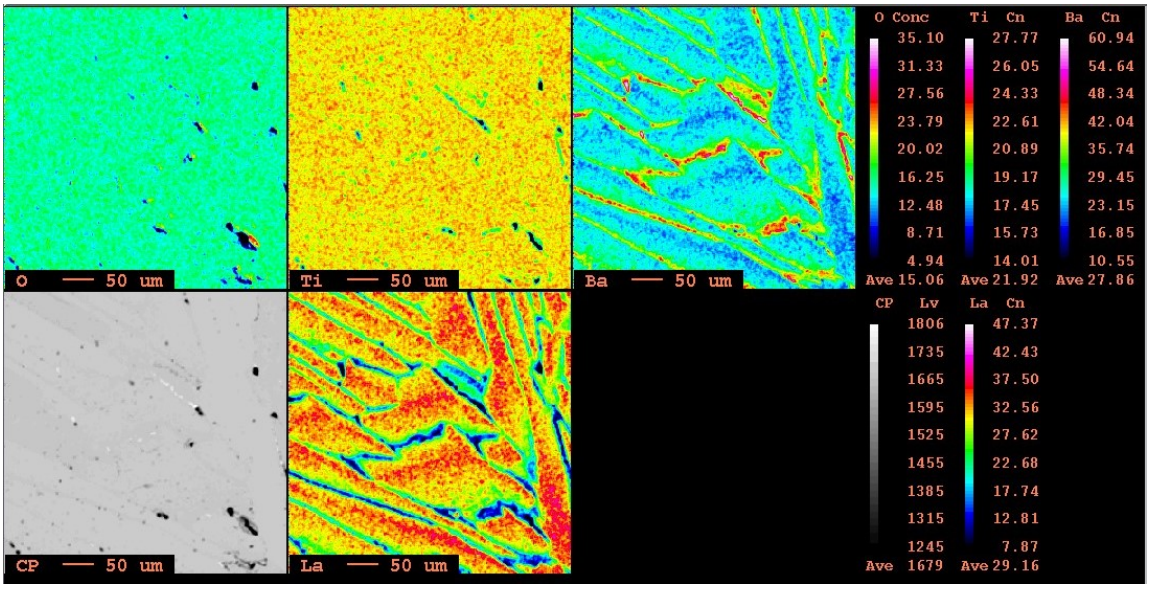


Figure 10.5: WDX element map of $La_{0.5}Ba_{0.5}TiO_3$, concentration in weight%.

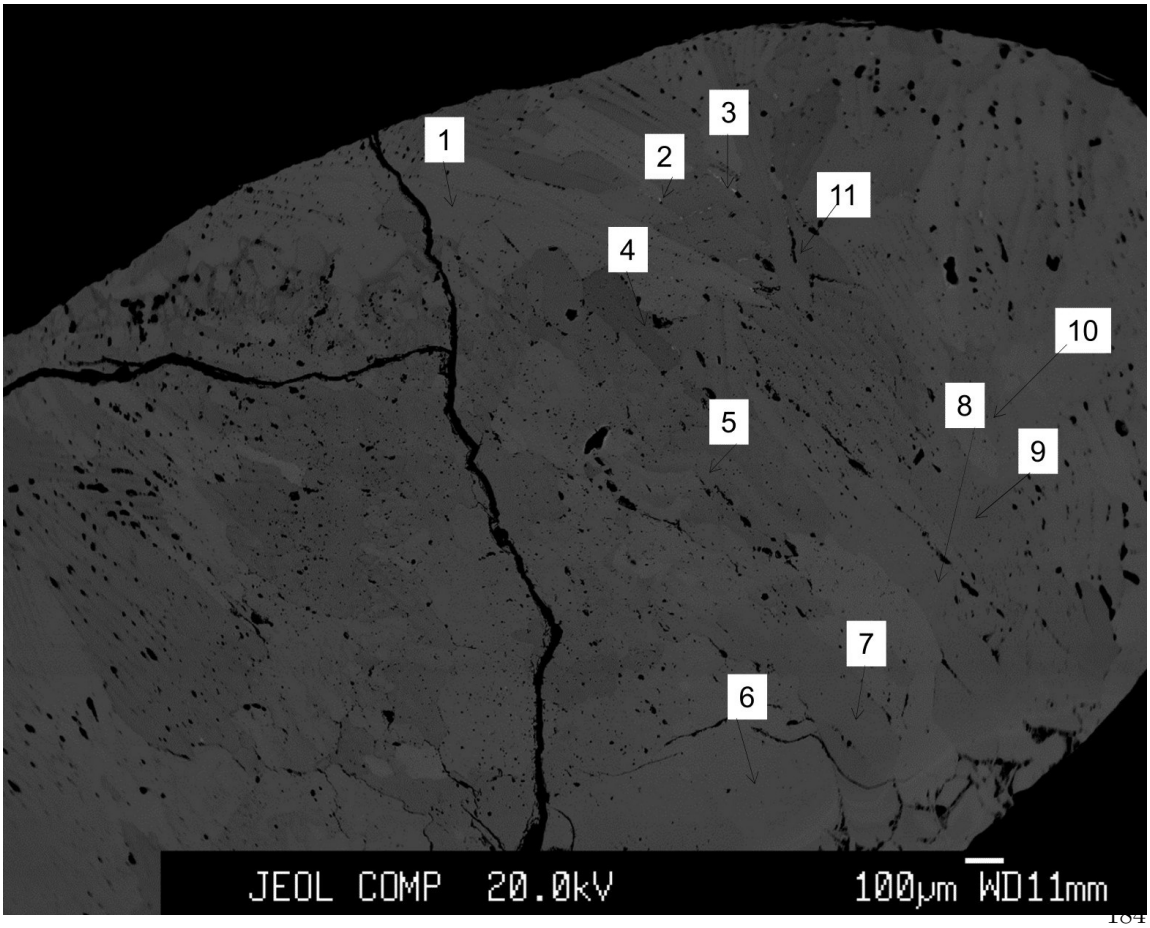


Figure 10.6: EPMA backscattered electrons image of $La_{0.5}Ba_{0.5}TiO_3$, element composition of the points in Table 10.3.

Table 10.4: Element composition of several points of $La_{0.6}Ba_{0.4}TiO_3$ by EPMA of Figure 10.8, concentration in atomic%.

Target	La	Ba	La+Ba	Ti	O	Total
40	12.83	6.12	18.95	19.38	61.67	101.92
41	13.27	5.75	19.01	19.44	61.55	101.19
42	13.15	5.85	19.00	19.25	61.74	101.96
43	12.27	6.56	18.83	19.46	61.70	101.19
44	11.59	7.42	19.01	19.22	61.77	101.67
45	11.71	7.43	19.14	19.23	61.63	101.75
46	10.89	8.01	18.90	19.30	61.80	101.6
47	11.54	7.58	19.12	19.19	61.69	102.06
Theoritical	12	8	20	20	60	100

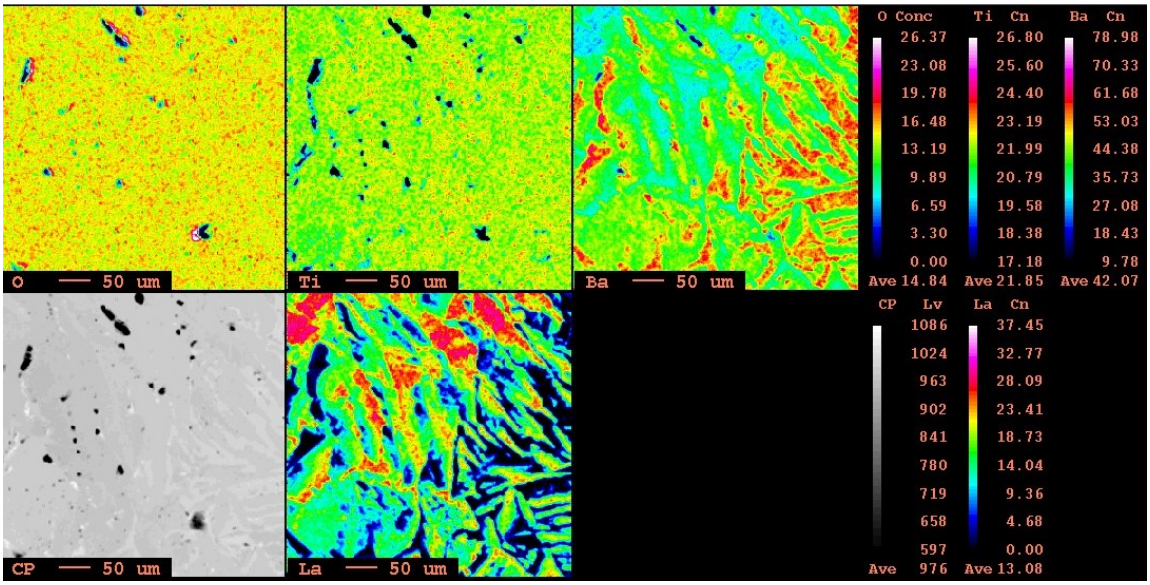


Figure 10.7: WDX element map of $La_{0.6}Ba_{0.4}TiO_3$, concentration in weight%.

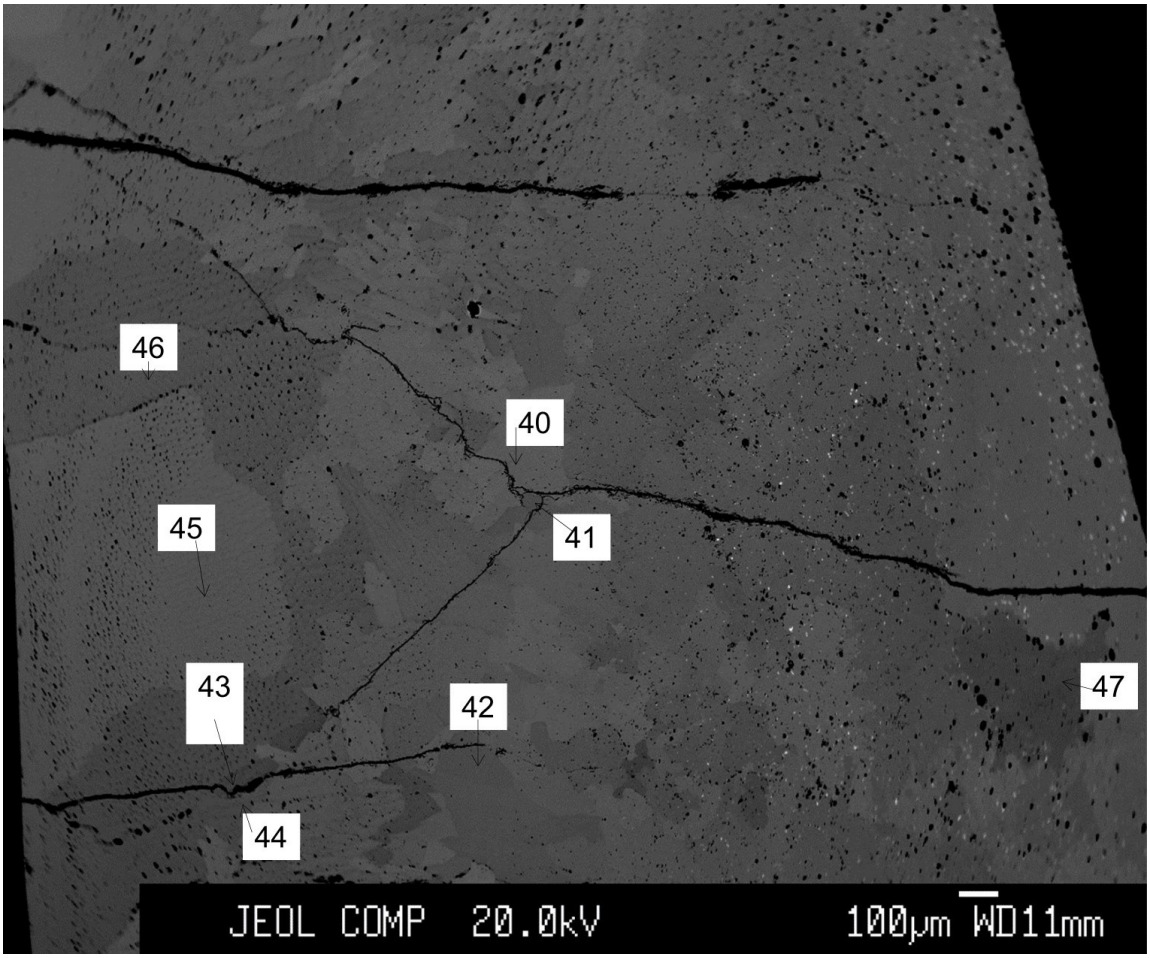


Figure 10.8: EPMA backscattered electrons image of $La_{0.6}Ba_{0.4}TiO_3$, element composition of the points in Table 10.4.

Table 10.5: Element composition of several points of $La_{0.8}Ba_{0.2}TiO_3$ by EPMA of Figure 10.10, concentration in atomic%.

Target	La (atm %)	Ba (atm %)	La + Ba (atm %)	Ti (atm %)	O (atm %)	Total (weight %, not normalised)
22	15.87	3.28	19.14	19.51	61.34	102.62
23	15.92	3.38	19.3	19.57	61.13	102.63
24	15.73	3.30	19.03	19.28	61.68	102.04
25	15.94	3.30	19.24	19.53	61.22	102.26
26	15.66	3.33	19.00	19.38	61.62	102.38
27	15.66	3.32	18.98	19.59	61.42	101.73
28	15.75	3.17	18.92	19.71	61.36	101.65
29	15.91	3.17	19.09	19.7	61.22	101.22
Theoretical	16	4	20	20	60	100

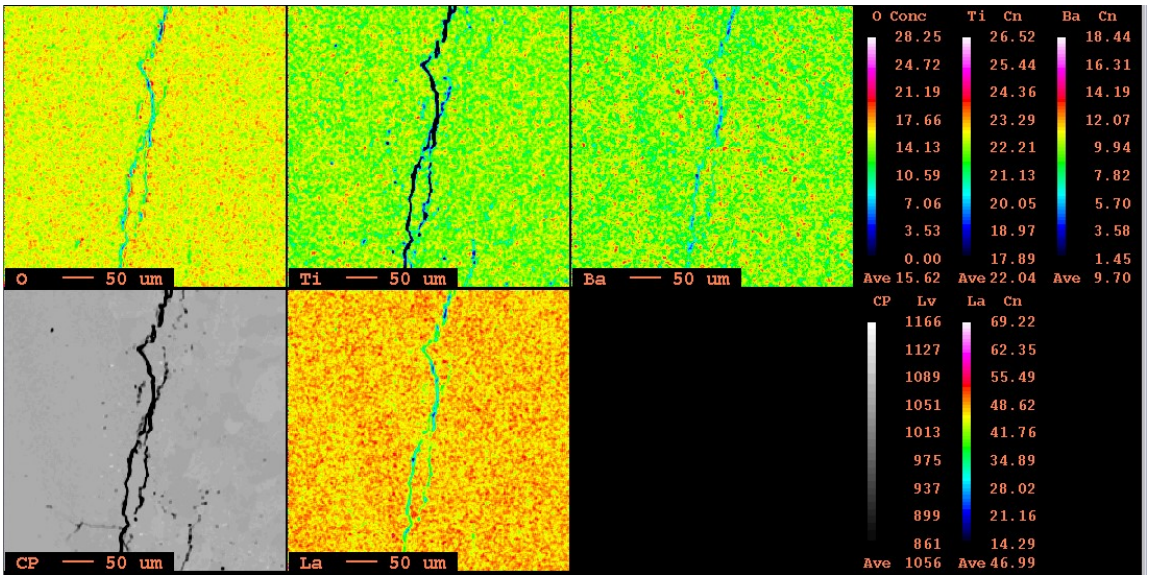


Figure 10.9: WDX element map of $La_{0.8}Ba_{0.2}TiO_3$, concentration in weight%.

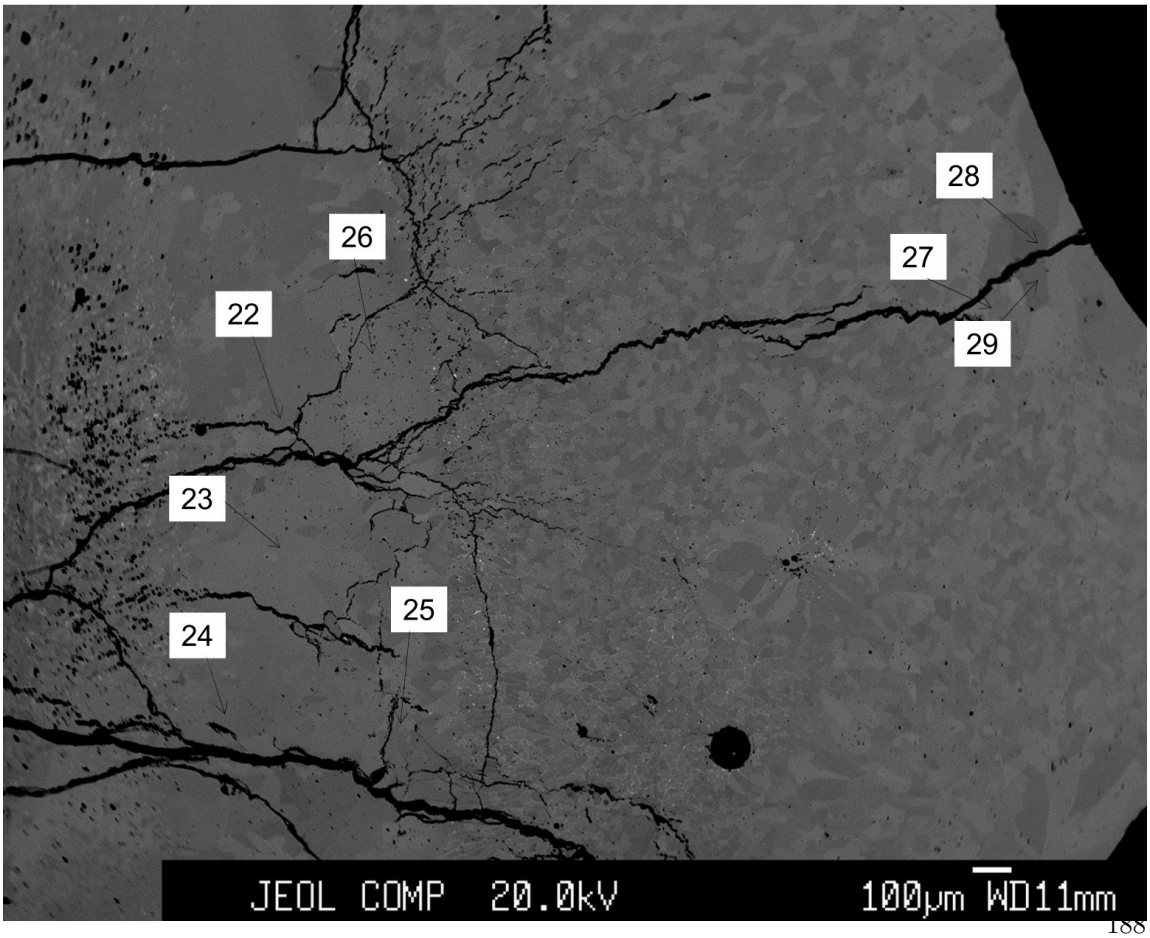


Figure 10.10: EPMA backscattered electrons image of $La_{0.8}Ba_{0.2}TiO_3$, element composition of the points in Table 10.5.

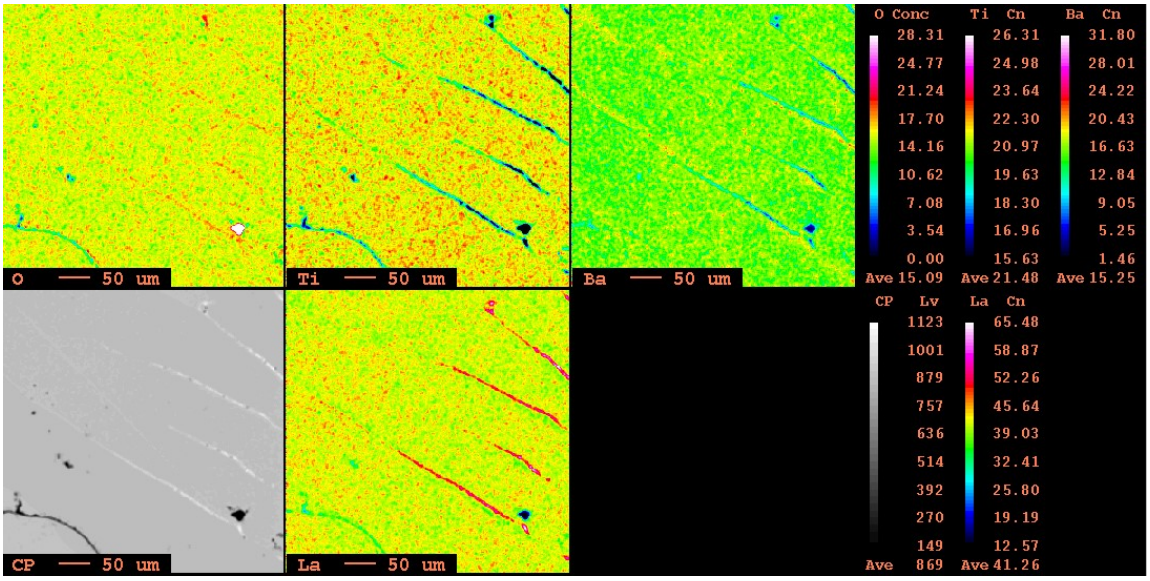


Figure 10.11: WDX element map of $La_{0.9}Ba_{0.1}TiO_3$, concentration in weight%.

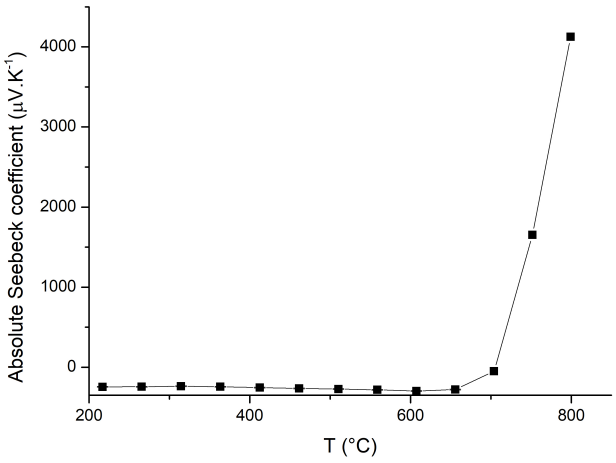


Figure 10.12: Full data of the temperature dependence of the Seebeck coefficient of $CaTiO_3$ melted in argon and sintered by SPS at 1450°C in high vacuum (diffusion pump) for 10 minutes with a heating and cooling rate of 100°C per minute and applied pressure of 40MPa, measurement carried in static He with a heating rate of 10°C per minute and a set gradient of 50°C.

List of Figures

1.1 Illustration of the Seebeck effect induced by a gradient of temperature at the junction of a material "a" and "b". The charge carriers (e.g. electrons or holes) move from the colder to the hotter side and are collected by the material "b" which closes the circuit. 4

1.2 Illustration of the Thomson effect, a gradient of temperature at a material with a temperature-dependent Seebeck coefficient induces a difference of Seebeck coefficient ΔS, then if an electric current J is imposed by a generator and pass through the material, it would result in a heat flow Q. 6

1.3 Thermoelectric generator circuit. Electricity is created from the movement of charge carriers of an n-type (electrons) and a p-type (holes) materials induced by a difference of temperature. 7

1.4 Thermoelectric cooler circuit. Heat flow is created from the electrical current passing through an n-type and a p-type materials with a temperature difference. 7

1.5 η against T_h for different ZT, reproduced with permission from ref [12]. 9

2.1 Plot of the maximum ZT of the state of art thermoelectric materials from 1960 to 2016, reproduced with permission from ref [14]. 10

2.2 Structure of Bi_2Te_3 from ref [15], reproduced with permission. 11

2.3 Chalcogenide structure of SnSe, Sn in grey and Se in red. From ref [24], reproduced with permission. 12

2.4 Cross section of hot pressed SnSe polycrystal, reproduced from ref [26] with permission. 13

2.5 a, Unit cell where only the 8c and 32f interstitial positions are shown with Cu atoms. b, Projected plane representation of the crystal structure along the cubic direction. The arrows indicate that the Cu ions can freely travel among the interstitial sites. There are two Cu layers between the neighbouring Se (111) planes. The structure changes to a monoclinic -phase by stacking the ordered Cu ions along the cubic [111] direction when cooled to room temperature. From ref [29], reproduced with permission. 13

2.6 $Ca_3Co_4O_9$ structure, reproduced from ref [42] with permission. 15

2.7 $NaCoO_2$ structure, reproduced from ref [43] with permission. 15
2.8 Crystal structure of the BiCuSeO from ref [55], reproduced with permission. 16
2.9 Microstructure of BiCuSeO from ref [56], reproduced with permission. 17
2.10 Pictures and draw of the texturation process by hot forging, from ref [64], reproduced with permission. 18
2.11 Example of a perovskite structure : $SrTiO_3$ at high temperature, Sr in green, Ti in blue, and O in red. From ref [82], reproduced with permission. 20
2.12 Schematic representing the carbon burial sintering, sample covered by graphite and placed in the crucible. 22
2.13 Schematic of an arc melter, the sample is melted by the electric arc formed between the chilled copper crucible and the tungsten cathode in a gas-controlled chamber. . . 31
3.1 Synthesis flow diagram of the arc melting and SPS densification method used for the study of the $La_xBa_{1-x}TiO_3$, the $La_xCa_{1-x}TiO_3$, and the $La_xCa_{1-(3/2x)}TiO_3$ sytems. . 40
3.2 Schematic of a filled SPS die between two graphite electrodes. With graphite paper between the sample/die wall and sample/punches. 45
3.3 Schematic of incident X-ray diffraction by the atoms of a solid during an XRD experiment. 46
3.4 Schematic of the principle of the wavelength separation of the sample's emitted X-ray by a rotating crystal for WDX analysis. 48
3.5 Schematic of a horizontal TGA, a crucible in a temperature-controlled chamber, sample holder on the sample arm connected to the microbalance. 49
3.6 Schematic of a gas and temperature-controlled four points probes (LSR-3), with the top and bottom probes as the electrodes, the middle probes for the potentiometer, secondary heater at the bottom electrode to generate a temperature gradient. 50
3.7 Plot of the Seebeck coefficient of the constantan reference sample before and after the calibration, the reference data, and the reference data +5% or -5%. 51

3.8 Schematic of a vertical LFA with a laser as the heat source at the bottom, the detector at the top, and the sample between. Sample placed in the gas and temperature controlled chamber. 52

3.9 Draw of a suitable LFA signal curve after that the sample was heated up by a pulse of light. 52

4.1 XRD patterns of different synthesis of $LaTiO_3$ with Ti or TiO precursors, with different delay after the melting, pattern of a sample that matched single phase $LaTiO_3$ and others with layered perovskite $La_2Ti_2O_7$. 56

4.2 TGA plot of $LaTiO_3$ powder in air with a heating and cooling rate of 10°C per minute and a dwell of two hours. 56

4.3 Powder XRD patterns of the system $La_xBa_{1-x}TiO_3$ produced by arc melting with argon atmosphere and commercial $BaTiO_3$. 59

4.4 Expanded powder XRD patterns of the system $La_xBa_{1-x}TiO_3$ produced by arc melting with argon atmosphere and commercial $BaTiO_3$. 60

4.5 Plot of the lattice edge length of the system $La_xBa_{1-x}TiO_3$ produced by arc melting, calculated from the XRD patterns. Error bars are smaller than the symbol size. . . . 61

4.6 Plot of the lattice volume of the system $La_xBa_{1-x}TiO_3$ produced by arc melting, calculated from the XRD patterns. Error bars are smaller than the symbol size. . . . 62

4.7 XRD pattern of the system $La_xBa_{1-x}TiO_3$ produced by arc melting with argon atmosphere followed by a SPS sintering at 1450°C for 10 minutes in high vacuum (diffusion pump) with a heating and cooling rate of 100°C/min and an applied pressure of 40 MPa. 64

4.8 Expanded XRD pattern of the system $La_xBa_{1-x}TiO_3$ produced by arc melting with argon atmosphere followed by a SPS sintering at 1450°C for 10 minutes in high vacuum (diffusion pump) with a heating and cooling rate of 100°C/min and an applied pressure of 40 MPa. 65

4.9 Plot of the lattice edge length of the system $La_xBa_{1-x}TiO_3$ produced by arc melting with argon atmosphere followed by a SPS sintering at 1450°C for 10 minutes in high vacuum (diffusion pump) with a heating and cooling rate of 100°C/min and an applied pressure of 40 MPa. Error bars are smaller than the symbol size. 66

4.10 Plot of the lattice volume of the system $La_xBa_{1-x}TiO_3$ after the arc melting with argon atmosphere and after the SPS sintering at 1450°C for 10 minutes in high vacuum (diffusion pump) with a heating and cooling rate of 100°C/min and an applied pressure of 40 MPa. Error bars are smaller than the symbol size. 66

4.11 Full width at half maximum of the samples $La_xBa_{1-x}TiO_3$ produced by arc melting with argon atmosphere, and produced by arc melting with argon atmosphere followed by a SPS sintering at 1450°C for 10 minutes in high vacuum (diffusion pump) with a heating and cooling rate of 100°C/min and an applied pressure of 40 MPa. 67

4.12 TGA plot of $La_xBa_{1-x}TiO_3$ in air from room temperature to 1000°C, with a heating and cooling rate of 10°C per minute, heating step plotted in solid line, cooling step plotted in dash line. Powder from crushed pellets produced by arc melting in argon. 68

4.13 Influence of the doping level on the difference of mass after the TGA for the series $La_xBa_{1-x}TiO_3$, plot in Figure 4.12. Powder from crushed pellets produced by arc melting in argon. 69

4.14 TGA of $La_xBa_{1-x}TiO_3$ powders in air from RT to 1000°C, with heating and cooling rate of 5°C/min with a flow of 100 mL/min, heating step plotted in solid line, cooling step in dash line. Powders from the crushed pellets SPS sintered at 1450°C in high vacuum (diffusion pump) for 10 minutes with a heating and cooling rate of 100°C/min and applied pressure of 40 MPa. 70

4.15 Influence of the doping level on the difference of mass after the TGA for the series $La_xBa_{1-x}TiO_3$, plot in Figure 4.14. Powders from the crushed pellet SPS sintered at 1450°C in high vacuum (diffusion pump) for 10 minutes with heating and cooling rate of 100°C/min and applied pressure of 40 MPa. 70

4.16 Powder XRD patterns of the powder after the TGA run in air at 1250°C, XRD scan of 30 minutes for $La_{0.2}Ba_{0.8}TiO_3$, XRD scan of 6 minutes for $La_{0.1}Ba_{0.9}TiO_3$. 71

4.17 Relative density of the SPS sintered pellets for different sintering temperatures for $La_{0.2}Ba_{0.8}TiO_3$ under vacuum, and an applied pressure of 40 MPa. 73

4.18 Relative density of the SPS sintered pellets for different applied pressures for $La_{0.2}Ba_{0.8}TiO_3$ at 1400°C under vacuum. 73

4.19 Relative density of the SPS sintered pellets for different cooling rates for $La_{0.2}Ba_{0.8}TiO_3$ at 1400°C under vacuum, with an applied pressure of 40 MPa. 74

4.20 Relative density of the SPS sintered pellets for different heating rates for $La_{0.2}Ba_{0.8}TiO_3$ at 1400°C under vacuum, with an applied pressure of 40 MPa. 74

4.21 Relative density of the samples $La_xBa_{1-x}TiO_3$ produced by arc melting in argon and sintered by SPS at different temperature in high vacuum (diffusion pump) for 10 minutes with a heating and cooling rate of 100°C per minute and an apllied pressure of 40MPa. 75

4.22 SEM images of $La_xBa_{1-x}TiO_3$ melted in argon and sintered by SPS at 1450°C in high vacuum (diffusion pump), with a heating and cooling rate of 100°C per minute and an applied pressure of 40MPa. 79

4.23 EDX spectra of $La_{0.2}Ba_{0.8}TiO_3$ sintered by SPS at 1450°C in high vacuum (diffusion pump) for 10 minutes with a heating and cooling rate of 100°C/min and an applied pressure of 40 MPa of the powder synthesized by arc melting in argon. 79

4.24 WDX element map fox $La_{0.1}Ba_{0.9}TiO_3$, concentration in weight%. 84

4.25 EPMA backscattered electrons image of $La_{0.1}Ba_{0.9}TiO_3$, element composition in Table 4.2. 84

4.26 WDX element map of $La_{0.4}Ba_{0.6}TiO_3$, concentration in weight%. 86

4.27 EPMA backscattered electrons image of $La_{0.4}Ba_{0.6}TiO_3$, element composition of the points in Table 4.3. 86

4.28 WDX element map of $La_{0.7}Ba_{0.3}TiO_3$, concentration in weight%. 89

4.29 EPMA backscattered electrons image of $La_{0.7}Ba_{0.3}TiO_3$, element composition of the points in Table 4.4. 89
4.30 Ternary diagramme of the normalised concentration of La, Ti and Ba detected by the WDX of $La_xBa_{1-x}TiO_3$ produced by arc melting in argon. 91
4.31 Normalised concentration of La, Ti and Ba detected by the WDX of $La_xBa_{1-x}TiO_3$ melted in argon and sintered by SPS at 1450°C in high vacuum (diffusion pump), with a heating and cooling rate of 100°C per minute and an applied pressure of 40MPa. 93
4.32 Ternary diagramme of the normalised concentration of La, Ti and Ba detected by the WDX of $La_xBa_{1-x}TiO_3$ produced by arc melting in argon and sintered by SPS at 1450°C in high vacuum (diffusion pump) for 10 minutes with a heating and cooling rate of 100°C per minute and applied pressure of 40MPa. 94
4.33 Temperature dependence of the electrical conductivity of $La_xBa_{1-x}TiO_3$ melted in argon and sintered by SPS at 1450°C in high vacuum (diffusion pump) for 10 minutes with a heating and cooling rate of 100°C per minute and applied pressure of 40MPa, measurement carried in static He with a heating rate of 10°C per minute. 96
4.34 Temperature dependence of the electrical conductivity of undoped $BaTiO_3$ melted in argon and sintered by SPS at 1450°C in high vacuum (diffusion pump) for 10 minutes with a heating and cooling rate of 100°C per minute and applied pressure of 40MPa, measurement carried in static He with a heating rate of 10°C per minute. 97
4.35 Temperature dependence of the electrical conductivity during the cooling step of $La_xBa_{1-x}TiO_3$ melted in argon and sintered by SPS at 1450°C in high vacuum (diffusion pump) for 10 minutes with a heating and cooling rate of 100°C per minute and applied pressure of 40MPa, measurement carried in static He with a cooling rate of 10°C per minute. 98
4.36 Temperature dependence of the absolute Seebeck coefficient of $La_xBa_{1-x}TiO_3$ melted in argon and sintered by SPS at 1450°C in high vacuum (diffusion pump) for 10 minutes with a heating and cooling rate of 100°C per minute and applied pressure of 40MPa, measurement carried in static He with a heating rate of 10°C per minute. 99

4.37 Temperature dependence of the power factor of $La_xBa_{1-x}TiO_3$ melted in argon and sintered by SPS at 1450°C in high vacuum (diffusion pump) for 10 minutes with a heating and cooling rate of 100°C per minute and applied pressure of 40MPa, measurement carried in static He with a heating rate of 10°C per minute. 100

4.38 Temperature dependence of the electrical conductivity of $La_xBa_{1-x}TiO_3$ melted in argon and sintered by SPS at different temperature in high vacuum (diffusion pump) for 10 minutes with a heating and cooling rate of 100°C per minute and applied pressure of 40MPa, carried in static air for measurements under 250°C, carried in flowing $H_2$5%/Ar95% for measurement over 250°C with a heating rate of 5°C per minute. 102

4.39 Temperature dependence of the thermal diffusivity of $La_xBa_{1-x}TiO_3$ melted in argon and sintered by SPS at different temperature in high vacuum (diffusion pump) for 10 minutes with a heating and cooling rate of 100°C per minute and applied pressure of 40MPa. Measurements carried in flowing $H_2$5%/Ar95%. 103

4.40 Arrhenius plot of the temperature dependence of the thermal diffusivity of $La_xBa_{1-x}TiO_3$ melted in argon and sintered by SPS at different temperature in high vacuum (diffusion pump) for 10 minutes with a heating and cooling rate of 100°C per minute and applied pressure of 40MPa. Measurements carried in flowing $H_2$5%/Ar95%. Linear fits for $La_{0.3}Ba_{0.7}TiO_3$. 104

4.41 Thermal diffusivity before and after measurements up to 800°C of $La_xBa_{1-x}TiO_3$ melted in argon and sintered by SPS at different temperature in high vacuum (diffusion pump) for 10 minutes with a heating and cooling rate of 100°C per minute and applied pressure of 40MPa. Measurements carried in flowing $H_2$5%/Ar95%. 104

5.1 Powder XRD patterns of melted $La_xCa_{1-x}TiO_3$. 108

5.2 Expanded powder XRD patterns of melted $La_xCa_{1-x}TiO_3$. 109

5.3 Plot of the lattice constants of $La_xCa_{1-x}TiO_3$ arc melted in argon. Error bars are smaller than the symbol size. 110

5.4 Plot of the lattice volume of $La_xCa_{1-x}TiO_3$ arc melted in argon. Error bars are smaller than the symbol size. 110

5.5 Powder XRD patterns of $La_xCa_{1-x}TiO_3$ melted in argon and sintered by SPS at 1450°C in high vacuum (diffusion pump) for 10 minutes with a heating and cooling rate of 100°C per minute and applied pressure of 40MPa. 112

5.6 Expanded powder XRD patterns of $La_xCa_{1-x}TiO_3$ melted in argon and sintered by SPS at 1450°C in high vacuum (diffusion pump) for 10 minutes with a heating and cooling rate of 100°C per minute and applied pressure of 40MPa. 113

5.7 Plot of the lattice edge length of the system $La_xCa_{1-x}TiO_3$ melted in argon and sintered by SPS at 1450°C in high vacuum (diffusion pump) for 10 minutes with a heating and cooling rate of 100°C per minute and applied pressure of 40MPa, calculated from the XRD patterns. Error bars are smaller than the symbol size. . . . 114

5.8 Plot of the lattice volume of the system $La_xCa_{1-x}TiO_3$ after arc melting with argon and after sintering by by SPS at 1450°C in high vacuum (diffusion pump) for 10 minutes with a heating and cooling rate of 100°C per minute and an apllied pressure of 40MPa, calculated from the XRD patterns. Error bars are smaller than the symbol size. 114

5.9 TGA plot of $La_xCa_{1-x}TiO_3$ in air from room temperature to 800°C, with a heating and cooling rate of 10°C per minute, heating step plotted in solid line, cooling step plotted in dash line. Powder from crushed pellets produced by arc melting in argon. 116

5.10 Influence of the doping level on the difference of mass after the TGA for the series $La_xCa_{1-x}TiO_3$, plot in Figure 5.9. Powder from crushed pellets produced by arc melting in argon. 116

5.11 TGA of $La_xCa_{1-x}TiO_3$ powders carried in air from room temperature to 1000°C, with a heating and cooling rate of 5°C per minute, gas flow of 100 $mL.min^{-1}$, heating step plotted in solid line, cooling step plotted in dash line. Powders from the crushed pellet SPS sintered at 1450°C in high vacuum (diffusion pump) for 10 minutes. . . . 118

5.12 Influence of the doping level on the difference of mass after the TGA for the series $La_xCa_{1-x}TiO_3$, plot in Figure 5.11. Powders from the crushed pellet SPS sintered at 1450°C in high vacuum (diffusion pump) for 10 minutes. 119

5.13 TGA of $La_xCa_{1-x}TiO_3$ powders carried in air from room temperature to 1000°C, with a heating and cooling rate of 5°C per minute, gas flow of 100 $mL.min^{-1}$, heating step plotted in solid line, cooling step plotted in dash line. Powders from the crushed pellet SPS sintered at different temperature in high vacuum (diffusion pump) for 10 minutes. 120

5.14 Powder XRD patterns of $La_{0.4}Ca_{0.6}TiO_3$ and $La_{0.6}Ca_{0.4}TiO_3$ SPS sintered at 1450°C. Powders oxidised in a muffle furnace at 1000°C, heating and cooling rate of 5°C per minute. XRD scan of 30 minutes. 121

5.15 Relative density of the samples $La_xCa_{1-x}TiO_3$ produced by arc melting in argon and sintered by SPS at different temperature in high vacuum (diffusion pump) for 10 minutes with a heating and cooling rate of 100°C per minute and an applied pressure of 40MPa 122

5.16 SEM images of $La_xCa_{1-x}TiO_3$ melted in argon and sintered by SPS at 1450°C in high vacuum (diffusion pump), with a heating and cooling rate of 100°C per minute and an applied pressure of 40MPa. 126

5.17 SEM images with EDX targets of $La_xCa_{1-x}TiO_3$ melted in argon and sintered by SPS at 1450°C in high vacuum (diffusion pump), with a heating and cooling rate of 100°C per minute and an applied pressure of 40MPa. EDX results in Tables 5.1 . . . 127

5.18 EDX spectra of the target number 8 of the sample $La_{0.4}Ca_{0.6}TiO_3$ melted in argon and sintered by SPS at 1450°C in high vacuum (diffusion pump)), with a heating and cooling rate of 100°C per minute and an applied pressure of 40MPa. 129

5.19 Normalised concentration of La, Ca and Ti detected by the WDX of $La_xCa_{1-x}TiO_3$ melted in argon and sintered by SPS at 1450°C in high vacuum (diffusion pump), with a heating and cooling rate of 100°C per minute and an applied pressure of 40MPa. 131

5.20 Ternary diagramme of the normalised concentration of La, Ca and Ti detected by the WDX of $La_xCa_{1-x}TiO_3$ melted in argon and sintered by SPS at 1450°C in high vacuum (diffusion pump), with a heating and cooling rate of 100°C per minute and an applied pressure of 40MPa. 132

5.21 Temperature dependence of the electrical conductivity of $La_xCa_{1-x}TiO_3$ after different SPS sintering in high vacuum (diffusion pump), measurement carried in static He with a heating rate of 10°C per minute. 134

5.22 Temperature dependence of the Seebeck coefficient of $La_xCa_{1-x}TiO_3$ after different SPS sintering temperature, sintering made in high vacuum (diffusion pump), measurement carried in static He with a heating rate of 10°C per minute and a set gradient of 50°C. 135

5.23 Temperature dependence of the power factor of $La_xCa_{1-x}TiO_3$ after a SPS sintering at 1450°C in high vacuum (diffusion pump) for 10 minutes with a heating and cooling rate of 100°C/min and an applied pressure of 40 MPa of the powder synthesized by arc melting in argon, measurement carried in static He with a heating rate of 10°C per minute and a set gradient of 50°C. 136

5.24 Temperature dependence of the electrical condutivity of $La_xCa_{1-x}TiO_3$ after a SPS sintering at 1450°C in high vacuum (diffusion pump) for 10 minutes with a heating and cooling rate of 100°C/min and an applied pressure of 40 MPa of the powder synthesized by arc melting in argon, measurement carried in 5% H_2/95%Ar with a heating rate of 5°C per minute. 138

5.25 Temperature dependence of the thermal diffusivity of $La_xCa_{1-x}TiO_3$ after a SPS sintering different temperature in high vacuum (diffusion pump) for 10 minutes with a heating and cooling rate of 100°C/min and an applied pressure of 40 MPa of the powder synthesized by arc melting in argon, measurement carried in N_2 flow. 139

5.26 Arrhenius plot of the temperature dependence of the thermal diffusivity of $La_xCa_{1-x}TiO_3$ after a SPS sintering different temperature in high vacuum (diffusion pump) for 10 minutes with a heating and cooling rate of 100°C/min and an applied pressure of 40 MPa of the powder synthesized by arc melting in argon, measurement carried in N_2 flow. 140

6.1 XRD patterns of $La_xCa_{1-(3/2x)}TiO_3$ melted in argon and sintered by SPS at 1450°C in high vacuum (diffusion pump), with a heating and cooling rate of 100°C per minute and an applied pressure of 40MPa. 143

6.2 Expanded XRD patternd of $La_xCa_{1-(3/2x)}TiO_3$ melted in argon and sintered by SPS at 1450°C in high vacuum (diffusion pump), with a heating and cooling rate of 100°C per minute and an applied pressure of 40MPa. 144

6.3 Expanded XRD patterns of $La_xCa_{1-(3/2x)}TiO_3$ and $La_xCa_{(1-x)}TiO_3$ melted in argon and sintered by SPS at 1450°C in high vacuum (diffusion pump), with a heating and cooling rate of 100°C per minute and an applied pressure of 40MPa. 144

6.4 Selection of SEM images of $La_xCa_{1-(3/2x)}TiO_3$ melted in argon and sintered by SPS at 1450°C in high vacuum (diffusion pump), with a heating and cooling rate of 100°C per minute and an applied pressure of 40MPa. 147

6.5 Temperature dependence of the electrical conductivity of $La_xCa_{1-(3/2x)}TiO_3$ melted in argon and sintered by SPS at 1450°C in high vacuum (diffusion pump) for 10 minutes with a heating and cooling rate of 100°C per minute and applied pressure of 40MPa, measurement carried in static He with a heating rate of 10°C per minute and a set gradient of 50°C. 150

6.6 Temperature dependence of the Seebeck coefficient of $La_xCa_{1-(3/2x)}TiO_3$ melted in argon and sintered by SPS at 1450°C in high vacuum (diffusion pump) for 10 minutes with a heating and cooling rate of 100°C per minute and applied pressure of 40MPa, measurement carried in static He with a heating rate of 10°C per minute and a set gradient of 50°C. 150

6.7 Temperature dependence of the power factor of $La_xCa_{1-(3/2x)}TiO_3$ melted in argon and sintered by SPS at 1450°C in high vacuum (diffusion pump) for 10 minutes with a heating and cooling rate of 100°C per minute and applied pressure of 40MPa, measurement carried in static He with a heating rate of 10°C per minute and a set gradient of 50 °C. 151

10.1 WDX element map of $La_{0.2}Ba_{0.8}TiO_3$, concentration in weight%. 180

10.2 EPMA backscattered electrons image of $La_{0.2}Ba_{0.8}TiO_3$, element composition of the points in Table 10.1. 180

10.3 WDX element map of $La_{0.3}Ba_{0.7}TiO_3$, concentration in weight%. 182

10.4 EPMA backscattered electrons image of $La_{0.3}Ba_{0.7}TiO_3$, element composition of the points in Table 10.2. 182

10.5 WDX element map of $La_{0.5}Ba_{0.5}TiO_3$, concentration in weight%. 184

10.6 EPMA backscattered electrons image of $La_{0.5}Ba_{0.5}TiO_3$, element composition of the points in Table 10.3. 184

10.7 WDX element map of $La_{0.6}Ba_{0.4}TiO_3$, concentration in weight%. 186

10.8 EPMA backscattered electrons image of $La_{0.6}Ba_{0.4}TiO_3$, element composition of the points in Table 10.4. 186

10.9 WDX element map of $La_{0.8}Ba_{0.2}TiO_3$, concentration in weight%. 188

10.10 EPMA backscattered electrons image of $La_{0.8}Ba_{0.2}TiO_3$, element composition of the points in Table 10.5. 188

10.11 WDX element map of $La_{0.9}Ba_{0.1}TiO_3$, concentration in weight%. 189

10.12 Full data of the temperature dependence of the Seebeck coefficient of $CaTiO_3$ melted in argon and sintered by SPS at 1450°C in high vacuum (diffusion pump) for 10 minutes with a heating and cooling rate of 100°C per minute and applied pressure of 40MPa, measurement carried in static He with a heating rate of 10°C per minute and a set gradient of 50°C. 189

List of Tables

2.1 Theoretical crystal structures from the Godlshmidt's tolerance factor. 20

2.2 Summary of the thermoelectric properties of some doped $SrTiO_3$ from the literature. Data partially taken from ref [127], data taken graphically from the publications if not written in the text by the authors, when not included in the publications the power factor σS^2T where calculated with the values obtained graphically. *Text claims at 1000K but figures show at 1100K. 25

2.3 Table of the approximative conductivity of doped $BaTiO_3$ reproduced with permission from ref [158]. 32

3.1 Mass of precursors to produce 2.5 g of $LaTiO_3$ 41

3.2 List of compositions and mass of precursors to produce 2.5 g of $La_xBa_{1-x}TiO_3$ by arc melting and the SPS sintering temperature used. 42

3.3 List of compositions and mass of precursors to produce 2.5 g of $La_xCa_{1-x}TiO_3$ by arc melting and the SPS sintering temperatures used. 43

3.4 List of compositions and mass of precursors to produce 2.5 g of $La_xCa_{1-3/2x}TiO_3$ by arc melting, and the SPS sintering temperatures used. 43

4.1 EDX targets results of Figures 4.22. 80

4.2 Element composition of several points of $La_{0.1}Ba_{0.9}TiO_3$ by EPMA of Figure 4.25, concentration in atomic %. 83

4.3 Element composition of several points of $La_{0.4}Ba_{0.6}TiO_3$ by EPMA of Figure 4.27, concentration in atomic%. 87

4.4 Element composition of several points of $La_{0.7}Ba_{0.3}TiO_3$ by EPMA of Figure 4.29. Concentration in atomic%. 88

5.1 EDX targets results of Figures 5.17. 128

6.1 EDX targets result of $La_{0.1}Ca_{0.85}TiO_3$ of Figure 6.4b. 148

6.2 EDX targets result of $La_{0.2}Ca_{0.7}TiO_3$ of Figure 6.4d. 148

6.3 EDX targets result of $La_{0.3}Ca_{0.55}TiO_3$ of Figures 6.4e and 6.4f. 148

10.1 Element composition of several points of $La_{0.2}Ba_{0.8}TiO_3$ by EPMA of Figure 10.2, concentration in atomic%. 179

10.2 Element composition of several points of $La_{0.3}Ba_{0.7}TiO_3$ by EPMA of Figure 10.4. Concentration in atomic%. 181

10.3 Normalised element composition of several points of $La_{0.5}Ba_{0.5}TiO_3$ by EPMA of Figure 10.6, total not normalised. 183

10.4 Element composition of several points of $La_{0.6}Ba_{0.4}TiO_3$ by EPMA of Figure 10.8, concentration in atomic%. 185

10.5 Element composition of several points of $La_{0.8}Ba_{0.2}TiO_3$ by EPMA of Figure 10.10, concentration in atomic%. 187